MICROSCOPIC ORIGIN OF MAGNETISM IN THE HEMATITE-ILMENITE SYSTEM

by
Seyed Hasan Sadat Nabi

PhD thesis

Submitted in Partial Fulfillment of the
Requirements for the Degree of
Dr. rer. nat.

at the

Faculty of Geosciences
Ludwig-Maximilians University
Munich, Germany

February 2010

Supervisor:
PD Dr. Rossitza Pentcheva

Supervisor:
Prof. Dr. Wolfgang Moritz

Date of Oral Examination: 27.05.2010

Ehrenwörtliche Versicherung

Ich versichere hiermit ehrenwörtlich, dass die Dissertation von mir selbständig und ohne Beihilfe angefertigt worden ist.

Seyed Hasan Sadat Nabi
München, February 2010

Erklärung

Hiermit erkläre ich, dass die Dissertation noch nicht in einem anderen Prüfungsverfahren vorgelegt und bewertet wurde.

Hiermit erkläre ich, dass ich mich nicht anderweitig einer Doktorprüfung ohne Erfolg unterzogen habe.

Seyed Hasan Sadat Nabi
München, February 2010

Contents

Introduction **1**

1 Introduction to *Ab-initio* Calculations **5**
- 1.1 Many-body quantum mechanics 5
  - 1.1.1 Principle of quantum mechanics 5
  - 1.1.2 Expectation values 6
  - 1.1.3 The Born-Oppenheimer approximation 8
- 1.2 Density Functional Theory 9
  - 1.2.1 The Kohn-Sham method 12
  - 1.2.2 The LDA and GGA potentials 15
  - 1.2.3 Beyond LDA/GGA: The LDA+U method 17
  - 1.2.4 Solving the Kohn-Sham equation 22
- 1.3 The WIEN2K code 25

2 Properties of Bulk α-Fe_2O_3 and $FeTiO_3$ **29**
- 2.1 Calculational details 30
- 2.2 Bulk properties of $FeTiO_3$ 31
  - 2.2.1 Structural properties 31
  - 2.2.2 Equation of state 32
  - 2.2.3 Electronic and magnetic properties: GGA vs. GGA+U 33
- 2.3 Bulk properties of α-Fe_2O_3 35
- 2.4 Summary 38

3 Origin of Magnetism in Hematite-Ilmenite Heterostructures **39**
- 3.1 Fe_2O_3-$FeTiO_3$ phase diagram 39
- 3.2 Fe_2O_3-$FeTiO_3$ interface 40
  - 3.2.1 Structural relaxation 44
  - 3.2.2 Compensation mechanism and energetic trends 44
  - 3.2.3 Phase diagram 45
  - 3.2.4 Summary 48
- 3.3 Strain effect 48
- 3.4 Magnetic exchange interaction parameters 53
  - 3.4.1 Calculation of magnetic interaction parameters 53
  - 3.4.2 Magnetic exchange interaction of the end members 55
  - 3.4.3 Magnetic interactions at the Fe_2O_3/$FeTiO_3$ interface 57
  - 3.4.4 Effect of strain on the magnetic interactions 60
  - 3.4.5 Summary 62

4 Bulk Properties of $EuTiO_3$ 63
4.1 Equilibrium lattice constant andbulk modulus 64
4.2 Electronic and magnetic structures of $EuTiO_3$ 65
4.3 Calculation of exchange integrals 66
4.4 Summary 67

5 Comparative Study on $EuLiH_3$ and $EuTiO_3$ 69
5.1 Results and discussion 70
5.2 Summary 74

6 Conclusions and Perspectives 75

A Functional Derivatives 79

B The Table of Magnetic Configurations 81

C The Interaction Type Matrix 85

D The Connectivity Matrix 87

Manuscript M1 89

Manuscript M2 95

Manuscript M3 101

Manuscript M4 109

Manuscript M5 121

Bibliography 133

Acknowledgements 135

Publications 137

Curriculum Vitae 139

List of Figures

1.1 WIEN2K flowchart 28

2.1 Crystal structure of Fe_2O_3 30
2.2 Ilmenite structure 31
2.3 Magnetic moment and total energy of ilmenite 32
2.4 DOS of ilmenite 34
2.5 Magnetic moment and total energy of hematite 36
2.6 DOS of hematite 37

3.1 Fe_2O_3-$FeTiO_3$ phase diagram 40
3.2 Structures modelled in a 30-atom unit cell 41
3.3 Structures modelled in a 60-atom unit cell 33% Ti-doped Fe_2O_3 . . . 42
3.4 Structures modelled for 17%, 50%, 66% and 83% Ti-doped Fe_2O_3 . . 43
3.5 DOS of 33% Ti-doped in Fe_2O_3 46
3.6 DOS of $Fe_{2-x}Ti_xO_3$ with x = 17%, 50%, 66% and 83% 47
3.7 Formation energy versus ilmenite concentration 48
3.8 TEM image of hematite exsolution lamellae 49
3.9 The c/a-ratio, volume and formation energy vs. ilmenite concentration 51
3.10 Density of states of $Fe_{1.67}Ti_{0.33}O_3$ 52
3.11 Definition of the pair magnetic exchange parameters 54
3.12 The magnetic pair interaction parameters 56
3.13 Structures used for magnetic interaction parameters at interface . . . 58
3.14 Comparison of magnetic interaction parameters at interface 59
3.15 The magnetic pair interaction parameters on an Al_2O_3 substrate . . . 61

4.1 Crystal structure of cubic $EuTiO_3$ 64
4.2 Total energy versus volume of cubic $EuTiO_3$ 65
4.3 Total and partial DOS of $EuTiO_3$ 66

5.1 Variation in J_1 and J_2 vs. U in $EuLiH_3$ 70
5.2 Variation in J_1 and J_2 vs. lattice parameter of $EuLiH_3$ 71
5.3 Variation in the relative energy vs. volume of $EuLiH_3$ 72
5.4 DOS of ferromagnetic $EuLiH_3$ 73
5.5 Variation in the band gap of $EuLiH_3$ and $EuTiO_3$ 73

List of Tables

2.1 Lattice parameters and bulk modulus of ilmenite 33
2.2 Band gap of ilmenite within HF, B3LYP, GGA, GGA+U and Exp. . 35
2.3 Magnetic moments and energy differences of ilmenite 35
2.4 Lattice parameters and bulk modulus of hematite 37

3.1 The cation-anion distances in the system 44
3.2 The experimental lattice constants of Fe_2O_3, $FeTiO_3$ and Al_2O_3 . . . 49
3.3 Néel temperature for hematite and ilmenite 57
3.4 The J_m^q for Fe_2O_3, $FeTiO_3$ and interface 59
3.5 The J_m^q for Fe_2O_3, $FeTiO_3$ and interface on an Al_2O_3 substrate 60

4.1 Values of J_1 and J_2 of $EuTiO_3$ 67

5.1 Relative energies of various magnetic structures of $EuLiH_3$ 70

B.1 E_{rel} and spin arrangements in Fe_2O_3 82
B.2 E_{rel} and spin arrangements in $FeTiO_3$ 83
B.3 E_{rel} and spin arrangements in interface-a 83
B.4 E_{rel} and spin arrangements in interface-b 84

Introduction

Transition metal oxides show a series of interesting and exciting magnetic and electronic properties. Among all these intriguing features, magnetism is a phenomenon occurring both at the microscopic and macroscopic scale and there is a particular interest to understand its origin. Not only inherent magnetic materials can show magnetic behavior, but also magnetism can occur spontaneously at the interface even of nonmagnetic materials [1].

Interfaces of complex oxides provide rich physics and new possibilities for functional devices in future applications, particularly in the growing field of spintronics [2, 3]. Spintronics is an emerging technology that exploits the intrinsic spin of the electron and its associated magnetic moment. This allows the elaboration of a new generation of devices, which are smaller and more versatile than those currently working based on electrical charge carriers. Although most of the interest on interface phenomena in the past years has been concentrated on heterostructures containing perovskites, this is not the only family of structures showing challenging properties. Already in the 1950's, Akimoto and Ishikawa [4] reported a remanent magnetization up to 900 K in the Fe_2O_3-$FeTiO_3$ system, although the end members are a canted antiferromagnet (CAF) (T_N = 948 K) and a room temperature paramagnet (T_N = 56 K), respectively, both with a corundum(-derived) structure. The system has a complex phase diagram due to the interplay between cation and magnetic ordering, as well as exsolution processes [5]. Exsolution phenomena occur down to the nanoscale (1-3 nm), which corresponds to a thickness of only 1-2 unit cells. This system has attracted attention in paleomagnetism as a possible cause of magnetic anomalies in the Earth's deep crust and on other planets [6].

Recently, Ti doped α-Fe_2O_3 has also received considerable attention in the spintronics area for future device applications [7, 8]. Most of the efforts on designing ferromagnetic semiconductors operating at room temperature concentrate on homogeneous doping of semiconductors with magnetic impurities [3, 9–12]. Furthermore, since the type of conductivity (*p*- or *n*-type) can be tuned by the concentration of Ti doped into hematite, this system is interesting for use in electronic devices such as low-voltage varistors [13].

Nowadays, with an increased ability to grow oxide heterostructures with atomic scale control, intensive theoretical study is demanded to shed more light on the origin of novel physical phenomena occurring at oxide interfaces. The application of quantum theory to solids has revolutionized our understanding of materials and their properties. To explain the unusually stable remanent magnetization observed in hematite-ilmenite natural samples, Robinson *et al.* suggested the presence of uncompensated spins within the mixed Fe^{2+}/Fe^{3+} contact layer between hematite and ilmenite lamellae. The so-called *lamellar magnetism hypothesis* [14] is based on Monte Carlo simulations with empirical magnetic and chemical parameters, but a material-specific understanding of this phenomenon was lacking at the beginning of this study. Therefore, in this work, systematic *ab-initio* calculations are performed in order to provide an atomistic insight into this phenomenon.

The goal of this study is (i) to identify the compensation mechanism and its influence on the electronic and magnetic properties, (ii) to determine the relative stability of layered configurations versus solid solutions and (iii) to extract accurate magnetic interaction parameters for the interface that are not accessible from experiment. These parameters can then be used for Monte Carlo simulations to study the equilibrium thermodynamical properties and magnetic ordering of the system at the mesoscopic scale.

To understand the underlying mechanisms of this system and to extract the magnetic interaction parameters, density functional theory (DFT) calculations are carried out with the all-electron full-potential linear augmented plane wave (FP-LAPW) method as implemented in the WIEN2K package [15]. Correlation effects are taken into account within the generalized gradient approximation by adding a Hubbard parameter (GGA+ U) [16]. By systematically varying the concentration, distribution and charge state of Ti (Fe) in a hematite (ilmenite) host, we compile a phase diagram of the stability with respect to the end members. Besides the *lamellar magnetism hypothesis* (Fe^{2+}, Fe^{3+}), further possible compensation mechanisms, *e.g.*, through Ti^{3+}/Ti^{4+} or $Fe^{3+}/Ti^{3+}$are considered in this work.

Another important aspect is the effect of strain on $Fe_{2-x}Ti_xO_3$ films grown on different substrates. Hematite/ilmenite films are typically grown on an Al_2O_3(0001)-substrate which causes a strong compressive strain. To explore this effect, a comparative study is carried out in $Fe_{2-x}Ti_xO_3$ films grown on three different substrates: Fe_2O_3(0001), $FeTiO_3$(0001) and Al_2O_3(0001). The effect of strain on the compensation mechanism is investigated. Also, the energetic stability of different arrangements (layered vs. solid solutions) strained on different substrates are considered. Furthermore, strain induced by the substrate can be used to tune the electronic properties. Thus, the influence of the strain on the electronic properties is investigated.

A further topic of research is the electronic structure and magnetism of $EuTiO_3$ and $EuLiH_3$. $EuTiO_3$ (ETO) is a perovskite with cubic symmetry (space group $Pm3m$) at ambient conditions and magnetically ordered below 5.5 K [17–19]. The dielectric permittivity of ETO exhibits an anomaly at the magnetic ordering temperature [17], suggesting magnetoelectric coupling of the polarization and magnetization. However, compared to other well-known magnetoelectrics [20–22], ETO has been less investigated. Although magnetic susceptibility measurements on ETO show features of antiferromagnetic ordering, these have not been investigated in detail, presumably due to the fact that naturally occurring Eu has a very large absorption cross-section for thermal neutrons. The results of DFT calculations for ETO are reported, using an all-electron approach and taking into account electronic correlations within the LSDA/GGA + U method. The system shows a sensitive balance between antiferromagnetic (G-type) and ferromagnetic states for realistic values of U. Furthermore, a comparative study is done between $EuTiO_3$ and ferromagnetic $EuLiH_3$ and the marked difference in magnetic behavior and magnitude of the nearest-neighbor exchange interaction are discussed.

This thesis is organized in six Chapters as following: In **Chapter 1** the theoretical methods are introduced. The electronic and magnetic properties of bulk hematite and ilmenite are presented in **Chapter 2**. **Chapter 3** is the main chapter showing the results on the origin of magnetism in the Fe_2O_3-$FeTiO_3$ system. The effect of substrate induced strain on the stability and electronic properties of Fe_2O_3-$FeTiO_3$ heterostructures is investigated. Furthermore, the magnetic coupling parameters at the Fe_2O_3-$FeTiO_3$ interface are extracted here for the first time from first principles. **Chapter 4** is devoted to the electronic and magnetic properties of bulk $EuTiO_3$. Thereafter, a comparative study between $EuTiO_3$ and $EuLiH_3$ is carried out in **Chapter 5**. Finally, the conclusions and future perspectives are presented in **Chapter 6**.

Chapter 1

Introduction to *Ab-initio* Calculations

Exploring the electronic, magnetic and structural properties of materials is one of the most interesting subjects in condensed matter physics. To understand the material properties from a theoretical point of view, quantum mechanics provides a rigorous tool to study the behavior of materials at the atomic scale. The main factor to determine is how atoms interact in solids and how these interactions influence their properties and behavior. However, this constitutes a many-body problem for which, with the available mathematical tools, exists no analytical solution. Although the exact solution is not known, there are many methods to deal with many-body problems by simplifying the general Hamiltonian with the introduction of some approximations. In this chapter, Density Functional Theory (DFT) is introduced as a method dealing with many-body systems. Therefore, in the following section, the main concepts of many-body quantum mechanics are briefly discussed. With the introduced terminology, a description of DFT is followed, in relation to the implementation used in this study. Finally, a brief description of the code used for the calculations is presented in the last section of this chapter.

1.1 Many-body quantum mechanics

It is worth to introduce some of the principles of many-body quantum mechanics applied to a system consisting of atomic nuclei and electrons. Thereafter, the Born-Oppenheimer approximation, used to decouple the nuclear motion from that of the electrons, is described in detail. As a consequence, the many-body Hamiltonian is reduced to a system of N interacting electrons moving in a static potential generated by the charge of the nuclei.

1.1.1 Principle of quantum mechanics

Quantum mechanics is based on the fundamental concepts of wave functions and operators [23, 24]. Wave functions are square-integrable functions of the system parameters and time which provide a complete description of the system. For a system containing atomic nuclei and electrons, the system parameters are the positions of all particles in the system. In order to refer to electronic and nuclear variables, small and capital letters are used respectively, *i.e.*, $\{\mathbf{r}_i, \mathbf{R}_j\}$. The wave function of the system is thus typically denoted by $\Psi(\mathbf{r}_i, \mathbf{R}_j; t)$. Another useful convention, to ease the typesetting of the related mathematical expressions, is to use Dirac's notation [25]. In this reference, the wave function is written as $|\psi\rangle$, known as a ket, which is one of the many representations of a single state-vector in Hilbert space. There also exists a dual space containing a bra vector, denoted by $\langle\psi|$ and defined as the conjugate of a ket. The scalar product of these vectors is written as a braket: $\langle\psi|\phi\rangle$. A set of normalized vectors can also be defined, such that the scalar product of the vector with its own conjugate equals unity:

$$\langle\psi|\psi\rangle = \int \prod_i d^3\mathbf{r}_i \prod_j d^3\mathbf{R}_j \psi^\star(\mathbf{r}_i, \mathbf{R}_j; t)\psi(\mathbf{r}_i, \mathbf{R}_j; t) = 1. \tag{1.1}$$

The operator corresponding to some observable is often written as $\hat{O}$. In general, when this operator acts on some state-vector $|\psi\rangle$, a different state-vector $|\phi\rangle$ will result:

$$\hat{O}|\psi\rangle = |\phi\rangle. \tag{1.2}$$

However, for each operator there exists a set of normalized eigenstates $\{|\chi_n\rangle\}$ which remain unchanged by the action of the operator, *i.e.*:

$$\hat{O}|\chi_n\rangle = \lambda_n|\chi_n\rangle, \tag{1.3}$$

where the constant λ_n is the eigenvalue of state $|\chi_n\rangle$.

The postulates of quantum mechanics [26] affirm that for a system in state $|\psi\rangle$:

1. The outcome of a measurement of a dynamical variable is always one of the eigenvalues λ_n of the corresponding operator.

2. Immediately following a measurement, the state-vector collapses to the eigenstate $|\chi_n\rangle$ corresponding to the measured eigenvalue.

3. The probability of such measurement is:

$$P(\lambda_n) = |\langle\chi_n|\phi\rangle|^2. \tag{1.4}$$

1.1.2 Expectation values

From Sturm-Liouville theory, the eigenstates of the operator $\hat{O}$ form a complete set, meaning that any valid state-vector can be expressed as a linear superposition of the eigenstates with appropriate coefficients $\{c_n\}$:

$$|\psi\rangle = \sum_n c_n|\chi_n\rangle. \tag{1.5}$$

The coefficients are easily obtained for hermitian operators because the eigenstates are orthogonal, which means that the scalar product of two different eigenstates vanishes:

$$\langle\chi_n|\chi_m\rangle = \delta_{nm}. \tag{1.6}$$

By taking the scalar product on both sides of equation (1.5) with the eigenstates $\langle\chi_m|$, or by using the following concise expression of completeness:

$$\sum_n |\chi_n\rangle\langle\chi_n| = 1, \tag{1.7}$$

the expansion coefficients $\{c_n\}$ are determined as:

$$c_n = \langle\chi_n|\psi\rangle, \tag{1.8}$$

where

$$|\psi\rangle = \sum_n |\chi_n\rangle\langle\chi_n|\psi\rangle. \tag{1.9}$$

Applying this result to the quantity $\langle\psi|\hat{O}|\psi\rangle$:

$$\begin{aligned}
\langle\psi|\hat{O}|\psi\rangle &= \sum_m \langle\chi_m|\psi\rangle^\star \langle\chi_m|\hat{O}\sum_n |\chi_n\rangle\langle\chi_n|\psi\rangle \\
&= \sum_m \langle\chi_m|\psi\rangle^\star \sum_n \lambda_n \langle\chi_m|\chi_n\rangle\langle\chi_n|\psi\rangle \\
&= \sum_m \langle\chi_m|\psi\rangle^\star \sum_n \lambda_n \delta_{nm}\langle\chi_n|\psi\rangle \\
&= \sum_m \lambda_m |\langle\chi_m|\psi\rangle|^2,
\end{aligned} \tag{1.10}$$

it is evident that only the eigenvalues $\{\lambda_n\}$ with corresponding probability $|\langle\chi_n|\psi\rangle|^2$ are the possible outcomes of the measurement of observable O, corresponding to operator $\hat{O}$. The quantity $\langle\psi|\hat{O}|\psi\rangle$ is interpreted as an expectation value of O for a system in state $|\psi\rangle$. The normalization condition establishes that the sum of probabilities is unity. Therefore, the expectation value is uniquely determined by the eigenvalues $\{\lambda_n\}$.

The final postulate of quantum mechanics states that the state-vector evolves in time according to the time-dependent Schrödinger equation:

$$\hat{H}|\Psi\rangle = i\hbar\frac{\partial}{\partial t}|\Psi\rangle, \tag{1.11}$$

where operator $\hat{H}$ is the energy operator and it is called the Hamiltonian of the system. For a system consisting of atomic nuclei and electrons, the non-relativistic Hamiltonian takes the form:

$$\begin{aligned}
\hat{H} = &-\frac{\hbar^2}{2}\sum_i \frac{\nabla^2_{\mathbf{r}_i}}{m_i} - \frac{\hbar^2}{2}\sum_i \frac{\nabla^2_{\mathbf{R}_i}}{M_i} - \frac{1}{4\pi\varepsilon_0}\sum_{i,j}\frac{e^2 Z_j}{|\mathbf{r_i} - \mathbf{R}_j|} \\
&+\frac{1}{8\pi\varepsilon_0}\sum_{i\neq j}\frac{e^2}{|\mathbf{r}_i - \mathbf{r}_j|} + \frac{1}{8\pi\varepsilon_0}\sum_{i\neq j}\frac{e^2 Z_i Z_j}{|\mathbf{R}_i - \mathbf{R}_j|},
\end{aligned} \tag{1.12}$$

with m_i and M_j the mass of the electron and of the nucleus positioned at $\mathbf{r}_i$ and $\mathbf{R}_j$, respectively.

The first two terms on the right hand side represent the kinetic energy operator of electrons and nuclei, respectively. The remaining terms describe the Coulomb interaction between electron and nucleus, between the electrons and between the nuclei, respectively. Finally, after solving the time-independent Schrödinger equation, the eigenvalue equation and the time-dependent wave function of the Hamiltonian takes a simple form. The following separation of variables is done:

$$|\Psi\rangle = \Psi(\mathbf{r}, \mathbf{R}; t) = \psi(\mathbf{r}, \mathbf{R})\Theta(t), \tag{1.13}$$

which leads to the following equations:

$$\begin{aligned} \hat{H}\psi(\mathbf{r}, \mathbf{R}) &= E\psi(\mathbf{r}, \mathbf{R}) && (1.14) \\ i\hbar\frac{d}{dt}\Theta(t) &= E\Theta(t), && (1.15) \end{aligned}$$

where E is the separation constant.

The ordinary differential equation (1.15) can be easily solved so that the eigenfunctions of the Hamiltonian with energy E take the form:

$$\Psi(\mathbf{r}, \mathbf{R}; t) = \psi(\mathbf{r}, \mathbf{R})\mathrm{e}^{-\mathrm{i}\frac{E}{\hbar}t}. \tag{1.16}$$

The states which are the eigenfunctions of the Hamiltonian are known as stationary states because the expectation value of any time-independent operator for these states is also independent in time:

$$\begin{aligned} \langle\Psi|\hat{O}|\Psi\rangle &= \int\prod_i d^3\mathbf{r}_i\prod_j d^3\mathbf{R}_j\Psi^\star(\mathbf{r}_i, \mathbf{R}_j; t)\hat{O}\Psi(\mathbf{r}_i, \mathbf{R}_j; t) \\ &= \int\prod_i d^3\mathbf{r}_i\prod_j d^3\mathbf{R}_j\psi^\star(\mathbf{r}_i, \mathbf{R}_j)\mathrm{e}^{\mathrm{i}\frac{E}{\hbar}t}\psi(\mathbf{r}_i, \mathbf{R}_j)\mathrm{e}^{-\mathrm{i}\frac{E}{\hbar}t} \\ &= \langle\psi(\mathbf{r}, \mathbf{R})|\hat{O}|\psi(\mathbf{r}, \mathbf{R})\rangle. && (1.17) \end{aligned}$$

From this point, the exponential time-dependent part of the eigenstates will be neglected to deal only with the stationary state $|\psi\rangle$ exclusively. Therefore, to determine the state of the system $\psi(\mathbf{r}, \mathbf{R}) = |\psi\rangle$, the corresponding Schrödinger equation has to be solved:

$$\hat{H}\Psi(\mathbf{r}, \mathbf{R}) = E\Psi(\mathbf{r}, \mathbf{R}), \tag{1.18}$$

which constitutes a many-body problem which cannot be treated analytically in systems containing more than two interacting particles.

1.1.3 The Born-Oppenheimer approximation

Since in practical systems the Hamiltonian contains an order of $\sim 10^{23}$ particles, the many-body problem cannot be solved without introducing some approximations. As the electromagnetic forces on both electrons and nuclei are of the same order of magnitude, the change in their momenta as a result of these forces must also be the same. Then, since the mass of electrons is much smaller than that of the nuclei, they must accordingly have much higher velocity (10^3 m/s). Therefore, it is plausible that on the typical time scale of nuclear motion, the electrons will very rapidly relax to the instantaneous ground-state configuration.

Thus, when solving the time-independent Schrödinger equation, the nuclei can be regarded as stationary and the electronic part can be solved first. Given the energy of the system in that configuration, the nuclear contribution is calculated then with classical mechanics and added to the electronic solution. This separation of electronic and nuclear motion is known as the Born-Oppenheimer or adiabatic approximation. The assumption of an instantaneous electronic equilibrium for every nuclear configuration implies that the electronic wave function is a solution of the Schrödinger equation for a Hamiltonian (1.12) with fixed nuclear positions as following:

$$\begin{aligned}\hat{H} = -\frac{\hbar^2}{2}\sum_i \frac{\nabla^2_{\mathbf{r}_i}}{m_i} - \frac{1}{4\pi\varepsilon_0}\sum_{i,j}\frac{e^2 Z_j}{|\mathbf{r}_i - \mathbf{R}_j|} + \frac{1}{8\pi\varepsilon_0}\sum_{i\neq j}\frac{e^2}{|\mathbf{r}_i - \mathbf{r}_j|} \\ +\frac{1}{8\pi\varepsilon_0}\sum_{i\neq j}\frac{e^2 Z_i Z_j}{|\mathbf{R}_i - \mathbf{R}_j|}.\end{aligned} \tag{1.19}$$

This Hamiltonian describes the electronic motion in the external potential produced by the nuclei. Subsequently, the nuclei can be shifted in order to minimize the forces on the atoms. The forces are calculated through the first derivative of the Hamiltonian with respect to the positions. Therefore, the Hamiltonian can be written in the following form:

$$\hat{H} = \hat{T} + \hat{V}_{ext} + \hat{V}_{ee} + \hat{V}_{NN}, \tag{1.20}$$

where the last term ($\hat{V}_{NN}$) contributes to the total energy as a constant amount. As a consequence, removing this term from the Hamiltonian will not affect the corresponding eigenfuntions. The resulting Hamiltonian becomes then:

$$\hat{H} = \hat{H}_e + \hat{V}_{NN}, \tag{1.21}$$

with:

$$\hat{H}_e = \hat{T} + \hat{V}_{ext} + \hat{V}_{ee}. \tag{1.22}$$

Equation (1.22) represents the electronic part of the Hamiltonian, where $\hat{T}$ represents the kinetic energy of the electrons, $\hat{V}_{ee}$ the electron-electron repulsions and $\hat{V}_{ext}$ the electron-nucleus interactions.

1.2 Density Functional Theory

Despite the separation of electronic and nuclear motion introduced with the Born-Oppenheimer approximation, the many-body Hamiltonian (1.21) is still too complex to be solved for a large system. In order to deal with realistic materials, further simplifications have to be made.

In the historically important Hartree-Fock (HF) approximation, the solution was constructed with Slater determinants. However, while the HF method fulfils the Pauli exclusion principle, the correlation effects are not taken into account. Therefore, the ground state energy converges to a minimum, known as the HF limit, which from variational principle is always higher than the actual ground state of the system. Moreover, the HF method is numerically demanding, both in time and memory space, and its implementation in periodic systems is difficult. For more details on the HF approximation the reader is referred to Ref. [27].

A breakthrough in the parameter free description of real materials was reached with the development of density functional theory by Hohenberg and Kohn [28] and Kohn and Sham [29]. With the introduction of DFT, the problem of finding the ground state energy was simplified to that of determining the electron density, rather than explicitly specifying the many-body wave function. To accomplish this simplification, which retains the exact description of the many-body interactions, a mapping is done from a system of interacting electrons to a fictitious system of non-interacting quasi-particles with the same ground state density.

Introducing some basic notation, in the framework of the Born-Oppenheimer approximation, the Coulomb potential arising from the nuclei is treated as a static external potential V_{ext} of the form:

$$V_{ext}(\mathbf{r}) = -\frac{1}{4\pi\varepsilon_0}\sum_j \frac{eZ_j}{|\mathbf{r}-\mathbf{R}_j|}, \tag{1.23}$$

so that, by defining the remaining part of Eq. (1.22) as:

$$\hat{F} = \hat{T} + \hat{V}_{ee} = -\frac{\hbar^2}{2}\sum_i \frac{\nabla^2_{\mathbf{r}_i}}{m_i} + \frac{1}{8\pi\varepsilon_0}\sum_{i\neq j}\frac{e^2}{|\mathbf{r}_i-\mathbf{r}_j|}, \tag{1.24}$$

the electronic Hamiltonian becomes $\hat{H}_e = \hat{F} + \hat{V}_{ext}$, with $\hat{V}_{ext} = \sum_i eV_{ext}(\mathbf{r}_i)$.

Since $\hat{F}$ is the same for all N-electron systems, the Hamiltonian and hence the ground state $|\Psi_0\rangle$, are completely determined by N and $V_{ext}(\mathbf{r})$. In the following, the first and second theorems of density functional theory, as introduced in 1964 by Hohenberg and Kohn [28], are described.

First theorem: The external potential $V_{ext}(\mathbf{r})$ is uniquely determined by the corresponding ground state electron density $n(\mathbf{r})$. In other words, there is a one-to-one correspondence between the ground state density $n(\mathbf{r})$ and the external potential $V_{ext}(\mathbf{r})$. An immediate consequence is that the ground state expectation value of any observable $\hat{O}$ is an unique functional of the exact ground state electron density:

$$\langle\Psi_0|\hat{O}|\Psi_0\rangle = O[n(\mathbf{r})]. \tag{1.25}$$

Proof: assume that a second different external potential $V'_{ext}(\mathbf{r})$ with ground state $|\Psi'_0\rangle$ gives rise to the same density $n(\mathbf{r})$. The ground state energies are $E_0 = \langle\Psi_0|\hat{H}_e|\Psi_0\rangle$ and $E'_0 = \langle\Psi'_0|\hat{H}'_e|\Psi'_0\rangle$, where $\hat{H}'_e = \hat{F} + \hat{V}'_{ext}$. Taking $|\Psi'_0\rangle$ as a trial wave function for the Hamiltonian $\hat{H}_e$, from the variational principle the following strict inequality is obtained:

$$\begin{aligned} E_0 &< \langle\Psi'_0|\hat{H}_e|\Psi'_0\rangle = \langle\Psi'_0|\hat{H}_e + \hat{H}'_e - \hat{H}'_e|\Psi'_0\rangle \\ &< \langle\Psi'_0|\hat{H}'_e|\Psi'_0\rangle + \langle\Psi'_0|\hat{H}_e - \hat{H}'_e|\Psi'_0\rangle \\ &< E'_0 + \int n(\mathbf{r})[V_{ext}(\mathbf{r}) - V'_{ext}(\mathbf{r})]d^3\mathbf{r}, \end{aligned} \tag{1.26}$$

whereas taking the $|\Psi_0\rangle$ as a trial wave function for $\hat{H}'_e$ gives:

$$\begin{aligned} E'_0 &< \langle\Psi_0|\hat{H}'_e|\Psi_0\rangle = \langle\Psi_0|\hat{H}'_e + \hat{H}_e - \hat{H}_e|\Psi_0\rangle \\ &< \langle\Psi_0|\hat{H}_e|\Psi_0\rangle + \langle\Psi_0|\hat{H}'_e - \hat{H}_e|\Psi_0\rangle \\ &< E_0 + \int n(\mathbf{r})[V'_{ext}(\mathbf{r}) - V_{ext}(\mathbf{r})]d^3\mathbf{r}. \end{aligned} \tag{1.27}$$

Since adding equation (1.26) to (1.27) results in a contradiction:

$$E_0 + E'_0 < E'_0 + E_0, \tag{1.28}$$

it is hereby demonstrated that solely the ground state density determines the external potential of the system. Once known, any ground state property can be calculated.

Second theorem: Assuming that the ground state E_{0e} of the electronic part of the Hamiltonian is known, the density $n(\mathbf{r})$ can be calculated in principle from the N-electron wave function, *i.e.*, from the ground state wave function $|\Psi_0\rangle$. Therefore:

$$E_{0e} = \langle\Psi_0|\hat{H}_e|\Psi_0\rangle. \tag{1.29}$$

Since $|\Psi_0\rangle$ is the ground state, E_{0e} must be the lowest possible value of $\langle\Psi|\hat{H}_e|\Psi\rangle$, that is:

$$E_{0e} = \min\langle\Psi|\hat{H}_e|\Psi\rangle. \tag{1.30}$$

Furthermore, as $|\Psi\rangle$ leads to the correct electron density $n(\mathbf{r})$, it also verifies that:

$$E_{0e} = \min_{|\Psi\rangle\to n(\mathbf{r})}\langle\Psi|\hat{H}_e|\Psi\rangle, \tag{1.31}$$

which formally expresses E_{0e} as a function of $n(\mathbf{r})$:

$$E_{0e} = E_{0e}[n(\mathbf{r})] = \min_{|\Psi\rangle\to n(\mathbf{r})}\langle\Psi|\hat{H}_e|\Psi\rangle. \tag{1.32}$$

If another density $n(\mathbf{r}) \neq n'(\mathbf{r})$ is inserted into the functional, according to the first theorem, two densities can not be constructed from the same wave function. Therefore, the wave function $|\Psi'\rangle$ leads to a minimum of:

$$E_e[n'(\mathbf{r})] = \min_{|\Psi'\rangle\to n'(\mathbf{r})}\langle\Psi'|\hat{H}_e|\Psi'\rangle, \tag{1.33}$$

which is not that of the ground state of the system. Therefore, any expectation value $\langle\Psi'|\hat{H}_e|\Psi'\rangle$ of equation (1.33) is larger than that of equation (1.32), *i.e.*, the energy functional obeys the variational principle with respect to the ground state density:

$$E_e[n'(\mathbf{r})] \geq E_{0e}[n(\mathbf{r})]. \tag{1.34}$$

This is the second Hohenberg-Kohn theorem, which states that $E_e[n'(\mathbf{r})]$ has a minimum for the correct ground state density $n(\mathbf{r})$.

1.2.1 The Kohn-Sham method

The Hohenberg-Kohn theorems do not provide a scheme for calculating the ground state properties from the electron density. This was accomplished in 1965 with the approach proposed by Kohn and Sham [29], from which DFT acquired a practical dimension.

Since the second theorem of Hohenberg-Kohn implies that:

$$\delta E_e[n(\mathbf{r})] = E_e[n(\mathbf{r}) + \delta n(\mathbf{r})] - E_e[n(\mathbf{r})] = 0, \tag{1.35}$$

where only the changes of $\delta n(\mathbf{r})$ which do not alter the total number of electrons are allowed, *i.e.*, $n(\mathbf{r})$ should verify that:

$$\int n(\mathbf{r}) d^3\mathbf{r} = N, \tag{1.36}$$

this constitutes a minimization problem in the presence of a constraint. Therefore, with the introduction of a Lagrange multiplier μ, Eq. (1.35) and (1.36) can be combined as:

$$\delta\{E_e[n(\mathbf{r})] - \mu[\textstyle\int n(\mathbf{r}) d^3\mathbf{r} - N]\} = 0, \tag{1.37}$$

which must hold for any variation in $n(\mathbf{r})$.

Applying the concept of functional derivatives, whose mathematical formulation is presented in Appendix A, Eq. (1.37) can be rewritten as:

$$\frac{\delta}{\delta n(\mathbf{r})}\{E_e[n(\mathbf{r})] - \mu[\textstyle\int n(\mathbf{r}) d^3\mathbf{r} - N]\} = 0, \tag{1.38}$$

where the term $E_e[n(\mathbf{r})]$ contains the kinetic energy $T = T[n(\mathbf{r})]$, the external potential $\int V_{ext}(\mathbf{r}) n(\mathbf{r}) d^3\mathbf{r}$, the averaged Coulomb interaction energy:

$$\frac{1}{2}\frac{1}{4\pi\varepsilon_0}\int\int \frac{n(\mathbf{r})n(\mathbf{r}')}{|\mathbf{r}-\mathbf{r}'|} d^3\mathbf{r} d^3\mathbf{r}' = \frac{1}{2}\int V_C(\mathbf{r}) n(\mathbf{r}) d^3\mathbf{r},$$

with:

$$V_C(\mathbf{r}) = \frac{1}{4\pi\varepsilon_0}\int \frac{n(\mathbf{r}')}{|\mathbf{r}-\mathbf{r}'|} d^3\mathbf{r}'$$

representing the Hartree term and further terms accounting for the exchange and correlation effects. A factor of 1/2 is included in the Coulomb interaction in order to avoid double counting. The exchange term accounts for the Pauli exclusion principle by introducing a repulsive interaction among electrons of the same spin. While exchange effects were already present in the Hartree-Fock approximation [27], other extra contribution arising from the correlation of the electronic motion were neglected. Both these effects are now included in E'_{xc}, where "*xc*" stands for exchange-correlation. Since all the other terms are written as a functional of $n(\mathbf{r})$, E'_{xc} must be a functional of $n(\mathbf{r})$ too.

In total, the electronic energy is given by:

$$E_e[n(\mathbf{r})] = T[n(\mathbf{r})] + \int V_{ext}(\mathbf{r}) n(\mathbf{r}) d^3\mathbf{r} + \frac{1}{2}\int V_C(\mathbf{r}) n(\mathbf{r}) d^3\mathbf{r} + E'_{xc}[n(\mathbf{r})], \tag{1.39}$$

so that taking the functional derivative of Eq. (1.39) with respect to $n(\mathbf{r})$ results in:

$$\begin{aligned}\frac{\delta E_e}{\delta n(\mathbf{r})} &= \frac{\delta T[n(\mathbf{r}')]}{\delta n(\mathbf{r})} + \frac{\delta}{\delta n(\mathbf{r})}\left[\int V_{ext}(\mathbf{r})n(\mathbf{r}')d^3\mathbf{r}' + \frac{1}{2}\frac{1}{4\pi\varepsilon_0}\int\int\frac{n(\mathbf{r})n(\mathbf{r}')}{|\mathbf{r}-\mathbf{r}'|}d^3\mathbf{r}d^3\mathbf{r}'\right] \\ &\quad + \frac{\delta E'_{xc}[n(\mathbf{r}')]}{\delta n(\mathbf{r})}. \end{aligned} \tag{1.40}$$

In order to calculate the functional derivative of the terms inside the bracket, a change in the variable $n(\mathbf{r})$ must be introduced as:

$$n(\mathbf{r}) \to n(\mathbf{r}) + \delta n(\mathbf{r}), \tag{1.41}$$

from where, considering only the first-order change and neglecting the second or higher order variations in $\delta n(\mathbf{r})$, it can be shown that:

$$\frac{\delta E_e}{\delta n(\mathbf{r})} = \frac{\delta T}{\delta n} + V_{ext}(\mathbf{r}) + V_C(\mathbf{r}) + \frac{\delta E'_{xc}}{\delta n}, \tag{1.42}$$

which by direct substitution in Eq. (1.38) results in:

$$\frac{\delta T}{\delta n} + V_{ext}(\mathbf{r}) + V_C(\mathbf{r}) + \frac{\delta E'_{xc}}{\delta n} = \mu. \tag{1.43}$$

The approach of Kohn-Sham is the following: They considered a fictitious system of non-interacting quasi-particles with the same energy and density as the real system. In order to ensure that both systems are equivalent, these particles are assumed moving in some effective external potential ($V_{\mathit{eff}}(\mathbf{r})$). However, as these particles are non-interacting, their total energy has a considerably simpler expression:

$$E_e = T_0[n(\mathbf{r})] + \int V_{\mathit{eff}}(\mathbf{r})n(\mathbf{r})d^3\mathbf{r}, \tag{1.44}$$

for which it can be shown that the analogous of Eq. (1.43) for a non-interacting system becomes:

$$\frac{\delta T_0}{\delta n} + V_{\mathit{eff}}(\mathbf{r}) = \mu, \tag{1.45}$$

where the kinetic energy T_0 is not identical to that of the interacting system T in Eq. (1.39), since these particles are different.

Therefore, equaling Eq. (1.45) to Eq. (1.43):

$$\begin{aligned} V_{\mathit{eff}}(\mathbf{r}) &= \frac{\delta T}{\delta n} - \frac{\delta T_0}{\delta n} + V_{ext}(\mathbf{r}) + V_C(\mathbf{r}) + \frac{\delta E'_{xc}}{\delta n} && (1.46) \\ &= V_{ext}(\mathbf{r}) + V_C(\mathbf{r}) + \frac{\delta}{\delta n}(T - T_0 + E'_{xc}) && (1.47) \end{aligned}$$

and defining $E_{xc} = T - T_0 + E'_{xc}$ as the energy of the system containing the corrections to the kinetic energy due to the electronic interactions, leads to the so-called exchange-correlation potential:

$$\frac{\delta E_{xc}}{\delta n} = V_{xc}(\mathbf{r}), \tag{1.48}$$

which substituted into Eq. (1.46) reduces it to:

$$V_{\mathit{eff}}(\mathbf{r}) = V_{ext}(\mathbf{r}) + V_C(\mathbf{r}) + V_{xc}(\mathbf{r}). \tag{1.49}$$

In this approach, the energy operator of the system is given by:

$$\hat{H}_{KS} = \hat{H}_e = \sum_{i=1}^{N} \left[-\frac{\hbar^2}{2m_e} \nabla^2_{\mathbf{r}_i} + V_{\mathit{eff}}(\mathbf{r}_i) \right] = \sum_{i=1}^{N} \hat{h}_{\mathit{eff}}(i), \tag{1.50}$$

which is known as the Kohn-Sham Hamiltonian.

As $\hat{H}_{KS}$ contains only single-particle operators:

$$\hat{h}_{\mathit{eff}}(i) = -\frac{\hbar^2}{2m_e} \nabla^2_{\mathbf{r}_i} + V_{\mathit{eff}}(\mathbf{r}_i), \tag{1.51}$$

it is a Schrödinger-like Hamiltonian for which the solution can be written exactly as a single Slater determinant:

$$\Psi = \det\{\psi_1, \psi_2, ..., \psi_N\}, \tag{1.52}$$

where the single-particle orbitals ψ_i are determined by the single-particle equation $\hat{h}_{\mathit{eff}}\psi_i = \varepsilon_i \psi_i$.

Density functional theory is therefore formulated in the following way: the exact ground state density of an N-electron system is:

$$n(\mathbf{r}) = \sum_{i=1}^{N} \psi_i^{\star}(\mathbf{r})\psi_i(\mathbf{r}) = \sum_{i=1}^{N} |\psi_i(\mathbf{r})|^2, \tag{1.53}$$

where the single-particle wave functions $\psi_i(\mathbf{r})$ are the N-lowest solutions of the Kohn-Sham equation $\hat{H}_{KS}\psi_i = \varepsilon_i \psi_i$.

Thus, instead of solving an equation for interacting particles, a system of N Schrödinger like equations is solved for non-interacting single-particles. Two additional remarks have to be made. First, the single-particle wave functions are not the wave functions of electrons: they describe mathematical quasi-particles, without any physical meaning. Second, the Kohn-Sham Hamiltonian depends on the electron density through the Coulomb and exchange-correlation terms, while the electron density depends on the calculated ψ_i. Therefore, this is a self-consistency problem, for which an iterative procedure must be implemented. In the first iteration, with a reasonable guess for the electron density, the Kohn-Sham Hamiltonian is constructed. Solving the equation results in a new set of ψ_i and, therefore, in a new electron density. A new $\hat{H}_{KS}$ is constructed with this new density and the process is repeated until the resulting density, as well as the total energy, are converged. Thus, the Kohn-Sham equation provides a practical tool to solve many-body systems.

Apart from the Born-Oppenheimer approximation, DFT conforms an exact theory. However, solving the Kohn-Sham equation requires the introduction of some approximations, to specify a functional for the exchange-correlation potential and to construct the eigenfunctions in an appropriate basis set. In following sections, the above mentioned topics are briefly discussed, maintaining a strict relationship with the approximations used in this study.

1.2.2 The LDA and GGA potentials

If the exact form of the exchange-correlation functional $E_{xc}[n]$ is known, the Kohn-Sham equation can be solved. However, as the analytical expression of this functional cannot be exactly derived, the introduction of an approximation is needed. Remarkably, a simple approximation for the exchange-correlation energy has been developed, which for much systems works reasonably well. This is the so-called local density approximation (LDA) [28–32], which remains to the present the most often used.

Another frequently used type of functionals are those formulated within the generalized gradient approximation (GGA) [33–35], which introduce a semi-local approximation and are used in this investigation. There are some other non-local methods, such as hybrid functionals, meta-GGA and the self-interaction-corrected approximation (SIC) which are not used in this investigation.

The central idea of LDA lays on the model of the homogeneous electron gas[1]. The assumption that E_{xc} can be written in the following form was already introduced in the original paper by Kohn-Sham [29]:

$$E_{xc}^{LDA}[n(\mathbf{r})] = \int n(\mathbf{r})\varepsilon_{xc}[n(\mathbf{r})]d^3\mathbf{r}, \tag{1.54}$$

where $\varepsilon_{xc}[n(\mathbf{r})]$ is the exchange-correlation energy of an uniform electron gas of density $n(\mathbf{r})$. This energy per particle is weighted with the probability $n(\mathbf{r})$ that there is in fact an electron at this position in space. The quantity $\varepsilon_{xc}[n(\mathbf{r})]$ can be further split into exchange and correlation contributions:

$$\varepsilon_{xc}[n(\mathbf{r})] = \varepsilon_x[n(\mathbf{r})] + \varepsilon_c[n(\mathbf{r})]. \tag{1.55}$$

The exchange part $\varepsilon_x[n(\mathbf{r})]$ for an electron in an uniform electron gas of a particular density was determined by Slater in his approximation of Hartree-Fock exchange and was originally derived by Bloch and Dirac in the late 1920's [36,37]. However, as there is no explicit expression for the correlation part $\varepsilon_c[n(\mathbf{r})]$, several approaches have been proposed. In the pioneering work of Ceperly and Adler [31], highly accurate Monte Carlo simulations of the homogeneous electron gas were used to construct a numerical solution for $\varepsilon_c[n(\mathbf{r})]$. Then, the most widely used analytical expression of $\varepsilon_c[n(\mathbf{r})]$ is based on the sophisticated quantum Monte Carlo interpolation scheme developed by Vosko, Wilk and Nusair [32]. Finally, the most recent and also most accurate approximation has been given by Perdew and Wang [34].

LDA is based on the local nature of the exchange-correlation potential and on the assumption that the density distribution does not vary too rapidly. However, as the local variations on the electron density can induce important correlation effects, incorporating the density gradient into ε_{xc} as in:

$$E_{xc}^{GGA}[n(\mathbf{r})] = \int n(\mathbf{r})\varepsilon_{xc}[n(\mathbf{r}), \nabla n(\mathbf{r})]d^3\mathbf{r}. \tag{1.56}$$

---

[1] This is a hypothetical system where electrons move in a positive background charge distribution of the nuclei, such that the total ensemble is electrically neutral. The uniform electron gas has a prominent place in DFT since it is the only system for which the exact form of the exchange and correlation effects are known.

leads to the generalized gradient approximation.

Since a straightforward expansion in terms of the gradient violates the sum rules for the exchange hole, different approaches to GGA have been proposed [33–35]. For applications in real systems, the GGA of Perdew *et al.* [35] is the most widely used.

There are several studies covering the advantages or disadvantages of LDA versus GGA in literature (see Refs. [35, 39] for example). Some of the tendencies observed through comparison with experiments are as following:

1. The lattice constants calculated using LDA are in general 2% smaller than the experimental ones, while GGA matches in most cases quite well with the experimental values or slightly overestimates them. This overcorrection can lead however to an underestimation of the bond strengths, in contrast to experiments and LDA.

2. LDA wrongly predicts a nonmagnetic fcc structure to be the most stable phase of Fe [38], while within GGA, the experimentally observed ferromagnetic bcc structure is reproduced as the ground state [39].

In order to treat magnetic systems, the total electron density needs to be separated into the spin-up and spin-down components as:

$$n(\mathbf{r}) = n_\uparrow(\mathbf{r}) + n_\downarrow(\mathbf{r}), \tag{1.57}$$

so, while for a nonmagnetic system:

$$n_\uparrow(\mathbf{r}) = n_\downarrow(\mathbf{r}), \tag{1.58}$$

for a spin-polarized system this is not the case, *i.e.*, the magnetization density:

$$m(\mathbf{r}) = n_\uparrow(\mathbf{r}) - n_\downarrow(\mathbf{r}) \tag{1.59}$$

is different from 0. The Hohenberg-Kohn theorems have to be extended so that E_e (or any other ground state property) becomes a functional of both $n(\mathbf{r})$ and $m(\mathbf{r})$ as:

$$E_e = E_e[n(\mathbf{r}), m(\mathbf{r})]. \tag{1.60}$$

In this framework, extending the local density approximation to the unrestricted (spin-polarized) case, leads to in the local spin density approximation (LSDA), which takes the following form:

$$E_{xc}^{LSDA}[n_\uparrow, n_\downarrow] = \int n(\mathbf{r})\varepsilon_{xc}[n_\uparrow(\mathbf{r}), n_\downarrow(\mathbf{r})]d^3\mathbf{r}. \tag{1.61}$$

The same argument can be applied for semi-local or non-local approximations. Therefore, the exchange-correlation energy for GGA can be written as:

$$E_{xc}^{GGA}[n_\uparrow, n_\downarrow] = \int n(\mathbf{r})\varepsilon_{xc}[n_\uparrow(\mathbf{r}), n_\downarrow(\mathbf{r}), \nabla n_\uparrow(\mathbf{r}), \nabla n_\downarrow(\mathbf{r})]d^3\mathbf{r}, \tag{1.62}$$

for its spin-polarized analogous.

1.2.3 Beyond LDA/GGA: The LDA+U method

Both the LSDA and GGA approximations work sufficiently well for a large number of systems. Nevertheless, they have been reported to encounter difficulties in describing the electronic properties of strongly correlated materials, such as transition metals and rare-earth ions. Since these approximations are orbital-independent, only the electron density is taken into account. When such a system is treated with LDA or GGA, a partially filled d (or f) band with a metallic character is found. This behavior arises because spin and orbital polarization are driven by the exchange-correlation of the homogeneous electron gas, instead of the screened on-site Coulomb interaction [41, 42]. As a consequence, LDA and GGA fail in describing orbital polarization correctly.

It was shown by Terakura *et al.* [43, 44] that for many of the transition metal oxides, the DFT-LSDA predicts a metallic ground state instead of the experimentally observed insulating one. Therefore, adequate description of the strong Coulomb repulsion beyond LSDA is needed to overcome this limitation [45–47].

In the folowing, the so-called LDA+U (Hubbard U parameter) approach, as it is relevant to this work, is described in detail.

The LDA+U energy

One way to tackle the strong electron correlation in a system is by introducing a Hubbard U parameter. A semiempirical functional is added to the conventional energy functional only for the d (or f) orbitals which are expected to have strong correlation. Simultaneously, the double counting of interaction is avoided, as these orbitals are already present in the LDA functional. The strength of the Coulomb interaction is introduced as an additional parameter. Therefore, this technique is no longer parameter free. In reward, the Hamiltonian becomes orbital dependent and treats the strong correlation explicitly.

The correction to the Hamiltonian is in principle an additional contribution from a Coulomb interaction (from electron pairs with antiparallel spins) and from an exchange interaction (from electron pairs with parallel spins) for the strongly correlated orbitals. The aim is to correct the orbital energy of the LSDA scheme. The calculation is therefore separated into pure LSDA(GGA) for delocalized orbitals and LSDA+U for the localized (d or f) part. Therefore, the LDA+U energy can be written as:

$$E^{LDA+U} = E^{LDA} + (E^{U} - E^{dc}), \tag{1.63}$$

where the E^U term is the electron-electron interaction energy of the localized electrons and E^{dc} is the double counting term which cancels the electron-electron interaction energy, included in the E^{LDA} part.

The E^U term is taken as the expectation value of an operator $\hat{W}$ containing the corrections to the Hamiltonian:

$$E^{U} = \langle \Psi | \hat{W} | \Psi \rangle, \tag{1.64}$$

where:

$$\hat{W} = \frac{1}{2} \sum_{i \neq j} \frac{e^2}{|\mathbf{r}_i - \mathbf{r}_j|} = \sum_{i \neq j} \hat{G}_{ij} \tag{1.65}$$

and

$$\Psi = det\{\psi_1(\mathbf{r}_1), \psi_2(\mathbf{r}_2), ..., \psi_n(\mathbf{r}_n)\} \tag{1.66}$$

is the single Slater determinant wave function.

Introducing a permutation operator as:

$$\hat{P} = \sum_{l=1}^{n} (-1)^l p_l[\psi_1(\mathbf{r}_1), \psi_2(\mathbf{r}_2), ..., \psi_n(\mathbf{r}_n)], \tag{1.67}$$

for each electron pair (i, j) with $i \neq j$, the outcome of Eq. (1.64) can be expressed in a simpler form:

$$\langle\Psi|\hat{G}_{ij}|\Psi\rangle = \langle\psi_1(\mathbf{r}_1)\psi_2(\mathbf{r}_2)...\psi_n(\mathbf{r}_n)|\hat{G}_{ij}|\hat{P}[\psi_1(\mathbf{r}_1)\psi_2(\mathbf{r}_2)...\psi_n(\mathbf{r}_n)]\rangle \tag{1.68}$$

and since by definition, all wave functions are orthonormal ($\langle\psi_i|\psi_j\rangle = \delta_{ij}$), when expanding the right hand side of Eq. (1.68), only those terms with index $i = j$ will contribute, while the remaining terms will vanish. Therefore:

$$\langle\Psi|\hat{G}_{ij}|\Psi\rangle \;=\; \langle\psi_i(\mathbf{r}_i)\psi_j(\mathbf{r}_j)|\hat{G}_{ij}|[\psi_i(\mathbf{r}_i)\psi_j(\mathbf{r}_j) - \psi_i(\mathbf{r}_j)\psi_j(\mathbf{r}_i)]\rangle \tag{1.69}$$

and thus:

$$\begin{aligned} E^U &= \langle\Psi|\hat{W}|\Psi\rangle = \sum_{i\neq j}\langle\Psi|\hat{G}_{i,j}|\Psi\rangle \\ &= \frac{1}{2}\sum_{i\neq j}\Bigg[\langle\psi_i(\mathbf{r}_i)\psi_j(\mathbf{r}_j)|\frac{e^2}{|\mathbf{r}_i-\mathbf{r}_j|}|\psi_i(\mathbf{r}_i)\psi_j(\mathbf{r}_j)\rangle \\ &\quad - \langle\psi_i(\mathbf{r}_i)\psi_j(\mathbf{r}_j)|\frac{e^2}{|\mathbf{r}_i-\mathbf{r}_j|}|\psi_i(\mathbf{r}_j)\psi_j(\mathbf{r}_i)\rangle\Bigg], \end{aligned} \tag{1.70}$$

where the first and the second terms in Eq. (1.70) correspond respectively to the direct and exchange interaction.

Since one electron wave functions ψ_i in quantum mechanics can be expressed as a linear combination of a position and spin-dependent basis set $\varphi_k(\mathbf{r})\chi_\sigma(\mathbf{s})$:

$$\psi_i(\mathbf{r}_i) = \sum_{k=1}^{N}\sum_{\sigma=\uparrow,\downarrow} C^i_{k\sigma}\varphi_k(\mathbf{r}_i)\chi_\sigma(\mathbf{s}), \tag{1.71}$$

by substituting Eq. (1.71) in Eq. (1.70) and using the orthogonality of the spin part $\langle\chi_{\sigma_i}|\chi_{\sigma_j}\rangle = \delta_{\sigma_i\sigma_j}$ and the definition of the density matrix as following:

$$\rho^{\sigma_1\sigma_2}_{k_1k_2} = \sum_{i\in occ.} C^i_{k_1\sigma_1}C^{i\star}_{k_2\sigma_2}, \tag{1.72}$$

it can be shown that:

$$
\begin{aligned}
E^U &= \frac{1}{2}\sum_{i\neq j}\Bigg[\sum_{\{k_1,k_2,k_3,k_4\}}\ \sum_{\{\sigma_1,\sigma_2,\sigma_3,\sigma_4\}} \rho^{\sigma_1\sigma_3}_{k_1k_3}\rho^{\sigma_2\sigma_4}_{k_2k_4} \\
&\quad \Bigg\{\langle\varphi_{k_1}(\mathbf{r}_i)\varphi_{k_2}(\mathbf{r}_j)|\frac{e^2}{|\mathbf{r}_i-\mathbf{r}_j|}|\varphi_{k_3}(\mathbf{r}_i)\varphi_{k_4}(\mathbf{r}_j)\rangle\delta_{\sigma_1\sigma_3}\delta_{\sigma_2\sigma_4} \\
&\quad - \langle\varphi_{k_1}(\mathbf{r}_i)\varphi_{k_2}(\mathbf{r}_j)|\frac{e^2}{|\mathbf{r}_i-\mathbf{r}_j|}|\varphi_{k_3}(\mathbf{r}_j)\varphi_{k_4}(\mathbf{r}_i)\rangle\delta_{\sigma_1\sigma_4}\delta_{\sigma_2\sigma_3}\Bigg\}\Bigg] \\
&= \frac{1}{2}\sum_{i\neq j}\Bigg[\sum_{\{k_1,k_2,k_3,k_4\}}\ \sum_{\{\sigma_1,\sigma_2\}}\Bigg\{\rho^{\sigma_1\sigma_1}_{k_1k_3}\rho^{\sigma_2\sigma_2}_{k_2k_4}\langle\varphi_{k_1}(\mathbf{r}_i)\varphi_{k_2}(\mathbf{r}_j)|\frac{e^2}{|\mathbf{r}_i-\mathbf{r}_j|}|\varphi_{k_3}(\mathbf{r}_i)\varphi_{k_4}(\mathbf{r}_j)\rangle \\
&\quad - \rho^{\sigma_1\sigma_2}_{k_1k_3}\rho^{\sigma_2\sigma_1}_{k_2k_4}\langle\varphi_{k_1}(\mathbf{r}_i)\varphi_{k_2}(\mathbf{r}_j)|\frac{e^2}{|\mathbf{r}_i-\mathbf{r}_j|}|\varphi_{k_3}(\mathbf{r}_j)\varphi_{k_4}(\mathbf{r}_i)\rangle\Bigg\}\Bigg]. \qquad (1.73)
\end{aligned}
$$

It is worth to mention that in Eq. (1.73), the direct part contains the diagonal spin-elements of the density matrix, while the non-diagonal spin-elements are incorporated into the exchange part. In order to describe the E^U term, a proper basis set for computational purposes must be defined. The discussion on the selection of an efficient basis set is presented later in section 1.2.4. In this section, a set of augmented plane waves (APW) is considered for the development of the following expressions, as it simplifies the mathematical formulation.

As it will be discussed in more detail, in this method space is divided into atomic spheres and the interstitial region and the basis functions have the following form:

$$
\varphi_{\mathbf{k}_n}(\mathbf{r}) = \begin{cases} \frac{1}{\sqrt{V}}\mathrm{e}^{\mathrm{i}\mathbf{k}_n.\mathbf{r}} & \text{if } \mathbf{r}\in \text{Interstitial} \\ \sum_{l=0}^{l_{max}}\sum_{m=-l}^{l} A^{\mathbf{k}_n}_{l,m}u_l(r)Y_{l,m}(\hat{\mathbf{r}}) & \text{if } \mathbf{r}\in \text{Sphere } \alpha, \end{cases} \qquad (1.74)
$$

where here V stands for the volume of the unit cell, $\mathbf{k}_n$ is the wave vector and $\hat{\mathbf{r}} = \mathbf{r}/|\mathbf{r}|$ is the unit vector.

Substituting $\varphi_{\mathbf{k}_n}(\mathbf{r})$ within the sphere in Eq. (1.73) and using the definition of occupation number matrix as following:

$$
\begin{aligned}
n^{\sigma_1\sigma_2}_{m_1m_2} &= \sum_{i\in occ.}\sum_{\mathbf{k}_{1n},\mathbf{k}_{2n}} C^{i}_{\mathbf{k}_{1n}\sigma_1}C^{i\star}_{\mathbf{k}_{2n}\sigma_2}A^{\mathbf{k}_{1n}}_{l,m_1}A^{\mathbf{k}_{2n}\star}_{l,m_2} \\
&= \sum_{\mathbf{k}_{1n},\mathbf{k}_{2n}} \rho^{\sigma_1\sigma_2}_{\mathbf{k}_{1n}\mathbf{k}_{2n}}A^{\mathbf{k}_{1n}}_{l,m_1}A^{\mathbf{k}_{2n}\star}_{l,m_2}, \qquad (1.75)
\end{aligned}
$$

results in:

$$
\begin{aligned}
E^U &= \frac{1}{2}\sum_{i\neq j}\sum_{l=0}^{l_{max}}\ \sum_{\{m_1,m_2,m_3,m_4\}}\ \sum_{\{\sigma_1,\sigma_2\}}\int d^3\mathbf{r}_i d^3\mathbf{r}_j \qquad (1.76) \\
&\quad \Bigg\{n^{\sigma_1\sigma_1}_{m_1m_3}n^{\sigma_2\sigma_2}_{m_2m_4}\frac{e^2u^\star_l(r_i)u^\star_l(r_j)u_l(r_i)u_l(r_j)}{|\mathbf{r}_i-\mathbf{r}_j|}Y^\star_{l,m_1}(\hat{\mathbf{r}}_i)Y^\star_{l,m_2}(\hat{\mathbf{r}}_j)Y_{l,m_3}(\hat{\mathbf{r}}_i)Y_{l,m_4}(\hat{\mathbf{r}}_j) \\
&\quad - n^{\sigma_1\sigma_2}_{m_1m_3}n^{\sigma_2\sigma_1}_{m_2m_4}\frac{e^2u^\star_l(r_i)u^\star_l(r_j)u_l(r_j)u_l(r_i)}{|\mathbf{r}_i-\mathbf{r}_j|}Y^\star_{l,m_1}(\hat{\mathbf{r}}_i)Y^\star_{l,m_2}(\hat{\mathbf{r}}_j)Y_{l,m_3}(\hat{\mathbf{r}}_j)Y_{l,m_4}(\hat{\mathbf{r}}_i)\Bigg\}.
\end{aligned}
$$

The matrix elements of the on-site Coulomb interaction are defined as following:

$$\begin{aligned} U_{m_1m_2m_3m_4} &= \langle m_1m_2|\frac{e^2}{|\mathbf{r}_i-\mathbf{r}_j|}|m_3m_4\rangle \\ &= \int_{r_i,r_j\leq R_{MT}} d^3\mathbf{r}_i d^3\mathbf{r}_j \frac{e^2|u_l(r_i)|^2|u_l(r_j)|^2}{|\mathbf{r}_i-\mathbf{r}_j|} Y^\star_{l,m_1}(\hat{\mathbf{r}}_i)Y^\star_{l,m_2}(\hat{\mathbf{r}}_j)Y_{l,m_3}(\hat{\mathbf{r}}_i)Y_{l,m_4}(\hat{\mathbf{r}}_j) \\ &= \int_{r_i,r_j\leq R_{MT}} d^3\mathbf{r}_i d^3\mathbf{r}_j \frac{e^2|u_l(r_i)|^2|u_l(r_j)|^2}{|\mathbf{r}_i-\mathbf{r}_j|}\langle lm_1|lm_3\rangle\langle lm_2|lm_4\rangle, \end{aligned} \tag{1.77}$$

by direct substitution in Eq. (1.76) yields:

$$\begin{aligned} E^U &= \tfrac{1}{2}\textstyle\sum_{i\neq j}\sum_{l=0}^{l_{max}}\sum_{\{m\}}\sum_{\{\sigma_1,\sigma_2\}} \\ & \left\{ n^{\sigma_1\sigma_1}_{m_1m_3}n^{\sigma_2\sigma_2}_{m_2m_4}U_{m_1m_2m_3m_4} - n^{\sigma_1\sigma_2}_{m_1m_3}n^{\sigma_2\sigma_1}_{m_2m_4}U_{m_1m_2m_4m_3}\right\}, \end{aligned} \tag{1.78}$$

where $U_{m_1m_2m_3m_4}$ and $U_{m_1m_2m_4m_3}$ are identified as the pair Coulomb and exchange interaction, respectively. For simplicity $\sum_{\{m\}}$ is used instead of $\sum_{\{m_1m_2m_3m_4\}}$.

By using the expansion of $\frac{1}{|\mathbf{r}_i-\mathbf{r}_j|}$ as a Legendre polynomial:

$$\begin{aligned} \frac{1}{|\mathbf{r}_i-\mathbf{r}_j|} &= \frac{1}{r_>}\sum_{k=0}^{\infty}(\frac{r_<}{r_>})^k p_k(\cos\gamma_{ij}) \\ \text{if}\quad r_i<r_j &\Rightarrow\quad r_i=r_< \text{ and } r_j=r_> \\ \text{else} &\Rightarrow\quad r_i=r_> \text{ and } r_j=r_< \end{aligned} \tag{1.79}$$

and applying the addition theorem in the spherical coordinate system:

$$\begin{aligned} p_k(\cos\gamma_{ij}) &= \frac{4\pi}{2k+1}\sum_{q=-k}^{k}(-1)^q Y_{k,q}(\theta_i,\varphi_i)Y_{k,-q}(\theta_j,\varphi_j) \\ Y_{k,-q}(\theta,\varphi) &= (-1)^q Y^\star_{k,q}(\theta,\varphi). \end{aligned} \tag{1.80}$$

it can be shown that Eq. (1.77) becomes:

$$\begin{aligned} U_{m_1m_2m_3m_4} = \int_{r_i,r_j\leq R_{MT}} & d^3\mathbf{r}_i d^3\mathbf{r}_j e^2|u_l(r_i)|^2|u_l(r_j)|^2\sum_{k=0}^{\infty}\frac{{r_<}^k}{{r_>}^{k+1}} \\ & \frac{4\pi}{2k+1}\sum_{q=-k}^{k}Y_{k,q}(\hat{\mathbf{\Omega}}_i)Y^\star_{k,q}(\hat{\mathbf{\Omega}}_j)\langle lm_1|lm_3\rangle\langle lm_2|lm_4\rangle. \end{aligned} \tag{1.81}$$

Separating the radial part from the angular part of the integrand in Eq. (1.81), i.e., $d^3\mathbf{r}_i = {r_i}^2 dr_i d\hat{\mathbf{\Omega}}_i$ where $d\hat{\mathbf{\Omega}}_i = \sin\theta_i d\theta_i d\phi_i$, Eq. (1.81) can be expressed as a Slater integral F_k:

$$U_{m_1m_2m_3m_4} = \sum_{k=0}^{\infty} a_k(m_1m_2m_3m_4)F_k, \tag{1.82}$$

where:

$$a_k(m_1m_2m_3m_4) = \frac{4\pi}{2k+1}\sum_{q=-k}^{k}\int\int d\hat{\mathbf{\Omega}}_i d\hat{\mathbf{\Omega}}_j\langle lm_1|Y_{k,q}(\hat{\mathbf{\Omega}}_i)|lm_3\rangle\langle lm_2|Y^\star_{k,q}(\hat{\mathbf{\Omega}}_j)|lm_4\rangle$$

and:

$$F_k = e^2 \int_0^\infty {r_i}^2 dr_i \int_0^\infty {r_j}^2 dr_j \frac{{r_<}^k}{{r_>}^{k+1}} |u_l(r_i)|^2 |u_l(r_j)|^2. \tag{1.83}$$

Similarly, for the exchange part $U_{m_1 m_2 m_4 m_3}$ in Eq. (1.78), it can be shown that:

$$U_{m_1 m_2 m_4 m_3} = \sum_{k=0}^{\infty} a_k^{ex}(m_1 m_2 m_4 m_3) F_k, \tag{1.84}$$

where:

$$a_k^{ex}(m_1 m_2 m_4 m_3) = \frac{4\pi}{2k+1} \sum_{q=-k}^{k} \int\int d\hat{\mathbf{\Omega}}_i d\hat{\mathbf{\Omega}}_j \langle lm_1 | Y_{k,q}(\hat{\mathbf{\Omega}}_i) | lm_4 \rangle \langle lm_2 | Y_{k,q}^{\star}(\hat{\mathbf{\Omega}}_j) | lm_3 \rangle.$$

Since the expansion is done inside the sphere ($r_i, r_j \leq R_{MT}$), the summation in Eq. (1.82) and (1.84), as well as in Eq. (1.79), has to terminate at a finite number ($2l_{max}$), which is the maximum orbital number included inside the sphere.

Finally, the E^U term can be written as following:

$$\begin{aligned} E^U = & \frac{1}{2} \sum_{i \neq j} \sum_{l=0}^{l_{max}} \sum_{\{m\}} \sum_{\{\sigma_1, \sigma_2\}} \sum_{k=0}^{2l} \\ & \left\{ n_{m_1 m_3}^{\sigma_1 \sigma_1} n_{m_2 m_4}^{\sigma_2 \sigma_2} a_k(m_1 m_2 m_3 m_4) - n_{m_1 m_3}^{\sigma_1 \sigma_2} n_{m_2 m_4}^{\sigma_2 \sigma_1} a_k^{ex}(m_1 m_2 m_4 m_3) \right\} F_k, \end{aligned} \tag{1.85}$$

but for simplicity, it is more convenient to use the Einstein summation convention to avoid repeating the $\sum$ symbols. Thus, Eq. (1.85) can now be written in the following form:

$$\begin{aligned} E^U = & \frac{1}{2} \sum_{\{m\}} \sum_{\{\sigma_1, \sigma_2\}} \\ & \left\{ n_{m_1 m_3}^{\sigma_1 \sigma_1} n_{m_2 m_4}^{\sigma_2 \sigma_2} a_k(m_1 m_2 m_3 m_4) - n_{m_1 m_3}^{\sigma_1 \sigma_2} n_{m_2 m_4}^{\sigma_2 \sigma_1} a_k^{ex}(m_1 m_2 m_4 m_3) \right\} F_k. \end{aligned} \tag{1.86}$$

The double counting term is diagonal in the spin-part and is given by:

$$E^{dc} = \frac{U}{2} n(n - \eta) - \frac{J}{2} \sum_{\sigma = \uparrow, \downarrow} n^\sigma (n^\sigma - \eta^\sigma), \tag{1.87}$$

where:

$$n^\sigma = \sum_{m=-l}^{l} n_{mm}^{\sigma\sigma} \qquad \text{and} \qquad \eta = \frac{\eta^\uparrow + \eta^\downarrow}{2}.$$

which can be specified in two ways: in the fully localized limit [16], $\eta^\sigma = 1$; while in the around mean field version [48], $\eta^\sigma = \langle n^\sigma \rangle$.

The LDA+U potential

The corresponding potential ($v_{mm'}^{\sigma\sigma'}$), which needs to be added to V^{LSDA}, can be calculated from the $E^U - E^{dc}$ term. By taking the functional derivative of the total energy with respect to the charge density of a particular orbital $\delta/\delta n_{mm'}^{\sigma\sigma'}$, its effective potential is obtained. This means that the matrix elements of the potential ($v_{mm'}^{\sigma\sigma'}$), which will be added to V^{LSDA} are:

$$v_{mm'}^{\sigma\sigma'} = \frac{\partial(E^U - E^{dc})}{\partial n_{mm'}^{\sigma\sigma'}}. \tag{1.88}$$

After simple algebra and by assuming that only the diagonal matrix elements are nonzero and equal to U, independent of m and m', the diagonal and off-diagonal terms of the potential are expressed as following:

$$\begin{aligned} v_{mm}^{\sigma\sigma} &= (U-J)(\frac{\eta}{2} - n_{mm}^{\sigma\sigma}) && (1.89) \\ v_{mm'}^{\sigma\sigma'} &= -Un_{mm'}^{\sigma'\sigma}. && (1.90) \end{aligned}$$

This potential reveals clearly the effect of the LDA+U method. The diagonal term (1.89) will shift the center of the orbital level depending on its average occupation. In the fully localized limit ($\eta = 1$), a completely empty state ($n = 0$) is moved upward by $\frac{1}{2}(U - J)$, while a completely filled state ($n = 1$) is shifted downward by an amount $-\frac{1}{2}(U - J)$.

In principle, it is possible to calculate the LDA+U parameters U and J from first principles. For example, the constrained LDA [50] or linear response method [49], propose a scheme with which both these values can be estimated.

1.2.4 Solving the Kohn-Sham equation

As explained before, the Kohn-Sham equations that resulted from the variational principle are:

$$\hat{H}_{KS}\psi_i(\mathbf{r}) = \epsilon_i\psi_i(\mathbf{r}), \tag{1.91}$$

for each single particle wave function ψ_i.

An important step to find the solution is to expand the single-particle wave functions in a suitable basis set, let's say $\{\phi_p|p = 1, 2, ..., P\}$:

$$\psi_i(\mathbf{r}) = \sum_{p=1}^{P} c_p\phi_p. \tag{1.92}$$

In principle, this basis set is infinite ($P = \infty$), although in practice it must have a finite dimension for numerical calculations. It is therefore important to determine a suitable limited basis set, from which a good approximation of ψ_i can be constructed. Then, the expectation value for the energy is written as:

$$\langle E\rangle = \frac{\int \psi_i^\star(c_1, ..., c_P)\hat{H}_{KS}\psi_i(c_1, ..., c_P)d^3\mathbf{r}}{\int \psi_i^\star(c_1, ..., c_P)\psi_i(c_1, ..., c_P)d^3\mathbf{r}}. \tag{1.93}$$

Since ψ_i is a trial wave function, which is a linear combination of basis functions ϕ_p, from the variational principle, the expectation value of any trial wave function is always greater than the eigenvalue of the exact wave function. Therefore, the minimization of $\langle E \rangle$ requires that the derivative with respect to c_p must vanish. This yields the following set of secular equations:

$$\sum_{q=1}^{P}(H_{pq}^{KS} - \alpha_p S_{pq})c_q = 0 \tag{1.94}$$

$$H_{pq}^{KS} = \int \phi_p^\star \hat{H}_{KS}\phi_q d^3\mathbf{r} \tag{1.95}$$

$$S_{pq} = \int \phi_p^\star \phi_q d^3\mathbf{r}, \tag{1.96}$$

where the H_{pq}^{KS} are the matrix elements of the single particle Kohn-Sham Hamiltonian and S_{pq} are the elements of the overlap matrix. Once the α_p are known, they can be substituted in Eq. (1.94) to determine the coefficients c_q and thus define the trial wave function ψ_i. This represents a general eigenvalue problem. Since Eq. (1.94) can be diagonalized, the many-body problem has been reduced to a solvable problem, which can be easily implemented in a computer code. As mentioned before, the choice of an adequate basis set is crucial. The accuracy of the approximation, as well as the needed computational time, strongly depend on the choice of the basis set. Not only the size of the basis set but also the shape of the basis functions play a major role in reducing the computational cost. Therefore, in the following sections some efficient basis sets are presented for this purpose.

The augmented plane wave method

Historically, an important example of a basis set are the augmented plane waves (APW) proposed by Slater in 1937 [36]. At first glance, the use of a plane wave basis set might appear appropriate, since, according to the Bloch theorem, every eigenfunction of the periodic Hamiltonian can be expanded in a plane wave basis set. Moreover, the $\psi_i(\mathbf{r}) = \sum_{p=1}^{P} c_p\phi_p$ and the energy ϵ_i can be labeled by the quantum numbers of Bloch theorem, now becoming ψ_i^n and ϵ_i^n, respectively. However, a large number of plane wave basis functions is needed in order to describe the oscillating behavior of the eigenfunctions close to the nucleus, which makes the expansion with plane waves highly inefficient. For this reason another description must be introduced around the nucleus.

In the region far from the nuclei, electrons behave like free electrons and hence, they can be described by plane waves. As in this region the potential is almost constant, the wave function is better described by plane waves which are the solution of the Schrödinger equation for a constant potential. Close to the nuclei, the electrons behave similar to the electrons of a free atom. Therefore, it is more suitable to describe them by atomic-like wave functions. Thus, the space is divided into two regions. Around each atom, a sphere (S_α) with radius R_α is defined and called the muffin tin sphere. The part of space occupied by the spheres is the muffin tin region and the remaining part is called the interstitial region (I) [27, 51]. The APW basis set can be thus defined as following:

$$\phi^{\mathbf{k}}_{\mathbf{K}}(\mathbf{r},E)=\begin{cases}\frac{1}{\sqrt{V}}\mathrm{e}^{\mathrm{i}(\mathbf{k}+\mathbf{K}).\mathbf{r}} & \text{if } \mathbf{r}\in \mathrm{I}\\ \sum_{l,m}A^{\alpha,\mathbf{k}+\mathbf{K}}_{l,m}u^{\alpha}_{l}(r',E)Y_{l,m}(\hat{\mathbf{r}'}) & \text{if } \mathbf{r}\in S_{\alpha},\end{cases} \tag{1.97}$$

where $\mathbf{k}$ is the wave vector in the first Brillouin zone, $\mathbf{K}$ is the lattice vector and with V representing again the volume of the unit cell. $A^{\alpha,\mathbf{k}+\mathbf{K}}_{l,m}$ are expansion coefficients and $u^{\alpha}_{l}(r',E)$ is the solution of the radial Schrödinger equation:

$$\left[\frac{d^2}{dr^2}+\frac{l(l+1)}{r^2}+V(r)-E\right](ru^{\alpha}_{l}(r,E))=0, \tag{1.98}$$

within the muffin tin sphere α at a given energy E. The $Y_{l,m}(\hat{\mathbf{r}'})$ are the spherical harmonics with angular momentum indexes l and m and where $\mathbf{r}'=\mathbf{r}-\mathbf{r}_{\alpha}$, with $\mathbf{r}_{\alpha}$ the atomic position within the unit cell of atom α.

The coefficients $A^{\alpha,\mathbf{k}+\mathbf{K}}_{l,m}$ are obtained by imposing the boundary condition that $u^{\alpha}_{l}(r',E)$ and the corresponding plane wave must be continuous at the muffin tin sphere. Therefore, the plane wave must be expanded in terms of the spherical harmonics about the origin of atom α:

$$\frac{1}{\sqrt{V}}\mathrm{e}^{\mathrm{i}(\mathbf{k}+\mathbf{K}).\mathbf{r}}=\frac{4\pi}{\sqrt{V}}\mathrm{e}^{\mathrm{i}(\mathbf{k}+\mathbf{K}).\mathbf{r}_{\alpha}}\sum_{l,m}\mathrm{i}^{l}j_{l}(|\mathbf{k}+\mathbf{K}||\mathbf{r}'|)Y^{\star}_{l,m}(\widehat{\mathbf{k}+\mathbf{K}})Y_{l,m}(\hat{\mathbf{r}'}),$$

where $j_l(x)$ is a Bessel function of order l. Therefore, at the sphere boundary, the condition becomes:

$$\sum_{l,m}A^{\alpha,\mathbf{k}+\mathbf{K}}_{l,m}u^{\alpha}_{l}(r',E)Y_{l,m}(\hat{\mathbf{r}'})\bigg|_{r'=R_{\alpha}}=\frac{1}{\sqrt{V}}\mathrm{e}^{\mathrm{i}(\mathbf{k}+\mathbf{K}).(\mathbf{r}'+\mathbf{r}_{\alpha})}\bigg|_{r'=R_{\alpha}}, \tag{1.99}$$

from which the coefficients $A^{\alpha,\mathbf{k}+\mathbf{K}}_{l,m}$ are uniquely defined by:

$$A^{\alpha,\mathbf{k}+\mathbf{K}}_{l,m}=\frac{4\pi\mathrm{i}^{l}\mathrm{e}^{\mathrm{i}(\mathbf{k}+\mathbf{K}).\mathbf{r}_{\alpha}}}{\sqrt{V}u^{\alpha}_{l}(R_{\alpha},E)}j_{l}(|\mathbf{k}+\mathbf{K}|R_{\alpha})Y^{\star}_{l,m}(\widehat{\mathbf{k}+\mathbf{K}}), \tag{1.100}$$

apart from the undetermined E.

In principle, there is an infinite number of coefficients, but for computational purposes, the summation is truncated at some practical value l_{max}. For a given l_{max}, $Y_{l_{max},m}(\theta,\varphi)$ can have at most $2l_{max}$ nodes on the α sphere. Therefore, the number of nodes per unit of length is $l_{max}/\pi R_{\alpha}$, while the plane wave with the shortest period $(2\pi/K_{max})$ has K_{max}/π nodes per unit of length. The cut-off parameter for the plane waves (K_{max}) and for the angular function (l_{max}) are comparable values if the number of nodes per unit of length is identical. This yields the condition $R_{\alpha}K_{max}=l_{max}$, which allows to determine a good l_{max} for a given K_{max}. However, if the muffin tin radii for different atoms are too different, there would not exist a suitable value of l_{max} for each atom.

Unfortunately, the APW method has an important drawback: the energy dependence of $u^{\alpha}_{l}(r',E)$. In order to describe the eigenfunction ψ_i of Kohn-Sham equation (1.91), they must be evaluated at the corresponding eigenvalue ϵ_i. Therefore, the secular equation (1.91) becomes non-linear in E and must be solved by an iterative process. As a consequence, the APW method is computationally expensive and it is no longer in practical use.

There exist another formulation of this method, called the KKR method [52,53], though it will not be an object of this discussion.

The linear augmented plane wave method

A great simplification was introduced with the so-called linear augmented plane wave (LAPW) method [54]. In this approximation, the non-linear eigenvalue problem is overcome by performing a Taylor expansion of the radial wave function around some fixed energy $E_0 = E_l^\alpha$ [51,54–56]. Truncating the Taylor series at the first order term results in:

$$\begin{aligned} u_l^\alpha(r', E = \epsilon_{\mathbf{k}}^n) &= u_l^\alpha(r', E_l^\alpha) + (E_l^\alpha - \epsilon_{\mathbf{k}}^n) \underbrace{\left. \frac{\partial u_l^\alpha(r', E)}{\partial E} \right|_{E=E_l^\alpha}}_{\dot{u}_l^\alpha(r', E_l^\alpha)} \\ &\quad + O((E_l^\alpha - \epsilon_{\mathbf{k}}^n)^2), \end{aligned} \tag{1.101}$$

where the linearization energy E_l^α is chosen such that it is close to the expected eigenvalue. Therefore, the wave function within the interstitial (I) and the atomic sphere (S_α) can be written as:

$$\phi_{\mathbf{K}}^{\mathbf{k}}(\mathbf{r}, E) = \begin{cases} \frac{1}{\sqrt{V}} \mathrm{e}^{\mathrm{i}(\mathbf{k}+\mathbf{K}).\mathbf{r}} & \text{if } \mathbf{r} \in \mathrm{I} \\ \sum_{l,m} \Big[A_{l,m}^{\alpha,\mathbf{k}+\mathbf{K}} u_l^\alpha(r', E_l^\alpha) & \\ + B_{l,m}^{\alpha,\mathbf{k}+\mathbf{K}} \dot{u}_l^\alpha(r', E_l^\alpha) \Big] Y_{l,m}(\hat{\mathbf{r'}}) & \text{if } \mathbf{r} \in S_\alpha. \end{cases} \tag{1.102}$$

In order to determine the augmentation coefficients $A_{l,m}^{\alpha,\mathbf{k}+\mathbf{K}}$ and $B_{l,m}^{\alpha,\mathbf{k}+\mathbf{K}}$, the wave function inside the muffin tin must match with the plane wave both in value and slope at the sphere boundary.

With E_l^α being fixed, the basis functions can be calculated in a single diagonalization step. The accuracy of the augmented plane wave basis set is determined by K_{max}. By reducing K_{max}, the size of matrix is restricted and, as matrix diagonalization is expensive, a large R_α can significantly reduce the computational time. On the other hand, R_α cannot be too large because the spherical harmonics can not be described suitably by a wave function in a region far away from the nucleus. Therefore, a better quantity to judge the accuracy in a LAPW basis set is $R_\alpha^{min} K_{max}$, where R_α^{min} is the smallest muffin tin radius among all atoms in the unit cell.

1.3 The WIEN2K code

This section briefly discusses the main functionalities of the code used in this study. For more details the reader can consult the WIEN2K user's guide [15]. In order to start, some input files must be created. Among them, the "case.struct" is the master input file which contains all the information about the structure, such as the lattice parameters, the fractional positions of the atoms inside the unit cell, the lattice type, the atomic number of each atom and the space group. After generating the "case.struct" file, several commands must be invoked to generate other necessary input files for running a self-consistent filed (SCF) cycle. To initialize the calculations, there exist the following commands:

- **instgen_lapw**: this command uses "case.struct" and generates a "case.inst" file which contains the atomic configurations ($1s^2/2s^2$, $2p^6/$,...), available also in the table of elements. Core state configurations (closed shells) are specified by the preceding inert gas (He, Ne, Ar,...).
- x **nn**: this command uses "case.struct" and calculates the nearest neighbor distance of all the atoms. Moreover, this program checks if the atomic spheres specified by the muffin tin radius for each atom overlap or not.
- x **sgroup**: this program uses the information of "case.struct" and determines the space group as well as all point groups of the non-equivalent sites. It can find possible smaller unit cells and produce a new structure file with the proper lattice type.
- x **symmetry**: This program generates the space group symmetry operations and writes them into "case.struct_st" file. In addition, the point group of each atomic site is determined and the quantum numbers (l, m) for the spherical harmonics are printed in "case.in2_sy" file.
- x **kgen**: this program generates the k-points within the irreducible part of the Brillouin zone. The k-mesh is written in "case.klist" file.
- x **lstart**: this program generates the atomic densities, which are used by **dstart** to generate the initial charge density as an input for running a SCF cycle. Furthermore, it generates all the necessary input files to control a SCF run, namely, "case.in0", "case.in1", "case.in2", "case.inc" and "case.inm". While running **lstart**, the user will be asked to specify the exchange correlation potential, *e.g.*, LSDA, GGA, and an energy parameter for separating core and valence states.
- x **dstart**: this program generates the initial charge density by a superposition of atomic densities generated by **lstart**. Information is written in "case.clmsum" file. In case of spin-polarized systems, x **dstart** must be called with a -up(-dn) switch to generate the "case.clmup(dn)" files.

After initialization, the SCF cycle calculation proceeds as following:

- **lapw0**: calculates the total potential as a sum of the exchange-correlation, Coulomb and external potential by using the total electron density as an input.
- **orb**: calculates the orbital dependent potential.
- **lapw1**: constructs the Hamiltonian and the overlap matrices and computes by diagonalization the eigenvectors and the eigenvalues. This is the most time consuming part of the program (80-90% of CPU time).

- **lapw2**: computes the Fermi energy and the expansion of the electronic charge density for each occupied state and each k-vector.
- **lapwdm**: calculates the density matrix needed for the orbital dependent potentials generated in **ORB**.
- **lcore**: computes the core state for the spherical part of the potential.
- **mixer**: combines the electron densities of core, semi-core and valence states to build up the new density for the next iteration. Therefore, in this step, the old and the generated density are mixed and the convergence criteria is checked.

In order to get more insight about all the described parts of the code above, Fig. 1.1 illustrate the program flow in WIEN2K code.

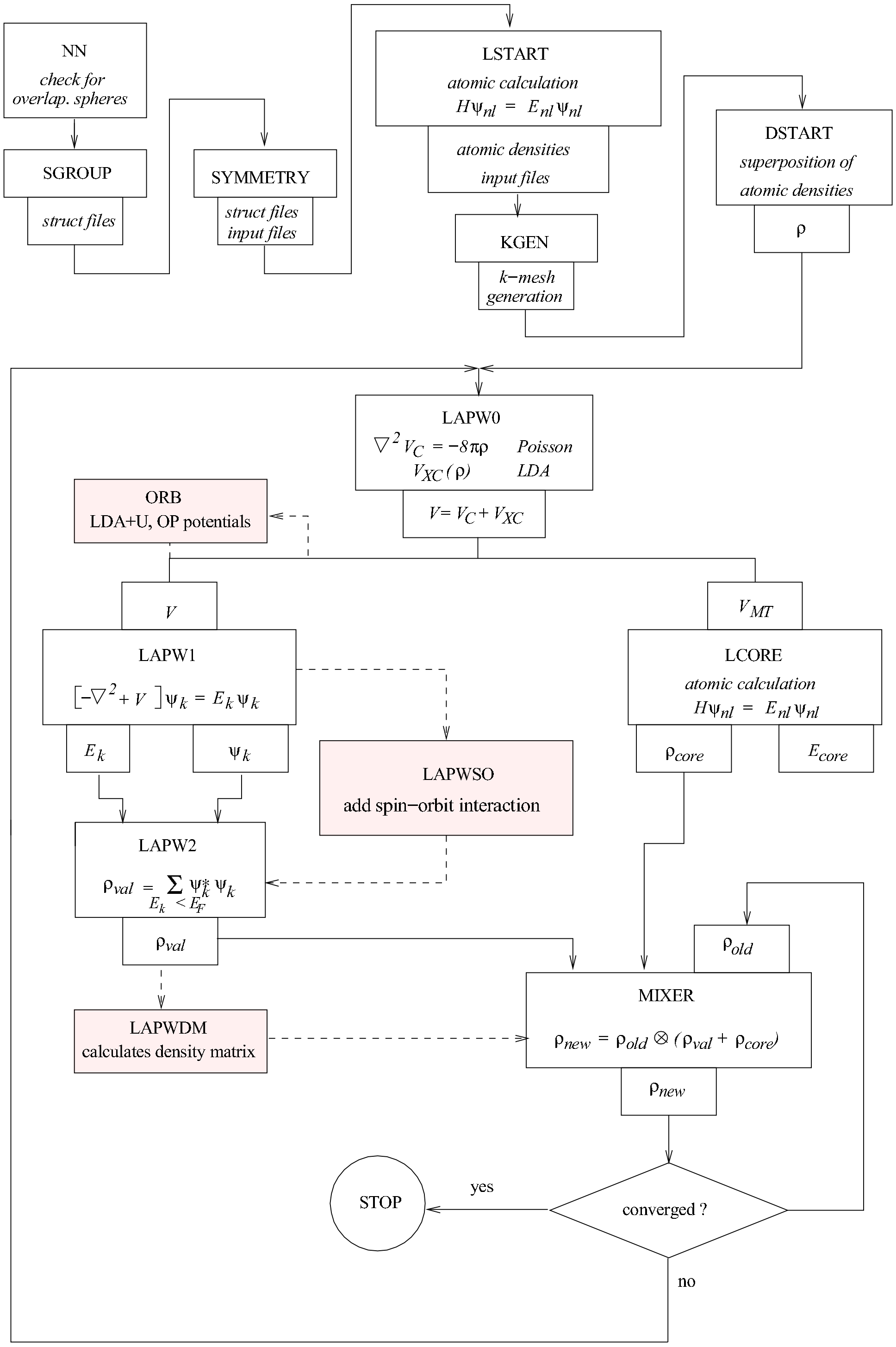

Figure 1.1: The flowchart showing the program flow in the WIEN2K code [15].

Chapter 2

Properties of Bulk α-Fe_2O_3 and $FeTiO_3$

Hematite and ilmenite are both transition metal oxides which have got fundamental importance in the study of rock magnetism. Ilmenite is an economically important mineral for the production of titania pigments. The solid solution of ilmenite and hematite is used to interpret the historical fluctuations in the Earth's magnetic field. Hematite is also an important end-member compound in geophysics for the understanding of the role of ferric oxides in the composition and dynamics of Earth's mantle. Both hematite ($a = 5.035\,\text{Å}$, $c = 13.751\,\text{Å}$ [57]) and ilmenite ($a = 5.177\,\text{Å}$, $c = 14.265\,\text{Å}$ [58]) crystallize in a corundum-like structure, shown in Fig. 2.1, where the oxygen ions form a distorted hexagonal close packed lattice and the cations occupy 2/3 of the octahedral sites. In hematite (space group $R\bar{3}c$), there is a natural modulation of electronic density along the [0001]-direction, where negatively charged $3O^{2-}$ layers alternate with positively charged $2Fe^{3+}$ layers. Hematite is a canted antiferromagnet below 948 K (Néel temperature): the Fe^{3+}-spins lie in the basal plane (perpendicular to the c-axis) with antiferromagnetic (AFM) coupling between neighboring layers. A small spin-canting in the basal plane above the Morin temperature (T_M=260 K) results in a weak net magnetic moment along the c-plane. Below the Morin temperature, the orientation of spins switches to parallel to the c-axis with a perfect AFM coupling.

In ilmenite ($FeTiO_3$), Fe- and Ti-layers alternate reducing the symmetry to space group $R\bar{3}$ and the corresponding sequence of layers along [0001] is $3O^{2-}$/ $2Fe^{2+}$/ $3O^{2-}$/ $2Ti^{4+}$. Above T_N=55 K ilmenite is paramagnetic, while below T_N the Fe^{2+} layers couple antiferromagnetically and are separated by magnetically inert Ti^{4+} layers. The spins of the Fe^{2+} layers align perpendicular to the c-axis.

In this chapter, the results on hematite and ilmenite obtained in the framework of DFT are presented. This chapter is organized as follows: the computational details are described in section 2.1. The results for ilmenite and hematite are discussed in section 2.2 and 2.3, respectively. The structural, electronic, magnetic properties and the comparison between GGA and GGA+U with previous studies (B3LYP and Hartree-Fock approximation) on ilmenite are described in subsection 2.2.1, 2.2.2 and 2.2.3, respectively. The results are summarized in section 2.4.

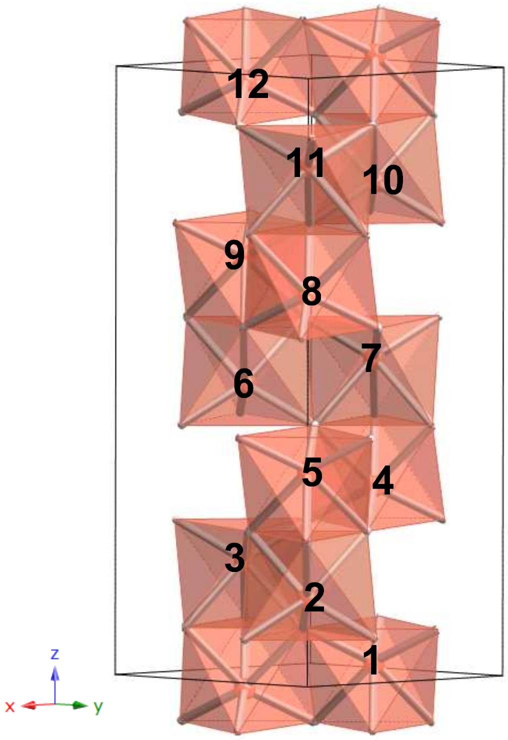

Figure 2.1: Crystal structure of Fe_2O_3, showing half of the 60-atom unit cell. The cation sites are numbered and oxygen occupies the edges of the octahedra. In $FeTiO_3$, Fe and Ti alternate in subsequent cation layers.

2.1 Calculational details

Density functional theory calculations were performed using the all-electron full-potential linear augmented plane wave (FP-LAPW) [15] method as implemented in the WIEN2K code. For the exchange-correlation potential the generalized gradient approximation (GGA) [35] is used and the electronic correlations are considered within GGA+U in the fully localized limit [16].

Bulk hematite and ilmenite are modelled in a hexagonal unit cell with 30 and 60 atoms, respectively, as shown in Fig. 2.1. For Fe and Ti a muffin tin (MT) radius of 1.80 bohr and for oxygen 1.60 bohr are used. Inside the muffin tins, wave functions are expanded in spherical harmonics up to $l_{\max}^{\mathrm{wf}} = 10$ and non-spherical contributions to the electron density and potential up to $l_{\max}^{\mathrm{pot.}} = 6$ are used. The energy cutoff for the plane wave representation in the interstitial is $E_{\max}^{\mathrm{wf}} = 19\,\mathrm{Ry}$ for the wave functions and $E_{\max}^{\mathrm{pot.}} = 196\,\mathrm{Ry}$ for the potential. In the irreducible part of the Brillouin zone, 15 and 24 k-points are used for the integration in reciprocal space for ilmenite and hematite, respectively. A full structural optimization of internal parameters within GGA+U is performed. The convergence criteria ensure a numerical accuracy in energy differences better than 0.01 eV/60-atom cell.

2.2 Bulk properties of $FeTiO_3$

2.2.1 Structural properties

Ilmenite is a weakly magnetic iron-black or steel-gray mineral. Depending on the pressure and temperature conditions, the polymorphs of $FeTiO_3$ crystallize in the ilmenite, lithium niobate ($LiNbO_3$) and perovskite structures. Ilmenite is a stable phase at ambient conditions, while perovskite is stable at high pressure and room temperature. In ilmenite, Fe and Ti form alternating bilayers with Fe-Ti-V-Ti-Fe (V: vacant) ordering along the *c*-axis. The Fe and Ti are octahedrally coordinated, where each octahedron shares one face with the adjacent octahedron of the other type cation and one face with an empty (vacant) octahedron along the (001)-direction (see Fig. 2.2a). Within the layers, octahedra form a honeycomb-like structure of edge-sharing octahedra (see Fig. 2.2b). Concerning the magnetic arrangements, ferromagnetic (FM) and antiferromagnetic (AFM) coupling to the next adjacent layer (inter-bilayers) are considered. Different oxidation states are contemplated: AFM^{+2} ($AFM\text{-}Fe^{2+}/Ti^{4+}$), FM^{+2} ($FM\text{-}Fe^{2+}/Ti^{4+}$), AFM^{+3} ($AFM\text{-}Fe^{3+}/Ti^{3+}$) and FM^{+3} ($FM\text{-}Fe^{3+}/Ti^{3+}$). Within the bilayers, only FM coupling is taken into account between the atoms, which is experimentally confirmed by Kato *et al.* [59]. Additionally, in their calculations, Wilson *et al.* [60] also investigated an AFM arrangement.

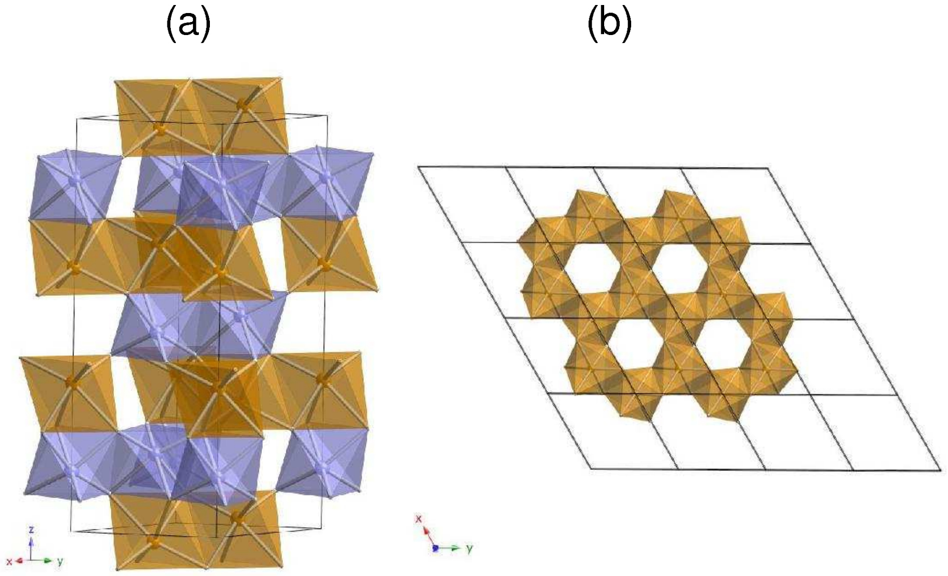

Figure 2.2: (a) The side view of ilmenite structure with Fe-Ti-V-Ti-Fe (V: empty space) ordering along the (001)-direction. (b) Top view of ilmenite structure, a honeycomb-like structure formed by Fe or Ti octahedron. Within the layer octahedra share the common edges.

2.2.2 Equation of state

The bulk properties of a crystalline material can be determined by calculating the total energy as a function of the cell volume. In order to find the ground state configuration, total energy versus volume calculations for AFM and FM arrangements of ilmenite, both within GGA and GGA+U, are performed. Within GGA, the volume is underestimated by 3.59% with respect to the experimental value (332 $Å^3$), while GGA+U gives a perfect agreement with experimental volume with only 0.24% deviation. Within GGA, the FM arrangement is found to be slightly more stable than AFM configuration by about 0.03 eV/f.u., while within GGA+U, the FM and AFM are almost degenerate with slight preference toward AFM arrangement. The total energies for AFM and FM configurations within GGA and GGA+U as a function of volume are fitted to the Murnaghan equation of state [61, 62] and displayed in Fig. 2.3-c and -d.

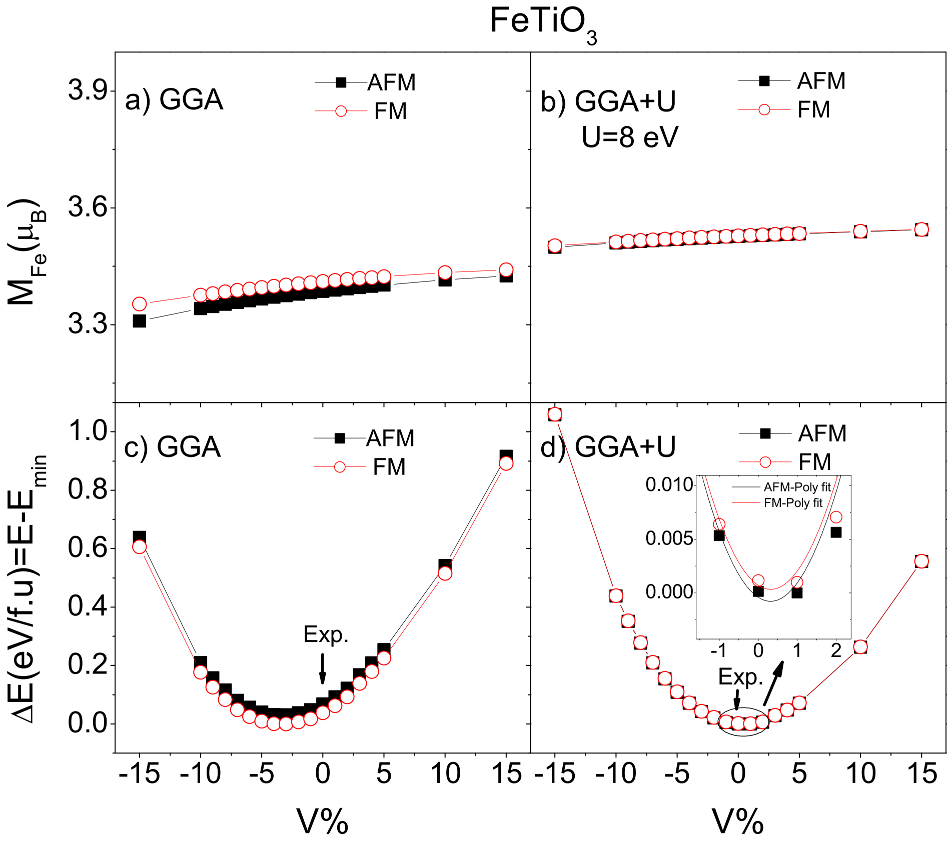

Figure 2.3: The absolute value of the magnetic moment of Fe in ilmenite within (a) GGA, (b) GGA+U (U = 8 eV) and total energies (c-d) as a function of volume. The volume is given in percent with respect to the experimental value which is set to 0% and marked with an arrow. Energies are given with respect to the configuration with lowest energy (set to 0).

The value of the bulk modulus B_0 and its pressure derivative B_0' are obtained by fitting to the Murnaghan equation of state:

$$E(V) = E_0 + \frac{1}{14703.6}\left[\frac{B_0V}{B_0'}\left(\frac{(V_0/V)^{B_0'}}{B_0'-1}+1\right) - \frac{B_0V_0}{B_0'-1}\right]. \tag{2.1}$$

From the calculated E(V) curve, B_0 and B_0' are found to be 192 GPa and 4.3 GPa, respectively for $U = 8$ eV. The bulk modulus calculated by GGA+U is in closer agreement with experiment (177 GPa) than that of GGA (201 GPa). In Table 2.1, the equilibrium lattice parameters computed within GGA, GGA+U (this study) and B3LYP [60] are compared with the experimental values by Wechsler *et al.* [63] and Harrison *et al.* [58].

Table 2.1: The lattice parameters and bulk modulus of ilmenite computed within GGA, GGA+U, B3LYP [60] and from experiment [58].

	Exp.	GGA	GGA+U	B3LYP (Ref. [60])
$a(\mathring{A})$	5.18	5.12	5.19	5.15
$c(\mathring{A})$	14.27	14.10	14.29	14.09
V ($\mathring{A}^3$)	331.6	319.6	332.4	323.6
$\Delta V(^{\circ}/_{\circ})$	—	-3.59	0.24	-2.53[a]
$B_0(GPa)$	177[b]	201	192	174
B'	4	4.6	4.3	4

[a] The experimental lattice constants (a=5.088, c=14.083 Å) used for the calculations by Wilson [60] are taken from Ref. [63]

[b] Refer to Ref. [63]

2.2.3 Electronic and magnetic properties: GGA vs. GGA+U

Ilmenite is a wide bandgap semiconductor with an experimental gap of ∼ 2.58 to 2.90 eV [64, 65]. The total energy and total density of states are calculated for two spin polarized magnetic configurations (AFM and FM) at two oxidation states (Fe^{2+}/Ti^{4+} and Fe^{3+}/Ti^{3+}) for the experimental lattice constants. The electronic properties can be described by the density of states (DOS). The total and projected DOS on Fe^{2+}, Ti^{4+} and O^{2-} states for the most stable configuration within GGA and GGA+U are plotted in Fig. 2.4. The value of the band gap is sensitive to the value of the Hubbard parameter, increasing with increasing U-value. For $0 \leq U \leq 3$ eV a metallic state is obtained between filled Fe-3d states and unfilled Ti-3d states. Beyond $U = 3$ eV a band gap opened and, considering the Fe^{2+} sites for one spin direction, all the Fe-3d orbitals are occupied. For the other spin direction the $3d_{z^2}$ (a_{1g}) orbital is occupied.

It is well known that the HF approximation considerably overestimates the band gap of materials, while B3LYP underestimates it by 10-20% for a wide range of materials. However, a better estimation of the band gap is possible using the GGA+U approach, which can treat correctly the electron correlation effects by choosing a proper U-value. In this study, a Hubbard U parameter of 8 eV was used, resulting

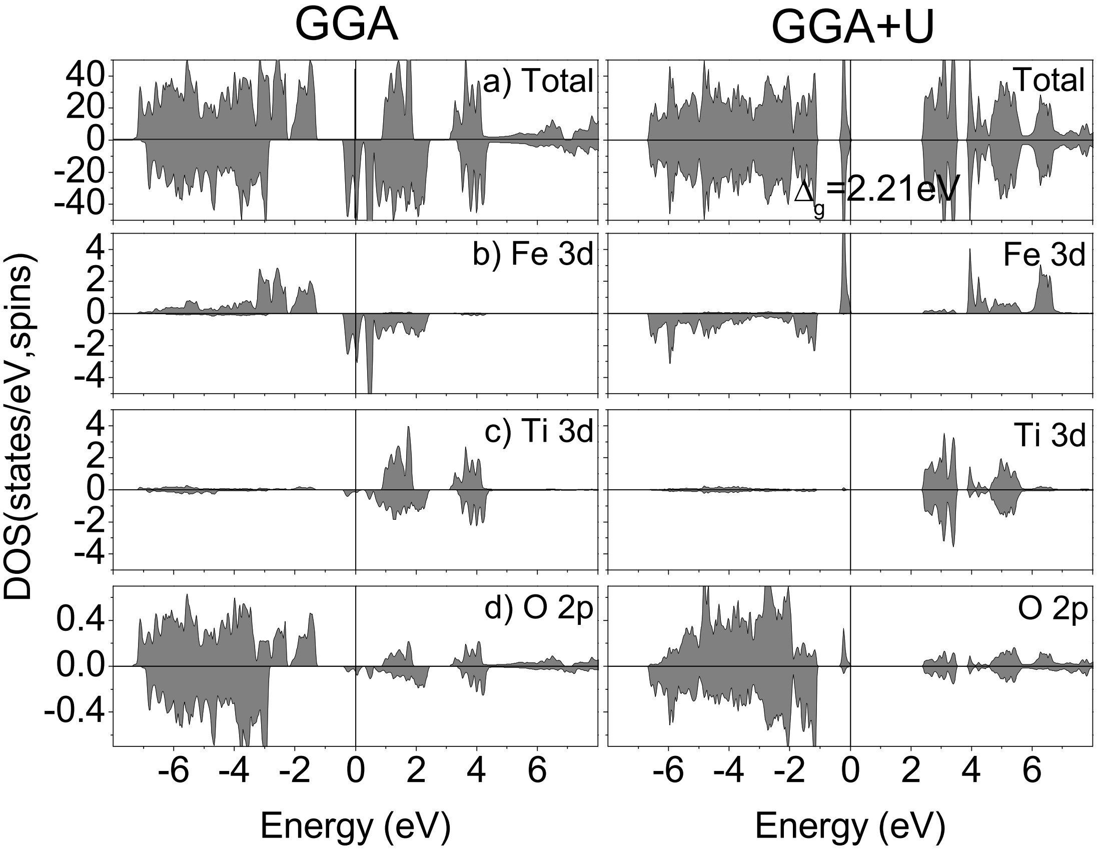

Figure 2.4: The total (a) and projected (b-d) density of states (DOS) for $FeTiO_3$ on Fe^{2+}, Ti^{4+} and O^{2-} states within GGA (left panel) and GGA+U (right panel) with $U = 8\,\text{eV}$. The band gap between the filled Fe-3d and unfilled Ti-3d states is 2.21 eV.

in a band gap of 2.21 eV. In Table 2.2, band gaps and the corresponding stable configurations for ilmenite obtained from different approaches (HF, B3LYP, GGA, GGA+U) and experiment are listed. Comparing all these methods, it is found that GGA+U with $U = 8\,\text{eV}$ and $J = 1\,\text{eV}$ predicts the experimentally observed configuration (AFM^{2+}) as a stable state with a fairly good value for the band gap as well.

Fig. 2.3-a and -b show the deviation of the absolute value of the iron magnetic moment (M_{Fe}) in $FeTiO_3$ with respect to the expansion or contraction of the volume within GGA and GGA+U, respectively. In fact, the M_{Fe} in the studied volume range did not vary much and no transition from high-spin (HS) to low-spin (LS) in FM and AFM configurations was observed.

Concerning the magnetic arrangement, within GGA (see Fig. 2.3c) it is found that AFM^{+2} is by 0.03 eV/f.u. less stable than FM^{+2}, while within GGA+U (see Fig. 2.3d), AFM^{+2} and FM^{+2} are almost degenerate (FM^{+2} lies 0.001 eV/f.u. above AFM^{+2}). The nearly degenerate solution is consistent with the low magnetic ordering temperature of ilmenite (T_N=55 K). The magnetic interaction parameters will be discussed in more detail in the next chapter (section 3.4.1), where also T_N will be estimated. The AFM^{+2} is also the experimentally spin-ordering observed by Kato *et al.* [59]. The FM^{+3} configuration lies 1.54 eV/f.u. above AFM^{+2} and AFM^{+3}

Table 2.2: The band gap, Δ_g (eV), and the corresponding stable configuration for ilmenite obtained by HF, B3LYP, GGA and GGA+U as well as experiment. The band gap by HF is highly overestimated while B3LYP predicts almost half of the experimental value. A metallic state within GGA is obtained, while the GGA+U with $U = 8$ eV showed an insulating state with a bandgap in fairly good agreement with the experimental one. See the text for more details about the stability of the different configurations.

Method	HF [60]	B3LYP [60]	GGA	GGA+U	Exp.
Δ_g (eV)	13.00	1.20	Metallic	2.21	2.58 to 2.90 [65]
Config.	FM^{+2}	AFM-(within-bilayer)	FM^{+2}	AFM^{+2}	AFM^{+2} [59]

is unstable, transforming to the AFM^{+2} configuration consistent with the B3LYP results [60]. The energy difference with respect to the stable configuration and the magnetic moment of iron are presented in Table 2.3.

Table 2.3: The magnetic moment of Fe and the energy difference relative to the lowest-energy state (set to 0) within GGA and GGA+U in the 60-atom cell.

Method	GGA		GGA+U			
Configuration	(AFM^{+2})	(FM^{+2})	(AFM^{+2})	(FM^{+2})	(AFM^{+3})	(FM^{+3})
M_{Fe} (μ_B)	3.4	3.4	3.5	3.5	Not stable	4.0
ΔE(eV/f.u.)	0.03	0.00	0.00	0.001	Not stable	1.54

Consistent with these results, Wilson *et al.* [60, 66] found a degenerate AFM^{+2} and FM^{+2} state within the Hartree-Fock (HF) approximation. In contrast, their B3LYP result predicts a configuration with AFM coupling within the bilayer for Fe^{2+}/Ti^{4+}-state as the ground state which is not supported by experiments. Furthermore, within the HF approximation they found FM^{+3} to be more stable than AFM^{+3} by 0.03 eV/f.u.

2.3 Bulk properties of α-Fe_2O_3

The electronic, magnetic and structural properties of hematite are described within GGA and GGA+U. The bulk properties of hematite have been intensively studied by several experimental [67–71] and theoretical [72–74] groups in literature. GGA+U turns out to be necessary in order to describe the correct electronic behavior consistent with the experiment. To determine the equilibrium geometry of α-Fe_2O_3, the plots of the total energy versus volume of the cell for the AFM and FM configurations are presented in Fig. 2.5. As shown in Fig. 2.5-c and -d, the AFM order is found to be the ground state both within GGA and GGA+U. The absolute value of the magnetic moment of Fe (M_{Fe}) within GGA reveals a transition from HS to LS by contraction of the volume, as shown in Fig. 2.5a. On the other hand, within GGA+U, M_{Fe} remained nearly constant (4.2 μ_B) in the studied volume range and no transition from HS to LS is observed (see Fig. 2.5b).

In Table 2.4, the calculated (GGA, GGA+U) and experimental values of the equilibrium lattice constants, volume and bulk modulus are listed. Concerning the

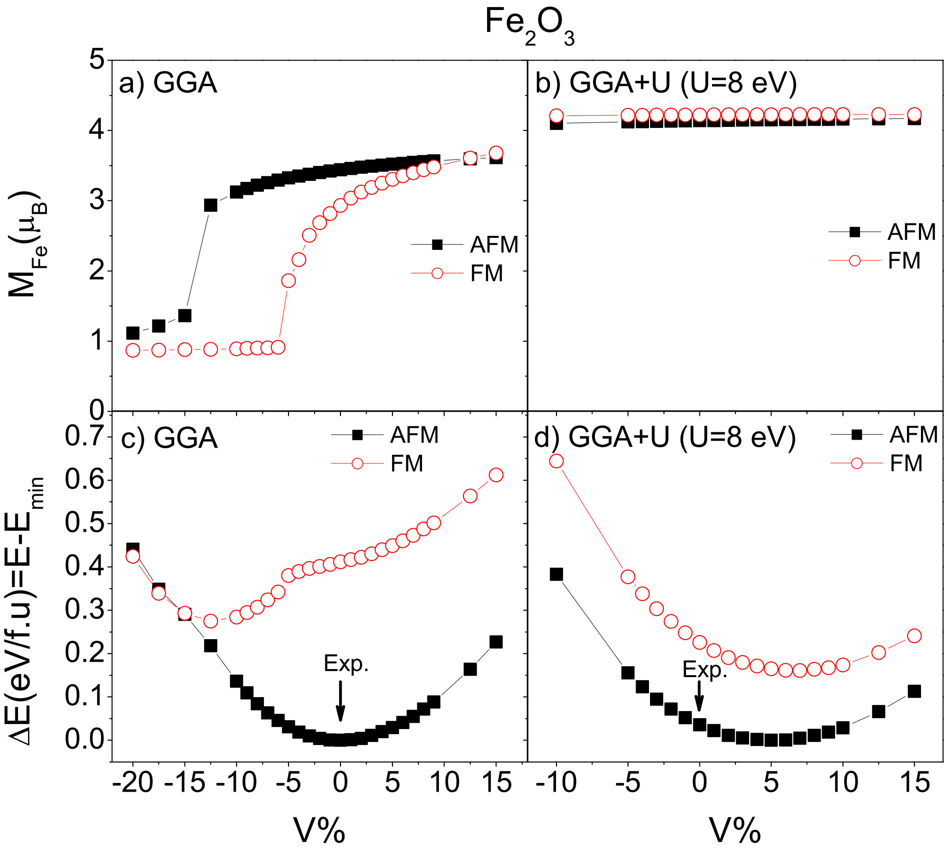

Figure 2.5: The absolute value of the magnetic moment of Fe in hematite within (a) GGA, (b) GGA+U and the total energies (c-d) as a function of volume. The volume is given in percent with respect to the experimental value which is set to 0% and marked with an arrow. Energies are given with respect to the configuration with lowest energy (set to 0).

structural properties, the volume calculated within GGA and GGA+U deviate from the experimental value (302 Å^3) by 0.76% and 5.0%, respectively.

Concerning the electronic behavior, the band gap of Fe_2O_3 is strongly underestimated (0.41 eV) within GGA. Using GGA+U with $U = 6$ eV and $J = 1$ eV, resulted in a band gap of 2.25 eV, in very good agreement with the reported experimental value (2.2 eV) by Gilbert *et al.* [67] and other groups (2.14-2.36 eV) [75, 76]. The type of band gap also changes from a Mott-Hubbard between occupied and empty Fe-3d within GGA, to a charge transfer type between occupied O-2p and empty Fe-3d within GGA+U. In Fig. 2.6, the total and the projected DOS are plotted within GGA and GGA+U. The calculation showed that the inclusion of an on-site Coulomb repulsion parameter is indispensable to obtain the band gap consistent with the experiment.

Table 2.4: The lattice parameters and bulk modulus of hematite computed by GGA and GGA+U. The starting values for the calculation in this study are taken from Ref. [57] and the experimental bulk moduli are from Ref. [70, 71].

	Exp.	GGA	GGA+U
$a(\mathring{A})$	5.04	5.07	5.29
$c(\mathring{A})$	13.75	13.85	14.44
V $(\mathring{A}^3)$	301.9	304.28	317.04
$\Delta V(^{\circ}/_{\circ})$	——	0.76	5.0
$B_0(GPa)$	231^a-178^b(258^c)	162	199
B'	4	3.2	3.9

[a] For P<3 (GPa) refer to Ref. [70]

[b] For 3<P<10 (GPa) refer to Ref. [70]

[c] This value corresponds to the volume of 301.76 $\mathring{A}^3$ taken from Ref. [71]

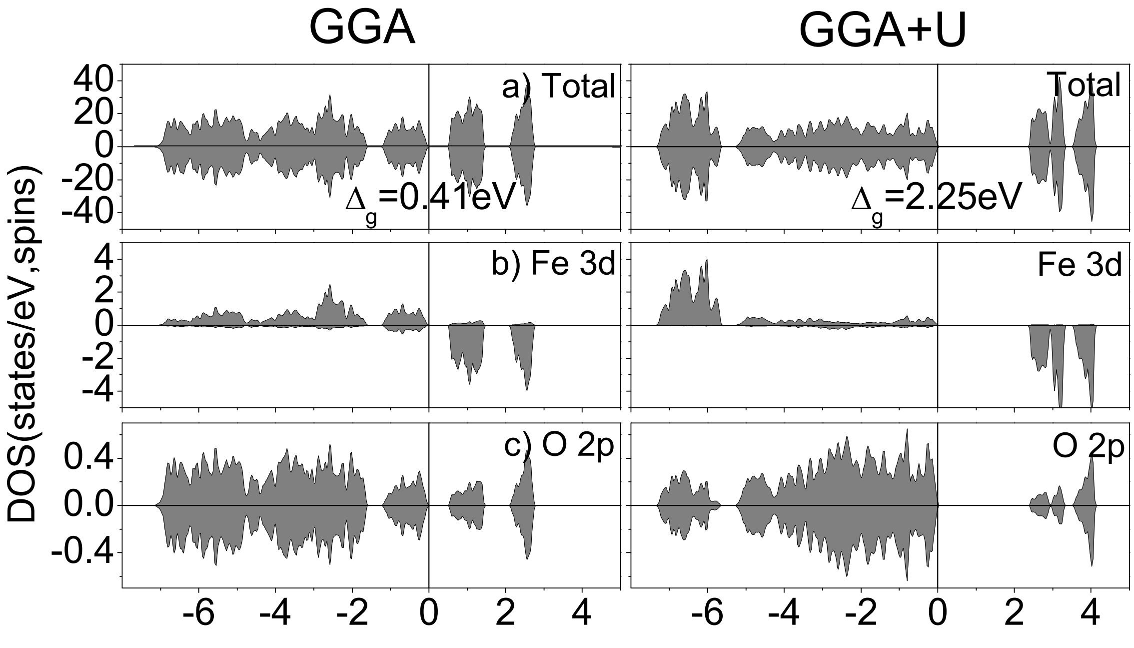

Figure 2.6: The total (a) and projected (b-c) density of states (DOS) for Fe_2O_3 on Fe^{3+} and O^{2-} states within GGA (left panel) and GGA+U (right panel) with $U = 6$ eV. The band gap within GGA+U between the empty Fe-3d and occupied O-2p states is 2.25 eV.

2.4 Summary

Ab-initio density functional theory calculations were carried out on α-Fe_2O_3 and $FeTiO_3$. Correlation effects were incorporated for the Fe-3*d* and Ti-3*d* orbitals within the GGA+U method. Different magnetic arrangements were considered for hematite and ilmenite (*e.g.* AFM, FM), as well as different oxidation states for ilmenite (Fe^{2+}/Ti^{4+} and Fe^{3+}/Ti^{3+}). The calculations for hematite show that the AFM configuration is the most stable one. However, for ilmenite, the AFM and FM are almost degenerate consistent with the low Néel temperature. GGA underestimates the band gap of hematite and for ilmenite a metallic behavior is predicted. Including the Hubbard parameter within GGA+U, an insulating behavior is reproduced for both hematite (Δ_g=2.25 eV) and ilmenite (Δ_g=2.21 eV), in good agreement with the experimentally observed band gap. Furthermore, a transition from high spin to low spin for hematite is found within GGA, while GGA+U did not show such a transition in the studied volume range. For ilmenite, no transition from HS to LS was observed in the studied volume range both within GGA and GGA+U.

Chapter 3

Origin of Magnetism in Hematite-Ilmenite Heterostructures

The previous chapter was devoted to the properties of bulk materials (α-Fe_2O_3, $FeTiO_3$). In this chapter, the origin of magnetism at the interface of these two oxides is investigated from first principles. This chapter includes the results of manuscripts M1, M2 and M3.

Before dealing with the interface properties, the phase diagram obtained by Burton [77] is briefly described. Ensuing, the effect of strain on the energetic stability is considered for systems grown on substrates of $Fe_2O_3(0001)$, $FeTiO_3(0001)$ and $Al_2O_3(0001)$. Finally, the magnetic interaction parameters are extracted from first principles in the last section of this chapter.

3.1 Fe_2O_3-$FeTiO_3$ phase diagram

The cluster variation method is used by Burton [77] in order to investigate theoretically the composition-temperature phase diagram of the Fe_2O_3-$FeTiO_3$ system. The calculated [78] and the experimental [79] phase diagram are shown in Fig. 3.1. In panel (a), the bulk composition is given in Ti_2O_3 mole fraction to emphasize that $FeTiO_3$ is the intermediate phase of the Fe_2O_3-Ti_2O_3 system at $X = 1/2$. The transition between $R\bar{3}c_{\mathrm{PM}}$ and $R\bar{3}_{\mathrm{PM}}$ (cation order-disorder transition in Fig. 3.1b) occurs in the Ti-rich region, while the transition between $R\bar{3}c_{\mathrm{PM}}$ and $R\bar{3}c_{\mathrm{CAF}}$ (magnetic order-disorder transition in Fig. 3.1b) occurs in the Ti-poor region. Concerning the symmetries, the region ($R\bar{3}c_{\mathrm{PM}} + R\bar{3}_{\mathrm{PM}}$) is asymmetric in the sense that more ilmenite will dissolve in hematite-solid solution (SS) than hematite in ilmenite-SS. Below this region, with decreasing temperature, the region ($R\bar{3}c_{\mathrm{CAF}} + R\bar{3}_{\mathrm{PM}}$) becomes approximately symmetric. An important equilibrium occurs at the eutectic point, in which the $R\bar{3}c_{\mathrm{PM}}$ phase breaks down on cooling to a mixture of antiferromagnetically ordered hematite-SS and paramagnetic ilmenite-SS ($R\bar{3}c_{\mathrm{CAF}} + R\bar{3}_{\mathrm{PM}}$).

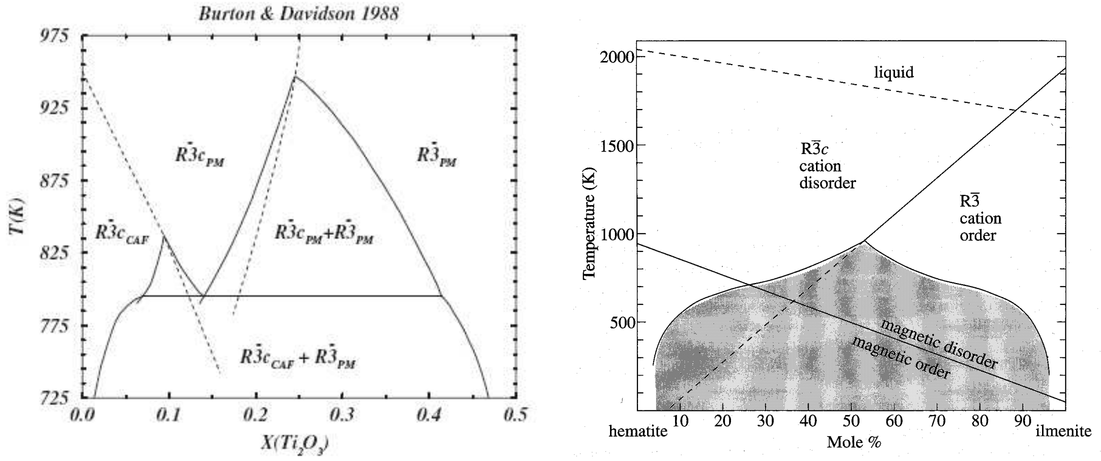

(a) Calculated phase diagram

(b) Experimental phase diagram

Figure 3.1: The calculated (a) and experimental (b) phase diagram of Fe_2O_3-$FeTiO_3$ system taken from Ref. [78] and [79],respectively. Subscripts on space group symbols indicate the paramagnetic (PM) and the canted antiferromagnetic (CAF) phases.

3.2 Fe_2O_3-$FeTiO_3$ interface

In order to design ferromagnetic semiconductors operating at room-temperature (RT) for spintronics devices, most of the efforts focus on homogeneous doping of semiconductors with magnetic impurities [9–12], but the interfaces in complex oxides prove to be another source of novel behavior [1, 80, 81]. Besides applications in spintronics, this material is also discussed in paleomagnetism as a possible cause of anomalies in the Earth's magnetic field, as well as for electronic devices (*e.g.*, varistors) because it is a wide band gap semiconductor that can be either *n*- or *p*-type depending on the doping concentration [13].

In Fe_2O_3 the charge is compensated by alternating layers of positively charged $2Fe^{3+}$ and negatively charged $3O^{2-}$, while $FeTiO_3$ is formed by stacking of $2Fe^{2+}$/ $3O^{2-}$/ $2Ti^{4+}$/ $3O^{2-}$ layers. Thus, at the interface between hematite and ilmenite, the charge neutrality is interrupted. One of the main questions is the charge compensation mechanism in the heterostructures or solid solutions of these two oxides. Based on bond valence models and kinetic Monte Carlo simulations with empirical chemical and magnetic interaction parameters, Robinson *et al.* [14] proposed the so-called *lamellar magnetism hypothesis*, stating that there is a mixture of Fe^{3+}/Fe^{2+} at the interface to compensate the disruption of charge neutrality. Since there were no first principles studies to explain the behavior at the atomic scale, we got motivated to investigate the microscopic origin of magnetism at the interface of Fe_2O_3-$FeTiO_3$. In order to resolve the question, different compensation mechanisms are studied, *e.g.*, disproportionation through Ti^{3+}/Ti^{4+} and Fe^{3+}/Fe^{2+}. Many different arrangements are contemplated, *e.g.*, layered versus more random distributions. We have varied systematically the concentration, distribution and the charge state in Ti doped Fe_2O_3 and Fe doped $FeTiO_3$. Some of the selected configurations in a 30- and 60-atom unit cell used in this study are shown in Figures 3.2, 3.3 and 3.4. The 33% Ti doped in a hematite host is shown in Fig. 3.3, while Fig. 3.4 illustrates the concentrations of 17%, 50%, 66% and 83%. For each structure the local and total magnetic moments are given.

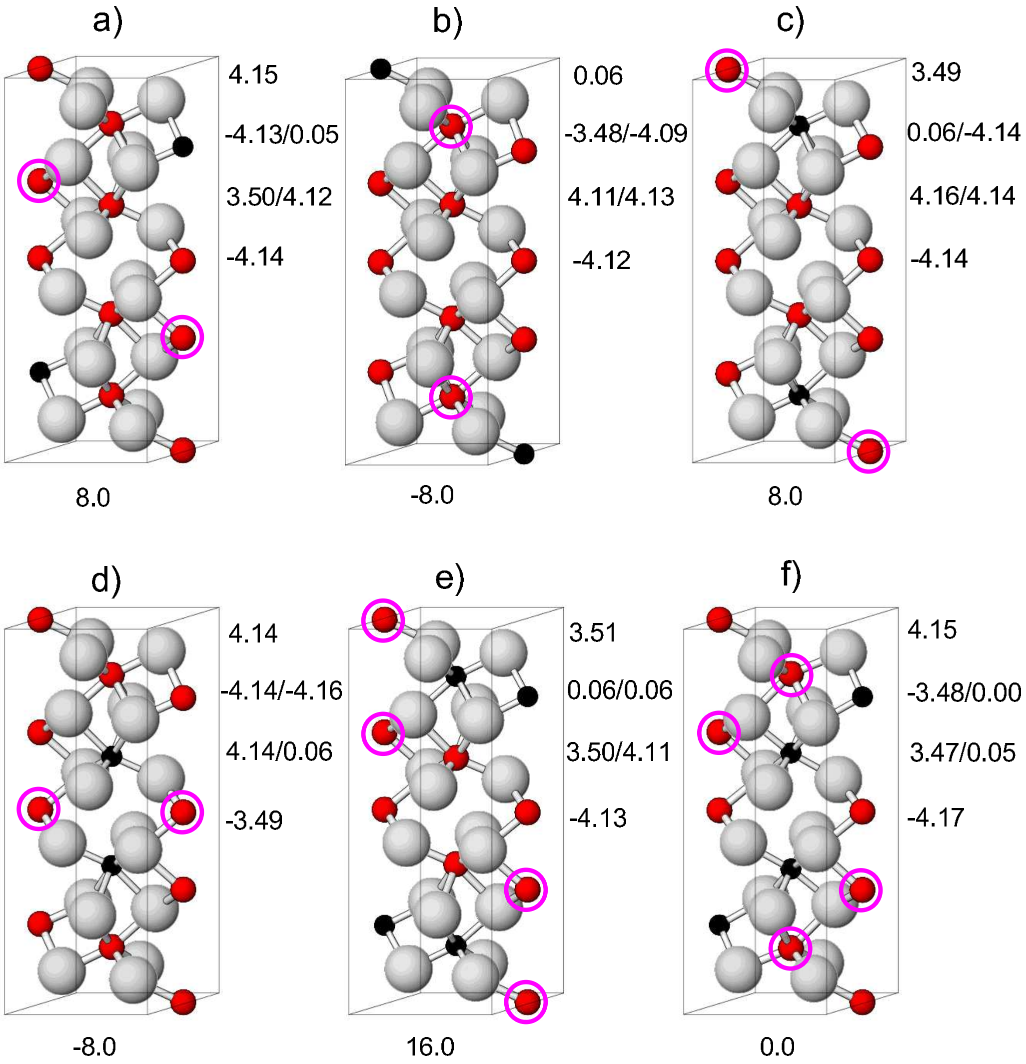

Figure 3.2: Selected structures modelled in a 30-atom unit cell together with the local magnetic moment and total magnetic moment under the cell. (a-d) correspond to 33% and (e-f) show 66% Ti doped Fe_2O_3. Fe, Ti and O are shown in red, black and grey spheres, respectively. Positions of the Fe^{2+} are marked by pink circles and the remaining iron atoms are Fe^{3+}.

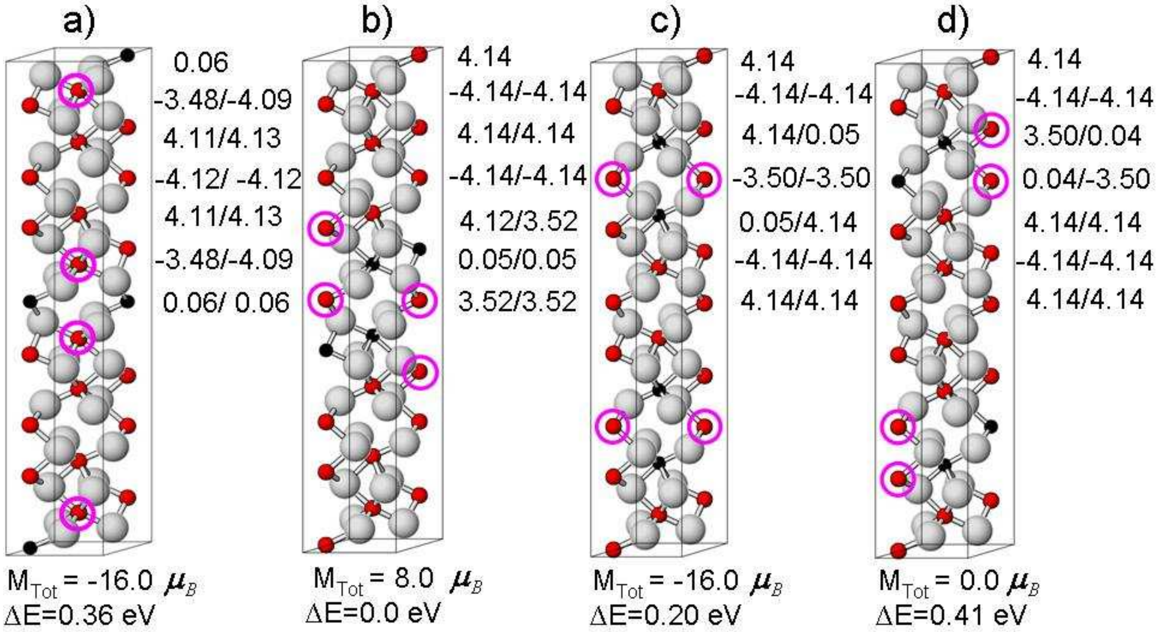

Figure 3.3: Selected structures modelled in a 60-atom unit cell together with the local magnetic moment and total magnetic moment under the cell. (a-d) show a concentration of 33% Ti doped Fe_2O_3. Fe, Ti and O are shown in red, black and grey spheres, respectively. Positions of the Fe^{2+} are marked by pink circles and the remaining iron atoms are Fe^{3+}. In (a) and (b) layered arrangements, while in (c) and (d) randomly distributed Ti in Fe_2O_3 are shown in the same and different spin sublattices, respectively.

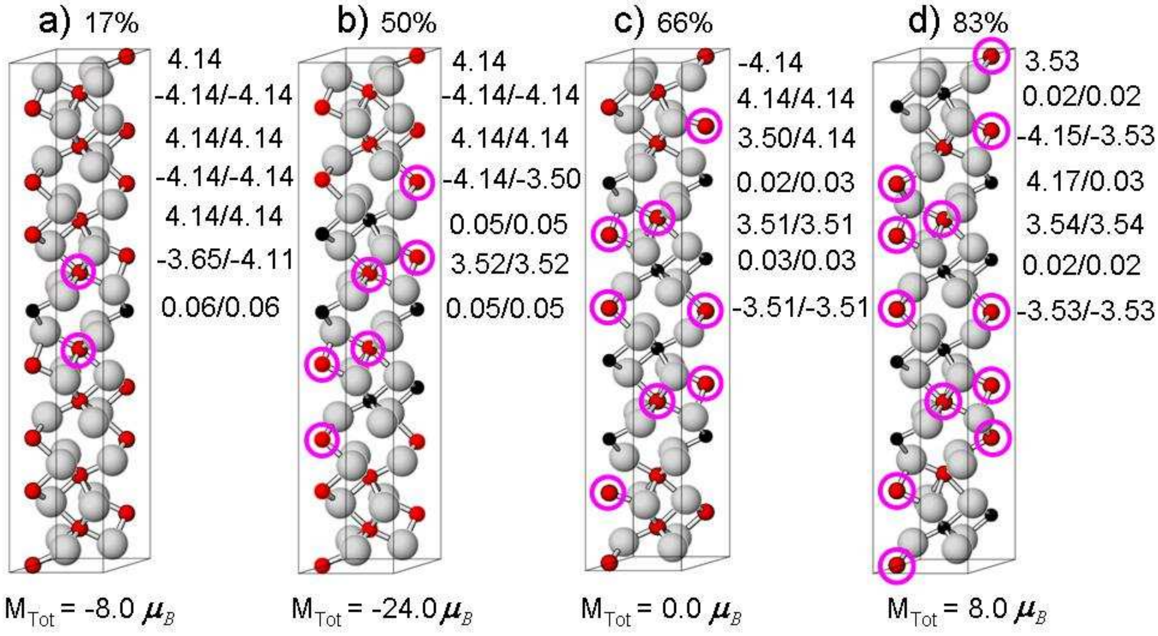

Figure 3.4: Selected structures modelled in a 60-atom unit cell together with the local magnetic moment and total magnetic moment under the cell: (a) is the single Ti layer with a concentration of 17%, (b) 50%, (c) 66% and (d) corresponds to 83% Ti doped Fe_2O_3. Fe, Ti and O are shown in red, black and grey spheres, respectively. Positions of the Fe^{2+} are marked by pink circles and the remaining iron atoms are Fe^{3+}.

3.2.1 Structural relaxation

A full structural optimization of the internal parameters has been performed. Table 3.1 lists the cation-anion distances up to the 6th nearest-neighbor in Fe_2O_3, $FeTiO_3$ and three different concentrations of Ti doped hematite (33%, 50% and 66%). An interesting trend is observed in the shortest cation-oxygen bond lengths, which tend to relax towards the values in the respective end member. While $d_{\mathrm{Fe}^{3+}\text{-}\mathrm{O}}$ remains close to the value in bulk hematite (1.96 Å), the bond lengths of the Ti-impurity ($d_{\mathrm{Ti}^{4+}\text{-}\mathrm{O}}$) and the neighboring Fe^{2+} ($d_{\mathrm{Fe}^{2+}\text{-}\mathrm{O}}$) relax towards the values in bulk ilmenite (1.94 and 2.11 Å, respectively).

Table 3.1: The cation-anion distances (given in Å) up to the 6th nearest-neighbor in Fe_2O_3, $FeTiO_3$ and three different concentrations of Ti doped hematite. Subscript IF refers to the cations at the interface. Δd_1 and Δd_2 are the deviation of the two shortest bond lengths in each system with respect to the values of the end member.

Systems	$d_{\mathrm{Cat.\text{-}Oxy.}}$(Å)	1st	Δd_1(%)	2nd	Δd_2(%)	3rd	4th	5th	6th
Fe_2O_3	$d_{\mathrm{Fe}^{3+}\text{-}\mathrm{O}}$	1.96		2.09		3.40	3.61	3.78	4.11
$FeTiO_3$	$d_{\mathrm{Fe}^{2+}\text{-}\mathrm{O}}$	2.11		2.25		3.41	3.68	3.94	4.20
	$d_{\mathrm{Ti}^{4+}\text{-}\mathrm{O}}$	1.94		2.06		3.60	3.83	3.84	4.28
33% Ti	$d_{\mathrm{Fe}^{2+}_{\mathrm{IF}}\text{-}\mathrm{O}}$	2.08	-1.42	2.12	-5.78	3.31	3.64	3.75	4.08
	$d_{\mathrm{Fe}^{3+}_{\mathrm{IF}}\text{-}\mathrm{O}}$	1.90	-3.06	2.18	4.31	3.40	3.53	3.86	4.14
	$d_{\mathrm{Fe}^{2+}\text{-}\mathrm{O}}$	2.04	-3.32	2.16	-4.00	3.35	3.66	3.81	4.09
	$d_{\mathrm{Ti}^{4+}\text{-}\mathrm{O}}$	1.89	-2.58	2.03	-1.46	3.48	3.71	3.77	4.09
	$d_{\mathrm{Fe}^{3+}\text{-}\mathrm{O}}$	1.95	-0.51	2.08	-0.48	3.41	3.64	3.76	4.07
50% Ti	$d_{\mathrm{Fe}^{2+}_{\mathrm{IF}}\text{-}\mathrm{O}}$	2.08	-1.42	2.11	-6.22	3.11	3.63	3.75	4.08
	$d_{\mathrm{Fe}^{3+}_{\mathrm{IF}}\text{-}\mathrm{O}}$	1.90	-3.06	2.18	4.31	3.39	3.51	3.86	4.14
	$d_{\mathrm{Fe}^{2+}\text{-}\mathrm{O}}$	2.04	-3.32	2.17	-3.56	3.34	3.63	3.80	4.08
	$d_{\mathrm{Ti}^{4+}\text{-}\mathrm{O}}$	1.90	-2.06	2.02	-1.94	3.51	3.72	3.74	4.14
	$d_{\mathrm{Fe}^{3+}\text{-}\mathrm{O}}$	1.95	-0.51	2.09	0.00	3.39	3.56	3.78	4.09
66% Ti	$d_{\mathrm{Fe}^{2+}_{\mathrm{IF}}\text{-}\mathrm{O}}$	2.03	-3.79	2.42	7.56	3.34	3.53	3.96	4.33
	$d_{\mathrm{Fe}^{3+}_{\mathrm{IF}}\text{-}\mathrm{O}}$	2.05	4.59	2.09	0.00	3.55	3.79	3.90	4.16
	$d_{\mathrm{Fe}^{2+}\text{-}\mathrm{O}}$	2.13	0.95	2.27	0.89	3.39	3.61	3.95	4.23
	$d_{\mathrm{Ti}^{4+}\text{-}\mathrm{O}}$	1.94	0.00	2.06	0.00	3.61	3.83	3.87	4.31
	$d_{\mathrm{Fe}^{3+}\text{-}\mathrm{O}}$	2.00	2.04	2.15	2.87	3.50	3.78	3.88	4.21

3.2.2 Compensation mechanism and energetic trends

We start the discussion with Ilm_{33} which corresponds to four Ti-ions out of 24 cations in the 60-atom cell. We find that the formation of a compact ilmenite-like block with a Fe-layer sandwiched between two Ti-layers (Fig. 3.3b), is by 0.36 eV more favorable than incorporation of single Ti layers in the hematite host (Fig. 3.3a). One can see that iron in the central layer turns into Fe^{2+} and the charge mismatch at the interface compensated by Fe^{2+} and Fe^{3+} in the contact layer [82]. The formation of layered arrangements (Fig. 3.3a) is favored compared to a more random distribution with 50% Ti-substituted cation layers (*e.g.*, Fig. 3.3-c and -d).

The Fe^{2+}-layer sandwiched between two Ti-layers in Fig. 3.3b is only weakly coupled to the next Fe-layer (parallel and antiparallel orientation of the magnetic moments are nearly degenerate as in the ilmenite end member). Therefore, at temperatures above the Néel temperature of ilmenite, such layers will not contribute to the total magnetization. In contrast, Fe^{2+} in the contact layer shows a strong antiferromagnetic coupling to the neighboring Fe-layer of the hematite host (for the structure in Fig. 3.3b the total magnetic moment is $8.0\,\mu_B$). These defect interface moments are responsible for the ferrimagnetic behavior of the system.

With respect to magnetism, each Ti ion adds a magnetic moment of $4\,\mu_B$ independent of whether the extra electron is localized at Ti (Ti^{3+}) or at a neighboring Fe (Fe^{2+}). Furthermore, it is found that the incorporation of Ti in the same spin sublattice (Fig. 3.3c), which maximizes the magnetic moment of the system, is favored compared to incorporation in the different spin sublattice (Fig. 3.3d) by 0.22 eV. The trend towards layered arrangements is retained for 66%, while for 83% the ordered and disordered phases are nearly degenerate. By substituting Fe for Ti in $FeTiO_3$, iron is Fe^{3+} and additionally one of the Fe in the next layer becomes Fe^{3+} to compensate the charge. Thus, a mixed Fe^{2+}, Fe^{3+} contact layer is formed. The substituted Fe shows a strong tendency to couple antiparallel to the neighboring Fe layer. The magnetic coupling at the interface of Fe_2O_3-$FeTiO_3$ between Fe^{2+} and Fe^{3+} are extracted and will be explained in section 3.4.

Concerning the electronic properties, doping Fe_2O_3 with Ti leads to an impurity level in the band gap arising from the d_{z^2} (a_{1g}) orbital of Fe^{2+} in the contact layer. The density of states (DOS) for $x = 33\%$ Ti doped hematite is plotted in Fig. 3.5. The Fe^{2+} formed in the contact layer has an impurity state pinned at the Fermi level for all the layered and solid solution structures shown in Fig. 3.3. This trend is robust with respect to the U-values, as well as to the concentration of Ti in the system, which is observed in most of the structures illustrated in Fig. 3.2 and Fig. 3.3.

For the concentrations $x = 17\%$, 50%, 66% and 83% of Ti-doped hematite the DOS plots are shown in Fig. 3.6, with the corresponding structures illustrated in Fig. 3.4. In other concentrations also the formation of Fe^{2+} in the contact layer leads to an impurity state in the band gap that is pinned at the Fermi level and reduces the band gap from ~ 2.1 eV in α-Fe_2O_3 to 1.65, 1.73, 1.64 and 1.29 for $x = 17\%$, 50%, 66% and 83%, respectively.

3.2.3 Phase diagram

Nearly 50 different systems are studied to compile a phase diagram of stability. The energetic stability with respect to the end members is described by the formation energy $E_f = E_{Fe_{2-x}Ti_xO_3} - (1-x)E_{Fe_2O_3} - xE_{FeTiO_3}$, where $E_{Fe_{2-x}Ti_xO_3}$, $E_{Fe_2O_3}$ and E_{FeTiO_3} are the total energies of the system with a concentration x of ilmenite and the two end members, respectively. The formation energy as a function of x is plotted in Fig. 3.7. We have found that the compensation mechanism through Ti^{4+} and a disproportionation of iron into Fe^{2+}, Fe^{3+} in the contact layer is more favorable than the mechanisms involving Ti^{3+}. Moreover, the layered arrangements are more stable than randomly distributed configurations for $17\% \leq x \leq 83\%$.

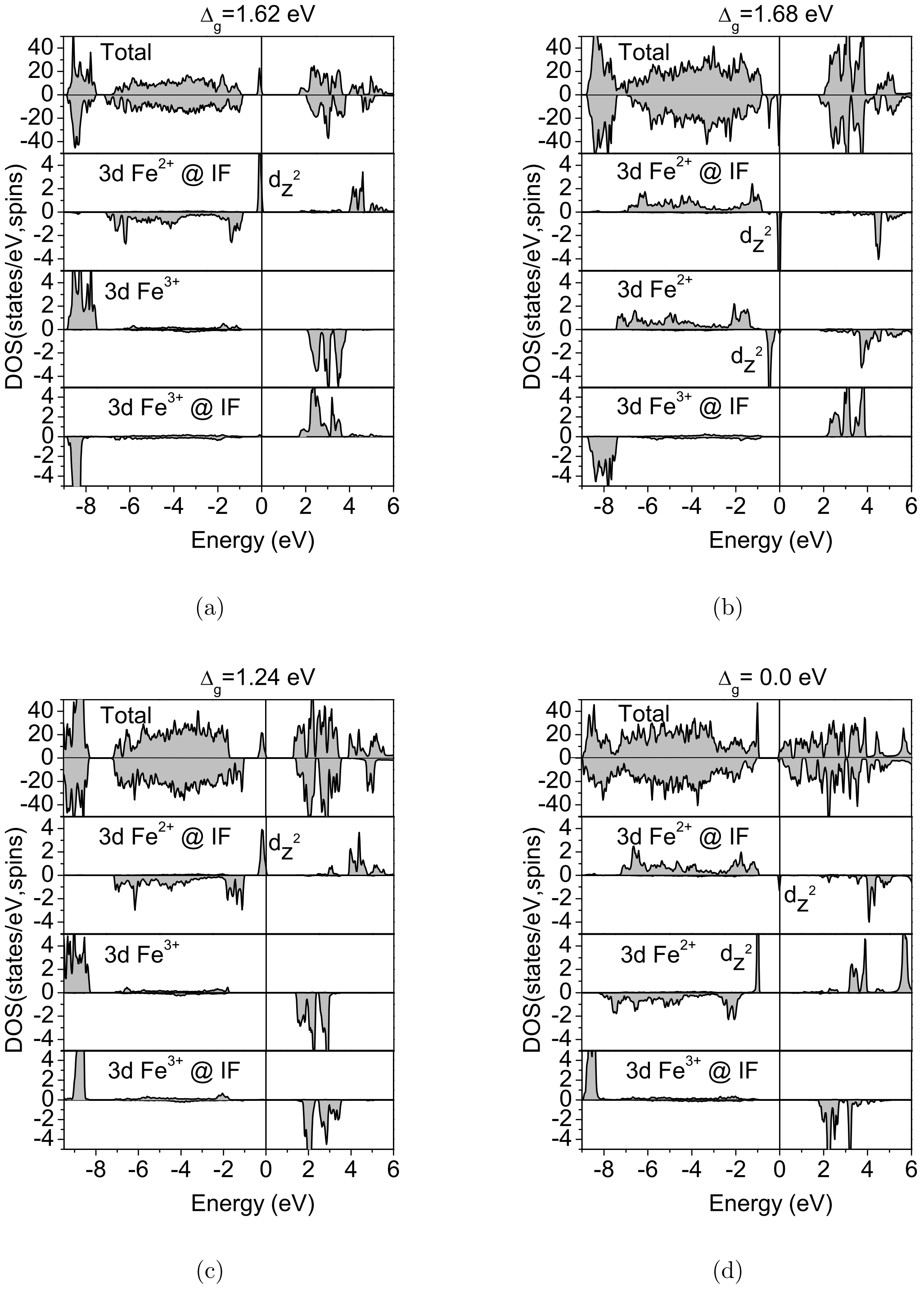

(a)

(b)

(c)

(d)

Figure 3.5: Density of states (DOS) of $Fe_{2-x}Ti_xO_3$ for $x = 33\%$: DOS of (a) a single Ti layer within Fe_2O_3 bulk (see Fig. 3.3a), (b) an ilmenite-like block in Fe_2O_3 (see Fig. 3.3b). In (c) and (d) the DOS of a solid solution with 50% Ti-substituted in layers with the same (Fig. 3.3c) and different spin orientation (Fig. 3.3d) are shown.

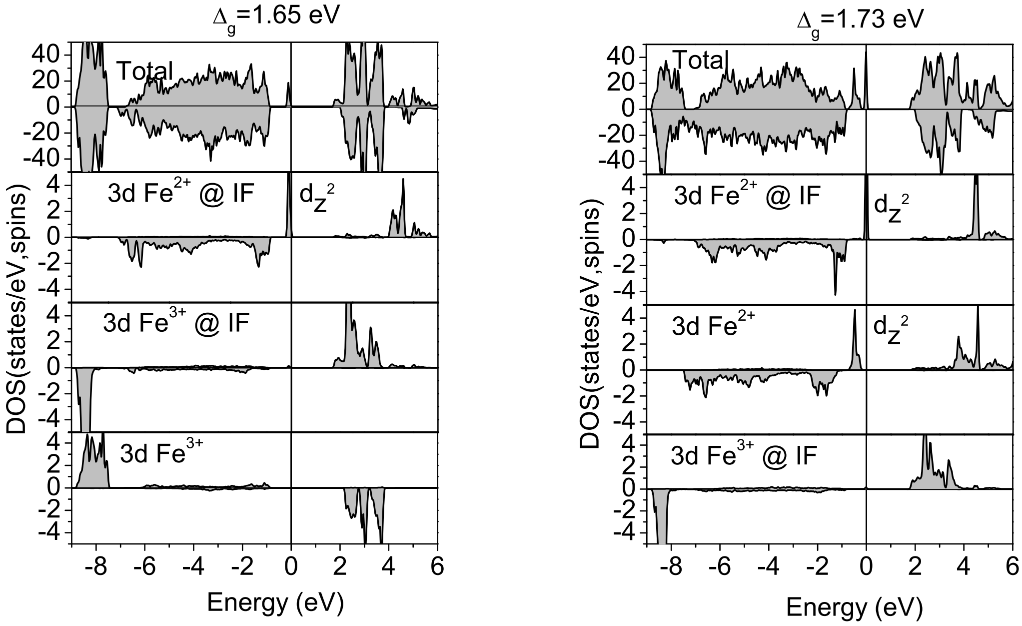

(a) 17% Ti-doped Fe_2O_3 (b) 50% Ti-doped Fe_2O_3

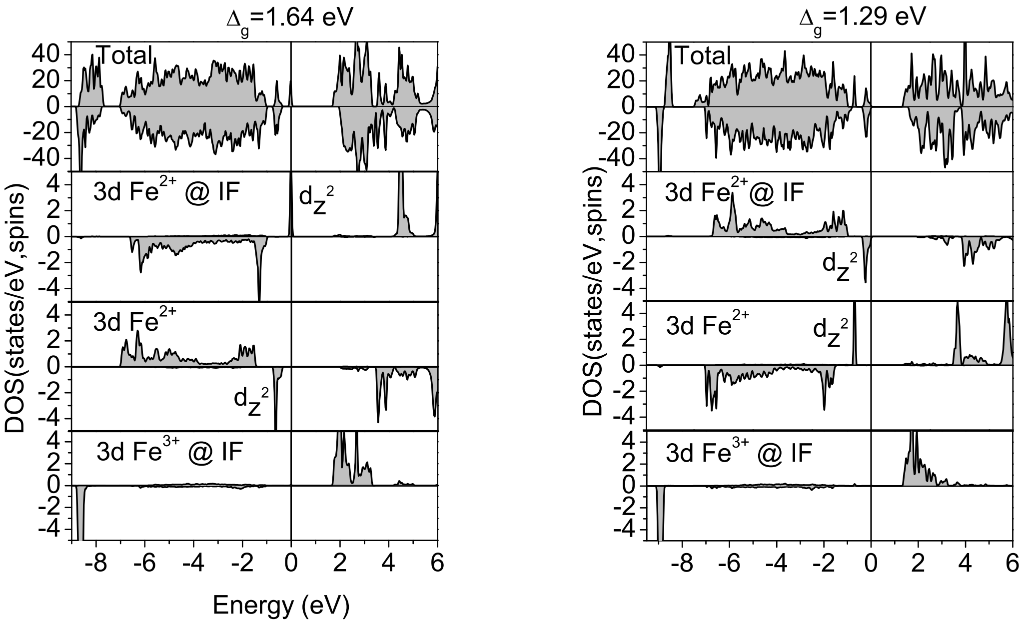

(c) 66% Ti-doped Fe_2O_3 (d) 83% Ti-doped Fe_2O_3

Figure 3.6: Density of states (DOS) of $Fe_{2-x}Ti_xO_3$ for x = 17%, 50%, 66% and 83%: For comparison also the DOS of cations further away from the interface are shown.

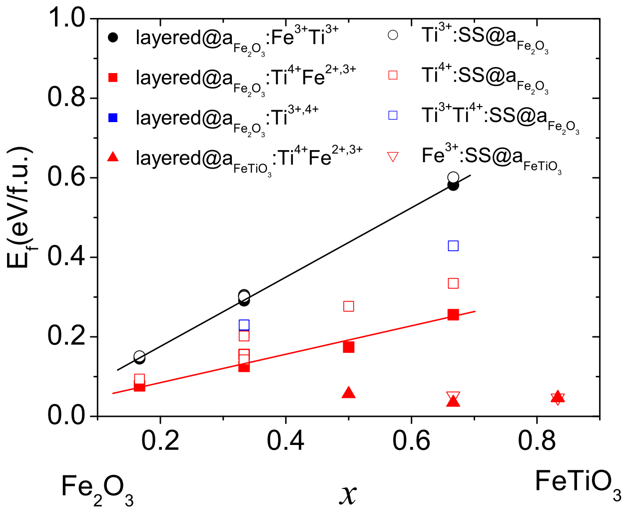

Figure 3.7: Formation energy (eV/f.u.) as a function of FeTiO$_3$ concentration, x, with respect to the end members. Layered arrangements and solid solutions (SS) are denoted by full and open symbols, respectively. (Lines are guide for the eyes)

The linear increase in the formation energy indicates that the systems with growing x become unstable when strained to the hematite lattice parameters. On the other hand, using the ilmenite lattice parameters instead of hematite, there is a gain of about 0.22 eV/f.u. in the energy (red filled up triangles in Fig. 3.7). The effect of strain on the stability and electronic properties will be considered in more detail in section 3.3 (results of manuscript M2).

3.2.4 Summary

In summary, a comprehensive GGA+U study of the cation, charge and magnetic order in the hematite-ilmenite system is presented. The results provide the first theoretical evidence for the *lamellar magnetism hypothesis* [14], where the polar discontinuity is accommodated with a disproportionated Fe^{2+}, Fe^{3+} contact layer [82]. The uncompensated moments that arise at the interface due to the charge mismatch have a strong tendency to couple antiferromagnetically to the next hematite layer, leading thus to a ferrimagnetic behavior of the system. The d$_{z^2}$ (a$_{1g}$) orbital of Fe^{2+} in the contact layer is at the Fermi level, resulting in an impurity state in most of the studied compositions.

3.3 Strain effect

The effect of strain on the stability and electronic properties of a $Fe_{2-x}Ti_xO_3$ film, as presented in manuscript M2, is described in this section.

The incorporation of Ti in hematite introduces a substantial strain: the volume of the end member ilmenite is 9.7% larger than the one of hematite. The experimental lattice constants and corresponding volumes are presented in Table 3.2. Indeed, lens-shaped dark contrasts around nanoscale hematite lamellae in an ilmenite host are

Table 3.2: The experimental lattice constants and corresponding volumes.

	Al_2O_3 [83]	Fe_2O_3 [57]	$FeTiO_3$ [58]
$a(\mathring{A})$	4.757	5.035	5.177
$c(\mathring{A})$	12.991	13.751	14.265
Volume($\mathring{A}^3$)	254.52	301.92	331.06

imaged by transmission electron microscopy (*cf.* Fig. 3.8) which indicate significant strain fields [14].

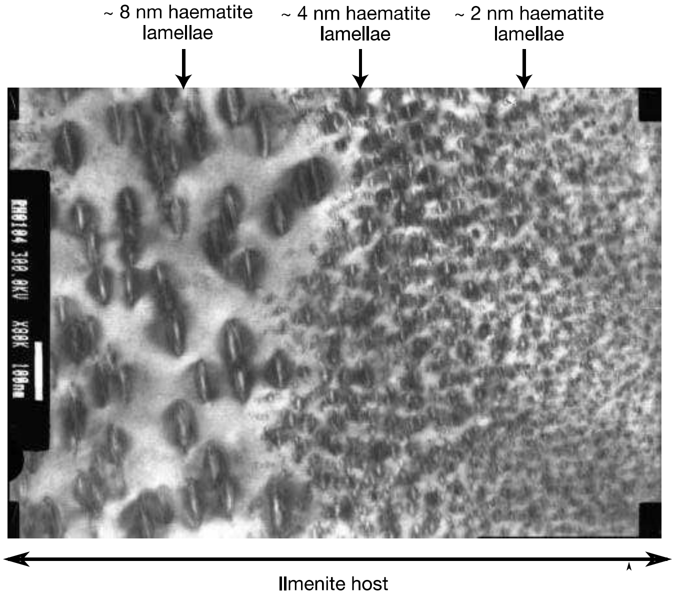

Figure 3.8: Transmission electron microscope image of hematite exsolution lamellae in an ilmenite host taken from Ref. [14]. Dark lens-shape fringes around lamellae indicate lattice strain.

Epitaxial $Fe_{2-x}Ti_xO_3$ films [8,9,13,84–86] are typically grown on an $Al_2O_3(0001)$-substrate which introduces a substantial compressive strain of 5.8% and 8.8% compared to Fe_2O_3 and $FeTiO_3$. Only rarely, a Cr_2O_3-buffer layer is used [10] to reduce the lattice mismatch.

Epitaxial strain can have a strong impact on the film properties. For example, it can tune the magnetic interactions in magnetoelastic composites [87], enhance ferroelectricity [88, 89] or even induce orbital reconstructions [90]. The goal of the present study is to explore the effect of strain on the properties of $Fe_{2-x}Ti_xO_3$. In particular we address its influence on (i) the energetic stability and compensation mechanism as well as on (ii) the electronic, magnetic and structural properties of the system. DFT calculations are performed on solid solution and layered configurations with $x = 0.17, 0.33, 0.50$ and 0.66; strained laterally at the lattice parameters of $Al_2O_3(0001)$, $Fe_2O_3(0001)$ and $FeTiO_3(0001)$.

The optimized c/a-ratio and volume (Fig. 3.9a-b) show a linear increase with x_{Ilm} in accordance with Vegard's law, similar to what was observed experimentally in synthetic hematite-ilmenite solid solutions [4]. Furthermore, for a given concentration, both c/a and V are largely independent of the distribution of Ti-impurities. The c/a-ratio of bulk $FeTiO_3$ (2.76) is slightly larger than the one of α-Fe_2O_3 and Al_2O_3 (2.73). Due to the small tensile/compressive strain, when using a_{FeTiO_3}/ $a_{Fe_2O_3}$, the c/a-ratio of $Fe_{2-x}Ti_xO_3$ is slightly reduced (-1.1 to -2.8%)/increased (3.1-5.2%), respectively. In contrast, due to the high compressive strain on an Al_2O_3-substrate, c/a increases strongly by 14.7-16.6%, which corresponds to $c_{rel} = 14.89 - 15.15\,\text{Å}$. Nevertheless, the volume does not completely relax: the volume of the system strained at the Al_2O_3-lateral lattice constant is 6.8% (10.2%) smaller than when strained at $a_{Fe_2O_3}$ (a_{FeTiO_3}). The volumes of $Fe_{2-x}Ti_xO_3$ strained at a_{FeTiO_3} and $a_{Fe_2O_3}$ lie between the ones of the end members Fe_2O_3 and $FeTiO_3$.

X-ray diffraction data for $Fe_{2-x}Ti_xO_3$ films on $Al_2O_3(0001)$ [91,92] indicate significant lateral strain relaxation: already in a 10 nm thick film, a relaxes to the bulk value of $FeTiO_3$ with only a small change in c/a (see Fig. 3.9a). The c/a values and volumes obtained by Takada *et al.* [92] are in good agreement with the DFT values of the systems strained at a_{FeTiO_3}.

Next we turn to the influence of strain on the energetic stability. The formation energy with respect to the end members as a function of x_{Ilm} is shown in (Fig. 3.9c) for the three different substrate lattice constants. For each Ti-concentration several different cation arrangements are considered, *e.g.*, for $x = 0.33$ these include an ordered arrangement with an Fe layer sandwiched between two Ti layers (Fig. 3.3b) or solid solutions with Ti ions either in the same (Fig. 3.3c) or different spin-sublattices (Fig. 3.3d). We find that compensation through Ti^{4+} and disproportionation in Fe^{2+}, Fe^{3+} is more favorable over mechanisms involving Ti^{3+}. Furthermore, the formation energy increases linearly with x_{Ilm}. These features are independent of the substrate lattice parameters. Systems strained laterally at a_{FeTiO_3} are more stable than the ones on $a_{Fe_2O_3}$. In contrast, the formation energy of films strained at $a_{Al_2O_3}$ increases by 0.7 eV as compared to films on $a_{Fe_2O_3}$. This implies that the strong compressive strain is energetically unfavorable. While for systems strained on hematite and ilmenite substrates, layered arrangements (full symbols) are more favorable than homogeneous distributions (open symbols), the trend is reversed for $x = 0.33$ and $x = 0.66$ on an $Al_2O_3(0001)$-substrate.

In solid solutions, Ti substitution in different spin-sublattices (*e.g.*, in adjacent layers) resulting in a zero net magnetization is less favorable compared to substitution in the same spin-sublattice, which maximizes the total magnetization. This trend leads to a ferrimagnetic behavior in the system.

Concerning the electronic properties of the hemo-ilmenite system, Fig. 3.10 plots the density of states of a Ti-double layer in a hematite host (Fig. 3.3b), but similar behavior is observed for all studied systems. Upon Ti^{4+} substitution, an iron ion from the neighboring layer turns Fe^{2+}, as observed also for isolated impurities by Velev *et al.* [93]. The $Fe^{2+}O_6$ and the TiO_6-octahedron are corner- (and not face-) sharing. The so formed Fe^{2+}-ions in the contact layer have an impurity state of a_{1g} symmetry (d_{z^2}) that is pinned at the Fermi level for systems strained at $a_{Fe_2O_3}$ and a_{FeTiO_3}. Such a mid-gap state was recently reported from x-ray valence band photoemission [94] and optical measurements [86], although it was attributed to the low oxygen pressure during deposition. The main feature related to strain is the change in bandwidth: while for tensile strain at a_{FeTiO_3} the bands are narrowed, for compressive strain at $a_{Al_2O_3}$ they are strongly broadened. This results in a reduction of the band gap (between the impurity state defining the Fermi level and the bottom of the conduction band) from 1.90 eV for a_{FeTiO_3} and 1.79 eV for $a_{Fe_2O_3}$ to 1.43 eV for $a_{Al_2O_3}$. For comparison, the corresponding values for $x = 66\%$ are 1.64 eV for a_{FeTiO_3} and 1.46 eV for $a_{Fe_2O_3}$ to 0.78 eV for $a_{Al_2O_3}$.

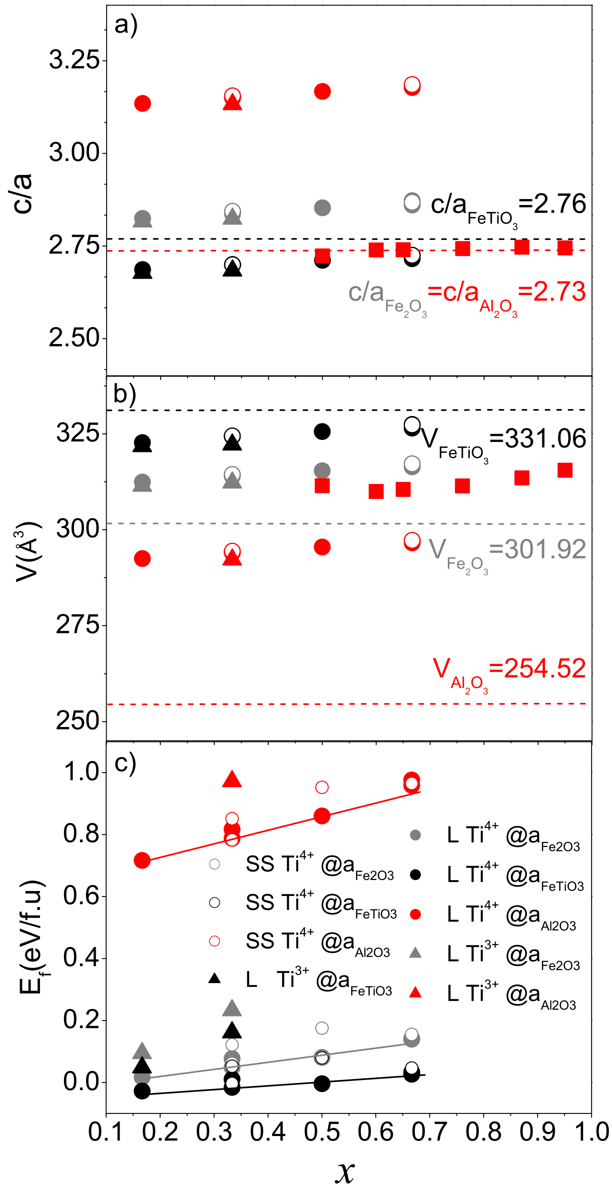

Figure 3.9: (a) c/a-ratio (b) volume and (c) formation energy (eV/f.u) versus ilmenite concentration x_{Ilm} for $Fe_{2-x}Ti_xO_3$ strained at the Al_2O_3 (red/dark grey), Fe_2O_3 (grey) and $FeTiO_3$ (black) lateral lattice constants. Circles (triangles) denote compensation involving Ti^{4+}(Ti^{3+}). Open/filled symbols refer to solid solutions (SS)/ layered configurations (L). Horizontal lines mark the bulk c/a ratio and the volume of the end members and Al_2O_3. Red (dark grey) squares indicate experimental data from Takada *et al.* [92].

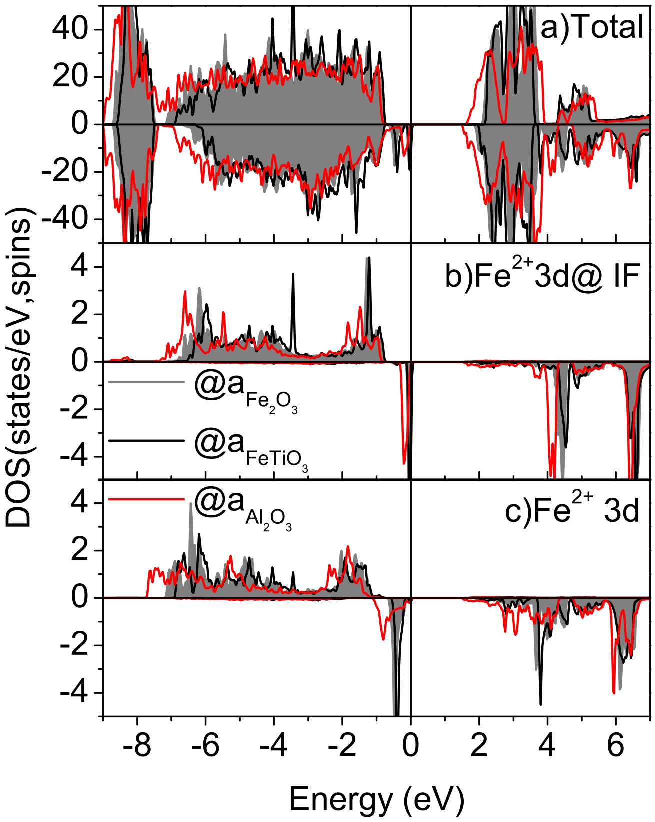

Figure 3.10: Density of states of $Fe_{1.67}Ti_{0.33}O_3$ containing two Ti-layers in a hematite host (shown in Fig. 3.3b) illustrating the total (a) and projected DOS on the Fe-3d states of Fe^{2+} in the interface layer (b) and between the two Ti-layers (c). The DOS of the system strained at the lateral lattice parameters of Fe_2O_3, Al_2O_3, and $FeTiO_3$ is shown with a grey shaded area, red (dark grey), and black line, respectively.

The local magnetic moments and total magnetization of the systems with $x = 0.33$ is displayed in Fig. 3.3a-d. Strain has only a small impact on the magnetic moments of Fe^{2+} ($\sim 3.5\,\mu_B$) and Fe^{3+} ($\sim 4.1\,\mu_B$) which are reduced by less than $0.05\,\mu_B$ at $a_{Al_2O_3}$. The Fe^{2+}-layer sandwiched between two Ti-layers in Fig. 3.3b is only weakly coupled to the next Fe-layer (parallel and antiparallel orientation of the magnetic moments are nearly degenerate as in the ilmenite end member). Therefore, at temperatures above the Néel temperature of ilmenite, such layers will not contribute to the total magnetization. In contrast, Fe^{2+} in the contact layer shows a strong antiferromagnetic coupling to the neighboring Fe^{3+}-layer of the hematite host. These defect interface moments are responsible for the ferrimagnetic behavior of the system ($M_{tot} = 8.0\,\mu_B$). In solid solutions, Ti substitution in different spin-sublattices (*e.g.* in adjacent layers as shown in Fig. 3.3d) resulting in a zero net magnetization is less favorable compared to substitution in the same spin-sublattice (Fig. 3.3c), which maximizes the total magnetization ($M_{tot} = -16.0\,\mu_B$). This trend promotes ferrimagnetic behavior in the system.

In conclusion, we find that in hematite-ilmenite heterostructures and solid solutions, the charge compensation takes place through a mixed Fe^{2+}, Fe^{3+} contact layer. This mechanism is robust with respect to substrate-induced strain. Furthermore, layered arrangements are more stable than solid solutions, but compressive strain at $a_{Al_2O_3}$ is likely to cause a stronger competition and even reverse the trend for $x = 0.33$ and $x = 0.66$. The growth of epitaxial films on an Al_2O_3-substrate is connected with a high energy cost. Therefore, in order to release strain, such films may roughen or buckle in the first layers as recently reported by Popova *et al.* [91]. In contrast, the growth on lattice matched substrates or even substrates that produce a small tensile strain like $FeTiO_3$ is energetically favored. Our DFT results indicate that strain can have a strong impact on the structural and electronic properties in the hematite-ilmenite system: *e.g.*, by tuning the bandwidth or the position of impurity levels in the band gap and thus changing the concentration of spin-polarized carriers.

3.4 Magnetic exchange interaction parameters

The polar discontinuity has been recognized as a driving force in the emergence of unexpected electronic phases at oxide interfaces. One example is the stable room temperature remanent magnetization observed in nanoscale intergrowths of the Fe_2O_3/ $FeTiO_3$ system [4]. Robinson *et al.* [14] proposed that this phenomenon arises due to a mixture of Fe^{2+} and Fe^{3+} at the interface. Recent GGA+U calculations have provided first theoretical evidence for this so-called *lamellar magnetism hypothesis* (LMH) [82]. The study of Robinson *et al.* [14] was based on Monte Carlo simulations that used an empirical set of magnetic interaction parameters based on the untested assumption that Fe^{3+}-Fe^{2+} interactions (for which there are no literature data) should have the same sign but lower magnitudes than the corresponding Fe^{3+}-Fe^{3+} interactions (for which literature data exist). Exchange interaction parameters can be derived for example by fitting inelastic neutron scattering data to the theoretical dispersion relation expression [95,96] and magnetic susceptibility [97]. On the other hand first principles calculations can be very useful to extract these quantities either by fitting total energy differences of several magnetic configurations on a Heisenberg Hamiltonian [98–101] or by using the second variation of the total energy [102]. Such methods have been applied in the past to bulk materials or impurities in diluted magnetic semiconductors [103]. In this section, we provide for the first time magnetic interaction parameters for an oxide interface, which are not accessible from experiment.

We have extracted the magnetic interaction parameters for the end members, Fe_2O_3 and $FeTiO_3$ from DFT calculations and compared with parameters available from inelastic neutron scattering data [59, 104–106]. For Fe_2O_3 we compare our results with previous theoretical study [107]. The main goal here is to determine the magnetic interaction parameters between Fe^{2+} and Fe^{3+} at the hematite-ilmenite interface (results of manuscript M3).

3.4.1 Calculation of magnetic interaction parameters

In order to map the total energy from the DFT calculations on a Heisenberg Hamiltonian, we separate it in a nonmagnetic (H_0) and magnetic contribution:

$$H = H_0 - \frac{1}{2}\sum_{i,j}\sum_{m=1}^{k} n_m J_m^q(r_{ij})\mathbf{S}_i.\mathbf{S}_j, \tag{3.1}$$

where the summation is over all distinct spin-pairs. $\mathbf{S}_i$ is the spin vector at the i^{th} lattice site, and $J_m^q(r_{ij})$ is the magnetic exchange interaction parameter between the magnetic moments on site i and j. The index m ranges from first to k^{th} neighbor, n_m is the multiplicity of neighbors corresponding to J_m and q defines the type of cations in the pair. For example, $J_m^{3+,3+}$ is an interaction between Fe^{3+}-pairs, while $J_m^{2+,3+}$ is an interaction between Fe^{2+} and Fe^{3+}. $J_m^q < 0$ (> 0) corresponds to antiferromagnetic (ferromagnetic) coupling. The interaction type (J_{ij}) and connectivity ($\mathbf{S}_i.\mathbf{S}_j$) matrix are given in appendix C and D, respectively.

Fig. 3.11 illustrates the magnetic pair exchange interactions used in our modelling. J_1 is the interlayer interaction between cations in face-sharing octahedra. J_2 is the intralayer interaction between cations in edge-sharing octahedra. J_3, J_4 and J_5 correspond to the interlayer interactions among cations with corner-sharing octahedra and J_6, J_7 and J_8 are the interactions with cations from the second nearest layer.

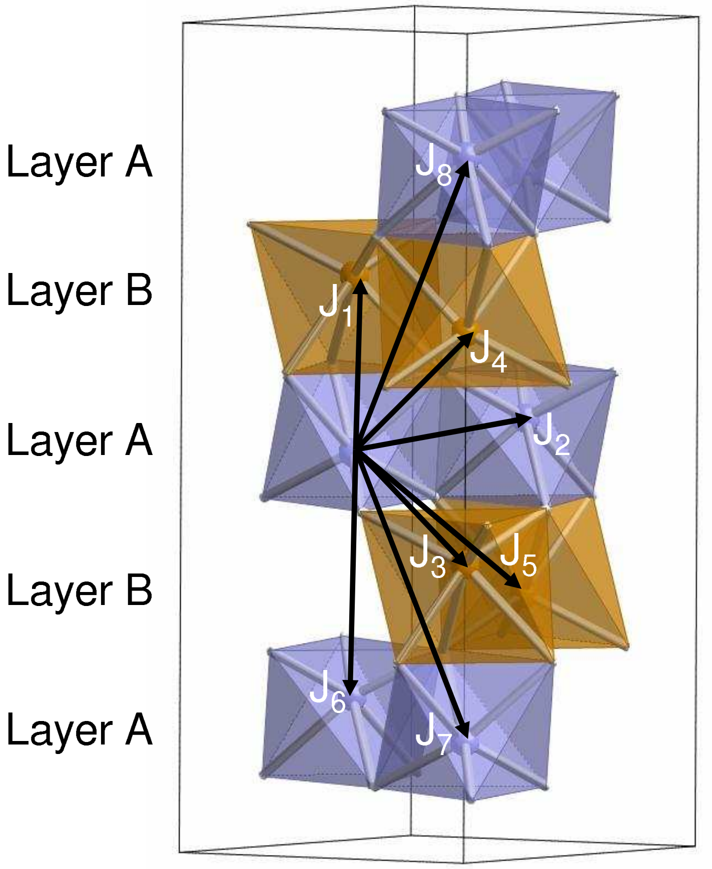

Figure 3.11: Definition of the pair magnetic exchange parameters J_1 to J_8 between the cations.

Because hematite does not show spin-canting below the Morin temperature, we have investigated only collinear magnetic configurations. $J_m^q(r_{ij})$ are calculated by mapping the energy differences of these spin-arrangements to the Heisenberg Hamiltonian in Eq. (3.1). The fitting of the DFT energy differences to the Hamiltonian is done by multi-variable least-squares method.

3.4.2 Magnetic exchange interaction of the end members

We first test the method for the end members for which we have calculated 23 and 10 different collinear spin arrangements, respectively, as presented in Table B.1 and B.2.

The calculated values for hematite ($J_m^{3+,3+}$) are displayed in Fig. 3.12a together with the values obtained from neutron scattering [104]. We find that for hematite, the dominating parameters are the interlayer magnetic interactions $J_3 = -72\,\mathrm{K}$, $J_4 = J_5 = -50\,\mathrm{K}$. The negative sign implies a strong antiferromagnetic coupling between the Fe^{3+}-layers and explains the AFM ground state of hematite. The values are in good agreement both with the experimental data of Samuelsen and Shirane [104] as well as with previous LDA/LDA+U calculations by Mazurenko and Anisimov [107], who also took into account spin-orbit coupling.

In contrast to experiment, J_1 and J_2 are found to be negative. However, both parameters are significantly smaller than J_3-J_5 and play therefore a minor role in the resulting magnetic ordering. Thus, the strong interlayer AFM coupling enforces ferromagnetic coupling within each Fe^{3+}-layer. Furthermore, our values support the assumption by Goodenough [108] and Anderson [109] that cation interactions mediated by an anion (superexchange) (J_3, J_4, J_5) are negative in sign and much stronger than direct interactions between cations in face (edge) sharing octahedra, J_1 (J_2).

The calculated values for ilmenite ($J_m^{2+,2+}$) are shown in Fig. 3.12b. In ilmenite, Fe^{2+}-layers alternate with Ti^{4+}-layers. Since Ti is in 4+ state (d^0), all the Fe-Ti interactions are zero (J_1, J_3, J_4, J_5). The positive J_2 implies that magnetic interactions within the Fe^{2+}-layer are ferromagnetic. On the other hand, J_6 and J_7 have a small negative value leading to an antiferromagnetic coupling with Fe in layers above and below the Ti layers. The positive J_2 and negative J_6 and J_7 determine the correct antiferromagnetic ground state for ilmenite. In fact, the total energies for FM and AFM coupling between the Fe^{2+}-layers are nearly degenerate, which explains the slightly lower values compared to the ones obtained by Kato *et al.* [59, 106] by fitting data at T= 12 K to the magnon dispersion relation.

From the magnetic interaction parameters we can estimate the Néel temperature for the end members. In the mean-filed approximation (MFA), the transition temperature is defined as:

$$k_{\mathrm{B}}\mathrm{T}^{\mathrm{MFA}} = \frac{1}{3}S(S+1)\sum_m n_m J_m, \tag{3.2}$$

where k_{B} is the Boltzmann constant.

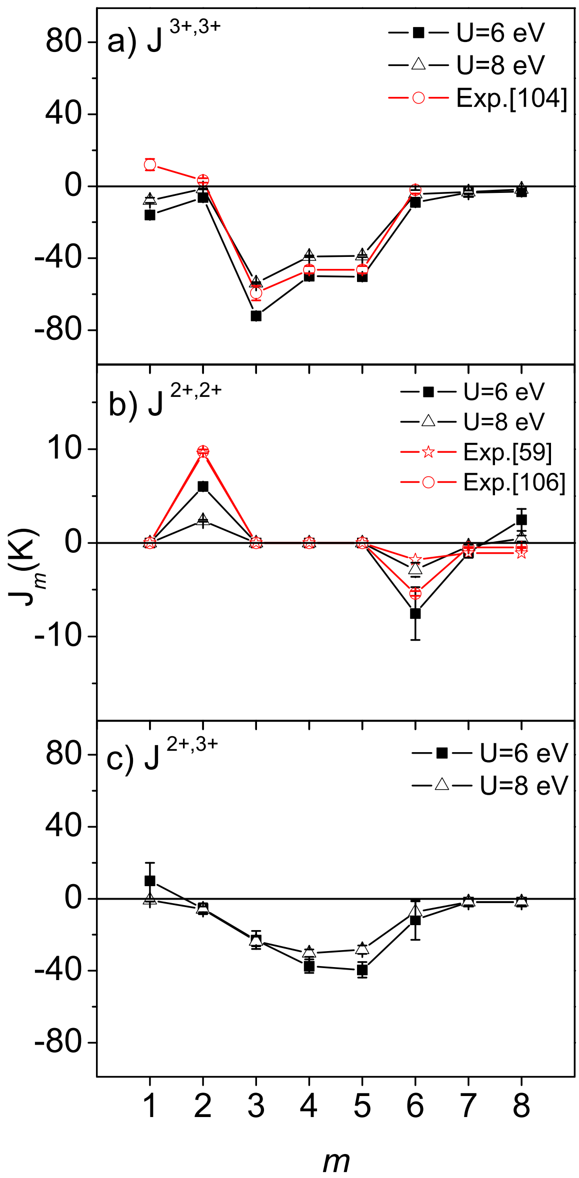

Figure 3.12: The magnetic pair interaction parameters $[J_m^q(K)]$ up to 8th neighbor are shown for (a) hematite ($J_m^{3+,3+}$), (b) ilmenite ($J_m^{2+,2+}$) and (c) the interface ($J_m^{2+,3+}$). Results for $U = 6$ and $8\,\mathrm{eV}$ are marked by filled squares and open triangles, respectively. The experimental value for hematite (open red/grey circle) are taken from Ref. [104] and for ilmenite (open red/grey circles and stars) are taken from Refs. [59,106]. The parameters for the interface in (c) are calculated for the configuration shown in Fig. 3.13b.

Table 3.3: Néel temperature for hematite and ilmenite calculated within the mean field approximation (MFA) and from Monte Carlo simulations for $U = 6$ and 8 eV.

	Monte Carlo		MFA	
Material	$U = 6\,\mathrm{eV}$	$U = 8\,\mathrm{eV}$	$U = 6\,\mathrm{eV}$	$U = 8\,\mathrm{eV}$
Fe_2O_3	1150 ± 10	910 ± 10	1416 ± 41	1107 ± 37
$FeTiO_3$	50 ± 2	15 ± 5	43 ± 18	19 ± 5

It is an established fact that MFA cannot give the exact value for the transition temperature but provides a qualitative estimation. The estimated Néel temperature for hematite and ilmenite within the mean field approximation (MFA) and from Monte Carlo simulations for $U = 6$ and 8 eV are listed in Table 3.3. Using equation (3.2) and the spin magnetic moment of $S = 5/2$ for Fe^{3+} we obtain $T_N^{MFA} = 1416 \pm 41\,\mathrm{K}$ ($1107 \pm 37\,\mathrm{K}$) for hematite with $U = 6$ (8) eV, respectively. A previous DFT study [110] reported a higher value (1711 K). Both MFA-values overestimate the experimental Néel temperature (953-966 K) [111]. Monte Carlo simulations, following the method of Harrison [112], were used to obtain a more accurate estimate of $T_N = 1150 \pm 10$ (910 ± 10) K for $U = 6(8)$ eV, which are closer to the experimentally observed value. For ilmenite, the mean-field estimated temperature using a spin magnetic moment of $S = 4/2$ for Fe^{2+} with $U = 6$ and 8 eV are $T_N^{MFA} = 43 \pm 18$ and $19 \pm 5\,\mathrm{K}$. Monte Carlo (MC) simulations yielded a value of 50 ± 2 (15 ± 5) K for $U = 6(8)$ eV.

The low Néel temperature for $U = 8\,\mathrm{eV}$ in ilmenite can be traced back to the small value of $J_2 = 2.4\,\mathrm{K}$, which is the interaction responsible for driving ferromagnetic ordering within the Fe-layers. Harrison *et al.* [113] found that a value of $J_2 = 10.8\,\mathrm{K}$ was required to obtain the correct Néel temperature for the end member ilmenite using Monte Carlo simulations, which is close to the empirical value obtained by Kato *et al.* [59,106]. The low value of J_2 is likely due to the high on-site Coulomb parameter $U = 8\,\mathrm{eV}$ which was used to describe correctly the size of the band gap. Using $U = 6\,\mathrm{eV}$, J_2 is significantly enhanced ($J_2 = 6.0\,\mathrm{K}$), resulting in a Néel temperature of $50 \pm 2\,\mathrm{K}$ from MC simulations. A similar dependence of the magnetic interaction parameters on U is obtained for hematite and reported for Cr_2O_3 [100]. For example, using $U = 8\,\mathrm{eV}$ instead of $U = 6\,\mathrm{eV}$ for hematite leads to a reduction of the J_i ($i = 3,4,5$) by $\sim 20\%$. This would result in an even stronger reduction of J_i ($i = 2,6$) in ilmenite up to $\sim 60\%$.

3.4.3 Magnetic interactions at the $Fe_2O_3/FeTiO_3$ interface

As mentioned previously, an Fe^{3+} and Fe^{2+} contact layer is formed at the Fe_2O_3/$FeTiO_3$ interface as a result of the disruption of charge neutrality [14,82]. In order to extract the magnetic interaction parameters at the interface ($J_m^{2+,3+}$), we have considered several cation configurations. Fig. 3.13a shows a heterostructure containing an ilmenite and a hematite block, while Fig. 3.13b contains a layered part as well as mixed Fe-Ti layers. Because not all interaction parameters are accessible in the former (*e.g.*, $J_{3,6}^{2+,3+}$), we have chosen the one in Fig. 3.13b to determine all

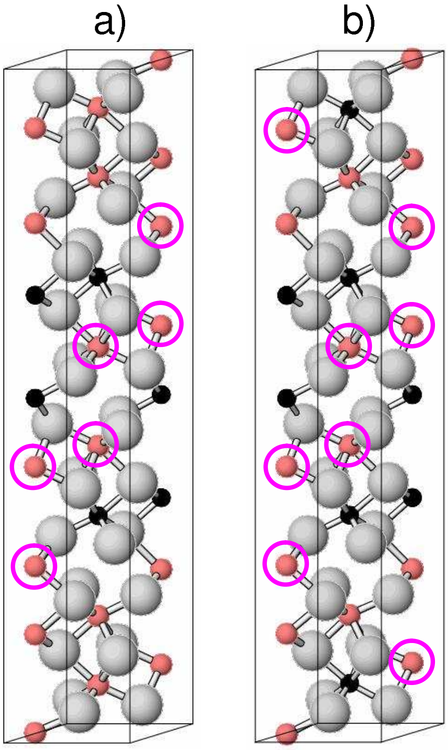

Figure 3.13: The structures with 60 atoms in the unit cell chosen for the calculation of interface magnetic interaction parameters. (a) ilmenite block in a hematite host and (b) a more solid solution-like structure in hematite part. The red, black and grey sphere are showing Fe, Ti and oxygen atoms respectively. The position of Fe^{2+} are marked with pink/grey circles and the remaining iron atoms are Fe^{3+}.

$J_m^{2+,3+}$. For the latter a total of 16 different spin-arrangements is calculated.

The extracted parameters for the interface ($J_m^{2+,3+}$) together with the ones for the end members ($J_m^{3+,3+}$ and $J_m^{2+,2+}$) are displayed in Fig. 3.12 and Table 3.4. The different magnetic arrangements used for the calculation are displayed in Tables B.3 and B.4. Similar to hematite, we find that the dominant interaction parameters at the interface are J_3, J_4 and J_5. These have the same sign but are lower in magnitude than the corresponding Fe^{3+}-Fe^{3+} interactions. This result validates the main assumption made in previous Monte Carlo studies of the solid solution [112, 113]. Although the absolute values of these interactions are generally smaller than in hematite, their negative value implies that Fe^{2+} in the contact layer couples antiferromagnetically to the next hematite layer. As a consequence, the direction of uncompensated magnetic moment at the interface will be pinned with respect to the hematite host, resulting in a ferrimagnetic behavior of the system. Monte Carlo simulations of magnetic ordering with a $4 \times 4 \times 4$ supercell were performed for the configuration in Fig. 3.13a, which corresponds to the ground state cation configuration for this bulk composition [82]. Magnetic transitions at 860 ± 10 (1080 ± 10) K were obtained in the hematite part of the heterostructure and 25 ± 5 (60 ± 5) K in ilmenite regions of the supercell with $U = 8(6)$ eV, respectively, suggesting that the magnetic ordering temperature of both phases is modified by the presence of the

Table 3.4: Magnetic pair exchange interactions in K for hematite ($J_m^{3+,3+}$), ilmenite ($J_m^{2+,2+}$) and the interface ($J_m^{2+,3+}$) for $U = 6$ and $8\,\mathrm{eV}$. The index m describes the type of interaction following the definition in Fig. 3.11, n_m is the multiplicity of J_m and d_{ij}(Å) is the distance between the cations in each system. Positive/negative signs of J correspond to FM/AFM coupling.

m	n_m	d_{ij}(Å)	$J_m^{3+,3+}$		d_{ij}(Å)	$J_m^{2+,2+}$		d_{ij}(Å)	$J_m^{2+,3+}$	
			$U = 6\,\mathrm{eV}$	$U = 8\,\mathrm{eV}$		$U = 6\,\mathrm{eV}$	$U = 8\,\mathrm{eV}$		$U = 6\,\mathrm{eV}$	$U = 8\,\mathrm{eV}$
1	1	2.86	-15.9±1.6	-7.9±1.4	2.92	0.0	0.0	2.84	10.0±10.0	-0.8±0.8
2	3	2.96	-6.3±0.2	-1.5±0.2	3.07	6.0±0.4	2.4±0.1	2.97	-5.5±3.0	-5.9±1.6
3	3	3.38	-72.1±0.5	-53.8±0.5	3.51	0.0	0.0	3.36	-23.0±5.0	-23.7±2.7
4	3	3.701	-50.1±0.5	-39.0±0.5	3.73	0.0	0.0	3.683	-37.5±3.8	-30.2±2.1
5	3	3.704	-50.2±0.7	-38.8±0.6	3.91	0.0	0.0	3.688	-39.6±4.3	-28.4±2.3
6	1	4.01	-9.0±2.3	-4.3±2.1	4.08	-7.5±2.8	-2.9±0.7	3.999	-11.7±11.1	-7.4±6.0
7	3	5.426	-3.4±1.0	-3.2±0.9	5.616	-1.0±0.6	-0.3±0.1	5.36	-1.9±1.9	-1.8±1.8
8	3	5.431	-3.1±0.4	-1.7±0.4	5.617	2.5±1.2	0.5±0.3	5.43	-1.9±1.9	-1.8±1.8

interface.

The slight decrease in Néel temperature for hematite can be explained by the reduced strength of magnetic interactions in the contact layer ($J_m^{2+,3+}$) and a lower average number of interactions per cation due to the presence of the paramagnetic ilmenite. The increase in Néel temperature of ilmenite is likely caused by interaction of Fe^{2+} spins within the ilmenite lamellae with the magnetically ordered Fe^{2+}-Fe^{3+} spins within the contact layers.

In Fig. 3.14 the calculated magnetic interaction parameters in this work for the interface model shown in Fig. 3.13b are compared with the guessed parameters used by Harrison [113] in order to model the magnetic ordering in the Fe_2O_3-$FeTiO_3$ solid solution. The guessed values are fairly close to our first principle values.

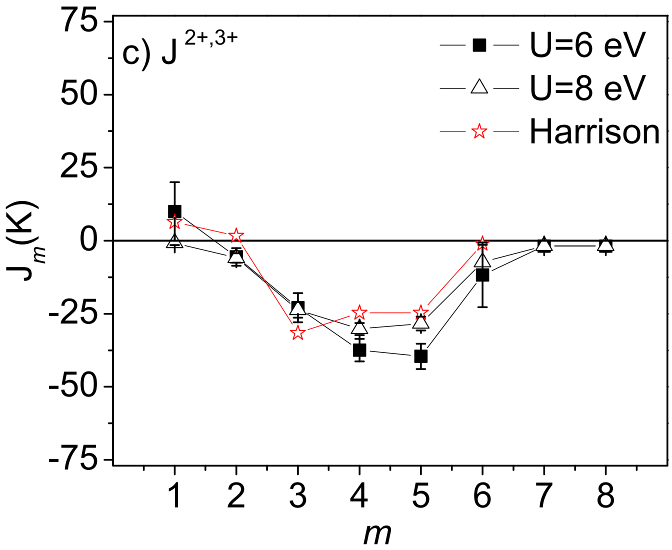

Figure 3.14: Comparison of the calculated values for $U = 6$ and $8\,\mathrm{eV}$ of $J_m^{2+,3+}$ for the interface model shown in Fig. 3.13b with the guessed values (red/grey stars) by Harrison taken from the Ref. [113].

3.4.4 Effect of strain on the magnetic interactions

In this section we have considered the effect of lateral strain on the magnetic interaction parameters by fixing the lateral lattice constant of the system to the Al_2O_3 bulk value. The c-lattice constant is relaxed.

Table 3.5 and Fig. 3.15a-c display the magnetic interaction parameters calculated for hematite, ilmenite and the interface model (Fig. 3.13b) on an Al_2O_3 (0001)-substrate. The main effect of strain is observed on $J_1^{3+,3+}$ due to the smaller lattice constant of Al_2O_3 ($\Delta a/a_{\mathrm{Fe_2O_3}} = -5.5\%$ and $\Delta c_{\mathrm{rel}}/c_{\mathrm{Fe_2O_3}} = 14.1\%$) and thus compressive strain induced by the Al_2O_3 substrate. All other magnetic interaction parameters in hematite on Al_2O_3 substrate did not show a significant change in their values compared to the bulk hematite values.

In ilmenite, J_2 is larger and J_6 is smaller on the Al_2O_3 substrate with both $U = 6$ and $8\,\mathrm{eV}$ compared to ilmenite bulk values as a result of strong strain ($\Delta a/a_{\mathrm{FeTiO_3}} = -8.1\%$ and $\Delta c_{\mathrm{rel}}/c_{\mathrm{FeTiO_3}} = 7.2\%$). For the interface model, the dominant parameters on the Al_2O_3 substrate are slightly larger than the values calculated without straining the system ($J_i(\mathrm{a}_{\mathrm{Al_2O_3}})/J_i \sim 0.9, 1.1, 1.9$ for $i = 3, 4$ and 5, respectively). In spite of the changes in the absolute values of the magnetic interaction parameters, the bulk systems did not show any change in the sign of the parameters. This implies that the magnetic ordering in the bulk systems is not influenced by straining the system on an Al_2O_3 substrate. Furthermore, for the interface interaction parameters ($J_m^{2+,3+}$), the main changes are in the absolute values of the parameters and no change in the sign of the dominant parameters were observed. This implies that the ferrimagnetic behavior observed at the contact layer in the interface model is not affected by straining the system on an Al_2O_3(0001) substrate.

Table 3.5: Magnetic pair exchange interactions in K for hematite ($J_m^{3+,3+}$), ilmenite ($J_m^{2+,2+}$) and the interface ($J_m^{2+,3+}$) for $U = 6$ and $8\,\mathrm{eV}$ on an Al_2O_3(0001) substrate for the structure presented in Fig. 3.13b. The index m describes the type of interaction following the definition in Fig. 3.11, n_m is the multiplicity of J_m and d_{ij}(Å) is the distance between the cations in each system. Positive/negative signs of J correspond to FM/AFM coupling.

m	n_m	d_{ij}(Å)	$J_m^{3+,3+}$		d_{ij}(Å)	$J_m^{2+,2+}$		d_{ij}(Å)	$J_m^{2+,3+}$	
			$U = 6\,\mathrm{eV}$	$U = 8\,\mathrm{eV}$		$U = 6\,\mathrm{eV}$	$U = 8\,\mathrm{eV}$		$U = 6\,\mathrm{eV}$	$U = 8\,\mathrm{eV}$
1	1	2.86	-83.3±11.3	-66.6±9.2	2.92	0.0	0.0	2.84	-22.1±15.6	-13.9±10.5
2	3	2.96	-2.7±1.7	3.5±1.4	3.07	12.2±0.4	1.0±0.1	2.97	3.5±3.5	-3.8±2.9
3	3	3.38	-65.5±3.8	-51.9±3.1	3.51	0.0	0.0	3.36	-20.8±7.1	-22.2±4.8
4	3	3.701	-58.8±3.8	-44.0±3.1	3.73	0.0	0.0	3.683	-42.8±5.5	-36.0±3.7
5	3	3.704	-48.9±5.1	-35.2±4.2	3.91	0.0	0.0	3.688	-75.5±6.2	-59.5±4.2
6	1	4.01	-23.4±16.7	-2.5±2.5	4.08	-5.2±3.0	-3.7±0.7	3.999	-13.4±13.4	-9.4±9.4
7	3	5.426	-13.3±7.2	-15.3±5.8	5.616	0.4±0.4	0.2±0.1	5.36	-7.5±5.4	-3.5±3.5
8	3	5.431	15.4±2.9	13.2±2.3	5.617	0.0±0.0	0.1±0.1	5.43	-7.5±5.4	-3.5±3.5

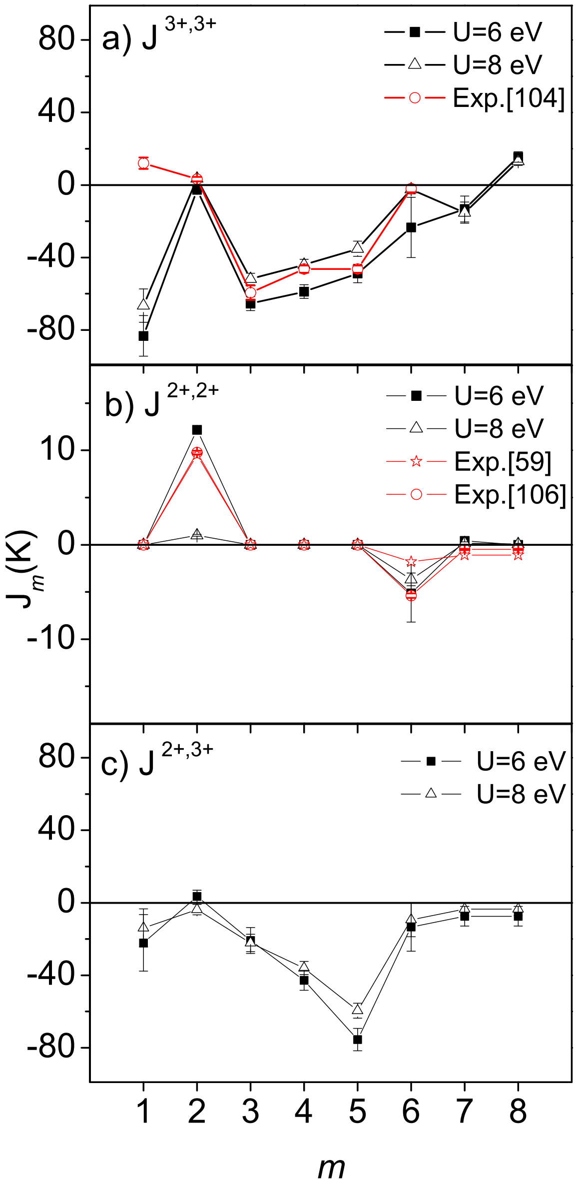

Figure 3.15: The magnetic pair interaction parameters on Al_2O_3 substrate $[J^q_m(K)]$ up to 8th neighbor are shown for (a) hematite $(J^{3+,3+}_m)$, (b) ilmenite $(J^{2+,2+}_m)$ and (c) the interface $(J^{2+,3+}_m)$. Results for $U = 6$ and $8\,\mathrm{eV}$ are marked by filled squares and open triangles, respectively. The experimental value for hematite (open red/grey circle) are taken from Ref. [104] and for ilmenite (open red/grey circles and stars) are taken from Refs. [59, 106]. The parameters for the interface in panel (c) are calculated for the configuration shown in Fig. 3.13b.

3.4.5 Summary

The magnetic pair exchange interaction parameters for the end members (hematite and ilmenite) are extracted based on DFT calculations by mapping the total energies on a Heisenberg Hamiltonian. For the end members, we find a good agreement with experimental values from inelastic neutron scattering data. The magnetic interaction parameters between Fe^{3+} and Fe^{2+} at the interface of hematite-ilmenite, which are not accessible from experiment, are extracted here for the first time. Similar to hematite, the dominating interaction is an antiferromagnetic coupling between Fe^{2+} in the contact layer and Fe^{3+} from the next hematite layer, fixing the orientation of the defect spins at the interface. Furthermore, while strain influences the absolute values of magnetic interaction parameters, the overall trend was not affected.

Chapter 4

Bulk Properties of $EuTiO_3$

$EuTiO_3$ (ETO) is one of the rare perovskites that exhibits cubic symmetry (space group $Pm3m$) at ambient conditions [115–117]. ETO is magnetically ordered below 5.5 K [17–19]. Furthermore, the dielectric permittivity of ETO also shows an anomaly at the magnetic ordering temperature [17], suggesting magnetoelectric coupling of the polarization and magnetization. However, compared to other well-known magnetoelectrics [20–22], ETO has been less investigated. Very recently, using first-principles calculations, a design strategy for magnetic and electric phase control in epitaxial ETO has been proposed [118]. Although magnetic susceptibility measurements on ETO show features of antiferromagnetic ordering, the features of magnetic ordering have not been investigated in detail, presumably due to the fact that naturally occurring Eu has a very large absorption cross-section for thermal neutrons. An old report, however, suggests a G-type antiferromagnetic (AFM) spin arrangement in ETO [18]. Magnetic susceptibility measurements have shown that ETO is one of the few antiferromagnetic materials with a positive Curie-Weiss constant ($\theta = +3.8\,\mathrm{K}$) [18].

Density functional theory calculations are carried out for the multiferroic $EuTiO_3$ using the LDA+U approach. Total-energy calculations for ferromagnetic (F), and antiferromagnetic A-, C- and G-type arrangements (see Fig. 4.1) show that the ground state depends very sensitively on the on-site Coulomb repulsion parameter U and volume. Calculations show that in the cubic phase, the ground-state magnetic configuration is G-type antiferromagnetic for $U = 6\,\mathrm{eV}$ and ferromagnetic for $U = 7\,\mathrm{eV}$. Values of first- and second-neighbor exchange integrals are extracted by mapping the energy difference between the different magnetic configurations to a Heisenberg Hamiltonian. The system seems to be critically balanced between ferromagnetic and antiferromagnetic states for realistic values of U and switches from antiferromagnetic to a ferromagnetic ground state on hydrostatic expansion of the volume. In this chapter, the results of manuscript M4 [114] are briefly discussed.

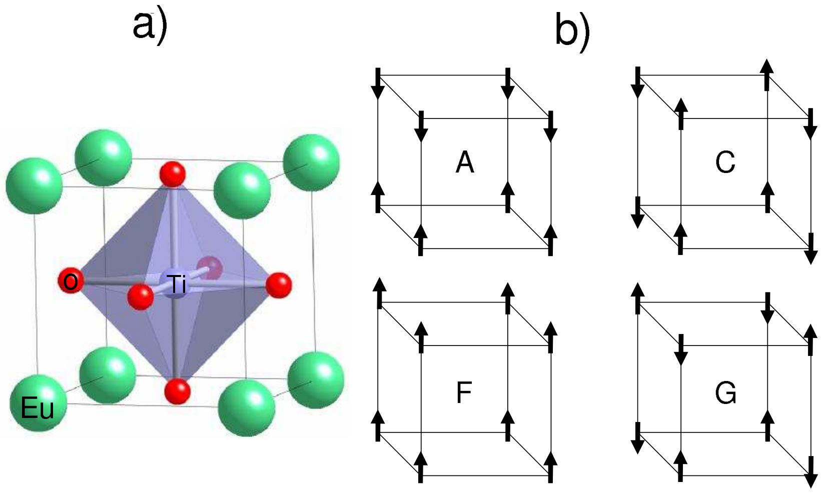

Figure 4.1: (a) Crystal structure of cubic $EuTiO_3$. The corner atoms represent Eu, and the atoms at the body-centered and the face-centered positions represent Ti and O, respectively. (b) Schematic diagram of the four collinear magnetic structures, A, C, F, and G, considered for cubic $EuTiO_3$. The arrows indicate spin directions at the Eu sublattice.

4.1 Equilibrium lattice constant and bulk modulus

Total energy calculations for four different collinear magnetic structures, A, C, F, and G, were considered in the present study. A schematic picture of the four magnetic structures with the crystal structure of cubic $EuTiO_3$ is shown in Fig. 4.1. For the A-type antiferromagnetic structure, the nearest-neighbor moments are ferromagnetically coupled within the *ab* plane and antiferromagnetically coupled along the *c*-direction. On the other hand, for a C-type antiferromagnetic, there is a FM coupling along the *c*-direction but AFM within the plane. For a G-type antiferromagnetic structure, all the nearest-neighbor moments are antiferromagnetically coupled.

Total energy versus volume calculations were performed to determine the equilibrium cell volume at $U = 0$, 3, 6 and 9 eV. Fig. 4.2 shows E(V) for $U = 6$ eV. The energy differences between the various magnetic configurations are very small, and on the scale shown in this figure, the energies of the four magnetic configurations at any particular volume appear nearly degenerate. The theoretical equilibrium volume ($\sim 246.6\ \AA^3$) is nearly insensitive to the different magnetic structures and also to the value of the U parameter used. The equivalent cubic lattice parameter, $a = (V/4)^{1/3} = 3.950$ Å, is larger than the experimentally reported value of 3.905 Å [17] by 1%.

The value of the bulk modulus B_0 and its pressure derivative B_0', were obtained by fitting the Murnaghan equation of state, to the calculated E(V) curve. For $U = 6$ eV, B_0 and B_0' were found to be 172.6 GPa and 4.1, respectively.

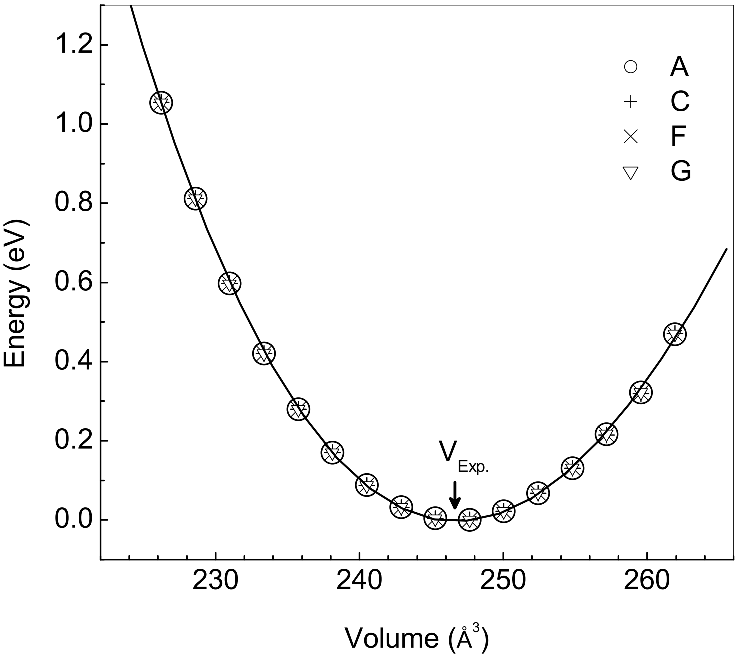

Figure 4.2: Total energy versus volume for F, A, C, and G magnetic structures of cubic $EuTiO_3$ calculated at $U = 6\,\text{eV}$.

4.2 Electronic and magnetic structures of $EuTiO_3$

The total energy and total density of states (DOS) were calculated for the four magnetic configurations, F, A, C, and G, at the experimental lattice constant for $U = 0$, 3, 5, 6, 7, 8 and $9\,\text{eV}$. It is found that the G-type AFM structure possesses lowest energy for $U \leq 6\,\text{eV}$. For $U \geq 7\,\text{eV}$, the ferromagnetic (F) structure becomes stable. Previous theoretical studies on divalent Eu compounds have reported that realistic values of U for Eu lie in the range $6 \leq U \leq 9\,\text{eV}$ [119, 120]. Interestingly enough, we found that at $U = 6\,\text{eV}$ the ground-state magnetic configuration changes from G-type AFM to ferromagnetic (F) on increasing the volume hydrostatically beyond the experimental value.

Fig. 4.3 shows the total and partial density of states (PDOS) for the O-2p states, Eu-f and d states, and Ti-d states in both spin channels. It is evident from this figure that the major contribution to the filled valence band comes from the O-2p states. A narrow occupied 4f band lies just below the Fermi level. A similar feature was also reported in the band structure of EuS [121]. The conduction band is formed by the Ti-3d states on the low-energy side and by the Eu-5d states at higher energies. Hybridization of the Ti-3d and O-2p states between -2 to $7\,\text{eV}$ is also observed, suggesting some covalent bonding between the Ti and O atoms, a feature common to most of the oxide perovskites. The absence of the Eu-6s states in the valence band part of the DOS suggests that Eu is almost completely ionized and forms ionic bonds with the O in the structure.

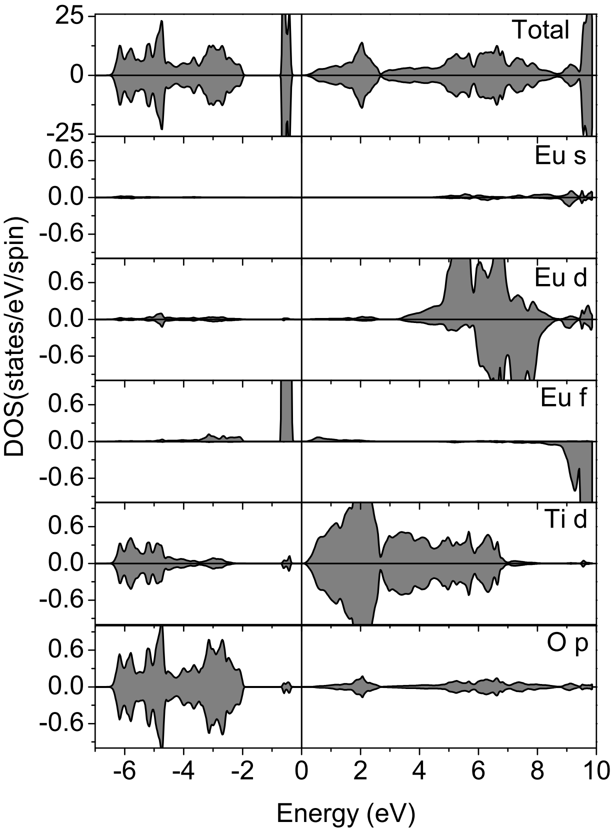

Figure 4.3: Total and partial density of states of Eu-s, Eu-d, Eu-f, Ti-d, and O-p orbitals for the G-type magnetic structure ($U = 6\,\mathrm{eV}$).

4.3 Calculation of exchange integrals

We have calculated the nearest-neighbor (nn) and next-nearest-neighbor (nnn) exchange interactions (J_{ij}^{nn} and J_{ij}^{nnn}) by mapping the energy difference between the different magnetic configurations of this system to the Heisenberg Hamiltonian as:

$$H = -2\sum_{i>j} J_{ij}\mathbf{S}_i.\mathbf{S}_j \tag{4.1}$$

The ground state of the Eu^{2+} ion corresponds to spin $S = 7/2$ and orbital moment $L = 0$. The zero orbital moment adds a simplification to the calculations in the sense that the exchange interaction can be considered isotropic to a good approximation. The total numbers of nn and nnn Eu^{2+} bonds in the tetragonal cell considered for calculating the total energies are 12 and 20 respectively. The corresponding energy expressions for the four magnetic configurations, F, A, C, and

Table 4.1: Values of the first-nearest-neighbor (J_{ij}^{nn}) and second-nearest-neighbor (J_{ij}^{nnn}) exchange integrals (in units of kelvin) obtained after mapping the difference in the total energies of the various configurations to a Heisenberg Hamiltonian (see text).

Exchange integral	U=0 eV	U=3	U=5	U=6	U=7	U=8	U=9
J_{ij}^{nn}(K)	-0.12	-0.24	-0.06	0.01	0.03	0.05	0.06
J_{ij}^{nnn}(K)	0.26	0.12	0.08	0.05	0.04	0.03	0.02

G can be written as:

$$\begin{aligned} E_F &= E_0 + 2|S|^2(-12J_{ij}^{nn} - 24J_{ij}^{nnn}) && (4.2)\\ E_A &= E_0 + 2|S|^2(-4J_{ij}^{nn} + 8J_{ij}^{nnn}) && (4.3)\\ E_C &= E_0 + 2|S|^2(4J_{ij}^{nn} + 8J_{ij}^{nnn}) && (4.4)\\ E_G &= E_0 + 2|S|^2(12J_{ij}^{nn} - 24J_{ij}^{nnn}). && (4.5) \end{aligned}$$

From $S = 7/2$, it follows that $|S|^2 = S(S+1) = 15.5$ for Eu^{2+}. The values of the exchange interactions obtained with least squares fitting procedure, in units of Kelvin, are listed in Table 4.1. While J_{ij}^{nn} changes sign from negative to positive between $U = 5$ and 6 eV, the sign of J_{ij}^{nnn} remains positive for all values of U under consideration. In general, it is noted that J_{ij}^{nn} increases and J_{ij}^{nnn} decreases upon increase of U. Values of exchange integrals in ETO have also been reported in the past using parameters derived from temperature-dependent magnetic susceptibility measurements [18, 19]. The values of J_{ij}^{nn} and J_{ij}^{nnn} reported in [18] are -0.02 and 0.04 K, respectively. Chien *et al.* [19], on the other hand, have reported slightly different values: J_{ij}^{nn} = -0.014 K and J_{ij}^{nnn}= 0.037 K. It is evident from Table 4.1, that a similar value of J_{ij}^{nn} is obtained theoretically for a value of U in the range $5 \leq U \leq 6$ eV. The small values of the exchange constants indicate a very weak interaction between the magnetic ions in ETO.

4.4 Summary

The electronic structure and magnetic properties of cubic EuTiO$_3$ were investigated using density functional theory + Hubbard U (LDA/GGA + U). The ground state corresponds to a G-type antiferromagnetic structure for $U = 6$ eV and a ferromagnetic (F) structure for $U = 7$ eV. The values of the first- and second-nearest-neighbor exchange integrals have been calculated by mapping the energy difference between four different magnetic configurations onto a Heisenberg Hamiltonian. The system is critically balanced between ferromagnetic and antiferromagnetic states for realistic values of U. The system switches from G-type AFM to a ferromagnetic ground state on increasing volume, opening a possibility of tailoring its magnetic properties and also the associated dielectric properties, *e.g.*, by appropriate chemical substitutions at the Ti site of this material.

Chapter 5

Comparative Study on $EuLiH_3$ and $EuTiO_3$

Divalent europium chalcogenides are among the important compounds in the area of magnetic semiconductors. This family of materials have attracted remarkable attention in developing new devices for future spintronics applications. In this family, while EuO and EuS exhibit a ferromagnetic (F) ground state, [123] EuSe and EuTe are antiferromagnetic [124] (AFM) at ambient pressure. The magnetism in these compounds arises from the half filled $4f$ band of the divalent Eu^{2+} ion. Apart from the chalcogenide family, the divalent oxidation state of Eu is also present in compounds crystallizing in the cubic perovskite structure such as $EuTiO_3$ (ETO) (Refs. [18, 19, 116]) and $EuLiH_3$ (ELH). ETO shows G-type AFM ordering below 5.5 K and exhibits significant spin-lattice coupling at low temperatures [17], while ELH exhibits ferromagnetic behavior [125–127] and hence, with regard to the magnetic structure, ELH is akin to EuO. Furthermore, it has been known that the magnitude of the effective nearest-neighbor (nn) exchange interaction (J_1) of ETO is considerably smaller than that of EuO and ELH [19, 125]. Chien *et al.* [19] have proposed an intra-atomic $4f$-$5d$ exchange interaction, according to the Goodenough [128] and Kasuya [129] rules, to explain this abnormal difference. It has been suggested that the exchange interaction (J_1) between the nearest-neighbor Eu cations is of the form $J_1 \sim J_{\text{intra}} b^2/\Delta^2$, where b is a transfer integral between nn cations, Δ is the energy separation between $4f$ and $5d$ levels of Eu, and J_{intra} is the Hund's rule coupling constant [19]. In view of the similarity of the Eu-Eu distance, to a first approximation, b was treated to be nearly constant for EuO, ETO, and ELH. The difference in the magnitudes of J_1 was therefore attributed to the difference in the magnitude of Δ, which in turn depends on the magnitude of the crystal field splitting of the $5d$ states. A larger crystal field splitting would cause the e_g level to come close to the $4f$ level and thereby, reduce the value of Δ [19]. In this scenario, the anomalously small magnitude of the J_1 in ETO, as compared to ELH and EuO, has been explained by proposing a relatively weak crystal field splitting of the Eu-$5d$ states in ETO as compared to ELH and EuO [19].

In this chapter, the properties of bulk $EuLiH_3$ in comparison to $EuTiO_3$ from first principles calculations are briefly discussed. These are the results of manuscript M5 [122].

Table 5.1: Relative energies in (eV) of the various magnetic structures of $EuLiH_3$ calculated at different values of U. For each U, the minimum energy among the four configurations is set to zero.

Mag. structure	U=0	U=3	U=4	U=5	U=6	U=7	U=8	U=9
F	0.0	0.0	0.0	0.0	0.0	0.0	0.0	0.0
A	0.110	0.039	0.029	0.021	0.015	0.009	0.006	0.002
C	0.175	0.066	0.051	0.038	0.030	0.022	0.017	0.012
G	0.186	0.071	0.055	0.042	0.033	0.026	0.021	0.017

5.1 Results and discussion

Similar to the calculations on $EuTiO_3$ described in the previous chapter, in $EuLiH_3$ four different magnetic structures were chosen, namely, ferromagnetic (F) and three AFM (A, C, and G types). The spin configurations corresponding to the four magnetic structures are shown in Fig. 4.1b. For more detail on the calculations refer to the manuscript M5. Table 5.1 lists the relative energies of the four magnetic structures of ELH for different values of U. It is evident that the ferromagnetic state has the lowest energy for all U. This may be contrasted with ETO, for which the lowest energy state switches from G-type AFM to ferromagnetic structure by increasing U beyond 6 eV (see previous chapter and manuscript M4). J_1 and J_2 were obtained in units of Kelvin by a least-square fitting to the Heisenberg Hamiltonian.

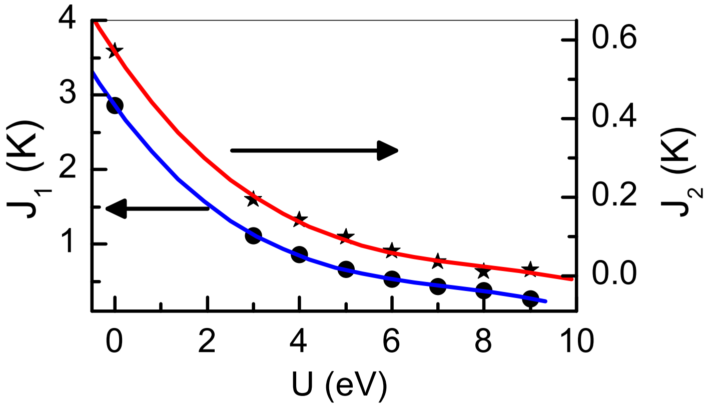

Figure 5.1: Variation in first (J_1) and second (J_2) nn effective exchange interactions of $EuLiH_3$ as a function of U.

Fig. 5.1 depicts the variation in the J_1 and J_2 as a function of U. Previous studies have shown that a realistic value of U for Eu-based systems lies in the range of 5-7 eV [114, 119, 120, 130, 131]. For ETO, a value of U between 5 to 6 eV was found to give exchange interactions, J_1 and J_2, very close to the experimentally obtained values [114]. Assuming the U parameter of Eu for ELH to be similar to that of ETO, $J_1 \sim 0.53\,\mathrm{K}$ and $J_2 \sim 0.06\,\mathrm{K}$ for ELH (Fig. 5.1) are obtained. These values are reasonably close (within the experimental error) to the experimental ones reported earlier ($J_1 = 0.8 \pm 0.2\,\mathrm{K}$, $J_2 = \pm 0.05\,\mathrm{K}$) using susceptibility data [126,127]. A comparison of the magnitudes of J_1 of ELH, ETO, and EuO reveals that it is more than an order of magnitude smaller in ETO ($J_1 \sim 0.01\,\mathrm{K}$) [131] than in ELH [126, 127] and in EuO ($J_1 = 0.72\,\mathrm{K}$) [119]. To investigate the sensitivity of J_1 to the nn Eu-Eu distance, calculations were performed at different cell volumes of ELH, so as to cover the Eu-Eu distance observed in EuO (3.63 Å) and ETO (3.905 Å).

Fig. 5.2 shows the exchange interactions (J_1 and J_2) as a function of the cubic lattice parameter, which is also the nn Eu-Eu distance for the perovskite structure. It is evident from this graph that J_1 and J_2 at 3.905 Å (corresponding to the Eu-Eu distance in ETO) are 0.41 and 0.03 K, respectively. The value of J_1 is still considerably larger than the value reported for ETO [114]. Furthermore, J_1 and J_2 obtained from extrapolation of the fitted curves at 3.63 Å (corresponding to the Eu-Eu distance in EuO) are found to be 1.0 and 0.17 K, respectively. Considering the fact that the crystal structure of EuO is different from that of ELH, these values are not very much off from what has actually been reported ($J_1 = 0.72\,\mathrm{K}$ and $J_2 = 0.22\,\mathrm{K}$) for EuO [119]. This analysis therefore suggests that the Eu-Eu distance cannot be the primary factor affecting the strength of J_1 in ETO.

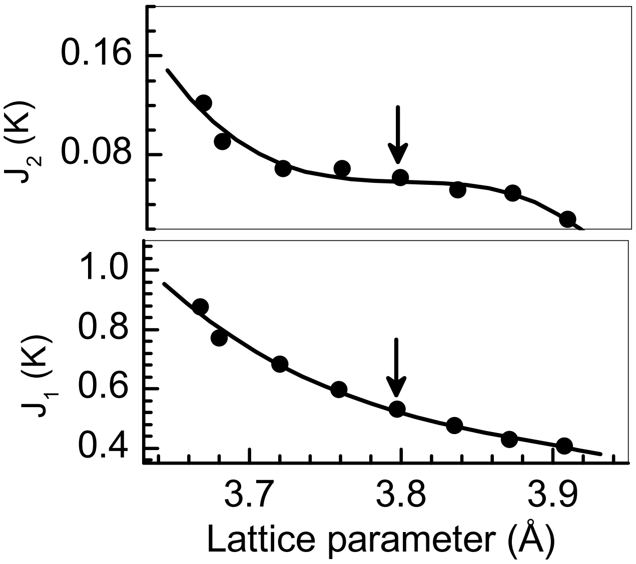

Figure 5.2: Variation in J_1 and J_2 with cubic lattice parameter of $\mathrm{EuLiH_3}$. The solid curves are fitted lines with a third order polynomial. The arrows indicate the lattice parameter corresponding to the equilibrium value.

Fig. 5.3 shows the total energy curves of ELH versus cell volume for the four magnetic structures mentioned above at $U = 6\,\mathrm{eV}$. The energy of the ferromagnetic state was found to be lowest for all volumes. The cubic lattice parameter corresponding to the equilibrium volume is 3.78 Å, which is almost the same as the experimental value of 3.79 Å reported for this compound [127].

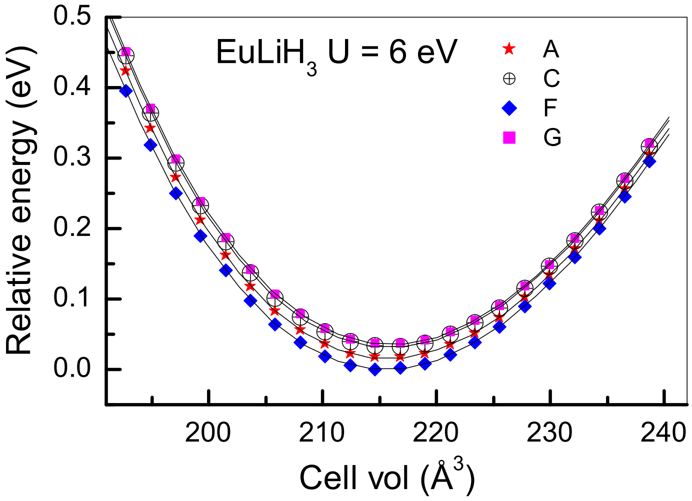

Figure 5.3: Variation in the relative energy of the A, C, F, and G magnetic structures of $EuLiH_3$ as a function of unit cell volume calculated for $U = 6\,\mathrm{eV}$. The minimum energy in the graph is chosen as the reference energy and it is set to zero. The volume corresponds to the bigger (tetragonal) unit cell whose volume is four times the cubic cell volume.

Fig. 5.4 shows the total and partial density of states (PDOS) of the ground state magnetic structures of ELH calculated at $U = 6\,\mathrm{eV}$. The absence of s states of Eu in the conduction band indicates that Eu forms highly ionic bonds with H and O in ELH and ETO, respectively. A noticeable hybridization between the Eu-5d and H-s states suggests however a considerable degree of covalent character in the Eu-H bond of ELH. Furthermore, the absence of Li-s states in the conduction band seems to suggest a strongly ionic nature of the Li-H bond. In contrast, the Ti-O bond in ETO has a significant covalent contribution as evident from the hybridization between the O-2p and Ti-3d states in Fig. 4.3.

The valence bands of both the ELH and ETO are formed by the valence states of their respective anions. The narrow Eu-4f band lies between the Fermi level and the broad valence band in both cases. A comparable feature has been reported for EuO as well [119]. Similar to EuO, the conduction band of ELH is formed by the Eu-5d states. This band starts at $\sim 0.8\,\mathrm{eV}$ above the Fermi level and spreads up to $\sim 11\,\mathrm{eV}$, *i.e.*, a bandwidth of about 10 eV. On the other hand, the conduction band in ETO is formed by Ti-3d states. The Eu-5d band starts at 3.5 eV above the Fermi level and persists up to 8.6 eV, *i.e.*, a bandwidth of $\sim 5\,\mathrm{eV}$. The width of the Eu-5d band in ETO is, therefore, nearly half the corresponding value in ELH. Furthermore, there is a significant overlap of the Eu-5d and Ti-3d bands in the energy range of 3.5-7 eV. In the framework of the mechanism proposed by Chien *et al.* [19], this feature may influence strongly the exchange interaction in this system as compared to ELH.

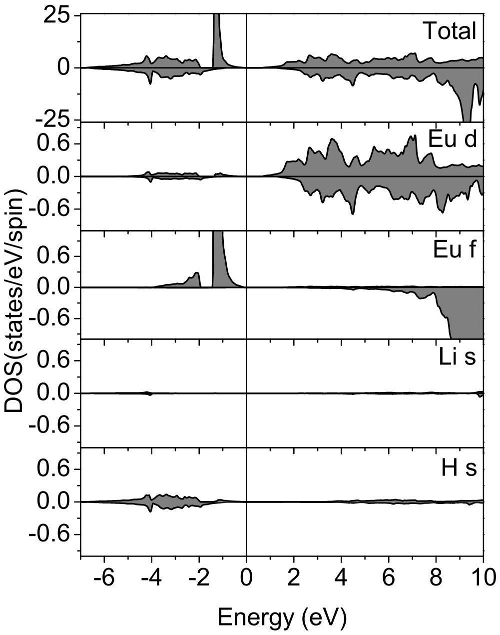

Figure 5.4: DOS of ferromagnetic $EuLiH_3$. The top panel is the total DOS and the remaining correspond to projected DOS on the Eu, Li and H states.

Fig. 5.5 shows the variation in the band gap of ELH, *i.e.*, the difference in the energy of the top of the Eu-4f band and the bottom of the Eu-5d conduction band as a function of U. For sake of comparison, the band gap variation with U of ETO was also included. It may be mentioned that, in the latter, the band gap is between the Eu-4f and the Ti-3d state. Linear extrapolation through the data points suggests that the gap in ELH and ETO opens above $U = 2.8\,\text{eV}$ and $4.6\,\text{eV}$, respectively. At the realistic value of the U, *i.e.*, $U = 6\,\text{eV}$, the gaps in ELH and ETO are $\sim$0.8 and $\sim$0.4 eV, respectively. Due to the larger gap, ELH is expected to exhibit a better insulating property than ETO at any finite temperature.

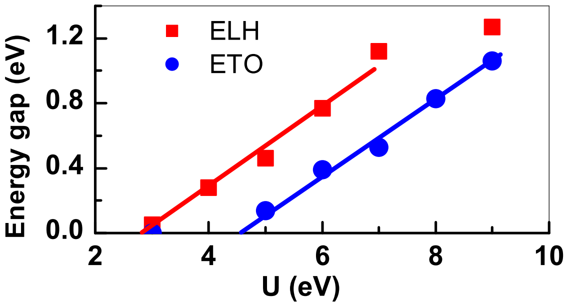

Figure 5.5: Variation in the band gap of ELH and ETO with U.

5.2 Summary

In conclusion, it is demonstrated that the GGA+U approach correctly predicts the ferromagnetic ground state of $EuLiH_3$. Mapping the total energies of four different magnetic structures on a Heisenberg Hamiltonian, the extracted first and second nn effective exchange interactions were found to be in good agreement with experimental values. With regard to the relative position of the $4f$ and $5d$ Eu bands in ELH and ETO, these results not only confirm the schematic model proposed earlier by Chien *et al.* [19], but also shed new light with regard to the factors at play in determining this energy difference. The intervening Ti-$3d$ states between the Eu-$4f$ and $5d$ states seem to push the Eu-$5d$ band to higher energies in ETO and to reduce its bandwidth. Furthermore, in the context of the exchange mechanism proposed by Chien *et al.* [19], the significant overlap of the Ti-$3d$ and Eu-$5d$ bands would imply that the Ti-$3d$ band should also participate in the exchange process. The results clearly demonstrate the unique role of Ti-$3d$ states in drastically decreasing the effective J_1 value in $EuTiO_3$ as compared to $EuLiH_3$ and EuO.

Chapter 6

Conclusions and Perspectives

This work represents a systematic first principles investigation of the origin of interface magnetism in Fe_2O_3-$FeTiO_3$ heterostructures and solid solutions.

As a starting point, the bulk properties of the end members α-Fe_2O_3 and $FeTiO_3$ were studied. Concerning the electronic properties, the band gap of Fe_2O_3 is underestimated within GGA and for $FeTiO_3$, even a metallic state is predicted. The results show that the incorporation of correlation effects within the GGA+U method is necessary in order to describe correctly the electronic behavior of the system. Within the GGA+U method, both compounds are insulating with a band gap of Δ_g=2.25 and 2.21 eV for Fe_2O_3 and $FeTiO_3$, respectively. The U-values of 6 eV for hematite and 8 eV for ilmenite, are used in order to reproduce the experimentally observed band gap. For bulk Fe_2O_3 and $FeTiO_3$ different magnetic arrangements (AFM and FM), as well as different oxidation states for $FeTiO_3$ ($Fe^{2+}Ti^{4+}O_3$ vs. $Fe^{3+}Ti^{3+}O_3$), are considered. The AFM arrangement is found to be the ground state configuration for hematite, while in ilmenite, $Fe^{2+}Ti^{4+}O_3$ is found to be the ground state with almost degenerate FM and AFM solutions, which is consistent with the low magnetic ordering temperature of this material.

Due to the stacking of $\cdots 2Fe^{3+}/\, 3O^{2-} \cdots$ in Fe_2O_3 and $\cdots 2Fe^{2+}/\, 3O^{2-}/\, 2Ti^{4+}\, /\, 3O^{2-} \cdots$ in $FeTiO_3$, the charge neutrality is disrupted at the Fe_2O_3-$FeTiO_3$ interface. Several possible compensation mechanisms were considered, such as disproportionation on the Fe sublattice through $Fe^{2+}/\, Fe^{3+}$, as well as other mechanisms involving Ti^{3+}, like $Ti^{3+}/\, Ti^{4+}$ and $Fe^{3+}/\, Ti^{3+}$. By systematically varying the concentration, distribution and charge state of Ti (Fe) doped into a hematite (ilmenite) host, the energetic stability, electronic and magnetic properties of the Fe_2O_3-$FeTiO_3$ system have been investigated. The GGA+U results show that the most favorable compensation mechanism is through a disproportionation into Fe^{2+}, Fe^{3+} in the contact layer [82], giving the first theoretical evidence for the *lamellar magnetism hypothesis* [14]. The formation of Fe^{2+} at the interface leads to impurity levels in the band gap that are pinned at the Fermi level for all studied concentrations ($x = 17, 33, 50, 66, 83\%$) of Ti doped in hematite. One of the main findings is that ordered configurations such as hematite/ilmenite heterostructures are more stable than solid solutions, except for very high Ti concentrations, in accordance to the experimental phase diagram of Fe_2O_3-$FeTiO_3$ [79, 82].

A further aspect studied was the effect of strain on the energetic stability of

$Fe_{2-x}Ti_xO_3$ heterostructures and solid solutions grown on different substrates like $Fe_2O_3(0001)$, $FeTiO_3(0001)$ and $Al_2O_3(0001)$. Due to the strong compressive strain of 5.8% and 8.8% with respect to the lattice parameter of Fe_2O_3 and $FeTiO_3$, systems grown on $Al_2O_3(0001)$ are found to be energetically unfavorable compared to the ones with a larger lateral lattice constant, *e.g.*, $FeTiO_3(0001)$. This gives a possible explanation to why a lateral strain relaxation occurs in $Fe_{2-x}Ti_xO_3$ films grown on $Al_2O_3(0001)$ [91,92]. The main feature related to strain is the change in bandwidth: while for tensile strain at a_{FeTiO_3} the bands are narrowed, for compressive strain at $a_{Al_2O_3}$ they are strongly broadened. Furthermore, the impurity state shifts to lower energies with respect to the Fermi level upon decrease of the lateral lattice constant, *e.g.*, from a_{FeTiO_3} to $a_{Al_2O_3}$. This provides a path to control the electronic properties of the system. Also, the calculations show that the trend of stability of cation order can change on an $Al_2O_3(0001)$-substrate. For example, the layered configurations are more stable on $Fe_2O_3(0001)$ and $FeTiO_3(0001)$-substrates, while the disordered (solid solutions) structures are in strong competition with the ordered phase, particularly for concentrations of $x = 33$ and 66% Ti in hematite [132].

Previous Monte Carlo simulations [113] on this system were carried out based on empirical parameters. One of the main goals of this study is to extract accurate magnetic interaction parameters from DFT calculations. This is done by calculating the total energies of different spin arrangements and mapping them on a Heisenberg Hamiltonian. The magnetic interaction parameters for bulk hematite ($J^{3+,3+}$) and ilmenite ($J^{2+,2+}$) are determined and found to be in good agreement with available theoretical and experimental data. Most importantly, the parameters at the Fe_2O_3-$FeTiO_3$ interface ($J^{2+,3+}$), which are not accessible from experiment, are obtained for the first time from first principles. We note that the uncompensated moments generated at the interface due to the charge mismatch show a strong tendency to couple antiferromagnetically to the next hematite layer, thus leading to ferrimagnetism in the system. The interface magnetism in this system is a further example of how the polar discontinuity at oxide interfaces can lead to novel functional properties, thereby opening possibilities for electronics and spintronics applications.

An interesting topic for future studies is to take into account the effect of noncollinearity and spin-orbit coupling in order to determine the direction of magnetic moments in the interface layer. This can give an insight into the mechanism of exchange-bias recently observed in this system [5].

Furthermore, the electronic structure and magnetic properties of cubic $EuTiO_3$ were investigated using density-functional theory and taking into account the correlation effects, by adding a Hubbard U parameter within the LDA/GGA + U method. The values of the first and second nearest-neighbor exchange interactions have been calculated by mapping the energies of four different magnetic configurations on a Heisenberg Hamiltonian. The system is critically balanced between ferromagnetic and antiferromagnetic states for realistic values of U and switches from G-type AFM to a ferromagnetic state upon volume increase. This opens a possibility to tailor the magnetic properties and also the associated dielectric properties, *e.g.*, by appropriate chemical substitutions at the Ti site of this material. This switchover of magnetic states by altering the volume was recently confirmed by experiments on the epitaxial thin films of $EuTiO_3$ grown on a $SrTiO_3$ substrate by pulsed laser deposition [133, 134].

The DFT total energies of $EuLiH_3$ were mapped on a Heisenberg Hamiltonian. The extracted first and second nearest-neighbor effective exchange interactions were found to be in good agreement with experimental values. A comparative study between $EuLiH_3$ and $EuTiO_3$ shows that the Ti-3d states, intervening between the Eu-4f and 5d states, seem to push the Eu-5d band to higher energies in ETO and to reduce its bandwidth. Moreover, in the context of the exchange mechanism proposed by Chien *et al.* [19], the significant overlap of the Ti-3d and Eu-5d bands implies that the Ti-3d band should also participate in the exchange process. The results clearly demonstrate the unique role of the Ti-3d states in drastically decreasing the effective J_1 value in $EuTiO_3$ as compared to $EuLiH_3$ and EuO.

Appendix A

Functional Derivatives

Compared with the well-known derivatives where a given function is differentiated with respect to one or more variables, we consider here a functional of some functions and differentiate this with respect to those functions. Let us first consider a function of several parameters (variables):

$$F = F(z_1, z_2, ..., z_N). \tag{A.1}$$

We will assume that each of the parameters z_i are a function of the parameter, r, *i.e.*:

$$z_i = z_i(r), \tag{A.2}$$

then

$$\frac{dF}{dr} = \sum_{i=1}^{N} \frac{\partial F}{\partial z_i} \frac{dz_i}{dr}. \tag{A.3}$$

Here, F is a function which depends on a set of parameters. We modify this example and let the set of z_i become a continuous set, then F becomes a functional of the function z. In principle, this corresponds to $N \rightarrow \infty$. Still z is a function of r and we will obtain as a generalization from (A.3) in the continuous form:

$$\frac{dF}{dr} = \int \frac{\delta F}{\delta z} \frac{dz}{dr} dz, \tag{A.4}$$

where $\delta F/\delta z$ is a functional derivative of F with respect to z. In general, the functional derivative of the functional F with respect to the function z is defined as:

$$\frac{\delta F[z(r)]}{\delta z(r)} = \lim_{\delta z(r) \rightarrow 0} \frac{F[z(r) + \delta z(r)] - F[z(r)]}{\delta z(r)}, \tag{A.5}$$

which is similar to the traditional derivative. If we suppose that $F = z$ in Eq. (A.4), then,

$$\frac{dz}{dr} = \int \frac{\delta z}{\delta z'} \frac{dz'}{dr} dz'. \tag{A.6}$$

This identity can be valid in the general case only if:

$$\frac{\delta z}{\delta z'} = \delta(z - z'), \tag{A.7}$$

which shows that any function can be written as a functional. For example:

$$\phi(t) = \int \phi(t')\delta(t - t')dt'. \tag{A.8}$$

This functional is a function of $\phi(t')$ only, therefore:

$$\frac{\delta\phi(t)}{\delta\phi(t')} = \delta(t - t'). \tag{A.9}$$

The main purpose is to find an extremum of a functional (maximum or minimum), suppose we have a function $F[z]$ of a function $z(r)$ which involves the integration of another function of r and z over the variable r:

$$F[z] = \int_a^b f(r, z)dr, \tag{A.10}$$

where the limits of integration are constant. To find an extremum of $F[z]$ with respect to changes in $z(r)$ in the interval $r \in [a, b]$, suppose we change z to z' by adding a function $\delta z(r) = \varepsilon\zeta(r)$:

$$z'(r) = z(r) + \delta z(r) = z(r) + \varepsilon\zeta(r), \tag{A.11}$$

where $\zeta(r)$ is an arbitrary function and ε is an infinitesimal quantity ($\varepsilon \to 0$). In addition, $\zeta(a) = \zeta(b) = 0$, so that we do not introduce changes in the limits of integral. Therefore, the corresponding F will be given by:

$$F[z'] = \int_a^b f(r, z')dr = \int_a^b f(r, z(r) + \varepsilon\zeta(r))dr. \tag{A.12}$$

Taking the derivative with respect to ε from the Eq. (A.12) and setting it equal to zero to obtain the extremum, we find:

$$\frac{dF[z']}{d\varepsilon} = \int_a^b \frac{\partial f}{\partial z'}\frac{dz'}{d\varepsilon}dr = \int_a^b \frac{\partial f}{\partial z'}\zeta(r)dr = 0. \tag{A.13}$$

Since this must hold for $\varepsilon \to 0$ and an arbitrary $\zeta(r)$, we conclude that we must have:

$$\frac{\delta F[z']}{\delta z} = \lim_{\varepsilon\to 0}\frac{\partial f(r, z)}{\partial z'} = \frac{\partial f(r, z)}{\partial z} = 0. \tag{A.14}$$

Thus, the necessary condition for finding an extremum of $F(z)$ with respect to variation in $z(r)$, is the vanishing of the partial derivative with respect to z of the integrand appearing in F.

Appendix B

The Table of Magnetic Configurations

Table B.1: The relative energies ΔE(Ry) of different spin arrangements in Fe_2O_3 with 30 atoms in the unit cell containing 12 iron atoms. The spin magnitude of Fe^{3+} is $S_1 = S_2 = ... = S_{12} = |S^{Fe^{3+}}| = 5/2$ and the spin orientations are shown by up and down arrows.

No.	S_1, S_2, S_3 ,..., S_{12}	ΔE
1	↑ ↑ ↓ ↓ ↓ ↓ ↑ ↑ ↑ ↑ ↓ ↓	-0.4013
2	↑ ↑ ↑ ↑ ↑ ↑ ↑ ↑ ↑ ↑ ↑ ↑	-0.1491
3	↓ ↓ ↑ ↑ ↑ ↑ ↑ ↑ ↑ ↑ ↑ ↑	-0.2376
4	↓ ↓ ↓ ↓ ↓ ↓ ↑ ↑ ↑ ↑ ↑ ↑	-0.2421
5	↑ ↑ ↓ ↓ ↑ ↑ ↑ ↑ ↑ ↑ ↑ ↑	-0.2387
6	↑ ↑ ↓ ↓ ↓ ↓ ↑ ↑ ↑ ↑ ↑ ↑	-0.3216
7	↑ ↑ ↓ ↓ ↓ ↓ ↓ ↓ ↓ ↓ ↑ ↑	-0.3249
8	↑ ↑ ↓ ↓ ↑ ↑ ↑ ↑ ↓ ↓ ↑ ↑	-0.3241
9	↑ ↑ ↑ ↑ ↓ ↓ ↑ ↑ ↑ ↑ ↑ ↑	-0.2399
10	↑ ↑ ↑ ↑ ↓ ↓ ↓ ↓ ↑ ↑ ↑ ↑	-0.2639
11	↑ ↑ ↑ ↑ ↑ ↑ ↓ ↓ ↑ ↑ ↑ ↑	-0.2400
12	↑ ↑ ↑ ↑ ↑ ↑ ↓ ↓ ↓ ↓ ↑ ↑	-0.3216
13	↑ ↑ ↑ ↑ ↑ ↑ ↑ ↑ ↓ ↓ ↑ ↑	-0.2387
14	↑ ↑ ↑ ↑ ↑ ↑ ↑ ↑ ↑ ↑ ↓ ↓	-0.2376
15	↑ ↑ ↓ ↑ ↑ ↑ ↑ ↑ ↑ ↑ ↑ ↑	-0.1934
16	↑ ↑ ↑ ↑ ↑ ↑ ↓ ↑ ↑ ↑ ↑ ↑	-0.1935
17	↑ ↑ ↑ ↑ ↑ ↑ ↑ ↑ ↓ ↑ ↑ ↑	-0.1934
18	↑ ↑ ↑ ↑ ↑ ↑ ↑ ↑ ↑ ↑ ↑ ↓	-0.1936
19	↑ ↑ ↑ ↑ ↑ ↑ ↑ ↑ ↓ ↓ ↓ ↓	-0.2120
20	↑ ↓ ↓ ↑ ↑ ↓ ↓ ↑ ↑ ↓ ↓ ↑	-0.2717
21	↑ ↑ ↑ ↑ ↑ ↑ ↓ ↑ ↓ ↑ ↓ ↑	-0.2249
22	↑ ↑ ↓ ↑ ↓ ↑ ↑ ↑ ↑ ↑ ↑ ↑	-0.2357
23	↑ ↑ ↑ ↑ ↑ ↑ ↑ ↑ ↓ ↓ ↑ ↓	-0.2251

Table B.2: The relative energies ΔE(Ry) of different spin arrangements in $FeTiO_3$ with 60 atoms in the unit cell containing 12 Fe^{2+} and 12 magnetically inert Ti^{4+} atoms. The spin magnitude of Fe^{2+} is $S_1 = S_2 = ... = S_{12} = |S^{Fe^{2+}}| = 4/2$ and the spin orientations are shown by up and down arrows.

No.	S_1, S_2, S_3 ,..., S_{12}	ΔE
1	↓ ↓ ↑ ↑ ↑ ↑ ↓ ↓ ↓ ↓ ↑ ↑	-0.1121
2	↑ ↑ ↑ ↑ ↑ ↑ ↑ ↑ ↑ ↑ ↑ ↑	-0.1114
3	↓ ↓ ↓ ↓ ↑ ↑ ↑ ↑ ↑ ↑ ↑ ↑	-0.1107
4	↓ ↓ ↑ ↑ ↑ ↑ ↑ ↑ ↑ ↑ ↑ ↑	-0.1118
5	↑ ↑ ↓ ↓ ↑ ↑ ↓ ↓ ↑ ↑ ↑ ↑	-0.1103
6	↑ ↑ ↓ ↓ ↑ ↑ ↑ ↑ ↓ ↓ ↑ ↑	-0.1106
7	↑ ↑ ↓ ↓ ↓ ↓ ↓ ↓ ↓ ↓ ↑ ↑	-0.1119
8	↑ ↑ ↓ ↓ ↓ ↓ ↑ ↑ ↑ ↑ ↑ ↑	-0.1120
9	↑ ↑ ↓ ↓ ↑ ↑ ↑ ↑ ↑ ↑ ↑ ↑	-0.1109
10	↓ ↓ ↓ ↓ ↓ ↓ ↑ ↑ ↑ ↑ ↑ ↑	-0.1117

Table B.3: The relative energies ΔE(Ry) and the corresponding spin arrangements of the Fe_2O_3-$FeTiO_3$ interface for 2 different sets of magnetic configurations with 60 atoms shown in Fig. 3.13a containing 18 Fe (12 Fe^{3+} and 6 Fe^{2+}) and 6 magnetically inert Ti^{4+} atoms. In set one (column ΔE_1) the energies with corresponding magnetic configuration are presented: $S_1^{3+} = S_2^{3+} = ... = S_{12}^{3+} = 5/2$ (hematite part) and $S_{13}^{2+} = S_{14}^{2+} = ... = S_{18}^{2+} = 4/2$ (ilmenite part). In set two (column ΔE_2) the magnetic state of S_{12} and S_{13} are exchanged now becoming $S_{12}^{2+} = 4/2$, $S_{13}^{3+} = 5/2$ and the reset of the magnetic moments are preserved like set one.

No.	S_1, S_2, S_3, S_4 ,..., S_{12}, S_{13} ,..., S_{18}	ΔE_1	ΔE_2
1	↑ ↑ ↓ ↓ ↓ ↓ ↑ ↑ ↑ ↑ ↓ ↓ ↓ ↓ ↓ ↓ ↓ ↓	-0.5559	-0.5351
2	↑ ↑ ↓ ↓ ↓ ↓ ↑ ↑ ↑ ↑ ↓ ↓ ↓ ↓ ↑ ↑ ↑ ↑	-0.5564	-0.5354
3	↑ ↑ ↑ ↑ ↑ ↑ ↑ ↑ ↑ ↑ ↑ ↑ ↑ ↑ ↓ ↓ ↓ ↓	-0.3623	-0.3503
4	↑ ↑ ↓ ↓ ↓ ↓ ↓ ↓ ↓ ↓ ↓ ↓ ↓ ↓ ↓ ↓ ↓ ↓	-0.4294	-0.4172
5	↑ ↑ ↓ ↓ ↓ ↓ ↑ ↑ ↓ ↓ ↓ ↓ ↓ ↓ ↓ ↓ ↓ ↓	-0.4931	-0.4718
6	↑ ↑ ↓ ↓ ↓ ↓ ↑ ↑ ↓ ↓ ↓ ↓ ↑ ↑ ↓ ↓ ↓ ↓	-0.5076	-0.5044
7	↑ ↑ ↓ ↓ ↓ ↓ ↑ ↑ ↓ ↓ ↑ ↑ ↓ ↓ ↓ ↓ ↓ ↓	-0.5080	-0.4819
8	↑ ↑ ↓ ↓ ↓ ↓ ↑ ↑ ↑ ↑ ↑ ↑ ↓ ↓ ↓ ↓ ↓ ↓	-0.5064	-0.5130
9	↑ ↑ ↓ ↓ ↓ ↓ ↑ ↑ ↑ ↑ ↑ ↑ ↑ ↑ ↓ ↓ ↓ ↓	-0.4930	-0.4810
10	↑ ↑ ↑ ↑ ↑ ↑ ↑ ↑ ↑ ↑ ↑ ↑ ↑ ↑ ↑ ↑ ↑ ↑	-0.3617	-0.3497
11	↑ ↑ ↑ ↑ ↑ ↑ ↑ ↑ ↑ ↑ ↑ ↑ ↑ ↑ ↓ ↓ ↑ ↑	-0.3607	-0.3489
12	↓ ↓ ↑ ↑ ↑ ↑ ↓ ↓ ↓ ↓ ↑ ↑ ↑ ↑ ↑ ↑ ↑ ↑	-0.5558	-0.5351
13	↑ ↑ ↑ ↑ ↑ ↑ ↑ ↑ ↑ ↑ ↓ ↓ ↑ ↑ ↑ ↑ ↑ ↑	-0.4190	-0.3795
14	↑ ↑ ↑ ↑ ↑ ↑ ↑ ↑ ↑ ↑ ↑ ↑ ↓ ↓ ↑ ↑ ↑ ↑	-0.3767	-0.3863
15	↑ ↑ ↑ ↑ ↑ ↑ ↑ ↑ ↑ ↑ ↓ ↓ ↓ ↓ ↑ ↑ ↑ ↑	-0.4309	-0.4089
16	↑ ↑ ↓ ↓ ↓ ↓ ↑ ↑ ↑ ↑ ↓ ↓ ↑ ↑ ↑ ↑ ↑ ↑	-0.5452	-0.5088

Table B.4: The relative energies ΔE(Ry) and the corresponding spin arrangements of the Fe_2O_3-$FeTiO_3$ interface with 60 atoms shown in Fig. 3.13b containing 16 Fe (8 Fe^{3+} and 8 Fe^{2+}) and 8 magnetically inert Ti^{4+} atoms. In this structure S_1, S_2 and S_7 to S_{12} are Fe^{3+} with the spin magnitude of 5/2 and the rest of the iron are Fe^{2+} with the spin magnitude of 4/2.

No.	S_1, S_2, S_3 ,..., S_{12}, S_{13} ,..., S_{16}	ΔE
1	↑ ↑ ↓ ↓ ↑ ↑ ↑ ↑ ↓ ↓ ↓ ↓ ↓ ↓ ↓ ↓	-0.2720
2	↑ ↑ ↓ ↓ ↑ ↑ ↑ ↑ ↓ ↓ ↓ ↓ ↑ ↑ ↑ ↑	-0.2726
3	↑ ↑ ↑ ↑ ↑ ↑ ↑ ↑ ↑ ↑ ↑ ↑ ↓ ↓ ↓ ↓	-0.1755
4	↑ ↑ ↓ ↓ ↓ ↓ ↓ ↓ ↓ ↓ ↓ ↓ ↓ ↓ ↓ ↓	-0.1849
5	↑ ↑ ↓ ↓ ↑ ↑ ↓ ↓ ↓ ↓ ↓ ↓ ↓ ↓ ↓ ↓	-0.2197
6	↑ ↑ ↓ ↓ ↑ ↑ ↓ ↓ ↓ ↓ ↑ ↑ ↓ ↓ ↓ ↓	-0.2338
7	↑ ↑ ↓ ↓ ↑ ↑ ↓ ↓ ↑ ↑ ↓ ↓ ↓ ↓ ↓ ↓	-0.2329
8	↑ ↑ ↓ ↓ ↑ ↑ ↑ ↑ ↑ ↑ ↓ ↓ ↓ ↓ ↓ ↓	-0.2203
9	↑ ↑ ↓ ↓ ↑ ↑ ↑ ↑ ↑ ↑ ↑ ↑ ↓ ↓ ↓ ↓	-0.2064
10	↑ ↑ ↑ ↑ ↑ ↑ ↑ ↑ ↑ ↑ ↑ ↑ ↑ ↑ ↑ ↑	-0.1748
11	↑ ↑ ↑ ↑ ↑ ↑ ↑ ↑ ↑ ↑ ↑ ↑ ↓ ↓ ↑ ↑	-0.1737
12	↓ ↓ ↑ ↑ ↓ ↓ ↓ ↓ ↑ ↑ ↑ ↑ ↑ ↑ ↑ ↑	-0.2719
13	↑ ↑ ↑ ↑ ↑ ↑ ↑ ↑ ↓ ↓ ↑ ↑ ↑ ↑ ↑ ↑	-0.2313
14	↑ ↑ ↑ ↑ ↑ ↑ ↑ ↑ ↑ ↑ ↓ ↓ ↑ ↑ ↑ ↑	-0.1894
15	↑ ↑ ↑ ↑ ↑ ↑ ↑ ↑ ↓ ↓ ↓ ↓ ↑ ↑ ↑ ↑	-0.2427
16	↑ ↑ ↓ ↓ ↑ ↑ ↑ ↑ ↓ ↓ ↑ ↑ ↑ ↑ ↑ ↑	-0.2612

Appendix C

The Interaction Type Matrix

$$\mathbf{J_{ij}} = \left(\begin{array}{cccccccccccccccccccccccc}
1 & 2 & 3 & 4 & 5 & 6 & 7 & 8 & 9 & 10 & 11 & 12 & 13 & 14 & 15 & 16 & 17 & 18 & 19 & 20 & 21 & 22 & 23 & 24 \\
\hline
J_1 & J_1 \\
J_2 & J_2 \\
J_2 & J_2 \\
J_2 & J_2 \\
J_3 & J_3 \\
J_3 & J_3 \\
J_3 & J_3 \\
J_4 & J_4 \\
J_4 & J_4 \\
J_4 & J_4 \\
J_5 & J_5 \\
J_5 & J_5 \\
J_5 & J_5 \\
J_6 & J_6 \\
J_7 & J_7 \\
J_7 & J_7 \\
J_7 & J_7 \\
J_7 & J_7 \\
J_7 & J_7 \\
J_7 & J_7 \\
J_8 & J_8 \\
J_8 & J_8 \\
J_8 & J_8 \\
J_9 & J_9 \\
J_9 & J_9 \\
J_9 & J_9
\end{array}\right)$$

Appendix D

The Connectivity Matrix

The connectivity matrix ($\mathbf{S_i}.\mathbf{S_j}$) is directly connected to the interaction type matrix ($\mathbf{J_{ij}}$) in appendix C. In this matrix ($\mathbf{S_i}.\mathbf{S_j}$) the first row give the index of the atom and columns of matrix show its connectivity to the other atoms in the unit cell and gives information on the multiplicity of a given interaction type. For instance in the first column atom 1 is connected once to atom 6 with interaction type J_1, three times to atom 2 with J_2 and three times to atom 3 with J_3, etc.

$$\mathbf{S_i.S_j} = \left(\begin{array}{cccccccccccccccccccccccc}
1 & 2 & 3 & 4 & 5 & 6 & 7 & 8 & 9 & 10 & 11 & 12 & 13 & 14 & 15 & 16 & 17 & 18 & 19 & 20 & 21 & 22 & 23 & 24 \\
\hline
S_6 & S_5 & S_9 & S_{10} & S_2 & S_1 & S_{13} & S_{14} & S_3 & S_4 & S_{17} & S_{17} & S_7 & S_8 & S_{21} & S_{22} & S_{11} & S_{12} & S_{24} & S_{23} & S_{15} & S_{16} & S_{20} & S_{19} \\
S_2 & S_1 & S_5 & S_6 & S_3 & S_4 & S_9 & S_{10} & S_7 & S_8 & S_{14} & S_{13} & S_{12} & S_{11} & S_{17} & S_{18} & S_{15} & S_{16} & S_{21} & S_{22} & S_{19} & S_{20} & S_{24} & S_{23} \\
S_2 & S_1 & S_5 & S_6 & S_3 & S_4 & S_9 & S_{10} & S_7 & S_8 & S_{14} & S_{13} & S_{12} & S_{11} & S_{17} & S_{18} & S_{15} & S_{16} & S_{21} & S_{22} & S_{19} & S_{20} & S_{24} & S_{23} \\
S_2 & S_1 & S_5 & S_6 & S_3 & S_4 & S_9 & S_{10} & S_7 & S_8 & S_{14} & S_{13} & S_{12} & S_{11} & S_{17} & S_{18} & S_{15} & S_{16} & S_{21} & S_{22} & S_{19} & S_{20} & S_{24} & S_{23} \\
S_3 & S_4 & S_1 & S_2 & S_7 & S_8 & S_5 & S_6 & S_{12} & S_{11} & S_{10} & S_9 & S_{16} & S_{15} & S_{14} & S_{13} & S_{19} & S_{20} & S_{17} & S_{18} & S_{23} & S_{24} & S_{21} & S_{22} \\
S_3 & S_4 & S_1 & S_2 & S_7 & S_8 & S_5 & S_6 & S_{12} & S_{11} & S_{10} & S_9 & S_{16} & S_{15} & S_{14} & S_{13} & S_{19} & S_{20} & S_{17} & S_{18} & S_{23} & S_{24} & S_{21} & S_{22} \\
S_3 & S_4 & S_1 & S_2 & S_7 & S_8 & S_5 & S_6 & S_{12} & S_{11} & S_{10} & S_9 & S_{16} & S_{15} & S_{14} & S_{13} & S_{19} & S_{20} & S_{17} & S_{18} & S_{23} & S_{24} & S_{21} & S_{22} \\
S_5 & S_6 & S_7 & S_8 & S_1 & S_2 & S_3 & S_4 & S_{13} & S_{14} & S_{15} & S_{16} & S_9 & S_{10} & S_{11} & S_{12} & S_{21} & S_{22} & S_{23} & S_{24} & S_{17} & S_{18} & S_{19} & S_{20} \\
S_5 & S_6 & S_7 & S_8 & S_1 & S_2 & S_3 & S_4 & S_{13} & S_{14} & S_{15} & S_{16} & S_9 & S_{10} & S_{11} & S_{12} & S_{21} & S_{22} & S_{23} & S_{24} & S_{17} & S_{18} & S_{19} & S_{20} \\
S_5 & S_6 & S_7 & S_8 & S_1 & S_2 & S_3 & S_4 & S_{13} & S_{14} & S_{15} & S_{16} & S_9 & S_{10} & S_{11} & S_{12} & S_{21} & S_{22} & S_{23} & S_{24} & S_{17} & S_{18} & S_{19} & S_{20} \\
S_4 & S_3 & S_2 & S_1 & S_9 & S_{10} & S_{12} & S_{11} & S_5 & S_6 & S_8 & S_7 & S_{18} & S_{17} & S_{19} & S_{20} & S_{14} & S_{13} & S_{15} & S_{16} & S_{24} & S_{23} & S_{22} & S_{21} \\
S_4 & S_3 & S_2 & S_1 & S_9 & S_{10} & S_{12} & S_{11} & S_5 & S_6 & S_8 & S_7 & S_{18} & S_{17} & S_{19} & S_{20} & S_{14} & S_{13} & S_{15} & S_{16} & S_{24} & S_{23} & S_{22} & S_{21} \\
S_4 & S_3 & S_2 & S_1 & S_9 & S_{10} & S_{12} & S_{11} & S_5 & S_6 & S_8 & S_7 & S_{18} & S_{17} & S_{19} & S_{20} & S_{14} & S_{13} & S_{15} & S_{16} & S_{24} & S_{23} & S_{22} & S_{21} \\
S_7 & S_8 & S_4 & S_3 & S_{12} & S_{11} & S_1 & S_2 & S_{16} & S_{15} & S_6 & S_5 & S_{20} & S_{19} & S_{10} & S_9 & S_{23} & S_{24} & S_{14} & S_{13} & S_{22} & S_{21} & S_{17} & S_{18} \\
S_1 & S_2 & S_3 & S_4 & S_5 & S_6 & S_7 & S_8 & S_9 & S_{10} & S_{11} & S_{12} & S_{13} & S_{14} & S_{15} & S_{16} & S_{17} & S_{18} & S_{19} & S_{20} & S_{21} & S_{22} & S_{23} & S_{24} \\
S_1 & S_2 & S_3 & S_4 & S_5 & S_6 & S_7 & S_8 & S_9 & S_{10} & S_{11} & S_{12} & S_{13} & S_{14} & S_{15} & S_{16} & S_{17} & S_{18} & S_{19} & S_{20} & S_{21} & S_{22} & S_{23} & S_{24} \\
S_1 & S_2 & S_3 & S_4 & S_5 & S_6 & S_7 & S_8 & S_9 & S_{10} & S_{11} & S_{12} & S_{13} & S_{14} & S_{15} & S_{16} & S_{17} & S_{18} & S_{19} & S_{20} & S_{21} & S_{22} & S_{23} & S_{24} \\
S_1 & S_2 & S_3 & S_4 & S_5 & S_6 & S_7 & S_8 & S_9 & S_{10} & S_{11} & S_{12} & S_{13} & S_{14} & S_{15} & S_{16} & S_{17} & S_{18} & S_{19} & S_{20} & S_{21} & S_{22} & S_{23} & S_{24} \\
S_1 & S_2 & S_3 & S_4 & S_5 & S_6 & S_7 & S_8 & S_9 & S_{10} & S_{11} & S_{12} & S_{13} & S_{14} & S_{15} & S_{16} & S_{17} & S_{18} & S_{19} & S_{20} & S_{21} & S_{22} & S_{23} & S_{24} \\
S_1 & S_2 & S_3 & S_4 & S_5 & S_6 & S_7 & S_8 & S_9 & S_{10} & S_{11} & S_{12} & S_{13} & S_{14} & S_{15} & S_{16} & S_{17} & S_{18} & S_{19} & S_{20} & S_{21} & S_{22} & S_{23} & S_{24} \\
S_9 & S_{10} & S_6 & S_5 & S_4 & S_3 & S_2 & S_1 & S_1 & S_2 & S_{19} & S_{20} & S_{22} & S_{21} & S_8 & S_7 & S_{10} & S_9 & S_{11} & S_{12} & S_{14} & S_{13} & S_{18} & S_{17} \\
S_9 & S_{10} & S_6 & S_5 & S_4 & S_3 & S_2 & S_1 & S_1 & S_2 & S_{19} & S_{20} & S_{22} & S_{21} & S_8 & S_7 & S_{10} & S_9 & S_{11} & S_{12} & S_{14} & S_{13} & S_{18} & S_{17} \\
S_9 & S_{10} & S_6 & S_5 & S_4 & S_3 & S_2 & S_1 & S_1 & S_2 & S_{19} & S_{20} & S_{22} & S_{21} & S_8 & S_7 & S_{10} & S_9 & S_{11} & S_{12} & S_{14} & S_{13} & S_{18} & S_{17} \\
S_8 & S_7 & S_{12} & S_{11} & S_{13} & S_{14} & S_{16} & S_{15} & S_{18} & S_{17} & S_4 & S_3 & S_5 & S_6 & S_{23} & S_{24} & S_{24} & S_{23} & S_{22} & S_{21} & S_{20} & S_{19} & S_{15} & S_{16} \\
S_8 & S_7 & S_{12} & S_{11} & S_{13} & S_{14} & S_{16} & S_{15} & S_{18} & S_{17} & S_4 & S_3 & S_5 & S_6 & S_{23} & S_{24} & S_{24} & S_{23} & S_{22} & S_{21} & S_{20} & S_{19} & S_{15} & S_{16} \\
S_8 & S_7 & S_{12} & S_{11} & S_{13} & S_{14} & S_{16} & S_{15} & S_{18} & S_{17} & S_4 & S_3 & S_5 & S_6 & S_{23} & S_{24} & S_{24} & S_{23} & S_{22} & S_{21} & S_{20} & S_{19} & S_{15} & S_{16}
\end{array}\right)$$

Manuscript M1

Interface magnetism in Fe_2O_3/$FeTiO_3$ heterostructures

Phys. Rev. B **77**, 172405, (2008)

Manuscript M2

Effect of strain on the stability and electronic
properties of ferrimagnetic $Fe_{2-x}Ti_xO_3$ heterostructures
from correlated band theory

J. Appl. Phys. **106**, 073912, (2009)

Manuscript M3

Magnetic coupling parameters at an oxide-oxide
interface from first principles: Fe_2O_3-$FeTiO_3$

Phys. Rev. B **81**, 214432 (2010)

Manuscript M4

Electronic structure and magnetism of $EuTiO_3$: a first-principles study

J. Phys.: Condens. Matter **19**, 406217, (2007)

Manuscript M5

First principles study of magnetism in divalent Eu perovskites

J. Appl. Phys. **105**, 053905, (2009)

Bibliography

[1] A. Brinkman, M. Huijben, M. van Zalk, J. Huijben, U. Zeitler, J. C. Maan, W. G. van der Wiel, G. Rijnders, D. H. A. Blank and H. Hilgenkamp, Nature Mater. **6**, 493 (2007).

[2] J. Chakhalian, J. W. Freeland, G. Srajer, J. Strempfer, G. Khaliullin, J. C. Cezar, T. Charlton, R. Dalgliesh, C. Bernhard, G. Cristiani, H.-U. Habermeier and B. Keimer, Nature Phys. **2**, 244 (2006).

[3] H. Yamada, Y. Ogawa, Y. Ishii, H. Sato, M. Kawasaki, H. Akoh and Y. Tokura, Science **305**, 646 (2004).

[4] Y. Ishikawa and S. Akimoto, J. Phys. Soc. Jpn. **12**, 1083 (1957).

[5] S. A. McEnroe, B. Carter-Stiglitz, R. J. Harrison, P. Robinson, K. Fabian and C. McCammon, Nature Nano. **2**, 631 (2007).

[6] T. Kasama, S. A. McEnroe, N. Ozaki, T. Kogure and A. Putnis, Earth Planet. Sci. Lett. **224**, 461 (2004).

[7] Y. Takada, M. Nakanishi, T. Fujii and J. Takada, J. Magn. Magn. Matter. **310**, 2108 (2007).

[8] H. Hojo, K. Fujita, K. Tanaka, and K. Hirao, Appl. Phys. Lett. **89**, 142503 (2006).

[9] S. Kuroda, N. Nishizawa, K. Takita, M. Mitome, Y. Bando, K. Osuch, and Tomasz Dietl, Nature Mater. **6**, 440 (2007).

[10] S. A. Chambers, T. C. Droubay, C. M. Wang, K. M. Rosso, S. M. Heald, D. A. Schwartz, K. R. Kittilstved, and D. R. Gamelin, Materials Today **9**, 28 (2006).

[11] J. M. D. Coey, M. Venkatesan, and C. B. Fitzgerald, Nature Mater. **4**, 173 (2005).

[12] A. H. MacDonald, P. Schiffer and N. Samarth, Nature Mater. **4**, 195 (2005).

[13] F. Zhou, S. Kotru and R. K. Pandey, Thin Solid Films, **408**, 33 (2002).

[14] P. Robinson, R. J. Harrison, S. A. McEnroe, and R. B. Hargraves, Nature **418**, 517 (2002).

[15] P. Blaha, K. Schwarz, G. K. H. Madsen, D. Kvasnicka, and J. Luitz, WIEN2k, An Augmented Plane Wave + Local Orbitals Program for Calculating Crystal Properties (Technical University of Wien, Austria, 2001), ISBN3-9501031-1-2.

[16] V. I. Anisimov, I. V. Solovyev, M. A. Korotin, M. T. Czyżyk and G. A. Sawatzky, Phys. Rev. B **48**, 16929, (1993).

[17] T. Katsufuji and H. Takagi, Phys. Rev. B **64**, 054415 (2001).

[18] T. R. McGuire, M. W. Shafer, R. J. Joenk, H. A. Alperin, and S. J. Pickart, J. Appl. Phys. **37**, 981 (1966).

[19] Chia-Ling Chien, S. DeBenedetti, and F. De S. Barros, Phys. Rev. B **10**, 3913 (1974).

[20] T. Kimura, T. Goto, H. Shintani, K. Ishizaka, T. Arima and Y. Tokura, Nature **426**, 55 (2003).

[21] M. Fiebig, J. Phys. D: Appl. Phys. **38**, R123 (2005).

[22] N. A. Hill, Annu. Rev. Mater. Res. **32**, 1 (2002).

[23] R. W. Robinett, *Quantum Mechanics, Classical Results, Modern Systems, and Visualized Examples*, Second edition, (Oxford University Press 2006).

[24] D. Griffiths, *Introduction to Quantum Mechnics*, (Prentice Hall, Inc. 1995).

[25] P. A. M. Dirac, *The Principles of Quantum Mechanics.* 4th edition, (Clarendon Press, Oxford, 1958).

[26] J. Schwinger, *Quantum Mechnics, Symbolism of Atomic Measurements*, (Springer Veralg 2001).

[27] G. Grosso and G. P. Parravicini, *Solid State Physics*, (Academic Press 2000).

[28] P. Hohenberg and W. Kohn, Phys. Rev. **136**(3B), 864, (1964).

[29] W. Kohn and L. J. Sham, Phys. Rev. **140**(4A), 1133, (1965).

[30] U. von Barth and L. Hedin, J. Phys. C: Solid State Phys. **5**,1629, (1972).

[31] D. M. Ceperley and B. J. Alder, Phys. Rev. Lett. **45**,566, (1980).

[32] S. H. Vosko, L. Wilk, and M. Nusair, Can. J. Phys. **58**,1200, (1980).

[33] J. P. Perdew and Y. Wang, Phys. Rev. B **33**, 8800, (1986).

[34] J. P. Perdew and Y. Wang, Phys. Rev. B **45**,13244, (1992).

[35] J. P. Perdew, K. Burke, and M. Ernzerhof, Phys. Rev. Lett. **77**, 3865, (1996).

[36] J. C. Slater, Phys. Rev. **51**, 846, (1937).

[37] J. C. Slater, Rev. Mod. Phys. **6**, 209, (1934).

[38] C. S. Wang, B. M. Klein and H. Krakauer, Phys. Rev. Lett. **54**, 1852, (1985).

[39] T. C. Leung, C. T. Chan, and B. N. Harmon, Phys. Rev. B **44**, 2923, (1991).

[40] R. M. Dreizler and E. K. U. Gross, Springer-Verlag Berlin Heidelberg, (1990).

[41] V. I. Anisimov, J. Zaanen, and O. K. Andersen, Phys. Rev. B **44**, 943, (1991).

[42] A. I. Liechtenstein, V. I. Anisimov, and J. Zaanen, Phys. Rev. B **52**, R5467, (1995).

[43] K. Terakura, T. Oguchi, A. R. Williams, and J. Kübler, Phys. Rev. Lett. **52**, 1830, (1984).

[44] K. Terakura, T. Oguchi, A. R. Williams, and J. Kübler, Phys. Rev. B **30**, 4734, (1984).

[45] J. P. Perdew and A. Zunger, Phys. Rev. B **23**, 5048, (1981).

[46] A. Svane and O. Gunnarsson, Phys. Rev. Lett. **65**, 1148, (1990).

[47] S. Massidda, M. Posternak, and A. Baldereschi, Phys. Rev. B **48**, 5058, (1993).

[48] M. T. Czyżyk and G. A. Sawatzky, Phys. Rev. B **49**, 14211, (1994).

[49] Matteo Cococcioni and Stefano de Gironcoli, Phys. Rev. B **71**, 035105, (2005).

[50] W. E. Pickett, S. C. Erwin, and E. C. Ethridge, Phys. Rev. B **58**, 1201, (1198).

[51] S. Cottenier, *DFT and the Family of (L)APW-methods: a step-by-step introduction*, ISBN 90-807215-1-4, (2004).

[52] J. Korringa, Physica, **13**, 392 (1947).

[53] W. Kohn and N. Rostoker, Phys. Rev. **94**, 1111, (1954).

[54] O. K. Andersen, Phys. Rev. B **12**, 3060, (1975)

[55] D. J. Singh, *Planewaves, Pseudopotentials and the LAPW method*, Kluwer Academic Publishers, Boston, 1994.

[56] D. D. Koelling and G. O. Arbman, J. Phys. F: Met. Phys. **5**, 2041, (1975).

[57] D. A. Perkins and J. P. Attfield, J. Chem. Soc., Chem. Commun., 229 (1991).

[58] R. J. Harrison, S. A. T. Redfern, R. I. Smith, Am. Mineral. **85**, 194 (2000).

[59] H. Kato, Y. Yamaguchi, M. Yamada, S. Funahashi, Y. Nakagawa and H. Takei, J. Phys. C: Solid State Phys **19**, 6993 (1986).

[60] N. C. Wilson, J. Muscat, D. Mkhonto, P. E. Ngoepe, and N. M. Harrison, Phys. Rev. B **71**, 075202 (2005).

[61] F. D. Murnaghan, Proc. Natl. Acad. Sci. U.S.A. **30**, 244 (1944).

[62] O. L. Anderson, Equations of state of Solids for Geophysics and Ceramic Science (Oxford University Press, New York, USA, 1995).

[63] B. A. Wechsler and C. T. Prewitt, Am. Min. **69**, 176, (1984).

[64] Y. Ishikawa, J. Phys. Soc. Jpn. **13**, 37 (1958).

[65] S. Sunkara and R. K. Pandey, Ceram. Trans. **60**, 83 (1995).

[66] N. C. Wilson, S. P. Russo, J. Muscat, and N. M. Harrison, Phys. Rev. B **72**, 024110 (2005).

[67] B. Gilbert, C. Frandsen, E. R. Maxey, and D. M. Sherman, Phys. Rev. B **79**, 035108 (2009).

[68] J. Badro, G. Fiquet, V. V. Struzhkin, M. Somayazulu, Ho-kwang Mao, G. Shen and T. Le Bihan, Phys. Rev. Lett. **89**, 205504 (2002).

[69] P. Kuiper, B. G. Searle, P. Rudolf, L. H. Tjeng and C. T. Chen, Phys. Rev. Lett. **70**, 1549 (1993).

[70] Y. Sato and Syun-iti Akimoto, J. Appl. Phys. **50**, 5285 (1979).

[71] G. Kh. Rozenberg, L. S. Dubrovinsky, M. P. Pasternak, O. Naaman, T. Le Bihan and R. Ahuja, Phys. Rev. B 65, 064112 (2002).

[72] N. C. Wilson and S. P. Russo, Phys. Rev. B **79**, 094113 (2009).

[73] M. Catti, G. Valerio and R. Dovesi, Phys. Rev. B **51**, 7441 (1995).

[74] G. Rollmann, A. Rohrbach, P. Entel, and J. Hafner, Phys. Rev. B **69**, 165107 (2004).

[75] D. Benjelloun, J.-P. Bonnet, J.-P. Doumerc, J.-C. Launay, M. Onillon and P. Hagenmuller, Mater. Chem Phys. **10**, 503 (1984).

[76] R. H. Chang and J. B. Wagner, J. Am. Cer. Soc. **55**, 211 (1972).

[77] B. P. Burton, Phys. Chem. Minerals, **11**, 132 (1984).

[78] B. P. Burton, A. Chaka, and D. J. Singh, Phase Trans. **78**, 239 (2005).

[79] A. Putnis, *Introduction to Mineral Science*, (Cambridge university Press, 1992).

[80] A. Ohtomo, D. A. Muller, J. L. Grazul and H. Y. Hwang, Nature **419**, 378 (2002).

[81] N. Reyren, S. Thiel, A. D. Caviglia, L. F. Kourkoutis, G. Hammerl, C. Richter, C. W. Schneider, T. Kopp, A.-S. Retschi, D. Jaccard, M. Gabay, D. A. Muller, J.-M. Triscone and J. Mannhart, Science **317**, 1196 (2007).

[82] R. Pentcheva, H. Sadat Nabi, Phys. Rev. B, **77**, 172405 (2008).

[83] S. Pillet, M. Souhassou, C. Lecomte, K. Schwarz, P. Blaha, M. Rérat, A. Lichanot and P. Roversi, Acta Crystallographica A, **57**, 290 (2001).

[84] T. Fujii, M. Kayano, Y. Takada, M. Nakanishi, and J. Takada, J. Mag. Mag. Mat. **272**, 2010 (2004).

[85] E. Popova, B. Warot-Fonrose, H. Ndilimabaka, M. Bibes, N. Keller, B. Berini, K. Bouzehouane, and Y. Dumont, J. Appl. Phys. **103**, 093909 (2008).

[86] H. Ndilimabaka, Y. Dumont, E. Popova, P. Desfonds, F. Jomard, N. Keller, M. Basletic, K. Bouzehouane, M. Bibes, and M. Godlewski, J. Appl. Phys. **103**, 07D137 (2008).

[87] W. Eerenstein, J. F. Scott, and N. D. Mathur, Nature **442**, 759 (2006).

[88] K. J. Choi, M. Biegalski, Y. L. Li, A. Sharan, J. Schubert, R. Uecker, P. Reiche, Y. B. Chen, X. Q. Pan, V. Gopalan, L.-Q. Chen, D. G. Schlom, and C. B. Eom, Science **306**, 1005 (2004).

[89] J. X. Zhang, Y. L. Li, Y. Wang, Z. K. Liu, L. Q. Chen, Y. H. Chu, F. Zavaliche, and R. Ramesh, J. Appl. Phys. **101**, 114105 (2007).

[90] M. Izumi, Y. Ogimoto, Y. Konishi, T. Manako, M. Kawasaki, and Y. Tokura, Mat. Sci. Eng. B**84**, 53 (2001).

[91] E. Popova, H. Ndilimabaka, B. Warot-Fonrose, M. Bibes, N. Keller, B. Berini, F. Jomard, K. Bouzehouane, and Y. Dumont, Appl. Phys. A **93**, 669 (2008).

[92] Y. Takada, M. Nakanishi, T. Fujii, J. Takada, and Y. Muraoka, J. Appl. Phys. **104**, 033713 (2008).

[93] J. Velev, A. Bandyopadhyay, W. H. Butler, and S. K. Sarker, Phys. Rev. B **71**, 205208 (2005).

[94] T. Droubay, K. M. Rosso, S. M. Heald, D. E. McCready, C. M. Wang, and S. A. Chambers, Phys. Rev. B **75**, 104412 (2007).

[95] U. Falk, A. Furrer, H. U. Güdel and J. K. Kjems, Phys. Rev. B **35**, 4888 (1987).

[96] U. Falk, A. Furrer, N. Furer, H. U. Güdel and J. K. Kjems, Phys. Rev. B **35**, 4893 (1987).

[97] F. Mila, P. Millet and J. Bonvoisin, Phys. Rev. B **54**, 11925 (1996).

[98] W. E. Pickett, Phys. Rev. Lett. **79**, 1746 (1997).

[99] M. P. Gelfand, Zheng Weihong, Rajiv R. P. Singh, J. Oitmaa, and C. J. Hamer, Phys. Rev. Lett. **77**, 2794 (1996).

[100] S. Shi, A. L. Wysocki, and K. D. Belashchenko, Phys. Rev. B **79**, 104404 (2009).

[101] O. Le Bacq, A. Pasturel, C. Lacroix and M. D. Núñez-Regueiro, Phys. Rev. B **71**, 014432 (2005).

[102] A. I. Liechtenstein, M. I. Katsnelson, V. P. Antropov and V. A. Gubanov, J. Magn. Magn. Matter. **67**, 65 (1987).

[103] S. Picozzi and M. ležaić, New Journal of Physics **10**, 055017 (2008).

[104] E. J. Samuelsen and G. Shirane, Phys. stat. sol. **42**, 241 (1970).

[105] E. J. Samuelsen and G. Shirane, Journal de Physique Colloques 32, 1064 (1971).

[106] H. Kato, S. Funahashi, Y. Yamaguchi, M. Yamada and H. Takei, J. Magn. Magn. Matter. **31**, 617 (1983).

[107] V. V. Mazurenko and V. I. Anisimov, Phys. Rev. B **71**, 184434 (2005).

[108] J. B. Goodenough, Phys. Rev. **117**, 1442 (1960).

[109] P. W. Anderson, Phys. Rev. **115**, 2 (1959).

[110] L. M. Sandratskii, M. Uhl and J. Kübler, J. Phys.: Condens. Matter **8**, 983 (1996).

[111] A. H. Morrish, *Canted Antiferromagnetism* , Hematite (World Scientific, Singapore, 1994).

[112] R. J. Harrison, Am. Miner. **91**, 1006 (2006).

[113] R. J. Harrison, S. A. McEnroe, P. Robinson, B. Carter-Stiglitz, E. J. Palin, and T. Kasama, Phys. Rev. B **76**, 174436 (2007).

[114] R. Ranjan, H. Sadat Nabi, and R. Pentcheva, J. Phys.: Condens. Matter **19**, 406217 (2007).

[115] J. Borous, I. Fankuchen, and E. Banks, Acta Crystallogr. **6**, 67 (1953).

[116] M. W. Shafer, J. Appl. Phys. **36**, 1145 (1965).

[117] D. L. Janes, R. E. Bodnar, and A. L. Taylor, J. Appl. Phys. **49**, 1452 (1978).

[118] C. J. Fennie and K. M. Rabe, Phys. Rev. Lett. **97**, 267602 (2006).

[119] J. Kuneš, W. Ku and W. E. Pickett, J. Phys. Soc. Japan **74**, 1408 (2005).(Preprint cond-mat/0406229)

[120] J. Kuneš and W. E. Pickett, Phys. Rev. B **69**, 165111 (2004).

[121] P. Larson and W. R. L. Lambrecht, J. Phys.: Condens. Matter **18**, 11333 (2006).

[122] R. Ranjan, H. Sadat Nabi, and R. Pentcheva, J. Appl. Phys., **105**, 053905 (2009).

[123] L. Passell, O. W. Dietrich, and J. Als-Nielsen, Phys. Rev. B **14**, 4897 (1976).

[124] M. Ishizuka, Y. Kai, R. Akimoto, M. Kobayashi, K. Amaya, and S. Endo, J. Magn. Magn. Mater. **166**, 211 (1997).

[125] J. E. Greedan, Cahi-Liang Chien, and R. G. Johnston, J. Solid State Chem. **19**, 155 (1976).

[126] Chia-Ling Chien and J. E. Greedan, Phys. Lett. **36A**, 197 (1971).

[127] J. E. Greedan, J. Phys. Chem. Solids **32**, 819 (1971).

[128] J. D. Goodenough, Magnetism and the Chemical Bond (Interscience, New York, 1963), pp. 146167.

[129] T. Kasuya, IBM J. Res. Dev. **14**, 214 (1970).

[130] J. Kuneš and R. Laskowski, Phys. Rev. B **70**, 174415 (2004).

[131] J. Kuneš and W. E. Pickett, Physica B **359361**, 205 (2005).

[132] H. Sadat Nabi and R. Pentcheva, J. Appl. Phys. **105**, 053905 (2009).

[133] K. Fujita, N. Wakasugi, S. Murai, Y. Zong and K. Tanaka, Appl. Phys. Lett. **94**, 062512 (2009).

[134] K. Hatabayashi, T. Hitosugi, Y. Hirose, X. Cheng, T. Shimada and T. Hasegawa, Jpn. J. Appl. Phys. **48**, 100208 (2009).

Acknowledgements

It is my pleasure to express my sincere gratitude to the people who helped me in different ways and gave me the possibility to give existence to this dissertation.

My first deep and sincere gratitude goes to my supervisor, PD Dr. Rossitza Pentcheva, for the continuous support throughout this study, for her patience and motivation. This work would have not been completed without her elaborate guidance in all the stages of this research. Also, an special acknowledgment to her for the careful reading of my thesis.

I would also like to express my gratitude to my co-advisor, Prof. Dr. W. Moritz, for giving me the opportunity to join his group and work in a friendly research area at the Ludwig-Maximilians-Universität. I am also thankful to Prof. Dr. Schmahl for his continuous interest and discussions in this work.

In addition, I want to thank our collaborators PD. Dr. M. Winklhofer, Dr. R. J. Harrison, Dr. S. A. McEnroe, Prof. P. Robinson and Dr. R. Ranjan, who contributed in different parts of the project and for all the stimulating discussions.

I would like to thank all my colleges and friends: Saeed Ansari, Saeed Aminiyan, Andreas Götz, Maike Lübbe, Narasimham Mulakaluri, Casjen Merkel, Katrin Otte, Oliver Riedl; with whom I used to discuss about scientific and nonscientific topics. I would like to add a distinctive mention to Carmen Quiroga, for the careful reading and correction of this manuscript.

Furthermore, the financial support of my project by the DFG (Pe883/4-1) and ESF within the European Mineral Science Initiative (EuroMinSci) are gratefully acknowledged.

Finally, I am grateful to my parents for their patience, *love* and constant support. Without them, this work would have never come to existence.

Seyed Hasan Sadat Nabi
February 2010

Publications

1. R. Ranjan, H. Sadat Nabi and R. Pentcheva, *Electronic structure and magnetism of $EuTiO_3$: a first-principles study*, J. Phys.: Cond. Matt. **19**, 406217 (2007).
2. R. Pentcheva and H. Sadat Nabi, *Interface Magnetism in $Fe_2O_3/FeTiO_3$ heterostructures*, Phys. Rev. B **77**, 172405 (2008).
3. R. Ranjan, H. Sadat Nabi and R. Pentcheva, *First principle study of magnetism in divalent Eu perovskites*, J. Appl. Phys. **105**, 053905 (2009).
4. H. Sadat Nabi and R. Pentcheva, *Effect of strain on the stability and electronic properties of ferromagnetic $Fe_{2-x}Ti_xO_3$ heterostructures from correlated band theory*, J. Appl. Phys. **106**, 073912 (2009).
5. H. Sadat Nabi, R. J. Harrison and R. Pentcheva, *Magnetic coupling parameters at an oxide-oxide interface from first principles: Fe_2O_3-$FeTiO_3$*, Phys. Rev. B **81**, 214432 (2010).
6. H. Sadat Nabi, R. Pentcheva and R. Ranjan, Ab-initio *electronic structures of rhombohedral and cubic $HgXO_3$ (X=Ti, Pb)*, J. Phys.: Cond. Matt. **22**, 045504 (2010).[1]
7. H. Sadat Nabi and R. Pentcheva, *Magnetic interactions in Fe_2O_3-Cr_2O_3 system: a first principle study*, in preparation.[1]
8. H. Hashemi, G. Fischer, W. Hergert, V. S. Stepanyuk, H. Sadat Nabi and R. Pentcheva, *Exchange interaction of Fe nanowires on vicinal Cu(111) surfaces*, in preparation.[1]

---

[1] Not presented in this thesis

Conference contributions

1. 1th EuroMinSci Conference, poster presentation, 26-29th March 2007, La Colle-Sur-loup, France.

2. Frontiers in Mineral Science, poster presentation, 26-28th June 2007, Cambridge, United Kingdom.

3. Deutsche Physikalische Gesellschaft (DPG), oral presentation, 25-29th February 2008, Berlin, Germany.

4. 2nd EuroMinSci Conference, oral and poster presentation, 31 March-02 April 2008, Gines, France.

5. Joint European Magnetics Symposia (JEMS 08), oral personation, 14-19th September 2008, Dublin, Ireland.

6. International workshop on NanoFerronics (Jülich), poster presentation, 9-10th October 2008, IBIS Aachen, Germany.

7. 3rd EuroMinsci Conference, poster presentation, 24-26th November 2008, Strasbourg, Obernei, France.

8. Deutsche Physikalische Gesellschaft (DPG), oral presentation, 22-27th March 2009, Dresden, Germany.

9. SPP 1236 workshop (crystal physics at extreme conditions), oral presentation, 10-12th March 2010, Oberursel, Hessen, Germany.

10. American Physical Society (APS) meeting, oral presentation, 15-19th March 2010, Portland, Oregon, USA.

11. Deutsche Physikalische Gesellschaft (DPG), oral presentation, 21-26th March 2010, Regensburg, Germany.

Curriculum Vitae

Personal data:

- **Surname:** Sadat Nabi
- **Name:** Seyed Hasan
- **Date and Place of Birth:** June 27, 1980; Bahar, Iran
- **Nationality:** Iranian

Education:	Schools
1986 - 1994	Elementary school, Bahar, Iran
1994 - 1998	High school, Hamadan, Iran

Studies:

1998 - July 2002	Bachelor of physics Department of physics, Bu-Ali Sina University, Hamadan, Iran
2002 - Aug. 2005	Master of condensed matter physics Department of physics, Institute for advanced studies in basic sciences, Zanjan, Iran
Since June 2006	PhD. of computational physics (material science) supervised by PD Dr. Rossitza Pentchva, Department of earth and environmental sciences, Ludwig-Maximilians University, Munich, Germany

PHYSICAL REVIEW B **77**, 172405 (2008)

Interface magnetism in $Fe_2O_3/FeTiO_3$ heterostructures

Rossitza Pentcheva* and Hasan Sadat Nabi
Department of Earth and Environmental Sciences, University of Munich, Theresienstrasse 41, 80333 Munich, Germany

(Received 10 April 2008; published 15 May 2008)

To resolve the microscopic origin of magnetism in the $Fe_2O_3/FeTiO_3$ system, we have performed density functional theory calculations that take into account on-site Coulomb repulsion. By systematically varying the concentration, distribution, and charge state of Ti in a hematite host, we compile a phase diagram of the stability with respect to the end members and find a clear preference to form layered arrangements as opposed to solid solutions. The charge mismatch at the interface is accommodated through Ti^{4+} and a disproportionation in the Fe contact layer into Fe^{2+}, Fe^{3+}, leading to uncompensated moments in the contact layer and giving first theoretical evidence for the *lamellar magnetism hypothesis*. This interface magnetism is associated with impurity levels in the band gap, showing a half-metallic behavior and making $Fe_2O_3/FeTiO_3$-heterostructures prospective materials for spintronics applications.

DOI: 10.1103/PhysRevB.77.172405 PACS number(s): 75.70.Cn, 73.20.Hb, 71.28.+d

A challenge of today's materials science is to design ferromagnetic semiconductors that operate at room temperature (RT) for spintronics devices. Most of the efforts concentrate on homogeneous doping of semiconductors with magnetic impurities,[1–4] but the interfaces in complex oxides prove to be another source of a novel behavior.[5–7] The unique magnetic properties of the hematite-ilmenite system[8–10] (a canted antiferromagnet and a RT paramagnet, respectively) currently receive revived interest as a possible cause of magnetic anomalies in Earth's deep crust and on other planets[11] as well as for future device applications.[3,12,13]

Both hematite [$a=5.035$ Å, $c=13.751$ Å (Ref. 14)] and ilmenite [$a=5.177$ Å, $c=14.265$ Å (Ref. 15)] crystallize in a corundum(-derived) structure, which is shown in Fig. 1, wherein the oxygen ions form a distorted hexagonal close packed lattice and the cations occupy 2/3 of the octahedral sites. In α-Fe_2O_3 (space group $R\bar{3}c$), there is a natural modulation of electronic density along the [0001] direction wherein negatively charged $3O^{2-}$ layers alternate with positively charged $2Fe^{3+}$ layers. At RT, the magnetic moments of subsequent iron layers couple antiferromagnetically (AFM) in-plane with a small spin canting, which is attributed to spin-orbit coupling.[16–18] In ilmenite $FeTiO_3$, Fe and Ti layers alternate, which reduces the symmetry to $R\bar{3}$, and the corresponding sequence is $3O^{2-}/2Fe^{2+}/3O^{2-}/2Ti^{4+}$ with AFM coupling between the Fe layers and $T_N=56-59$ K.[19]

At the interfaces (IFs) in hematite-ilmenite exsolutions, the charge neutrality is disrupted. One way to balance the excess charge at the interface is by a disproportionation in the Fe layer, which now becomes mixed Fe^{2+} and Fe^{3+}. This *lamellar magnetism hypothesis (LMH)* was proposed by Robinson *et al.*[20] based on bond valence models and kinetic Monte Carlo (kMC) simulations with empirical chemical and magnetic interaction parameters. The increased technological interest in this system calls for an atomistic material specific understanding that can only be obtained from first principles calculations. A previous density functional theory (DFT) study within the generalized gradient approximation (GGA) found no evidence for the LMH.[21] However, electronic correlations, which are not included in the local (spin-) density approximation (LSDA) or the GGA of the DFT, play an important role in transition metal oxides. Such effects were recently considered within LSDA+U[22] or by using hybrid functionals[23] for single Ti impurities in hematite; however, layered arrangements and interfaces were not addressed.

In this Brief Report, we have performed DFT calculations including a Hubbard U[24] for the end members Fe_2O_3 and $FeTiO_3$, as well as their interfaces and solid solutions (SS). By systematically varying the concentration, distribution, and charge state of Ti incorporated in a α-Fe_2O_3 host, we explore different scenarios for the charge compensation mechanism and its consequences for the magnetic and electronic behavior. Finally, we compile a phase diagram of the stability of the different configurations with respect to the end members as a function of Ti doping by also taking the effect of strain into account.

Our DFT-GGA[25] calculations are performed by using the all-electron full-potential augmented plane waves method, as

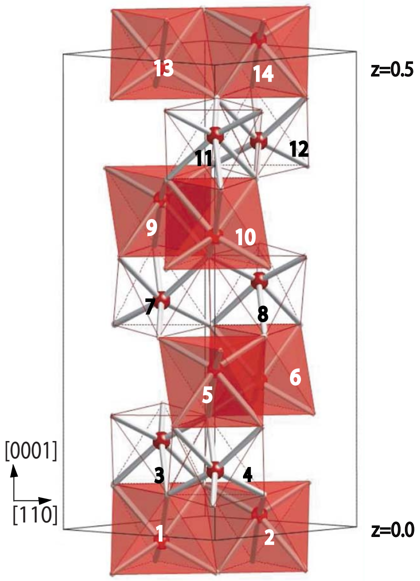

FIG. 1. (Color online) Crystal structure of $FeTiO_3$ showing half of the 60-atom unit cell. The cation sites are numbered and oxygen occupies the edges of the octahedra.

TABLE I. Relative stability (eV/60-atom cell) of the different cation arrangements in the Ti^{4+}, Fe^{2+}, Fe^{3+} charge state (strained at the Fe_2O_3 lattice parameters) with respect to the most stable configuration, whose energy is set to 0.0 eV. The positions occupied by Ti are denoted as subscripts according to Fig. 1 (SSL: spin sublattice). The total magnetic moment, electronic behavior (hm and m denote half-metallic and metallic, respectively), as well as the Ti^{4+}-O and Fe^{2+}-O distances at the interface are also displayed.

System	ΔE (eV)	$d_{Ti^{4+}-O}$ Å	$d_{Fe^{2+}-O}$ Å	M_{tot} (μ_B)	Δ (eV)
Ilm_{17}					
$T_{1,2}$: 1 Ti layer	0.0	1.90	2.08	−8.0	hm
T_7: single impurity	0.20	1.93	2.02	12.0	hm
Ilm_{33}					
$T_{1,2,13,14}$: 1 Ti layer	0.36	1.90	2.08	−16.0	hm
$T_{3,4}$: 2 Ti layers	0.00	1.89	2.08	16.0	hm
$T_{5,10}$: same SSL	0.19	1.86	2.04	−16.0	hm
$T_{5,7}$: different SSL	0.41	1.92	2.02	0.0	m
$T_{5,8}$: different SSL	1.24	1.86	2.06	0.0	hm
Ilm_{50}					
$T_{1,2,5,6}$: 3 Ti layers	0.00	1.90	2.07	−24.0	hm
$T_{3,4,7}$: Ti-Fe@IF	1.23	1.96	2.00	8.0	hm
Ilm_{66}					
$T_{3,4,11,12}$: 4 Ti layers	0.00	1.90	2.07	16.0	hm
$T_{3,6,9,12}$: SS	0.95	1.92	2.02	0.0	hm

implemented in WIEN2K.[26] Electronic correlations are considered within the fully localized limit (LDA+U).[24] The systems are modeled in the hexagonal primitive unit cell (shown in Fig. 1) containing 30 and 60 atoms. For these, 24 and 15 k points in the irreducible part of the Brillouin zone were used, respectively. Inside the muffin tins ($R_{MT}^{Fe,Ti}=1.80$ bohr, $R_{MT}^{O}=1.60$ bohr) wave functions are expanded in spherical harmonics up to $l_{max}^{wf}=10$ and nonspherical contributions to the electron density and potential up to $l_{max}^{pot.}=6$ are used. The energy cutoff for the plane wave representation in the interstitial is $E_{max}^{wf}=19$ Ry for the wave functions and $E_{max}^{pot.}=196$ Ry for the potential. These convergence parameters ensure a numerical accuracy of energy differences better than 0.01 eV/60-atom cell. A full structural optimization of internal parameters within GGA+U[27] has been performed.

As a starting point, we have modeled the end members Fe_2O_3 and $FeTiO_3$. In agreement with previous calculations,[22,28] GGA+U considerably improves the band gap of hematite from 0.43 eV (GGA) to 2.2 eV for $U=6$ eV and $J=1$ eV in close agreement with measured values of 2.14–2.36 eV.[29,30] Also, the type of band gap changes from a Mott–Hubbard between Fe3d-Fe3d states to charge transfer after the scheme of Zaanen *et al.*[31] between occupied O 2p and empty Fe 3d states.

For ilmenite, the GGA incorrectly predicts a metallic state;[32] hence, the inclusion of Hubbard U ($U=8$ eV, $J=1$ eV) is decisive to obtain a Mott–Hubbard gap of 2.18 eV ($\Delta^{exp}=2.54$ eV[9]) between the occupied Fe d_{z^2} orbital and the unoccupied Fe 3d states in one spin channel (all Fe 3d orbitals being occupied in the other spin channel). These U and J values are used both on Fe and Ti in the following: A Fe^{3+}/Ti^{3+} charge arrangement lies 0.63 eV/p.f.u. above the ground state Fe^{2+}/Ti^{4+}. For $Fe^{2+}Ti^{4+}O_3$, the AFM and FM couplings between Fe layers are nearly degenerate, which is consistent with the low T_N.

In the following, we vary the concentration and distribution of Ti in a Fe_2O_3 host. The positions of the Ti ions are given as subscripts and follow the notation in Fig. 1, e.g., $T_{3,4,7,8,11,12}$ describes pure ilmenite. Table I contains the energetic stability, structural, magnetic, and electronic properties of different cation arrangements and concentrations. We start the discussion with Ilm_{33}, which corresponds to four Ti ions out of 24 cations in the 60-atom cell. We find that the formation of a compact ilmenite-like block with a Fe layer sandwiched between two Ti layers ($T_{3,4}$) is 0.36 eV more favorable than the incorporation of the single Ti layers in the hematite host ($T_{1,2,13,14}$). The spin density of $T_{3,4}$ plotted in Fig. 2(a) shows that the central Fe layer turns into Fe^{2+} and the charge mismatch at the IF is compensated by Fe^{2+}, Fe^{3+} in the contact layer, which gives theoretical evidence from first principles for the lamellar magnetism hypothesis of Robinson *et al.*[20] Our GGA+U calculations show that Ti_4^{4+} shares faces with Fe_5^{3+}, while Fe_6^{2+} shares faces with Fe_8^{3+} from the next hematite layer. Such a configuration was proposed by using bond-valence sums[33] and kMC simulations[34] only after considering both chemical and magnetic interactions.

The formation of layered arrangements ($T_{3,4}$) is favored compared to a more random distributions with 50% substituted cation layers (e.g., $T_{5,10}$, $T_{5,7}$, or $T_{5,8}$). With respect to magnetism, each Ti ion adds a magnetic moment of $4\mu_B$ independent of whether the extra electron is localized at Ti (Ti^{3+}) or at a neighboring Fe (Fe^{2+}). In solid solutions, the total magnetic moment depends on the site and sublattice

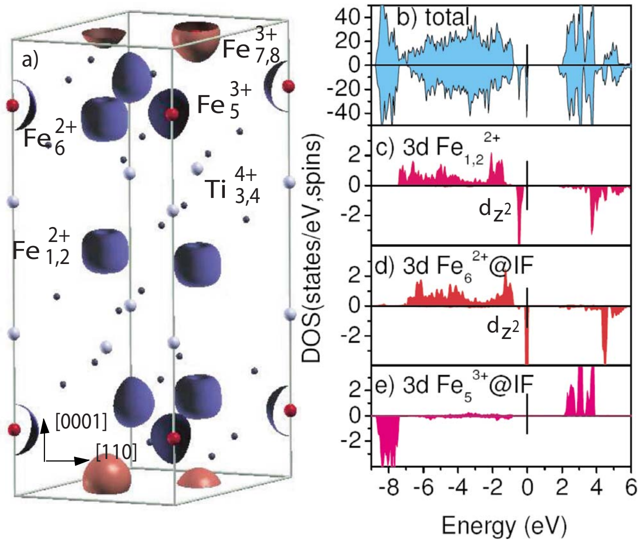

FIG. 2. (Color online) (a) Spin density distribution and [(b)–(e)] total and projected density of states of Ti double layer in hematite ($T_{3,4}$) with $Fe^{2+}_{1,2}$, $Ti^{4+}_{3,4}$ and a disproportioned Fe^{3+}_{5}, Fe^{2+}_{6} layer at the interface. The position of the Fermi level is set to 0.0 eV and denoted by a short line. In (a), positions of Ti, Fe, and O are marked by the light gray, red (dark gray), and small black circles, respectively.

where Ti is built in. We find that incorporation in the same spin-sublattice $T_{5,10}$ (which maximizes the magnetic moment) is favored by 0.22 eV compared to the AFM $T_{5,7}$. Taking local lattice relaxations into account enhances the energy gain compared to previous calculations by Velev *et al.*[22] (0.08 eV). Still, some degree of Ti disorder is likely in quickly cooled samples, which reduces the expected magnetization as observed by Chambers *et al.*[3] ($0.5 \pm 0.15 \mu_B/\text{Ti}$ for $x_{\text{Ti}}=0.15$). For higher Ti concentrations and longer annealing steps, the formation of the thermodynamically more stable layered ferrimagnetic phase is expected, which is consistent with the strong correlation between cation order and ferrimagnetism found in annealed samples[8,12] and the saturation magnetization of $3\mu_B/\text{mol}$ measured in epitaxial films with $x_{\text{Ti}} \leq 0.63$.[13] Below the ordering temperature of ilmenite, only ilmenite lamella with an odd number of Ti layers are expected to carry a nonzero magnetization, whereas, above 56 K, the net magnetic moment will be solely due to the uncompensated magnetic moments in the contact layers, which is independent of the number of Ti layers within the paramagnetic ilmenite lamella.

Concerning the electronic properties, doping Fe_2O_3 with Ti leads to impurity levels in the band gap arising from the occupied d_{z^2} orbital of Fe^{2+} ions in the contact layer. The density of states plotted in Fig. 2(d) shows that these states are pinned at the Fermi level, which leads to fully spin-polarized carriers and half-metallic behavior for $T_{3,4}$. This trend is robust with respect to U (Ref. 35) and is observed for most of the studied cation concentrations and arrangements after structural relaxation. Experimentally, a semiconducting behavior and a drop in resistivity of several orders with respect to the end members is measured.[3,9,12,13] The measured values suggest localized rather than itinerant carriers consistent with the picture, we obtain from LDA+U.

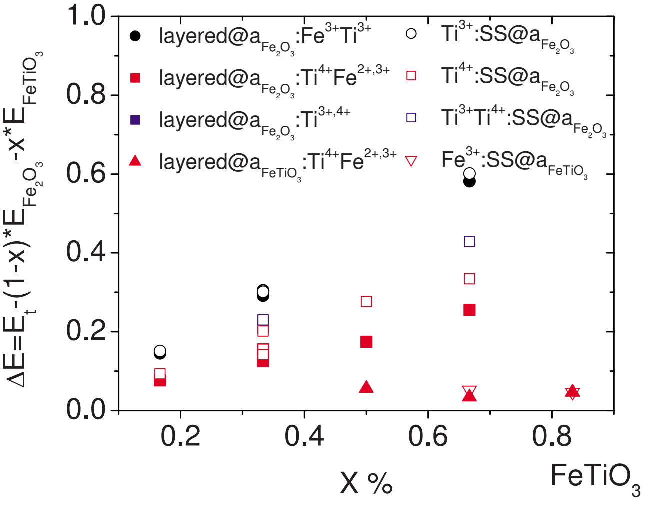

FIG. 3. (Color online) Formation energy (eV/p.f.u) with respect to the end members as a function of ilmenite concentration x. Layered arrangements (solid solutions) are denoted by the full (open) symbols.

Next, we turn to the energetic stability as a function of the Ti concentration displayed in Table I and the phase diagram in Fig. 3. Charge compensation through Ti^{4+} and disproportionation of iron into Fe^{2+}, Fe^{3+} is strongly favored compared to compensation involving Ti^{3+}, especially after optimization of the internal structural parameters. Moreover, the formation of layered configurations (full symbols) is preferred over disordered arrangements (empty symbols) except for very high (>83%) and very low concentrations (<17%), which is consistent with the miscibility gap from thermodynamic data (e.g., Refs. 21 and 36). The linear increase in formation energy in the range between Ilm_{17} and Ilm_{66} indicates that straining Ti doped Fe_2O_3 to the Fe_2O_3 lattice parameters gets increasingly unfavorable with growing x. On the other hand, using the ilmenite lattice parameters at $x=66\%$ instead of hematite (volume increase of 8.7%) leads to an energy gain of 0.22 eV/p.f.u. for $T_{7,8,11,12}$ (red filled up triangles in Fig. 3).

An interesting trend is observed in the shortest cation-oxygen bond lengths (cf. Table I), which tend to relax toward the values in the respective end member. While $d_{Fe^{3+}-O}$ (not shown) remains close to the value in bulk hematite (1.96 Å), the bond lengths of the Ti impurity and the neighboring Fe^{2+} relax toward the values in bulk ilmenite (1.92 and 2.07 Å, respectively).

In Fe doped ilmenite, the trend toward layered arrangements is retained for 66%, e.g., $T_{7,8,11,12}$ is favored by 0.21 eV compared to $T_{3,8,11,12}$, but ordered and disordered phases are nearly degenerate at 83%. Fe substituting for Ti in the ilmenite lattice is Fe^{3+}. Additionally, one Fe in the neighboring layer turns Fe^{3+} to compensate the charge, which forms a Fe^{2+}, Fe^{3+} contact layer. The substituted Fe shows a strong tendency to couple antiparallel to the neighboring Fe layers.

In summary, we present a comprehensive GGA+U study of the cation, charge, and magnetic order in the hematite-ilmenite system, which shows a strong preference toward formation of layered configurations as opposed to solid solutions. At the interface between hematite and ilmenite blocks, we find evidence for the lamellar magnetism hypothesis[20] with a disproportionated Fe^{2+}, Fe^{3+} contact layer to accommodate the polar discontinuity. These uncompensated moments lead to the ferrimagnetic behavior of the system. The d_{z^2} orbital in one spin channel (all d orbitals being occupied in the other) at the Fe^{2+} sites in the contact layer crosses the Fermi level leading to half-metallic behavior in most of the studied compositions. The ferrimagnetism emerging at the interface of two antiferromagnetic oxides such as hematite and ilmenite is an impressive example of the novel functionality that can arise as a consequence of a polar discontinuity and the richer possibilities to compensate it that complex oxides offer.[37,38] Recently, an exchange bias of more than 1 T was reported in this system.[39] Further phenomena such as oscillatory exchange coupling and spin-polarized transport remain to be explored in controlled epitaxial $\mathrm{Fe_2O_3}$-$\mathrm{FeTiO_3}$ multilayers on the route to possible device applications.

We gratefully acknowledge discussions with M. Winklhofer, W. Moritz, R. Harrison, P. Robinson, and S. McEnroe as well as funding by the DFG (Grant No. Pe883/4-1) and ESF within the European Mineral Science Initiative (EuroMinSci). Simulations were performed on the high performance supercomputer at the Leibniz Rechenzentrum.

---

*pentcheva@lrz.uni-muenchen.de

[1] J. M. D. Coey, M. Venkatesan, and C. B. Fitzgerald, Nat. Mater. **4**, 173 (2005).

[2] A. H. MacDonald, P. Schiffer, and N. Samarth, Nat. Mater. **4**, 195 (2005).

[3] S. A. Chambers *et al.*, Mater. Today **9**, 28 (2006).

[4] S. Kuroda *et al.*, Nat. Mater. **6**, 440 (2007).

[5] A. Ohtomo *et al.*, Nature (London) **419**, 378 (2002).

[6] A. Brinkman *et al.*, Nat. Mater. **6**, 493 (2007).

[7] N. Reyren *et al.*, Science **317**, 1196 (2007).

[8] Y. Ishikawa and S. Akimoto, J. Phys. Soc. Jpn. **12**, 1083 (1957).

[9] Y. Ishikawa, J. Phys. Soc. Jpn. **13**, 37 (1958).

[10] C. M. Carmichael, Proc. R. Soc. London, Ser. A **263**, 508 (1961).

[11] T. Kasama *et al.*, Earth Planet. Sci. Lett. **224**, 461 (2004).

[12] Y. Takada *et al.*, J. Magn. Magn. Mater. **310**, 2108 (2007).

[13] H. Hojo *et al.*, Appl. Phys. Lett. **89**, 142503 (2006).

[14] D. A. Perkins and J. P. Attfield, J. Chem. Soc., Chem. Commun. **4**, 229 (1991).

[15] R. J. Harrison, S. A. T. Redefern, and R. I. Smith, Am. Mineral. **85**, 194 (2000).

[16] L. M. Sandratskii and J. Kübler, Europhys. Lett. **33**, 447 (1996).

[17] I. J. Dzyaloshinsky, Phys. Chem. Solids **4**, 241 (1958).

[18] T. Moriya, Phys. Rev. **120**, 91 (1960).

[19] P. F. McDonald *et al.*, J. Appl. Phys. **69**, 1104 (1991).

[20] P. Robinson *et al.*, Nature (London) **418**, 517 (2002).

[21] B. P. Burton, A. Chaka, and D. J. Singh, Phase Transitions **78**, 239 (2005).

[22] J. Velev, A. Bandyopadhyay, W. H. Butler, and S. Sarker, Phys. Rev. B **71**, 205208 (2005).

[23] T. Droubay, K. M. Rosso, S. M. Heald, D. E. McCready, C. M. Wang, and S. A. Chambers, Phys. Rev. B **75**, 104412 (2007).

[24] V. I. Anisimov, I. V. Solovyev, M. A. Korotin, M. T. Czyzyk, and G. A. Sawatzky, Phys. Rev. B **48**, 16929 (1993).

[25] J. P. Perdew, K. Burke, and M. Ernzerhof, Phys. Rev. Lett. **77**, 3865 (1996).

[26] P. Blaha, K. Schwarz, G. K. H. Madsen, D. Kvasnicka, and J. Luitz, WIEN2k, An Augmented Plane Wave+Local Orbitals Program for Calculating Crystal Properties (Technical University Wien, Austria, 2001), ISBN3-9501031-1-2.

[27] F. Tran, J. Kunes, P. Novak, P. Blaha, and L. D. Marks (unpublished).

[28] G. Rollmann, A. Rohrbach, P. Entel, and J. Hafner, Phys. Rev. B **69**, 165107 (2004).

[29] D. Benjelloun *et al.*, Mater. Chem. Phys. **10**, 503 (1984).

[30] R. H. Chang and J. B. Wagner, J. Am. Ceram. Soc. **55**, 211 (1972).

[31] J. Zaanen, G. A. Sawatzky, and J. W. Allen, Phys. Rev. Lett. **55**, 418 (1985).

[32] N. C. Wilson, J. Muscat, D. Mkhonto, P. E. Ngoepe, and N. M. Harrison, Phys. Rev. B **71**, 075202 (2005).

[33] P. Robinson, R. J. Harrison, and S. A. McEnroe, Am. Mineral. **91**, 67 (2006).

[34] R. J. Harrison, Am. Mineral. **91**, 1006 (2006).

[35] The same half-metallic behavior is also obtained for a lower U value of 6 eV.

[36] S. A. McEnroe *et al.*, Geophys. J. Int. **151**, 890 (2002).

[37] R. Pentcheva and W. E. Pickett, Phys. Rev. B **74**, 035112 (2006).

[38] R. Pentcheva and W. E. Pickett, Phys. Rev. Lett. **99**, 016802 (2007).

[39] S. A. McEnroe *et al.*, Nat. Nanotechnol. **2**, 631 (2007).

JOURNAL OF APPLIED PHYSICS **106**, 073912 (2009)

Effect of strain on the stability and electronic properties of ferrimagnetic $Fe_{2-x}Ti_xO_3$ heterostructures from correlated band theory

Hasan Sadat Nabi and Rossitza Pentcheva[a]
Department of Earth and Environmental Sciences, University of Munich, Theresienstr. 41, 80333 Munich, Germany

(Received 13 June 2009; accepted 1 September 2009; published online 13 October 2009)

Based on density functional theory calculations including an on-site Hubbard U term, we investigate the effect of substrate-induced strain on the properties of ferrimagnetic hematite-ilmenite solid solutions and heterostructures. While the charge compensation mechanism through formation of a mixed Fe^{2+}, Fe^{3+}-contact layer is unaffected, strain can be used to tune the electronic properties of the system, e.g., by changing the position of impurity levels in the band gap. Straining $Fe_2O_3-FeTiO_3$ films at the lateral lattice parameters of $Al_2O_3(0001)$, commonly used as a substrate, is found to be energetically unfavorable as compared to films on $Fe_2O_3(0001)$ or $FeTiO_3(0001)$-substrates. © *2009 American Institute of Physics*. [doi:10.1063/1.3243083]

I. INTRODUCTION

In the fabrication of ferromagnetic semiconductors for spintronics applications a lot of research focuses on the homogeneous doping of conventional or oxide semiconductors with 3*d* ions.[1–4] However, the coupling between magnetic impurities and charge carriers is often too weak, leading to Curie temperatures (T_C) way below room temperature (RT). On the other hand, materials such as $Fe_{2-x}Ti_xO_3$ exhibit intrinsic semiconducting and ferrimagnetic properties, although the end members α-Fe_2O_3 and $FeTiO_3$ are antiferromagnetic insulators with $T_N=948$ and 56 K, respectively. Besides applications in spintronics, this material is also discussed in paleomagnetism as a possible cause of anomalies in Earth's magnetic field, as well as for electronics devices (e.g., varistors) because it is a wide band gap semiconductor that can be either *n*- or *p*-type depending on the doping concentration.[5] A Curie temperature above RT and a reduction in resistivity were observed in synthetic solid solutions (SSs) with Ti concentrations up to 70%.[6,7] Moreover, T_C was found to increase upon annealing both in these samples and in thin epitaxial films.[8] This behavior can be attributed to cation ordering phenomena related to a miscibility gap in the rather complex phase diagram of the system.[9]

The origin of ferrimagnetic behavior remained unclear until recently. Both materials have a corundum (-related) structure (see Fig. 1) with a stacking of $2Fe^{3+}/3O^{2-}$ in hematite (space group $R\bar{3}c$) and $2Fe^{2+}/3O^{2-}/2Ti^{4+}/3O^{2-}$ in ilmenite ($R\bar{3}$) along the [0001]-direction. Thus at an interface or in a SS, charge is not compensated, if all ions preserved their bulk valence states. Density functional theory (DFT) calculations considering correlation effects within LDA+U (Ref. 10) showed that the charge mismatch is accommodated by a mixed Fe^{3+}, Fe^{2+} contact layer at the interface,[11] providing first theoretical evidence for the *lamellar magnetism hypothesis*.[12] The Fe^{2+}-ions at the interface give rise to uncompensated moments and also to impurity states in the band gap.

The incorporation of Ti in hematite[13] ($a=5.04$ Å, $c=13.75$ Å) introduces a substantial strain: The volume of the end member ilmenite[14] ($a=5.18$ Å, $c=14.27$ Å) is 9.7% larger than the one of hematite. Indeed, lens-shaped dark contrasts around nanoscale hematite lamellae in an ilmenite host, imaged by transmission electron microscopy, indicate significant strain fields.[12]

Epitaxial $Fe_{2-x}Ti_xO_3$ films[5,8,15–18] are typically grown on an $Al_2O_3(0001)$-substrate ($a=4.76$ Å, $c=12.99$ Å), which introduces substantial compressive strains of 5.8% and 8.8% compared to Fe_2O_3 and $FeTiO_3$ and only rarely, a Cr_2O_3-buffer layer is used[19] to reduce the lattice mismatch.

Epitaxial strain can have a strong impact on the film

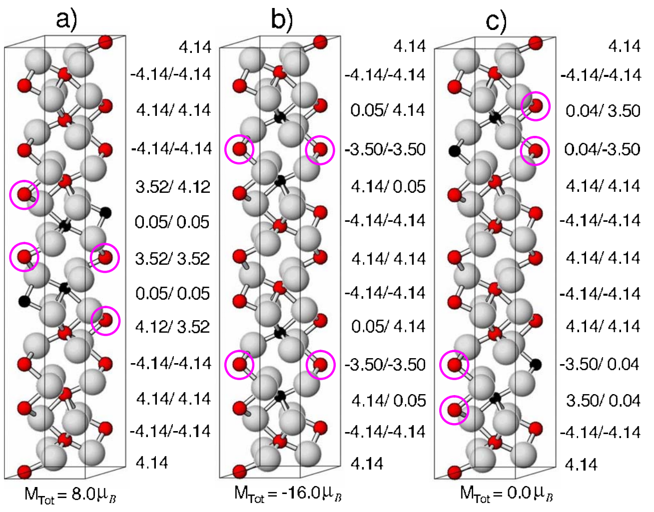

FIG. 1. (Color online) Crystal structure of the 60-atom unit cell of $Fe_{2-x}Ti_xO_3$ for $x=0.33$ with (a) a layered and more homogeneous arrangement of the Ti-cations with Ti in the (b) same and (c) different spin sublattices. Oxygen, Fe, and Ti are shown with light gray, red (gray), and black spheres, respectively. Pink (gray) circles mark the Fe^{2+}-positions, while the rest of the iron are Fe^{3+}. The local magnetic moments at the cation sites and the total magnetization of the system in μ_B are given on the right side and bottom of each configuration, respectively.

---

[a] Electronic mail: pentcheva@lrz.uni-muenchen.de.

0021-8979/2009/106(7)/073912/4/$25.00

properties, e.g., by tuning the magnetic interactions in magnetoelastic composites,[20] enhancing ferroelectricity[21,22] or even inducing orbital reconstructions.[23] The goal of the present study is to explore the effect of strain on the properties of $Fe_{2-x}Ti_xO_3$. In particular we address its influence on (i) the energetic stability and compensation mechanism as well as on (ii) the electronic, magnetic, and structural properties of the system. DFT calculations are performed on SS and layered configurations with $x=0.17$, 0.33, 0.50 and 0.66, strained laterally at the lattice parameters of Al_2O_3, Fe_2O_3, and $FeTiO_3$.

II. CALCULATIONAL DETAILS

We use the all-electron full-potential linear augmented plane wave method as implemented in the WIEN2K code[24] and the generalized gradient approximation (GGA).[25] Within LDA+U (Ref. 10) $U=8.0$ eV and $J=1.0$ eV are applied to the Fe and Ti $3d$ states. These values were found to reproduce correctly the ground state of $FeTiO_3$.[11] The systems are simulated in a hexagonal unit cell with 60 atoms (Fig. 1). Besides the layered configurations [cf. Fig. 1(a)] more homogeneous distributions are generated by substituting 50% of Fe in a bilayer by Ti, as shown, e.g., in Figs. 1(b) and 1(c). For further details on the calculation see (Ref. 11).

III. RESULTS AND DISCUSSION

The optimized c/a-ratio and volume [Figs. 2(a) and 2(b)] show a linear increase with x_{Ilm} in accordance with Vegard's law, similar to what was observed experimentally in synthetic hematite-ilmenite SSs.[6] Furthermore, for a given concentration both c/a and V are largely independent of the distribution of Ti-impurities. The c/a-ratio of bulk $FeTiO_3$ (2.76) is slightly larger than the one for α-Fe_2O_3 and Al_2O_3 (2.73). Due to the small tensile/compressive strain when using $a_{FeTiO_3}/a_{Fe_2O_3}$ the c/a-ratio of $Fe_{2-x}Ti_xO_3$ is slightly reduced (−1.1% to −2.8%)/increased (3.1%–5.2%), respectively. In contrast, due to the high compressive strain on an Al_2O_3-substrate, c/a increases strongly by 14.7%–16.6%, which corresponds to $c_{\text{rel}}=14.89-15.15$ Å. Nevertheless, the volume does not completely relax: The volume of the system strained at the Al_2O_3-lateral lattice constant is 6.8% (10.2%) smaller than when strained at $a_{Fe_2O_3}$ (a_{FeTiO_3}). The volumes of $Fe_{2-x}Ti_xO_3$ strained at a_{FeTiO_3} and $a_{Fe_2O_3}$ lie between the ones for the end members Fe_2O_3 and $FeTiO_3$.

X-ray diffraction data for $Fe_{2-x}Ti_xO_3$ films on $Al_2O_3(0001)$ (Refs. 26 and 27) indicate significant lateral strain relaxation: already in a 10 nm thick film a relaxes to the bulk value of $FeTiO_3$ with only a small change in c/a [see Fig. 2(a)]. The c/a values and volumes obtained by Takada *et al.*[27] are in good agreement with the DFT values of the systems strained at a_{FeTiO_3}.

Next we turn to the influence of strain on the energetic stability. The formation energy with respect to the end members as a function of x_{Ilm} is shown in Fig. 2(c) for the three different substrate lattice constants. For each Ti-concentration we have considered several different cation arrangements, e.g., for $x=0.33$ these include an ordered arrangement with an Fe-layer sandwiched between two Ti-layers [Fig. 1(a)] or SSs with Ti ions either in the same [Fig. 1(b)] or different spin sublattices [Fig. 1(c)]. We find that compensation through Ti^{4+} and disproportionation in Fe^{2+}, Fe^{3+} is more favorable over mechanisms involving Ti^{3+}. Furthermore, the formation energy increases linearly with x_{Ilm}. These features are independent of the substrate lattice parameters. Systems strained laterally at a_{FeTiO_3} are more stable than the ones on $a_{Fe_2O_3}$. In contrast, the formation energy of films strained at $a_{Al_2O_3}$ increases by 0.7 eV as compared to films on $a_{Fe_2O_3}$. This implies that the strong compressive strain is energetically unfavorable and gives a possible explanation why a lateral strain relaxation occurs in $Fe_{2-x}Ti_xO_3$ films.[26,27] While for systems strained on hematite and ilmenite substrates layered arrangements (full symbols) are more favorable than homogeneous distributions (open symbols), the trend is reversed for $x=0.33$ and $x=0.66$ on an $Al_2O_3(0001)$-substrate.

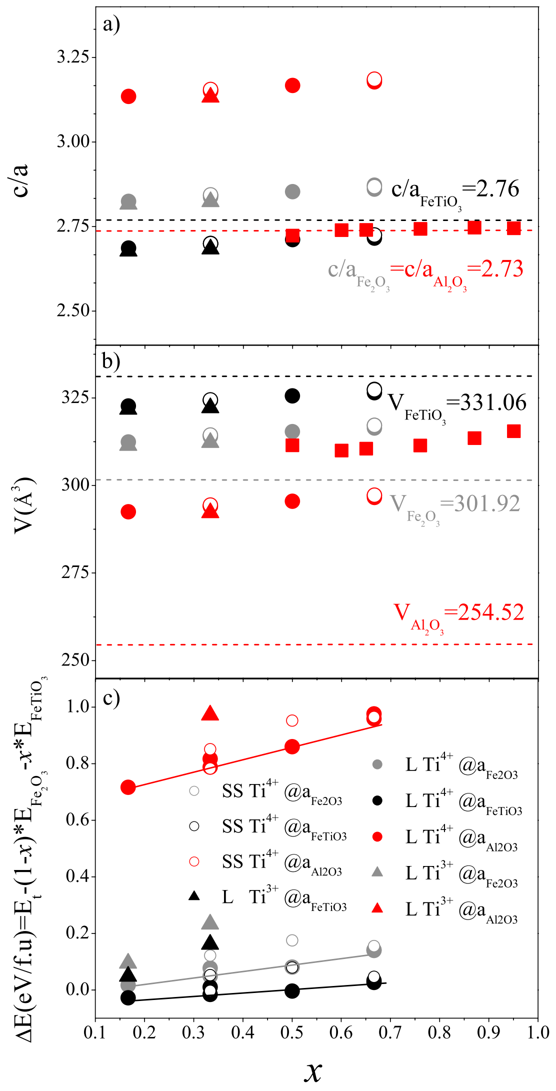

FIG. 2. (Color online) (a) c/a-ratio, (b) volume, and (c) formation energy (eV/f.u.) vs ilmenite concentration x_{Ilm} for $Fe_{2-x}Ti_xO_3$ strained at the Al_2O_3 (red/dark gray), Fe_2O_3 (gray), and $FeTiO_3$ (black) lateral lattice constants. Circles (triangles) denote compensation involving Ti^{4+}(Ti^{3+}). Open/filled symbols refer to SSs/layered configurations (l). Horizontal lines mark the bulk c/a ratio and volume of the end members and Al_2O_3. Red (dark gray) squares indicate experimental data from Ref. 27.

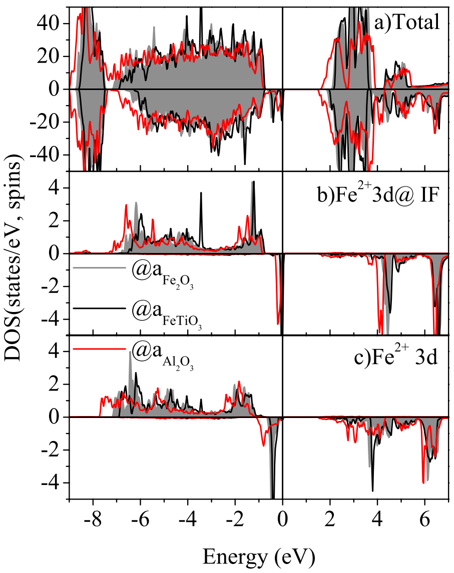

FIG. 3. (Color online) Density of states of $Fe_{1.67}Ti_{0.33}O_3$ containing two Ti-layers in a hematite host [shown in Fig. 1(a)]: (a) Total; (b) and (c) projected of the 3d states of Fe^{2+} at the interface and between the two Ti-layers. The DOS of the system strained at the lateral lattice parameters of Fe_2O_3, Al_2O_3, and $FeTiO_3$ is shown with a gray shaded area, red (dark gray), and black lines, respectively.

Concerning the electronic properties of the hemoilmenite system, we have plotted in Fig. 3 the density of states of a Ti-double layer in a hematite host [Fig. 1(a)], but similar behavior is observed for all studied systems. Upon Ti^{4+} substitution, an iron ion from the neighboring layer turns Fe^{2+}, as observed also for isolated impurities by Velev *et al.*[28] The $Fe^{2+}O_6$ and the TiO_6-octahedron are corner (and not face) sharing. The so formed Fe^{2+}-ions in the contact layer have an impurity state of a_{1g} symmetry (d_{z^2}) that is pinned at the Fermi level for systems strained at $a_{Fe_2O_3}$ and a_{FeTiO_3}. Such a midgap state was recently reported from x-ray valence band photoemission[29] and optical measurements,[17] although it was related to the low oxygen pressure during deposition. The main feature related to strain is the change in bandwidth: While for tensile strain at a_{FeTiO_3} the bands are narrowed, for compressive strain at $a_{Al_2O_3}$ they are strongly broadened. This results in a reduction in the band gap (between the impurity state defining the Fermi level and the bottom of the conduction band) from 1.90 eV for a_{FeTiO_3} and 1.79 eV for $a_{Fe_2O_3}$ to 1.43 eV for $a_{Al_2O_3}$. The corresponding values for $x=66\%$ show the same trend but are smaller: 1.64 eV for a_{FeTiO_3} and 1.46 eV for $a_{Fe_2O_3}$ to 0.78 eV for $a_{Al_2O_3}$.

The local magnetic moments and total magnetization for the three systems with $x=0.33$ are displayed in Fig. 1. Strain has only a small impact on the magnetic moments of Fe^{2+} ($\sim 3.5\mu_B$) and Fe^{3+} ($\sim 4.1\mu_B$), respectively, which are reduced by less than $0.05\mu_B$ at $a_{Al_2O_3}$. The Fe^{2+}-layer sandwiched between two Ti-layers in Fig. 1(a) is only weakly coupled to the next Fe-layer (parallel and antiparallel orientations of the magnetic moments is nearly degenerate as in the ilmenite end member). Therefore, at temperatures above the Néel temperature of ilmenite, such layers will not contribute to the total magnetization. In contrast, Fe^{2+} in the contact layer shows a strong antiferromagnetic coupling to the neighboring Fe-layer of the hematite host. These defect interface moments are responsible for the ferrimagnetic behavior of the system ($M_{tot}=8.0\mu_B$). In SSs, Ti substitution in different spin sublattices [e.g., in adjacent layers, as shown in Fig. 1(c)], resulting in a zero net magnetization, is less favorable compared to substitution in the same spin sublattice [Fig. 1(b)], which maximizes the total magnetization ($M_{tot}=-16.0\mu_B$). This trend promotes ferrimagnetic behavior in the system.

IV. CONCLUSIONS

DFT calculations within GGA+U show that the charge compensation in hematite-ilmenite heterostructures and SSs take place through a mixed Fe^{2+}, Fe^{3+} contact layer. This mechanism is robust with respect to substrate-induced strain. For $Fe_2O_3(0001)$ or $FeTiO_3(0001)$ substrates layered arrangements are more stable than SSs. However, the compressive strain at $a_{Al_2O_3}$ is likely to cause a stronger competition and even reverse the trend for $x=0.33$ and $x=0.66$. The growth of epitaxial films on an Al_2O_3-substrate is connected with a high energy cost. Therefore, in order to release strain such films may roughen or buckle in the first layers, as recently reported by Popova *et al.*[26] In contrast, the growth on lattice matched substrates or even substrates that produce a small tensile strain like $FeTiO_3$ is energetically favored. Our DFT results indicate that strain can have a strong impact on the structural and electronic properties in the hematite-ilmenite system, e.g., by tuning the bandwidth or the position of impurity levels in the band gap and thus changing the concentration of spin-polarized carriers.

ACKNOWLEDGMENTS

Funding by the DFG (Grant No. Pe883/4-1), the ESF (EuroMinSci), and computational time at the Leibniz Rechenzentrum are gratefully acknowledged.

[1] H. Ohno, Science **281**, 951 (1998).
[2] Y. Matsumoto, M. Murakami, T. Shono, T. Hasegawa, T. Fukumura, M. Kawasaki, P. Ahmet, T. Chikyow, S. Koshihara, and H. Koinuma, Science **291**, 854 (2001).
[3] J. M. D. Coey, M. Venkatesan, and C. B. Fitzgerald, Nature Mater. **4**, 173 (2005).
[4] A. H. MacDonald, P. Schiffer, and N. Samarth, Nature Mater. **4**, 195 (2005).
[5] F. Zhou, S. Kotru, and R. K. Pandey, Thin Solid Films **408**, 33 (2002).
[6] Y. Ishikawa and S. Akimoto, J. Phys. Soc. Jpn. **12**, 1083 (1957).
[7] Y. Ishikawa, J. Phys. Soc. Jpn. **13**, 37 (1958).
[8] H. Hojo, K. Fujita, K. Tanaka, and K. Hirao, Appl. Phys. Lett. **89**, 142503 (2006).
[9] P. Robinson, R. J. Harrison, S. A. McEnroe, and R. B. Hargraves, Am. Mineral. **89**, 725 (2004).
[10] V. I. Anisimov, I. V. Solovyev, M. A. Korotin, M. T. Czyżyk, and G. A. Sawatzky, Phys. Rev. B **48**, 16929 (1993).
[11] R. Pentcheva and H. Sadat Nabi, Phys. Rev. B **77**, 172405 (2008).
[12] P. Robinson, R. J. Harrison, S. A. McEnroe, and R. B. Hargraves, Nature (London) **418**, 517 (2002).
[13] D. A. Perkins and J. P. Attfield, J. Chem. Soc., Chem. Commun. **1991**, 229.
[14] R. J. Harrison, S. A. T. Redefern, and R. I. Smith, Am. Mineral. **85**, 194 (2000).
[15] T. Fujii, M. Kayano, Y. Takada, M. Nakanishi, and J. Takada, J. Magn. Magn. Mater. **272–276**, 2010 (2004).
[16] E. Popova, B. Warot-Fonrose, H. Ndilimabaka, M. Bibes, N. Keller, B. Berini, K. Bouzehouane, and Y. Dumont, J. Appl. Phys. **103**, 093909

(2008).

[17] H. Ndilimabaka, Y. Dumont, E. Popova, P. Desfonds, F. Jomard, N. Keller, M. Basletic, K. Bouzehouane, M. Bibes, and M. Godlewski, J. Appl. Phys. **103**, 07D137 (2008).

[18] S. Kuroda, N. Nishizawa, K. Takita, M. Mitome, Y. Bando, K. Osuch, and T. Dietl, Nature Mater. **6**, 440 (2007).

[19] S. A. Chambers, T. C. Droubay, C. M. Wang, K. M. Rosso, S. M. Heald, D. A. Schwartz, K. R. Kittilstved, and D. R. Gamelin, Mater. Today **9**, 28 (2006).

[20] W. Eerenstein, J. F. Scott, and N. D. Mathur, Nature (London) **442**, 759 (2006).

[21] K. J. Choi, M. Biegalski, Y. L. Li, A. Sharan, J. Schubert, R. Uecker, P. Reiche, Y. B. Chen, X. Q. Pan, V. Gopalan, L.-Q. Chen, D. G. Schlom, and C. B. Eom, Science **306**, 1005 (2004).

[22] J. X. Zhang, Y. L. Li, Y. Wang, Z. K. Liu, L. Q. Chen, Y. H. Chu, F. Zavaliche, and R. Ramesh, J. Appl. Phys. **101**, 114105 (2007).

[23] M. Izumi, Y. Ogimoto, Y. Konishi, T. Manako, M. Kawasaki, and Y. Tokura, Mater. Sci. Eng., B **84**, 53 (2001).

[24] P. Blaha, K. Schwarz, G. K. H. Madsen, D. Kvasnicka, and J. Luitz, *WIEN2k: An Augmented Plane Wave+Local Orbitals Program for Calculating Crystal Properties* (Techn. Universität, Wien, Austria, 2001).

[25] J. P. Perdew, K. Burke, and M. Ernzerhof, Phys. Rev. Lett. **77**, 3865 (1996).

[26] E. Popova, H. Ndilimabaka, B. Warot-Fonrose, M. Bibes, N. Keller, B. Berini, F. Jomard, K. Bouzehouane, and Y. Dumont, Appl. Phys. A: Mater. Sci. Process. **93**, 669 (2008).

[27] Y. Takada, M. Nakanishi, T. Fujii, J. Takada, and Y. Muraoka, J. Appl. Phys. **104**, 033713 (2008).

[28] J. Velev, A. Bandyopadhyay, W. H. Butler, and S. K. Sarker, Phys. Rev. B **71**, 205208 (2005).

[29] T. Droubay, K. M. Rosso, S. M. Heald, D. E. McCready, C. M. Wang, and S. A. Chambers, Phys. Rev. B **75**, 104412 (2007).

PHYSICAL REVIEW B **81**, 214432 (2010)

Magnetic coupling parameters at an oxide-oxide interface from first principles: Fe_2O_3-$FeTiO_3$

Hasan Sadat Nabi,[1,*] Richard J. Harrison,[2] and Rossitza Pentcheva[1]
[1]*Department of Earth and Environmental Sciences, Section Crystallography, University of Munich, Theresienstr. 41, 80333 Munich, Germany*
[2]*Department of Earth Sciences, University of Cambridge, Downing Street, Cambridge CB2 3EQ, United Kingdom*

(Received 26 December 2009; revised manuscript received 23 April 2010; published 21 June 2010)

Charge mismatch at the interface between canted antiferromagnetic hematite (α-Fe_2O_3) and antiferromagnetic ilmenite ($FeTiO_3$) is accommodated by the formation of mixed Fe^{2+} and Fe^{3+} contact layers, leading to uncompensated magnetic moments in the system. To derive the magnetic exchange interaction parameters of the end members and interface, we map total-energy differences of collinear spin arrangements obtained from density-functional theory calculations to a Heisenberg Hamiltonian using the least-squares method. Parameters for the end members, hematite ($J_m^{3+,3+}$) and ilmenite ($J_m^{2+,2+}$) are in good agreement with the values obtained from inelastic neutron-scattering data. The magnetic interaction parameters between Fe^{2+} and Fe^{3+} ($J_m^{2+,3+}$) in the contact layer show a strong antiferromagnetic coupling to the adjacent hematite layers and thus explain the ferrimagnetism in the system.

DOI: 10.1103/PhysRevB.81.214432 PACS number(s): 75.30.Et, 75.70.Cn, 75.47.Lx, 73.20.−r

I. INTRODUCTION

The polar discontinuity has been recognized as a driving force in the emergence of unexpected electronic phases at oxide interfaces. One example is the stable room-temperature remanent magnetization observed in nanoscale intergrowths of hematite and ilmenite.[1] In this system, the valence mismatch arises at the interface due to a stacking of $2Fe^{3+}/3O^{2-}$ in hematite and $2Fe^{2+}/3O^{2-}/2Ti^{4+}$ in ilmenite. Robinson *et al.*[2] proposed that magnetism emerges due to a mixture of Fe^{2+} and Fe^{3+} at the interface. Recent density-functional theory calculations with an on-site Coulomb repulsion term have provided theoretical evidence for this compensation mechanism and the resulting interface (lamellar) magnetism.[3] The study of Robinson *et al.*[2] was based on Monte Carlo (MC) simulations that used an empirical set of magnetic interaction parameters based on the untested assumption that Fe^{3+}-Fe^{2+} interactions (for which there are no literature data) should have the same sign but lower magnitudes than the corresponding Fe^{3+}-Fe^{3+} interactions (for which literature data exist).

Obtaining accurate magnetic exchange interaction parameters is thus essential in understanding and modeling the magnetic behavior of this material. Exchange interaction parameters can be derived, for example, by fitting inelastic neutron-scattering data to the theoretical dispersion-relation expression[4,5] and magnetic susceptibility.[6] On the other hand, first-principles calculations can be very useful to extract these quantities either by fitting total-energy differences of several magnetic configurations to a Heisenberg Hamiltonian[7–10] or by using the second variation in the total energy.[11] Such methods have been applied in the past to bulk materials or impurities in diluted magnetic semiconductors.[12] In this paper, we provide magnetic interaction parameters for an oxide interface, which are not accessible, e.g., from experiment.

Both end members, hematite (α-Fe_2O_3) and ilmenite ($FeTiO_3$), crystallize in a corundumlike structure with space group $R\bar{3}c$ and $R\bar{3}$, respectively. The oxygen ions form a distorted hexagonal-closed-packed lattice and cations occupy 2/3 of the octahedral sites resulting in buckled layers. Hematite is a canted antiferromagnet below 948 K: the Fe^{3+} spins lie in the basal plane (perpendicular to the *c*-axis) with antiferromagnetic (AFM) coupling between neighboring layers. A small spin canting above the Morin temperature ($T_M=260$ K) results in a weak net magnetic moment within the basal plane. Below the Morin temperature, the orientation of spins switches to be almost parallel to the *c*-axis. Ilmenite is an antiferromagnet below $T_N=55$ K: Fe^{2+} layers separated by magnetically inert Ti^{4+} layers couple antiferromagnetically with Fe^{2+} spins oriented parallel and antiparallel to the *c*-axis.

The magnetic interaction parameters extracted here from DFT calculations for the end members, Fe_2O_3 and $FeTiO_3$ are compared with available inelastic neutron-scattering data.[13–16] Previous theoretical work on Fe_2O_3 (Ref. 17) is also discussed. The main goal of the paper is to determine the magnetic interaction parameters between Fe^{2+} and Fe^{3+} at the hematite-ilmenite interface.

Briefly, in this paper Sec. II is devoted to details of the DFT calculation. Section III describes the method applied to extract the magnetic interaction parameters. The results for the bulk phases (Fe_2O_3 and $FeTiO_3$) as well as the interface are discussed together in Secs. III A and III B with implications for the magnetic properties of the interface. The main findings are summarized in Sec. IV.

II. CALCULATIONAL DETAILS

Density-functional theory calculations have been performed using the all-electron full-potential linear augmented plane-wave method as implemented in the WIEN2K code.[18] For the exchange-correlation potential, the GGA (Ref. 19) is used and electronic correlations are considered by including a Coulomb repulsion parameter *U* within the fully localized limit of LDA (local density approximation)/GGA (generalized gradient approximation)+*U* method.[20] For hematite, $U=6$ eV and $J=1$ eV is used to reproduce the experimental band gap while for ilmenite, $U=8$ eV and $J=1$ eV is needed. Thus the latter values have been used for $FeTiO_3$ and the intermediate members. In order to explore how the value of U affects the absolute values of the magnetic interaction, we have also performed calculations with $U=6$ eV. We note that similar values are typically used to describe iron bearing oxides.[21–24] For comparison, the U values obtained from constrained LDA (Ref. 25) for magnetite are 6.2 eV for Fe^{2+} in octahedral coordination and 7.69 and 8.73 eV for Fe^{3+} in a tetrahedral and octahedral site, respectively.[26]

The systems are modeled in a hexagonal unit cell with 30 atoms for Fe_2O_3 and 60 atoms for $FeTiO_3$ and intermediate members. The muffin-tin radii are 1.80 bohrs for Fe and Ti and 1.60 bohrs for oxygen. Inside the muffin tins, wave functions are expanded in spherical harmonics up to $l_{\max}^{\mathrm{wf}}=10$ and nonspherical contributions to the electron density and potential up to $l_{\max}^{\mathrm{pot.}}=6$ are used. The energy cutoff for the plane-wave representation in the interstitial is $E_{\max}^{\mathrm{wf}}=25$ Ry for the wave functions and $E_{\max}^{\mathrm{pot.}}=196$ Ry for the potential. For hematite and the intermediate members, the lattice parameters of hematite[27] ($a=5.04$ Å, $c=13.75$ Å) are used while for ilmenite, the corresponding bulk lattice constants of ilmenite[28] ($a=5.18$ Å, $c=14.27$ Å) are used. For each spin configuration, the internal degrees of freedom are fully relaxed.[29] For the integration in reciprocal space, we have used 24 and 15 k-points in the irreducible part of Brillouin zone for hematite and ilmenite, respectively. The convergence criteria ensure a numerical accuracy of energy differences better than 0.1 mRy/60-atom cell.

III. CALCULATION OF MAGNETIC INTERACTION PARAMETERS

In order to map the total energy from the DFT calculations onto a Heisenberg Hamiltonian, we separate it into a nonmagnetic (H_0) and magnetic contribution,

$$H = H_0 - \frac{1}{2}\sum_{i,j} J_{ij}\mathbf{S}_i \cdot \mathbf{S}_j, \tag{1}$$

where the summation is over all distinct spin pairs. $\mathbf{S}_i$ is the spin vector at the ith lattice site and J_{ij} is the isotropic magnetic exchange interaction parameter between the magnetic moments on-site i and j. In the following, we use $J_{ij}=J_m^q(r_{ij})$, where the index m ranges from first to eighth neighbor and q defines the type of cations in the pair. For example, $J_m^{3+,3+}$ is an interaction between Fe^{3+}-Fe^{3+} pairs while $J_m^{2+,3+}$ is an interaction between Fe^{2+} and Fe^{3+}. $J_m^q<0(>0)$ corresponds to antiferromagnetic [ferromagnetic (FM)] coupling.

Figure 1 illustrates the magnetic pair exchange interactions which are used in our modeling. J_1 is the interlayer interaction between cations in face-sharing octahedra. J_2 is the intralayer interaction between cations in edge-sharing octahedra. J_3, J_4, and J_5 correspond to the interlayer interactions among cations with corner-sharing octahedra and J_6, J_7, and J_8 are the interactions with cations from the second-nearest layer.

Because we focus here on the properties of the Fe_2O_3-$FeTiO_3$ interface and not on the origin of spin canting of the end-member hematite which occurs above the Morin temperature, we have investigated only collinear magnetic configurations. Isotropic $J_m^q(r_{ij})$ are calculated by mapping the energy differences of these spin arrangements to the Heisenberg Hamiltonian in Eq. (1). The energy differences depend on the type of spin configuration: while some can be 10–40 mRy/30-atom cell, for hematite, the maximum energy difference between the ground-state AFM and a FM configuration is 250 mRy, consistent with the high magnetic ordering temperature of this material. The fitting of the DFT energy differences to the Hamiltonian is done by a multivariable least-squares (LS) method. The error bars for the obtained parameters from LS method are calculated within the confidence level of 0.99.

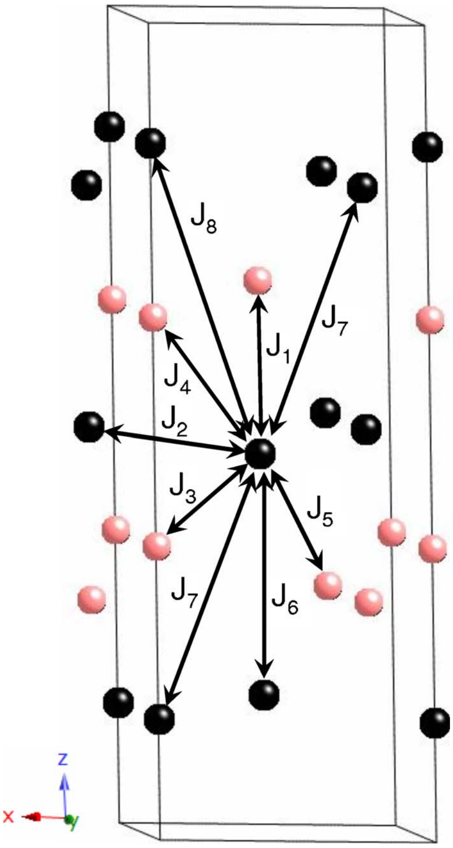

FIG. 1. (Color online) Side view of the corundum structure showing only the cation positions with alternating cationic layers denoted by light and dark atoms. Additionally, the pair magnetic exchange parameters J_1 to J_8 between the cations are defined.

A. Bulk phase: Fe_2O_3 and $FeTiO_3$

We first test the method for the end members for which we have calculated 23 and 10 different collinear spin arrangements, respectively. The calculated values for hematite ($J_m^{3+,3+}$) are displayed in Fig. 2(a) together with the values obtained from neutron scattering.[13] We find that for hematite, the dominant parameters are the interlayer magnetic interactions $J_3=-72$ K, $J_4=J_5=-50$ K. The negative sign implies a strong antiferromagnetic coupling between the Fe^{3+} layers and explains the AFM ground state of hematite. The values

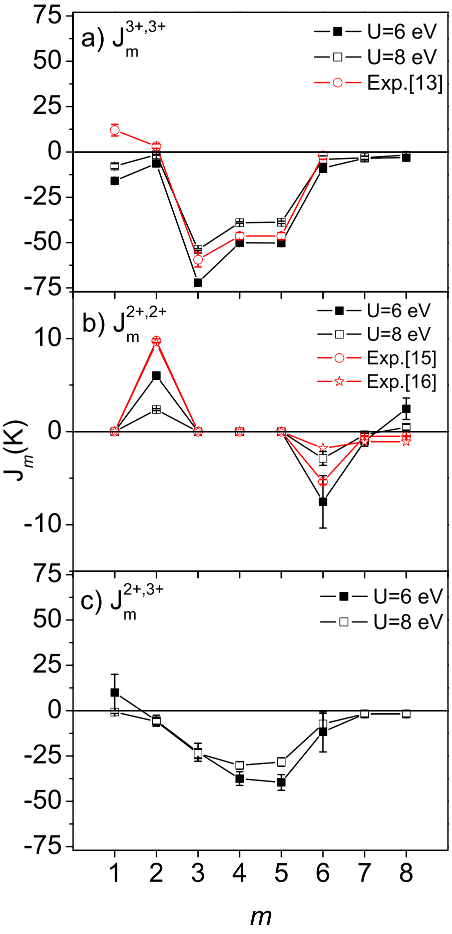

FIG. 2. (Color online) The magnetic pair interaction parameters $[J_m^q(K)]$ up to eighth neighbor are shown in (a) for hematite ($J_m^{3+,3+}$), (b) for ilmenite ($J_m^{2+,2+}$), and (c) for the interface ($J_m^{2+,3+}$). Results for $U=6$ and 8 eV are marked by filled and open squares, respectively. The experimental values for hematite (open red/gray circle) are taken from Ref. 13 and for ilmenite (open red/gray circles and stars) are taken from Refs. 15 and 16. The parameters for the interface in panel (c) are calculated for the configuration shown in Fig. 3(b).

are in good agreement both with the experimental data of Samuelsen and Shirane[13] as well as with previous LDA and LDA+U calculations by Mazurenko and Anisimov[17] who additionally took into account spin-orbit coupling. In contrast to experiment, J_1 and J_2 are found to be negative. However, both parameters are significantly smaller than J_3-J_5 and play therefore a minor role in the resulting magnetic ordering. Thus the strong interlayer AFM coupling enforces ferromagnetic coupling within each Fe^{3+} layer. Furthermore, our values support the reasoning of Goodenough[30] and Anderson[31] that cation interactions mediated by an anion (superexchange) with cation-anion-cation angles between $120°-180°$ (J_3, J_4, J_5) are negative in sign and much stronger than direct interactions between cations in face- (edge-) sharing octahedra, J_1 (J_2).

The calculated values for ilmenite ($J_m^{2+,2+}$) are shown in Fig. 2(b). In ilmenite, Fe^{2+} layers alternate with Ti^{4+} layers. Since Ti is in 4+ state (d^0), all the Fe-Ti interactions are zero (J_1, J_3, J_4, and J_5). The positive J_2 implies that magnetic interactions within the Fe^{2+} layer are ferromagnetic. On the other hand, J_6 and J_7 have a small negative value leading to an antiferromagnetic coupling with Fe in layers above and below the Ti layers. The positive J_2 and negative J_6 and J_7 determine the correct antiferromagnetic ground state for ilmenite. However, the absolute values are lower compared to the experimental ones obtained by Kato *et al.*[15,16] by fitting data at $T=12$ K to the magnon dispersion relation.

TABLE I. Néel temperature for hematite and ilmenite calculated within the MFA and from Monte Carlo simulations for $U=6$ and 8 eV.

	Monte Carlo		MFA	
Material	$U=6$ eV	$U=8$ eV	$U=6$ eV	$U=8$ eV
Fe_2O_3	1150 ± 10	910 ± 10	1416 ± 41	1107 ± 37
$FeTiO_3$	50 ± 2	15 ± 5	43 ± 18	19 ± 5

Useful comparisons with previous results for hematite can be made by calculating the Néel temperature using the mean-field approximation (MFA), defined as $k_B T^{MFA} = \frac{1}{3} S(S+1) \Sigma_m n_m J_m$, where k_B is the Boltzmann constant and n_m is the multiplicity of neighbors corresponding to J_m. It is an established fact that MFA cannot give the exact value for the transition temperature but provides a qualitative estimation. Using the MFA expression above and the spin magnetic moment of $S=5/2$ for Fe^{3+}, we obtain $T_N^{MFA}=1416 \pm 41$ K (1107 ± 37 K) for hematite with $U=6(8)$ eV, respectively (Table I). A previous DFT study[32] reported a higher value (1711 K). Both MFA values overestimate the experimental Néel temperature (953–966 K).[33] A recent LDA+DMFT (Dynamical Mean Field Theory) study obtained $T_N=1600$ K for hematite.[34] Monte Carlo simulations, following the method of Harrison[35] were used to obtain a more accurate estimate of $T_N=1150 \pm 10$ (910 ± 10) K for $U=6(8)$ eV, which are closer to the experimentally observed value. For ilmenite, the mean-field estimated temperatures using a spin magnetic moment of $S=4/2$ for Fe^{2+} with $U=6$ and 8 eV are $T_N^{MFA}=43 \pm 18$ and 19 ± 5 K. Monte Carlo (MC) simulations yielded a value of 50 ± 2 (15 ± 5) K for $U=6(8)$ eV.

The low Néel temperature for $U=8$ eV in ilmenite can be traced back to the small value of $J_2=2.4$ K, which is the interaction responsible for the ferromagnetic ordering within the Fe layers. Harrison *et al.*[36] found a value of $J_2=10.8$ K was required to obtain the correct Néel temperature for end-member ilmenite using Monte Carlo simulations, which is close to the empirical values obtained by Kato *et al.*[15,16] The low value of J_2 is likely due to the high on-site Coulomb parameter $U=8$ eV which was used in order to describe correctly the size of the band gap. Using $U=6$ eV, J_2 is significantly enhanced ($J_2=6.0$ K), resulting in a Néel temperature of 50 ± 2 K from MC simulations. A similar dependence of the magnetic interaction parameters on U is obtained for hematite and reported for Cr_2O_3.[9] For example, using $U=8$ eV instead of $U=6$ eV for hematite leads to a reduction in J_m ($m=3,4,5$) by ~20%.

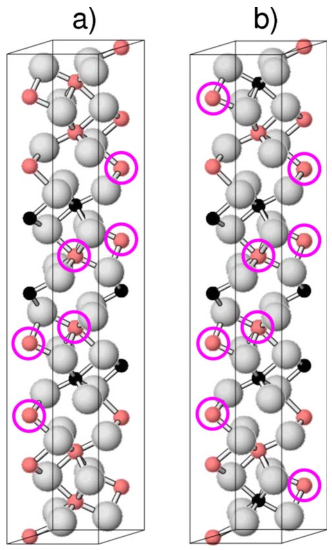

FIG. 3. (Color online) Side view of the configurations with 60 atoms in the unit cell chosen for the calculations of interface magnetic interaction parameters: (a) represents an ilmenite block (three Ti^{4+} layers separated by Fe^{2+} layers) within a hematite host and (b) contains additionally mixed Fe-Ti layers in the hematite part. The red, gray, and black spheres are showing Fe, Ti, and oxygen atoms, respectively. The positions of Fe^{2+} are marked with pink/gray circles and the rest of the iron are Fe^{3+}.

B. Magnetic interactions at the interface of Fe_2O_3 and $FeTiO_3$

As mentioned previously, a Fe^{3+} and Fe^{2+} contact layer is formed at the $Fe_2O_3/FeTiO_3$ interface as a result of the disruption of charge neutrality.[2,3] The sixth electron of Fe^{2+} occupies an a_{1g} orbital. This localized state is pinned at the Fermi level (for more details on the electronic properties, the reader is referred to Refs. 3 and 37). In order to extract the magnetic interaction parameters at the interface ($J_m^{2+,3+}$), we have considered several cation configurations. Figure 3(a) shows a heterostructure containing an ilmenite and a hematite block while Fig. 3(b) contains a layered part as well as mixed Fe-Ti layers. Because not all interaction parameters are accessible in the former (e.g., $J_{3,6}^{2+,3+}$), we have chosen the one in Fig. 3(b) to determine all $J_m^{2+,3+}$. For the latter, a total of 16 different spin arrangements were calculated.

The extracted parameters for the interface ($J_m^{2+,3+}$) together with the ones for the end members ($J_m^{3+,3+}$ and $J_m^{2+,2+}$) are displayed in Fig. 2 and Table II. Similar to hematite, we find that the dominant interaction parameters at the interface are J_3, J_4, and J_5. These have the same sign but are lower in magnitude than the corresponding Fe^{3+}-Fe^{3+} interactions. This result validates the main assumption made in previous Monte Carlo studies of the solid solution.[35,36] Although the absolute values of these interactions are generally smaller than in hematite, their negative value implies that Fe^{2+} in the contact layer couples antiferromagnetically to the next hematite layer. As a consequence, the direction of uncompensated magnetic moments at the interface will be pinned with respect to the hematite host, resulting in a ferrimagnetic behavior of the system. Monte Carlo simulations of magnetic ordering with a $4\times4\times4$ supercell were performed for the configuration in Fig. 3(a), which corresponds to the ground-state cation configuration for this bulk composition.[3] Magnetic transitions at 860 ± 10 (1080 ± 10) K were obtained in the hematite part of the heterostructure and 25 ± 5 (60 ± 5) K in ilmenite regions of the supercell with $U=8(6)$ eV, respectively, suggesting that the magnetic ordering temperature of both phases is modified by the presence of the interface.

The slight decrease in Néel temperature for hematite can be explained by the reduced strength of magnetic interactions in the contact layer ($J_m^{2+,3+}$) and a lower average number of interactions per cation due to the presence of the paramagnetic ilmenite. The increase in Néel temperature of ilmenite is likely caused by interaction of Fe^{2+} spins within the ilmenite lamellae with the magnetically ordered Fe^{2+}-Fe^{3+} spins within the contact layers.

IV. SUMMARY

The isotropic magnetic pair exchange interactions for the end members (hematite and ilmenite) are extracted from DFT calculations by mapping the total energies on a Heisen-

TABLE II. Isotropic magnetic pair exchange interactions in kelvin for hematite ($J_m^{3+,3+}$), ilmenite ($J_m^{2+,2+}$), and the interface ($J_m^{2+,3+}$) for $U=6$ and 8 eV. The index m describes the type of interaction following the definition in Fig. 1, n_m is the multiplicity of J_m. r_{ij}(Å) is the distance between the cations in each compound. Positive/negative signs of J_m^q correspond to FM/AFM coupling.

			$J_m^{3+,3+}$			$J_m^{2+,2+}$			$J_m^{2+,3+}$	
m	n_m	r_{ij} (Å)	$U=6$ eV	$U=8$ eV	r_{ij} (Å)	$U=6$ eV	$U=8$ eV	r_{ij} (Å)	$U=6$ eV	$U=8$ eV
1	1	2.86	-15.9 ± 1.6	-7.9 ± 1.4	2.92	0.0	0.0	2.84	10.0 ± 10.0	-0.8 ± 0.8
2	3	2.96	-6.3 ± 0.2	-1.5 ± 0.2	3.07	6.0 ± 0.4	2.4 ± 0.1	2.97	-5.5 ± 3.0	-5.9 ± 1.6
3	3	3.38	-72.1 ± 0.5	-53.8 ± 0.5	3.51	0.0	0.0	3.36	-23.0 ± 5.0	-23.7 ± 2.7
4	3	3.701	-50.1 ± 0.5	-39.0 ± 0.5	3.73	0.0	0.0	3.683	-37.5 ± 3.8	-30.2 ± 2.1
5	3	3.704	-50.2 ± 0.7	-38.8 ± 0.6	3.91	0.0	0.0	3.688	-39.6 ± 4.3	-28.4 ± 2.3
6	1	4.01	-9.0 ± 2.3	-4.3 ± 2.1	4.08	-7.5 ± 2.8	-2.9 ± 0.7	3.999	-11.7 ± 11.1	-7.4 ± 6.0
7	3	5.426	-3.4 ± 1.0	-3.2 ± 0.9	5.616	-1.0 ± 0.6	-0.3 ± 0.1	5.36	-1.9 ± 1.9	-1.8 ± 1.8
8	3	5.431	-3.1 ± 0.4	-1.7 ± 0.4	5.617	2.5 ± 1.2	0.5 ± 0.3	5.43	-1.9 ± 1.9	-1.8 ± 1.8

berg Hamiltonian. For hematite, we find a good agreement with experimental values from inelastic neutron-scattering data. For ilmenite, the ground state is reproduced correctly but with a weaker intralayer interaction parameter. We attribute this to the higher value of $U=8$ eV needed to obtain the experimental band gap of ilmenite. The magnetic interaction parameters between Fe^{3+} and Fe^{2+} at the interface of hematite-ilmenite, extracted here, are dominated by a strong antiferromagnetic coupling between the interfacial Fe^{2+} and Fe^{3+} from the next hematite layer, similar to the end member hematite. Although the absolute values are lower than in hematite, the negative sign fixes the orientation of defect spins at the interface leading to a ferrimagnetic behavior in the heterostructure.

ACKNOWLEDGMENTS

Funding by the DFG (Grant No. Pe883/4-1), ESF (EuroMinSci), and computational time at the Leibniz Rechenzentrum are gratefully acknowledged.

---

*hasan.sadat@lrz.uni-muenchen.de

[1] Y. Ishikawa and S. Akimoto, J. Phys. Soc. Jpn. **12**, 1083 (1957).
[2] P. Robinson, R. J. Harrison, S. A. McEnroe, and R. B. Hargraves, Nature (London) **418**, 517 (2002).
[3] R. Pentcheva and H. Sadat Nabi, Phys. Rev. B **77**, 172405 (2008).
[4] U. Falk, A. Furrer, H. U. Güdel, and J. K. Kjems, Phys. Rev. B **35**, 4888 (1987).
[5] U. Falk, A. Furrer, N. Furer, H. U. Güdel, and J. K. Kjems, Phys. Rev. B **35**, 4893 (1987).
[6] F. Mila, P. Millet, and J. Bonvoisin, Phys. Rev. B **54**, 11925 (1996).
[7] W. E. Pickett, Phys. Rev. Lett. **79**, 1746 (1997).
[8] M. P. Gelfand, Z. Weihong, R. R. P. Singh, J. Oitmaa, and C. J. Hamer, Phys. Rev. Lett. **77**, 2794 (1996).
[9] S. Shi, A. L. Wysocki, and K. D. Belashchenko, Phys. Rev. B **79**, 104404 (2009).
[10] O. Le Bacq, A. Pasturel, C. Lacroix, and M. D. Núñez-Regueiro, Phys. Rev. B **71**, 014432 (2005).
[11] A. I. Liechtenstein, M. I. Katsnelson, V. P. Antropov, and V. A. Gubanov, J. Magn. Magn. Mater. **67**, 65 (1987).
[12] S. Picozzi and M. Ležaić, New J. Phys. **10**, 055017 (2008).
[13] E. J. Samuelsen and G. Shirane, Phys. Status Solidi **42**, 241 (1970).
[14] E. J. Samuelsen and G. Shirane, J. Phys. Colloq. **32**, 1064 (1971).
[15] H. Kato, S. Funahashi, Y. Yamaguchi, M. Yamada, and H. Takei, J. Magn. Magn. Mater. **31-34**, 617 (1983).
[16] H. Kato, Y. Yamaguchi, M. Yamada, S. Funahashii, Y. Nakagawa, and H. Takei, J. Phys. C **19**, 6993 (1986).
[17] V. V. Mazurenko and V. I. Anisimov, Phys. Rev. B **71**, 184434 (2005).
[18] P. Blaha, K. Schwarz, G. K. H. Madsen, D. Kvasnicka, and J. Luitz, *WIEN2k, An Augmented Plane Wave Plus Local Orbitals Program for Calculating Crystal Properties* (Technische Universität Wien, Austria, 2001).
[19] J. P. Perdew, K. Burke, and M. Ernzerhof, Phys. Rev. Lett. **77**, 3865 (1996).
[20] V. I. Anisimov, I. V. Solovyev, M. A. Korotin, M. T. Czyžyk, and G. A. Sawatzky, Phys. Rev. B **48**, 16929 (1993).
[21] G. Rollmann, A. Rohrbach, P. Entel, and J. Hafner, Phys. Rev. B **69**, 165107 (2004).
[22] I. Leonov, A. N. Yaresko, V. N. Antonov, M. A. Korotin, and V. I. Anisimov, Phys. Rev. Lett. **93**, 146404 (2004).
[23] H.-T. Jeng, G. Y. Guo, and D. J. Huang, Phys. Rev. Lett. **93**, 156403 (2004).
[24] H. P. Pinto and S. D. Elliot, J. Phys.: Condens. Matter **18**, 10427 (2006).
[25] V. I. Anisimov and O. Gunnarsson, Phys. Rev. B **43**, 7570 (1991).
[26] G. K. H. Madsen and P. Novak, Europhys. Lett. **69**, 777 (2005).
[27] D. A. Perkins and J. P. Attfield, J. Chem. Soc., Chem. Commun. **4**, 229 (1991).
[28] R. J. Harrison, S. A. T. Redefern, and R. I. Smith, Am. Mineral. **85**, 194 (2000).
[29] F. Tran, J. Kunes, P. Novak, P. Blaha, and L. D. Marks, Comput. Phys. Commun. **179**, 784 (2008).
[30] J. B. Goodenough, Phys. Rev. **117**, 1442 (1960).
[31] P. W. Anderson, Phys. Rev. **115**, 2 (1959).
[32] L. M. Sandratskii, M. Uhl, and J. Kübler, J. Phys.: Condens. Matter **8**, 983 (1996).
[33] A. H. Morrish, *Canted Antiferromagnetism: Hematite* (World Scientific, Singapore, 1994).
[34] J. Kuneš, Dm. M. Korotin, M. A. Korotin, V. I. Anisimov and P. Werner, Phys. Rev. Lett. **102**, 146402 (2009).
[35] R. J. Harrison, Am. Mineral. **91**, 1006 (2006).
[36] R. J. Harrison, S. A. McEnroe, P. Robinson, B. Carter-Stiglitz, E. J. Palin, and T. Kasama, Phys. Rev. B **76**, 174436 (2007).
[37] H. Sadat Nabi and R. Pentcheva, J. Appl. Phys. **106**, 073912 (2009).

IOP PUBLISHING JOURNAL OF PHYSICS: CONDENSED MATTER

J. Phys.: Condens. Matter **19** (2007) 406217 (9pp) doi:10.1088/0953-8984/19/40/406217

Electronic structure and magnetism of $EuTiO_3$: a first-principles study

Rajeev Ranjan[1,2], **Hasan Sadat Nabi**[2] **and Rossitza Pentcheva**[2]

[1] School of Materials Science and Technology, Institute of Technology, Banaras Hindu University, Varanasi-221005, India
[2] Department fur Geo- und Umweltwissenschaften, Sektion Kristallographie, Ludwig Maximilians Universität, Theresienstrasse 41, 80333 München, Germany

Received 13 July 2007, in final form 21 August 2007
Published 12 September 2007

Abstract

Density-functional theory calculations were carried out for the multiferroic $EuTiO_3$ using the LDA + U approach. Total-energy calculations for ferromagnetic (F), and antiferromagnetic A-, C-, and G-type arrangements in the cubic phase shows that the ground-state magnetic configuration is G-type antiferromagnetic for $U \leqslant 6$ eV and ferromagnetic for $U \geqslant 7$ eV. Values of first- and second-neighbour exchange integrals have been calculated by mapping the energy difference between the different magnetic configurations to a Heisenberg Hamiltonian. The system seems to be critically balanced between ferromagnetic and antiferromagnetic states for realistic values of U, and switches from antiferromagnetic to a ferromagnetic ground state on hydrostatic expansion of volume.

1. Introduction

$EuTiO_3$ (ETO), like $SrTiO_3$ (STO), $KTaO_3$ (KTO) and $BaZrO_3$ (BZO), is one of the rare perovskites that exhibits cubic symmetry (space group $Pm3m$) at ambient conditions [1–3]. However, unlike the other cubic perovskites, mentioned above, ETO exhibits magnetic ordering below 5.5 K [4–6]. The dielectric permittivity of ETO also exhibits an anomaly at the magnetic ordering temperature [4], suggesting magnetoelectric coupling of the polarization and magnetization. However, compared to other well-known magnetoelectrics [7–9], ETO has been less investigated. Very recently, using first-principles technique, a design strategy for magnetic and electric phase control in epitaxial ETO has been proposed [10]. Although magnetic susceptibility measurements on ETO show features of antiferromagnetic ordering, the details of magnetic ordering have not been investigated in detail, presumably due to the fact that naturally occurring Eu has a very large absorption cross section for thermal neutrons. An old report, however, suggests a G-type antiferromagnetic (AFM) spin arrangement in ETO [5]. Magnetic susceptibility measurements have shown that ETO is one of the few antiferromagnetic materials with a positive Curie–Weiss constant ($\theta = +3.8$ K) [5]. Since the magnetic ion,

0953-8984/07/406217+09$30.00

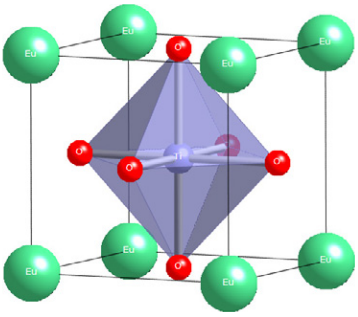

Figure 1. Crystal structure of cubic $EuTiO_3$. The corner atoms represent Eu, and the atoms at the body-centred and the face-centred positions represent Ti and O, respectively.

(This figure is in colour only in the electronic version)

Eu^{2+}, in ETO occupies the A-site of the cubic perovskite structure (see figure 1), the nearest-neighbour (nn) Eu^{2+} magnetic ions see each other directly. On the other hand, the O^{2-} ions intercept in between the next-nearest-neighbour (nnn) Eu^{2+} ions. The Eu^{2+} valency results in a half-filled 4f shell. However, due to the localized nature of the f electrons, the exchange interaction between the nn and nnn Eu^{2+} ions is only possible through mediation of the other valence electronic states. A small intra-atomic admixture of 5d wavefunctions to the 4f states has been suggested in the past [6] as a possible mechanism of exchange in Eu compounds. With advances in *ab initio* electronic structure calculations based on density-functional theory (DFT), it has become possible to explain the electronic and magnetic properties of transition metal and rare earth compounds in significant detail. In this paper we report the results of DFT calculations for ETO using an all-electron approach and taking into account electronic correlations in the LSDA + U method. The magnetic ground state of this material is found to be dependent on the U parameter. The system seems to be critically balanced between antiferromagnetic (G-type) and ferromagnetic states for realistic values of U, and switchover from one state to another is possible by tuning the volume.

2. Computational details

Density-functional theory calculations were performed using the all-electron full-potential linearized augmented-plane-wave (FPLAPW) method as implemented in the WIEN2k code [11]. The LAPW method is among the most accurate band structure methods currently available. The exchange–correlation potential is approximated by the generalized-gradient approximation (GGA) of Perdew *et al* [12]. The maximum l-value in the radial sphere expansion of the wavefunction was $l_{\mathrm{max}} = 10$, and the largest l-value for the non-spherical part of potential and density was $l_{\mathrm{max,ns}} = 6$. The cut-off energy, K^2_{max}, was fixed at 19 Ryd for the plane waves and $G_{\mathrm{max}} = 14$ for the charge density, so that no shape approximation to the potential occurs. The muffin-tin radii for Eu, Ti and O were chosen as 2.5, 1.9 and 1.6 au, respectively. We have used 30 k-points in the irreducible part of the Brillouin zone (IBZ). Increasing the number of k-points to 140 in the IBZ led to changes in total energy smaller than 0.01–0.02 mRyd. In view of the small energy difference between the various magnetic configurations, the total energy was calculated with an accuracy of 0.02 mRyd.

A Hubbard-type on-site Coulomb repulsion parameter U was used to account for the strong correlations of the f electrons of Eu, as well as to ensure an insulating behaviour of this

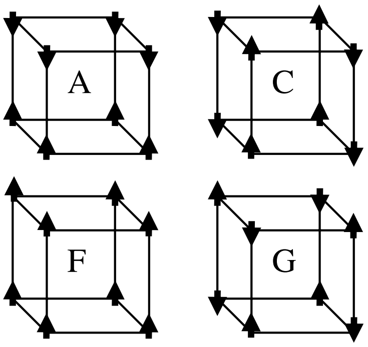

Figure 2. Schematic diagram of the four collinear magnetic structures, A, C, F, and G, considered for cubic $EuTiO_3$. The arrows indicate spin directions at the Eu sublattice.

compound in the band structure calculations [13]. Although the standard parameterization of the on-site Coulomb interaction involves two parameters, U and J, the completely filled spin-up f shell and completely empty spin-down f shell reduce the role of J to merely normalize the U value. We can, therefore, set $J = 0$ and make use of an effective U in the calculations. Recent reports of DFT calculations on some europium compounds have validated the use of this approach for divalent Eu compounds as well [14–18].

3. Results and discussion

3.1. Equilibrium lattice constant and bulk modulus

Since the structure of ETO has been reported to be cubic ($Pm3m$) down to the lowest temperature, the only variable structural parameter is the lattice parameter, a_c. In general, for cubic perovskites, different magnetically ordered structures are possible [19, 20]. Total-energy calculations for four different collinear magnetic structures, A, C, F, and G, were considered in the present study. Of these, F corresponds to the ferromagnetic structure, while the other three correspond to different antiferromagnetic spin arrangements. A schematic diagram of the four magnetic structures is shown in figure 2. For the A-type antiferromagnetic structure, the nearest-neighbour moments are ferromagnetically coupled within a defined plane, and antiferromagnetically coupled between neighbouring planes. The reverse situation occurs for a C-type antiferromagnetic structure. For a G-type antiferromagnetic structure, all the nearest-neighbour moments are antiferromagnetically coupled. For the sake of technical consistency and to minimize the numerical error, we have chosen a tetragonal unit cell with four formula units of ETO for all the four magnetic structures considered above. The lattice parameters of the tetragonal cell (a_t and c_t) are related to a_c in the following manner: $a_t = \sqrt{2}a_c$, $c_t = 2a_c$. Total-energy versus volume calculations were performed to determine the equilibrium cell volume at $U = 0$, 3, 6 and 9 eV. Figure 3 shows $E(V)$ for $U = 6$ eV. The energy differences between the various magnetic configurations are very small, and on the scale shown in this figure, the energies of the four magnetic configurations at any particular volume appear nearly degenerate. The theoretical equilibrium volume ($\sim$246.6 Å^3) is nearly insensitive to the different magnetic structures and also to the value of the U parameter used. The equivalent cubic lattice parameter, $a = (V/4)^{1/3} = 3.950$ Å, is larger than the experimentally reported value of 3.905 Å [4] by 1%.

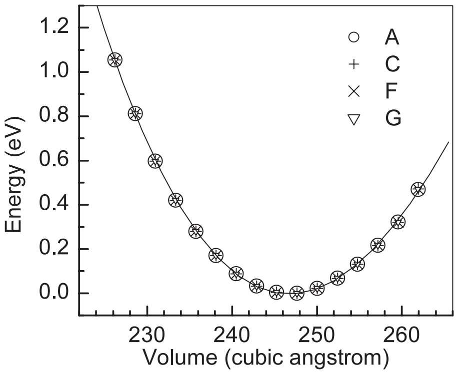

Figure 3. Total energy versus volume for F, A, C, and G magnetic structures of cubic $EuTiO_3$ calculated at $U = 6$ eV. The volume of the true cubic cell is four times smaller.

Table 1. Relative total energies of four different magnetic configurations of $EuTiO_3$ at different values of U, calculated at the experimental lattice parameter. For each U, the lowest energy has been set to zero.

Magnetic configuration	Relative total energy (meV)						
	$U = 0$ eV	$U = 3$ eV	$U = 5$ eV	$U = 6$ eV	$U = 7$ eV	$U = 8$ eV	$U = 9$ eV
F	8.4	18.1	5.5	0.9	0.0	0.0	0.0
A	22.7	17.6	8.9	4.3	3.6	3.5	3.1
C	30.8	20.9	11.5	5.9	5.0	4.3	3.6
G	0.0	0.0	0.0	0.0	2.0	3.4	3.8

The value of the bulk modulus, B_0, and its pressure derivative B_0', were obtained by fitting the Murnaghan equation of state [21, 22]:

$$E(V) = E_0 + \frac{B_0 V}{B_0'}\left(\frac{(V_0/V)^{B_0'}}{B_0' - 1} + 1\right) - \frac{B_0 V_0}{B_0' - 1} \tag{1}$$

to the calculated E–V curve. B_0 and B_0' were found to be 172.6 GPa and 4.1, respectively for $U = 6$ eV. Since corresponding values from experiments are lacking, it was not possible to compare these numbers with corresponding experimental values for this material.

3.2. Electronic and magnetic structures of $EuTiO_3$

The total energy and total density of states (DOS) were calculated for the four magnetic configurations, F, A, C, and G, at the experimental lattice constant for $U = 0$, 3, 5, 6 7, 8, and 9 eV. Table 1 lists the relative energies of the different configurations for each value of U. The lowest energy is assigned the value zero as reference energy. It is found that the G-type AFM structure possesses lowest energy for $U \leqslant 6$ eV. For $U \geqslant 7$ eV, the ferromagnetic (F) structure becomes stable (see table 1). Previous theoretical studies on divalent Eu compounds have reported that realistic values of U for Eu lie in the range $6 \leqslant U \leqslant 9$ eV [16, 17]. Interestingly enough, we found that, at $U = 6$ eV, the ground-state magnetic configuration changes from G-type AFM to ferromagnetic (F) on increasing the volume hydrostatically beyond the experimental value. Figure 4 shows the DOS plots for the F-, A-, C-, and G-type magnetic structures for $U = 6$ eV. The essential features of the DOS plots for all the

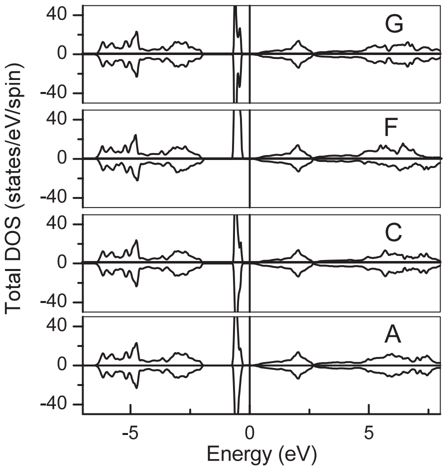

Figure 4. Total density of states for A, C, F, and G magnetic structures of $EuTiO_3$ with $U = 6$ eV.

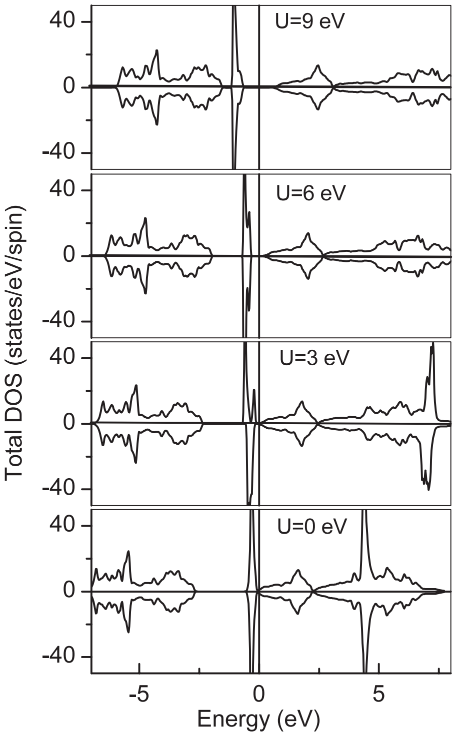

Figure 5. Total density of states for different values of U for the G-type magnetic structure of $EuTiO_3$.

configurations appear similar. Figure 5 shows representative DOS plots for the G-type AFM structure calculated at different U values. It is interesting to note that, compared to the occupied lower Hubbard f band, the unoccupied upper Hubbard f band shifts quite drastically with increasing U. For $U = 0$ and 3 eV, the Fermi energy lies near the edge of the Ti 3d band,

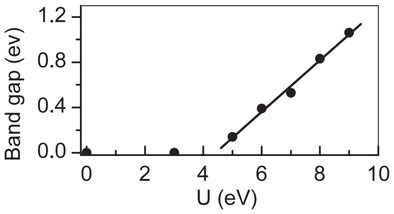

Figure 6. Variation of band gap of $EuTiO_3$ with U.

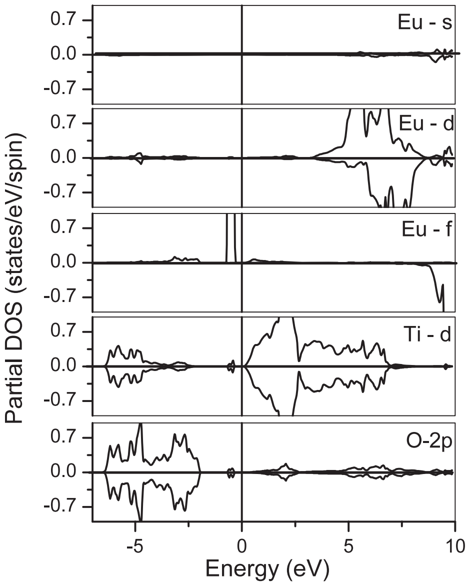

Figure 7. Partial density of states of Eu s, Eu d, Eu f, Ti d, and O p orbitals for the G-type magnetic structure ($U = 6$ eV).

resulting in a metallic behaviour. A gap opens up for $U \geqslant 5$ eV. Figure 6 shows the variation of band gap with U. The band gap increases from 0.14 eV at $U = 5$–1.1 eV for $U = 9$ eV. A band structure plot revealed that the minimum of the band gap corresponds to the Γ point. The filled f band just below the Fermi level was nearly dispersionless. The maximum value of the gap (2.1 eV for $U = 6$ eV) occurs at the R and X points of the cubic Brillouin zone.

Figure 7 shows the partial density of states (PDOS) for the O p states, Eu f and d states, and Ti d states in both spin channels. It is evident from this figure that the major contribution to the filled valence band comes from the O 2p states. A narrow occupied 4f band lies just below the Fermi level. A similar feature was also reported in the band structure of EuS [14]. The conduction band is formed by the Ti 3d states on the low-energy side and by the Eu 5d states at higher energies. Some fraction of the Ti d states is also occupied, suggesting some covalent bonding between the Ti and the O atoms, a feature common to most of the oxide perovskites. The absence of the Eu s states in the valence band part of the DOS suggests that Eu is almost completely ionized and forms ionic bonds with the O in the structure.

Table 2. Values of the first-nearest-neighbour (J_{ij}^{nn}) and second-nearest-neighbour (J_{ij}^{nnn}) exchange integrals (in units of kelvin) obtained after mapping the difference in the total energies of the various configurations, mentioned above, to a Heisenberg Hamiltonian (see text).

Exchange integral	$U = 0$ eV	$U = 3$ eV	$U = 5$ eV	$U = 6$ eV	$U = 7$ eV	$U = 8$ eV	$U = 9$ eV
J_{ij}^{nn} (K)	−0.12	−0.24	−0.06	0.01	0.03	0.05	0.06
J_{ij}^{nnn} (K)	0.26	0.12	0.08	0.05	0.04	0.03	0.02

3.3. Estimation of exchange integrals

We have calculated the nearest-neighbour (nn) and next-nearest-neighbour (nnn) exchange interactions (J_{ij}^{nn} and J_{ij}^{nnn}) by mapping the energy difference between the different magnetic configurations of this system to the Heisenberg Hamiltonian as [23]

$$H = -2 \sum_{i>j}^{N} J_{ij} S_i \cdot S_j . \tag{2}$$

The ground state of Eu^{2+} ion corresponds to spin $S = 7/2$ and orbital moment $L = 0$. The zero orbital moment adds a simplification to the calculations in the sense that the exchange interaction can be treated isotropic to a good approximation. The total numbers of nn and nnn Eu^{2+} bonds in the tetragonal cell considered for calculating the total energies are 12 and 20 respectively. The corresponding energy expressions for the four magnetic configurations, F, A, C, and G can be written as

$$E_{\mathrm{F}} = E_0 + 2|S|^2(-12J_{ij}^{\mathrm{nn}} - 24J_{ij}^{\mathrm{nnn}}) \qquad \text{for F type,} \tag{3}$$

$$E_{\mathrm{A}} = E_0 + 2|S|^2(-4J_{ij}^{\mathrm{nn}} + 8J_{ij}^{\mathrm{nnn}}) \qquad \text{for A type,} \tag{4}$$

$$E_{\mathrm{C}} = E_0 + 2|S|^2(4J_{ij}^{\mathrm{nn}} + 8J_{ij}^{\mathrm{nnn}}) \qquad \text{for C type,} \tag{5}$$

and

$$E_{\mathrm{G}} = E_0 + 2|S|^2(12J_{ij}^{\mathrm{nn}} - 24J_{ij}^{\mathrm{nnn}}) \qquad \text{for G type.} \tag{6}$$

Since $S = 7/2$, $|S|^2 = S(S+1) = 15.5$ for Eu^{2+}. The values of the exchange interactions obtained with least squares fitting procedure, in units of kelvin, are listed in table 2. While J_{ij}^{nn} changes sign from negative to positive between $U = 5$ and 6 eV, the sign of J_{ij}^{nnn} remains positive for all values of U under consideration. In general, it is noted that the value of J_{ij}^{nn} increases and that of J_{ij}^{nnn} decreases upon increase of U. Values of exchange integrals in ETO have also been reported in the past using parameters derived from temperature-dependent magnetic susceptibility measurements [5, 6]. The values of J_{ij}^{nn} and J_{ij}^{nnn} reported in [5] are −0.02 and 0.04 K, respectively. Chien *et al* [6], on the other hand, have reported a slightly different value, $J_{ij}^{\mathrm{nn}} = -0.014$ K and $J_{ij}^{\mathrm{nnn}} = 0.037$ K. It is evident from table 2 that a similar value of J_{ij}^{nn} can be obtained theoretically for a value of U somewhere in the range $5 \leqslant U \leqslant 6$ eV. The small values of the exchange constants indicate a very weak interaction between the magnetic ions in ETO. For EuO ($T_{\mathrm{C}} = 69$ K), the values of J_{ij}^{nn} and J_{ij}^{nnn} have been reported to be 0.72 and 0.22 K, respectively [14]. As can be noted, J_{ij}^{nn} in EuO is nearly 35 times larger than in ETO. This difference can be attributed in part to the larger Eu–Eu bond distances in ETO compared to EuO, and also to the relative arrangement of the oxygen ions around the Eu. In ETO the first-nearest-neighbour and the second-nearest-neighbour Eu ions lie at 3.91 Å, and 5.53 Å, respectively, while in EuO they are at 3.63 Å and 5.14 Å [24]. The second important factor is the fact that there are 12 oxygen atoms surrounding each Eu ion in the ETO structure as compared to 6 in EuO. This would result in a stronger shielding of the d-state-mediated direct exchange interactions between the Eu ions in ETO compared to EuO, thereby weakening the strength of the exchange interactions in the former compound. In addition, the increased number of 90° cation–anion–cation superexchange between nearest-neighbour Eu atoms may promote ferromagnetic order, leading to a small negative value of J_{ij}^{nn} in ETO.

3.4. *Incipient magnetoelectricity and possibility of non-collinear magnetic structure*

As noted above, the exchange interactions are very weak in ETO, and J_{ij}^{nn} even changes sign in the critical region of U. The system seems to be critically balanced between a ferromagnetic (F) state and a G-type antiferromagnetic state. Further, the fact that the system is known to exhibit a dielectric anomaly at the magnetic ordering temperature (5.5 K) suggests that ETO may be considered as an incipient magnetoelectric multiferroic material. In the normal magnetoelectric multiferroics such as $\mathrm{RMnO_3}$ (with R = Tb, Gd) [7, 25], $\mathrm{RMn_2O_5}$ (R = Y, Tb etc) [26], and hexaferrite [27], the ferroelectric order preferentially develops in spiral or helicoidal magnetic structures. The inversion symmetry in spiral magnetic structures is intrinsically broken, and such systems are close to becoming ferroelectric. The magnetic spiral can influence the charge and lattice via Dzyaloshinskii's antisymmetric exchange [28] to produce a ferroelectric state [29]. Although no ferroelectric behaviour has been reported in ETO, the anomaly in the dielectric permittivity at 5.5 K is indicative of a tendency to develop such an order. Since the temperature concerned is quite low, the quantum-mechanical fluctuations of the lattice, as has been reported in $\mathrm{SrTiO_3}$ [30], can suppress the onset of a regular ferroelectric state. In view of these recent developments in the understanding of the magnetoelectric multiferroic materials, and also the small energy difference between the various magnetic configurations observed in our calculations, a possibility of a non-collinear magnetic configuration in ETO cannot be completely ruled out. It may be mentioned again that due to very large absorption cross section of naturally occurring Eu for thermal neutrons, it is not easy to determine the magnetic structure of Eu compounds by neutron diffraction experiments.

4. Summary

We have studied the electronic structure and magnetic properties of cubic $\mathrm{EuTiO_3}$ using density-functional theory + Hubbard U (LDA + U). The lowest-energy state corresponds to a G-type antiferromagnetic structure for $U \leqslant 6$ eV and a ferromagnetic (F) structure for $U \geqslant 7$ eV. The values of the first- and second-nearest-neighbour exchange integrals have been calculated by mapping the energy difference between four different magnetic configurations onto a Heisenberg Hamiltonian. The system is critically balanced between ferromagnetic and antiferromagnetic states for realistic values of U. The system switches from G-type AFM to a ferromagnetic ground state on increasing volume, opening a possibility of tailoring its magnetic properties, and also perhaps the associated dielectric properties, by appropriate chemical substitutions at the Ti site of this material.

Acknowledgments

RR is grateful to the Alexander von Humboldt foundation for the award of a Humboldt research fellowship during his stay in Germany. We thank Jan Kuneš for helpful discussions.

References

[1] Borous J, Fankuchen I and Banks E 1953 *Acta Crystallogr.* **6** 67
[2] Shafer M W 1965 *J. Appl. Phys.* **36** 1145

[3] Janes D L, Bodnar R E and Taylor A L 1978 *J. Appl. Phys.* **49** 1452
[4] Katsufuji T and Takagi H 2001 *Phys. Rev.* B **64** 054415
[5] McGuire T R, Shafer M W, Joenk R J, Alperin H A and Pickart S J 1966 *J. Appl. Phys.* **37** 981
[6] Chien C-L, De Benedetti S and Barros F De S 1974 *Phys. Rev.* B **10** 3913
[7] Kimura T, Goto T, Shintani H, Ishizaka K, Arima T and Tokura Y 2003 *Nature* **426** 55
[8] Fiebig M 2005 *J. Phys. D: Appl. Phys.* **38** R123
[9] Hill N A 2002 *Annu. Rev. Mater. Res.* **32** 1
[10] Fennie C J and Rabe K M 2006 *Phys. Rev. Lett.* **97** 267602
[11] Blaha P, Schwarz K, Madsen G K H, Kvasnicka D and Luitz J 2001 *WIEN 2k, An Augmented Plane Wave + Local Orbitals Program for Calculating Crystal Properties* Karlheinz Schwarz, Techn. Universität Wien, Wien (ISBN 3-9501031-1-2)
[12] Perdew J P, Bruke K and Ernzerhof M 1996 *Phys. Rev. Lett.* **77** 3865
[13] Anisimov V I, Solovyev I V, Korotin M A, Czyzyk M T and Swatzky G A 1993 *Phys. Rev.* B **48** 16929
[14] Larson P and Lambrecht W R L 2006 *J. Phys.: Condens. Matter* **18** 11333
[15] Kuneš J and Pickett W E 2005 *Physica* B **359–361** 205
[16] Kuneš J, Ku W and Pickett W E 2005 *J. Phys. Soc. Japan* **74** 1408 (*Preprint* cond-mat/0406229)
[17] Kuneš J and Pickett W E 2004 *Phys. Rev.* B **69** 165111
[18] Kuneš J and Laskowski R 2004 *Phys. Rev.* B **70** 174415
[19] Søndenå R, Ravindran P, Stølen S, Grande T and Hanfland M 2006 *Phys. Rev.* B **74** 144102
[20] Ravindran P, Kjekshus A, Fjellvåg H, Delin A and Eriksson O 2002 *Phys. Rev.* B **65** 064445
[21] Murunaghan F D 1944 *Proc. Natl Acad. Sci. USA* **30** 244
[22] Anderson O L 1995 *Equations of State of Solids for Geophysics and Ceramic Science* (New York: Oxford University Press)
[23] Yosida K 1996 *Theory of Magnetism* (*Springer Series in Solid State Sciences* vol 122) (Berlin: Springer) chapter 6
[24] Mc Guire T R and Shafer M W 1964 *J. Appl. Phys.* **35** 984
[25] Kenzelman M, Harris A B, Jonas S, Broholm C, Schefer J, Kim S B, Zhang C L, Cheong S-W, Vajk O P and Lynn J W 2005 *Phys. Rev. Lett.* **95** 087206
[26] Hur N *et al* 2004 *Nature* **429** 392
[27] Kimura T, Lawes G and Ramirez A P 2005 *Phys. Rev. Lett.* **94** 137201
[28] Segienko I E and Dagotto E 2005 *Preprint* cond-mat/0508075
[29] Anderson P W and Blount E I 1965 *Phys. Rev. Lett.* **4** 217
[30] Müller K A and Burkard H 1979 *Phys. Rev.* B **19** 3593

JOURNAL OF APPLIED PHYSICS **105**, 053905 (2009)

First principles study of magnetism in divalent Eu perovskites

Rajeev Ranjan,[1,a)] Hasan Sadat Nabi,[2] and Rossitza Pentcheva[2]
[1]*Department of Materials Engineering, Indian Institute of Science, Bangalore-560012, India*
[2]*Department fur Geo-und Umweltwissenschaften, Sektion Kristallographie, Ludwig Maximilians Universität, Theresienstr. 41, 80333 München, Germany*

(Received 16 November 2008; accepted 6 January 2009; published online 5 March 2009)

A comparative first principles study has been carried out for $EuLiH_3$ (ELH) and $EuTiO_3$ (ETO) using the generalized gradient approximation $+U$ approach. While ELH exhibits ferromagnetic ground state for all volumes, the magnetic ground state of ETO has the tendency to switch from *G*-type antiferromagnetic to a ferromagnetic state with change in volume. The marked difference in magnetic behavior and magnitude of the nearest neighbors exchange interaction of both the compounds are shown to be related to the difference in their respective electronic structure near the Fermi level. The Ti 3*d* states are shown to play predominant role in weakening the strength of the exchange interaction in ETO. © *2009 American Institute of Physics*. [DOI: 10.1063/1.3079791]

I. INTRODUCTION

With the emergence of "spintronics," there is significant interest in the area of magnetic semiconductors. Divalent europium chalcogenides are among the important compounds in this regard.[1] In this family, while EuO and EuS exhibit a ferromagnetic (*F*) ground state,[2] EuSe and EuTe are antiferromagnetic[3] (AFM) at ambient pressure. The magnetism in these compounds arises from the half filled 4*f* orbitals of the divalent Eu^{2+} ion. Apart from the chalcogenide family, the divalent oxidation state of Eu is also present in compounds crystallizing in the cubic perovskite structure such as $EuTiO_3$ (ETO) (Refs. 4–6) and $EuLiH_3$ (ELH).[7–9] ETO shows *G*-type AFM ordering below 5.5 K and exhibits significant spin-lattice coupling at low temperatures.[10] A possibility of multiferroic behavior in thin ETO film has also been predicted recently.[11] ELH, on the other hand, exhibits ferromagnetic behavior,[7–9] and hence with regard to the magnetic structure, ELH is akin to EuO. Furthermore, it has been known that the magnitude of the effective nearest neighbor (nn) exchange interaction (J_1) of ETO is considerably smaller than that of EuO and ELH.[5,7] Chien *et al.*[5] have proposed intra-atomic 4*f*-5*d* exchange interaction, on the lines of Goodenough[12] and Kasuya,[13] to explain for this abnormal difference. It has been suggested that the exchange interaction (J_1) between the nn Eu cations is of the form $J_1 \sim J_{intra} b^2/\Delta^2$, where b is a transfer integral between nn cations, Δ is the energy separation between 4*f* and 5*d* levels of Eu, and J_{intra} is the Hund's rule coupling constant.[5] In view of the similarity of the Eu-Eu distance, to a first approximation b was treated to be nearly constant for EuO, ETO, and ELH. The difference in the magnitudes of J_1 was therefore attributed to the difference in the magnitude of Δ, which in turn is dependent on the magnitude of the crystal field splitting of the 5*d* states. A larger crystal field splitting would cause the e_g level to come close to the 4*f* level and thereby reduce the value of Δ.[5] In this scenario, the anomalously small magnitude of the J_1 in ETO, as compared to ELH and EuO, has been explained by proposing a relatively weak crystal field splitting of the Eu 5*d* states in ETO as compared to ELH and EuO.[5] In this paper, we have examined this issue using first principles calculations. It is demonstrated that the similarity of the magnetic behavior of ELH and EuO is closely related to similarity of their respective electronic structures near the Fermi level. The presence of Ti 3*d* states just above the Fermi level in ETO completely alters the relative disposition of the Eu 4*f* and 5*d* bands, and weakens the exchange interaction.

II. COMPUTATIONAL DETAILS

LSDA+U method was used to describe the correct filling and positions of the Eu 4*f* bands.[14] This approach has been successful in predicting the magnetic behavior of the Eu-based systems.[11,15–20] Furthermore, the divalent state of Eu (Eu^{2+}) results in half filling of the Eu 4*f* shell and thereby reduces the role of J to merely normalizing the U value. We can, therefore, set $J=0$ and make use of an effective U in the calculations.[16–19] The calculations were performed using the WIEN2K[21] implementation of the full-potential linearized augmented-plane-waves (FLAPW) method. The exchange-correlation potential is approximated by the generalized-gradient approximation (GGA) of Perdew *et al.*[22] The muffin-tin radii of Eu, Li, and H were fixed at 2.7, 1.6, and 1.2 bohr, respectively. A cutoff of $R_{mt}K_{max}=5$ and a total of 800-*k*-grid points (84 irreducible *k* points) are used to achieve an energy convergence of ±0.04 mRy. A tetragonal unit cell, the *a* and *b* lattice parameters of which are face diagonals of one of the cube face, and the *c* parameter of which is twice the lattice parameter, was chosen to realize four different magnetic structures: namely, ferromagnetic (*F*) and three AFM (*A*, *C*, and *G* types), within the same volume. The spin configurations corresponding to the four magnetic structures are shown in Fig. 1. The total energies were calculated as a function of volume for different U values. For each spin configuration E_{tot}^{min} was mapped on a Heisenberg Hamiltonian,

---

[a)] Author to whom correspondence should be addressed. Electronic mail: rajeev@materials.iisc.ernet.in.

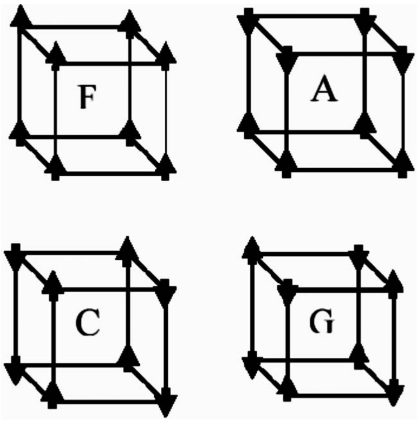

FIG. 1. Schematic depiction of the F, A, C, and G type magnetic structures. The arrows represent spin direction in a cubic lattice.

$$H = -2\sum_{i>j}^{N} J_{ij} S_i \cdot S_j, \tag{1}$$

to determine the first (J_1) and second (J_2) nn effective exchange interactions.

III. RESULTS AND DISCUSSION

Table I lists the relative energies of the four magnetic structures of ELH for different values of U. It is evident that the ferromagnetic state has the lowest energy for all U. This may be contrasted with ETO for which it has been reported that, on increasing U beyond 6 eV, the lowest energy state switches from G-type AFM to ferromagnetic structure.[20] The total number of nn and next nearest neighbor (nnn) Eu^{2+} bonds in the tetragonal cell considered are 12 and 24, respectively. Energy expression (1) for the four magnetic configurations, F, A, C, and G, therefore takes the form:

$$E_F = E_0 + 2|S|^2(-12J_1 - 24J_2) \quad \text{for } F \text{ type}, \tag{2}$$

$$E_A = E_0 + 2|S|^2(-4J_1 + 8J_2) \quad \text{for } A \text{ type}, \tag{3}$$

$$E_C = E_0 + 2|S|^2(4J_1 + 8J_2) \quad \text{for } C \text{ type}, \tag{4}$$

and

$$E_G = E_0 + 2|S|^2(12J_1 - 24J_2) \quad \text{for } G \text{ type}, \tag{5}$$

where E_0 is the part of the total energy without exchange interaction. By subtracting any two of the above expressions, we obtain a total of six equations. J_1 and J_2 were obtained in units of Kelvin by least-squares fitting of these six difference equations. Figure 2 depicts the variation in the J_1 and J_2 as a function of U. Previous studies have shown that the realistic value of U for Eu-based systems lies in the range of 5–7 eV.[16–20] For ETO, U close to 6 eV was found to give exchange interactions, J_1 and J_2, very close to the experimentally obtained values.[20] Assuming the U parameter of Eu for ELH to be similar to that for the ETO, we obtain $J_1 \sim 0.53$ K and $J_2 \sim 0.06$ K for ELH (Fig. 2). These values are reasonably close (within the experimental error) to the ones reported earlier ($J_1 = 0.8 \pm 0.2$ K, $J_2 = \pm 0.05$) using susceptibility data.[8,9] A comparison of the magnitudes of J_1 of ELH, ETO, and EuO reveals that it is more than an order of magnitude smaller in ETO ($J_1 \sim 0.01$ K) (Ref. 19) than ELH (Refs. 8 and 9) and EuO ($J_1 = 0.72$ K).[16] To investigate the sensitivity of J_1 to the nn Eu-Eu distance, calculations were performed at different cell volume of ELH so as to cover the Eu-Eu distance observed in EuO (3.63 Å) and ETO (3.905 Å).

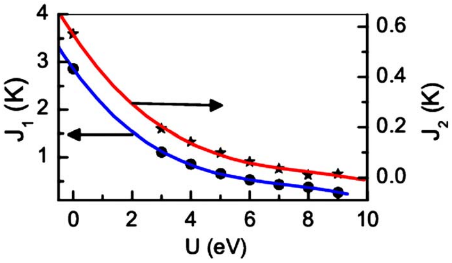

FIG. 2. (Color online) Variation in first (J_1) and second (J_2) nn effective exchange interactions of $EuLiH_3$ with U.

Figure 3 shows the total energy curves of ELH versus cell volume for the four magnetic structures mentioned above at $U = 6$ eV. The energy of the ferromagnetic state was found to be lowest for all volumes. The cubic lattice parameter corresponding to the equilibrium volume is 3.78 Å, which is almost the same as the experimental value of 3.79 Å reported for this compound.[9] Figure 4 shows the exchange interactions (J_1 and J_2) as a function of the cubic lattice parameter, which is also the nn Eu-Eu distance for the perovskite structure. It is evident from this graph that J_1 and J_2 at 3.905 Å (corresponding to the Eu-Eu distance in ETO) are 0.41 and 0.03 K, respectively. The value of J_1 is still considerably larger than the value reported for ETO.[20] Furthermore, J_1 and J_2 obtained from extrapolation of the fitted curves at 3.63 Å (corresponding to the Eu-Eu distance in EuO) are found to be 1.0 and 0.17 K, respectively. Considering the fact that the crystal structure of EuO is different from that of ELH, these values are not very much off from

TABLE I. Relative energies of the various magnetic structures of $EuLiH_3$ calculated at different values of U. For each U, the minimum energy among the four configurations has been set to zero.

	Relative energy (eV)							
Magnetic structure	$U=0$ eV	$U=3$ eV	$U=4$ eV	$U=5$ eV	$U=6$ eV	$U=7$ eV	$U=8$ eV	$U=9$ eV
F	0	0	0	0	0	0	0	0
A	0.110	0.039	0.029	0.021	0.015	0.009	0.006	0.002
C	0.175	0.066	0.051	0.038	0.030	0.022	0.017	0.012
G	0.186	0.071	0.055	0.042	0.033	0.026	0.021	0.017

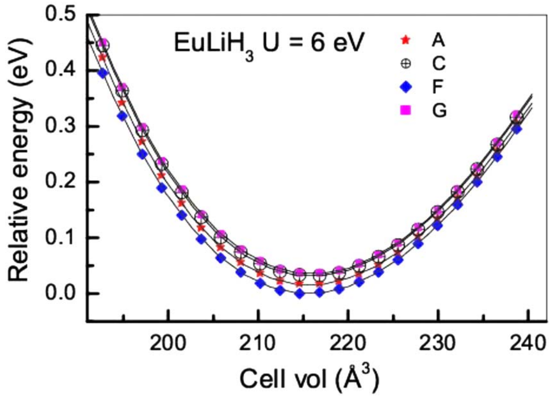

FIG. 3. (Color online) Variation in the relative energy of the A, C, F, and G magnetic structures of $EuLiH_3$ as a function of unit cell volume calculated for $U=6$ eV. The minimum energy in the graph is chosen as the reference energy and is set at zero. The volume corresponds to the bigger (tetragonal) unit cell whose volume is four times the cubic cell volume.

what has actually been reported ($J_1=0.72$ K and $J_2=0.22$ K) for EuO.[16] This analysis, therefore, suggests that the Eu-Eu distance cannot be the primary factor affecting the strength of J_1 in ETO.

Figure 5 shows the energy difference between the two competing magnetic states F and G of ETO as a function of volume. A switching from a G-type AFM state to a ferromagnetic state is observed around the experimental volume for $U\sim6$ eV [Fig. 5(b)]. The critical volume is, however, sensitive to U as shown in Figs. 5(a) and 5(c). A similar trend was observed for biaxial and uniaxial strains as well although the energy difference between the G and F states was noted to decrease further when decreasing the dimensionality of strain. This prediction of a transition to a ferromagnetic state during change in volume is in conformity with the ferromagnetic state reported recently in thin ETO films.[23]

Figure 6 shows the partial density of states (DOS) of the ground state magnetic structures of ELH and ETO, both calculated at $U=6$ eV. The absence of s states of Eu in the conduction band indicates that Eu forms highly ionic bonds with H and O in ELH and ETO, respectively. A noticeable hybridization between the Eu 5d and H s states, however, suggests a considerable degree of covalent character in the Eu-H bond of ELH. Furthermore, the absence of Li s states in the conduction band seems to suggest a strongly ionic nature of the Li-H bond. In contrast, the Ti-O bond in ETO has a significant covalent contribution as evident from the hybridization between the O 2p and Ti 3d states.

The valence bands of both the ELH and ETO are formed by the valence states of their respective anions. The narrow Eu 4f band lies between the Fermi level and the broad valence band in both the cases. A similar feature has been reported for EuO as well.[16] Similar to EuO, the conduction

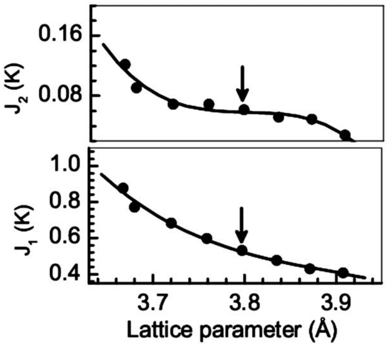

FIG. 4. Variation in J_1 and J_2 with cubic lattice parameter of $EuLiH_3$. The solid curves are fitted lines with a third order polynomial. The arrows indicate the lattice parameter corresponding to the equilibrium value.

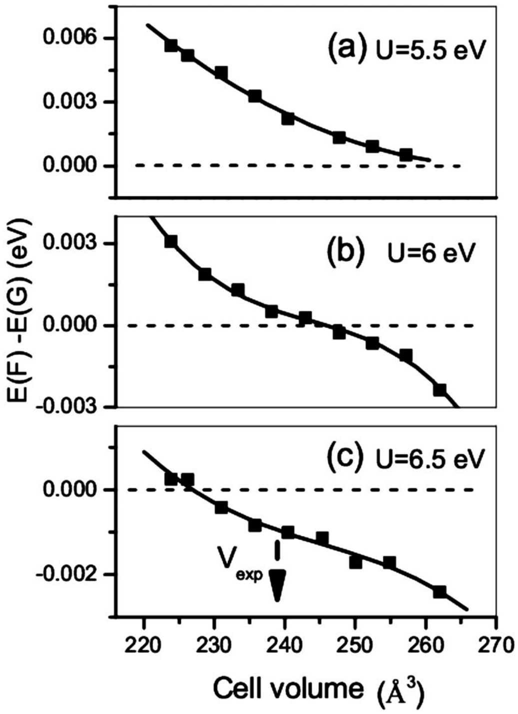

FIG. 5. Energy difference between F and G magnetic structures of $EuTiO_3$ as a function of cell volume. The arrow in the figure denotes the equilibrium volume.

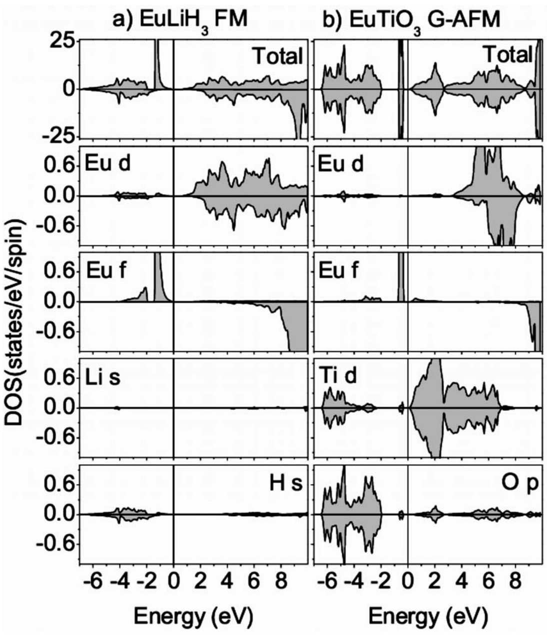

FIG. 6. (a) DOS of ferromagnetic $EuLiH_3$ and (b) G-type AFM of $EuTiO_3$ at $U=6$ eV. The top panel is the total DOS while the rest corresponds to partial DOS.

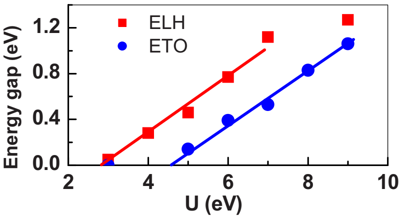

FIG. 7. (Color online) Variation in the band gap of ELH and ETO with U.

band of ELH is formed by the Eu $5d$ states. This band starts at ~0.8 eV above the Fermi level and spreads up to ~11 eV, i.e., a bandwidth of about 10 eV. On the other hand, the conduction band in ETO is formed by Ti $3d$ states. The Eu $5d$ band starts at 3.5 eV above the Fermi level and persists up to 8.6 eV, i.e., a bandwidth of ~5 eV. The width of the Eu $5d$ band in ETO is, therefore, nearly half the corresponding value in ELH. Furthermore, there is a significant overlap of the Eu $5d$ and Ti $3d$ bands in the energy range of 3.5–7 eV. In the framework of the mechanism proposed by Chien *et al.*,[5] this feature may influence strongly the exchange interaction in this system as compared to ELH. Figure 7 shows the variation in the band gap of ELH, i.e., the difference in the energy of the top of the $4f$ band and the bottom of the Eu $5d$ conduction band, with U. For sake of comparison we have also included the band gap variation with U of ETO. It may be mentioned that, in the later case, the band gap is between the Eu $4f$ and the Ti $3d$ state. Linear extrapolation through the data points suggests that the gap in ELH and ETO opens above $U=2.8$ eV and 4.6 eV, respectively. At the realistic value of the U, i.e., $U=6$ eV, the gaps in ELH and ETO are ~0.8 and ~0.4 eV, respectively. Due to the larger gap, ELH is expected to exhibit a better insulating property than ETO at any finite temperature.

In conclusion, we have shown that GGA+U approach correctly predicts the ferromagnetic ground state of $\mathrm{EuLiH_3}$. Mapping the total energies of four different magnetic structures on a Heisenberg Hamiltonian, the extracted first and second nn effective exchange interactions was found to be in good agreement with experimental values. With regard to the relative position of the $4f$ and $5d$ Eu bands in ELH and ETO, our results not only confirm the schematic model proposed earlier by Chien *et al.*[5] but also throw new light with regard to the factors at play in determining this energy difference. The intervening Ti $3d$ states between the Eu $4f$ and $5d$ states seem to push the Eu $5d$ band to higher energies in ETO. Furthermore, in the context of the exchange mechanism proposed by Chien *et al.*,[5] the significant overlap of the Ti $3d$ and Eu $5d$ bands would imply that the Ti $3d$ band should also participate in the exchange process. The results clearly demonstrate the unique role of Ti $3d$ states in drastically decreasing the effective J_1 value in $\mathrm{EuTiO_3}$ as compared to $\mathrm{EuLiH_3}$ and EuO.

ACKNOWLEDGMENTS

We acknowledge gratefully the computational grant at the Leibniz Rechenzetrum. R.P. acknowledges discussions with Darrell Schlom.

[1] A. Mauger and C. Godart, Phys. Rep. **141**, 51 (1986).
[2] L. Passell, O. W. Dietrich, and J. Als-Nielsen, Phys. Rev. B **14**, 4897 (1976).
[3] M. Ishizuka, Y. Kai, R. Akimoto, M. Kobayashi, K. Amaya, and S. Endo, J. Magn. Magn. Mater. **166**, 211 (1997).
[4] M. W. Shafer, J. Appl. Phys. **36**, 1145 (1965).
[5] Chia-Ling Chien, S. DeBenedetti, and F. De S. Barros, Phys. Rev. B **10**, 3913 (1974).
[6] T. R. McGuire, M. W. Shafer, R. J. Joenk, H. A. Alperin, and S. J. Pickart, J. Appl. Phys. **37**, 981 (1966).
[7] J. E. Greedan, Cahi-Liang Chien, and R. G. Johnston, J. Solid State Chem. **19**, 155 (1976).
[8] Chia-Ling Chien and J. E. Greedan, Phys. Lett. **36A**, 197 (1971).
[9] J. E. Greedan, J. Phys. Chem. Solids **32**, 819 (1971).
[10] T. Katsufuji and H. Takagi, Phys. Rev. B **64**, 054415 (2001).
[11] C. J. Fennie and K. M. Rabe, Phys. Rev. Lett. **97**, 267602 (2006).
[12] J. D. Goodenough, *Magnetism and the Chemical Bond* (Interscience, New York, 1963), pp. 146–167.
[13] T. Kasuya, IBM J. Res. Dev. **14**, 214 (1970).
[14] V. I. Anisimov, I. V. Solovyev, M. A. Korotin, M. T. Czyzyk, and G. A. Sawatzky, Phys. Rev. B **48**, 16929 (1993).
[15] P. Larson and W. R. L. Lambrecht, J. Phys.: Condens. Matter **18**, 11333 (2006).
[16] J. Kuneš, W. Ku, and W. E. Pickett, J. Phys. Soc. Jpn. **74**, 1408 (2005).
[17] J. Kuneš and W. E. Pickett, Phys. Rev. B **69**, 165111 (2004).
[18] J. Kuneš and R. Laskowski, Phys. Rev. B **70**, 174415 (2004).
[19] J. Kuneš and W. E. Pickett, Physica B **359–361**, 205 (2005).
[20] R. Ranjan, H. S. Nabi, and R. Pentcheva, J. Phys.: Condens. Matter **19**, 406217 (2007).
[21] P. Blaha, K. Schwarz, G. K. H. Madsen, D. Kvasnicka, and J. Luitz, *2001 WIEN 2k, An Augmented Plane Wave + Local Orbitals for Calculating Crystal Properties* (Karlheinz Schwarz, Techn Universität Wien, Wien).
[22] J. P. Perdew, K. Bruke, and M. Ernzerhof, Phys. Rev. Lett. **77**, 3865 (1996).
[23] K. Kugimiya, K. Fujita, K. Tanaka, and K. Hirao, J. Magn. Magn. Mater. **310**, 2268 (2007).